Self-Assembly of Block Copolymers in Thin Films

A DISSERTATION
SUBMITTED TO THE FACULTY OF THE GRADUATE SCHOOL
OF THE UNIVERSITY OF MINNESOTA
BY

Sangwon Kim

IN PARTIAL FULFILLMENT OF THE REQUIREMENTS
FOR THE DEGREE OF
DOCTOR OF PHILOSOPHY

Frank S. Bates, Advisor

August 2013

© Sangwon Kim 2013

Acknowledgements

First of all, I cannot express how grateful I am towards my supervisor Prof. Frank S. Bates for giving me this rare opportunity to learn and conduct research in the field of polymer physics while my background comes from a completely different discipline (B.S. and M.S. in Electrical Engineering). It could not have been a rewarding experience without his educational support. I would like to thank Prof. Paul F. Nealey, not just for his guidance, but also for encouragement and thoughtful arrangements that really allowed me to go freely to Madison and conduct research. I also would like to express my gratitude for all the committee members.

I have had fortunate opportunities to work with multiple research groups at different institutions. I am grateful to Prof. Paul F. Nealey, Prof. Juan de Pablo, Prof. Padma Gopalan, and their group members (University of Wisconsin at Madison). Especially, I would like to thank Adam Welander, Umang Nagpal, Paulina Rincon, and Lance Williamson, who worked with me on various research projects. The polymers provided by Chris Thode and Eungnak Han have been useful for my thin-film research. I would like to thank Lei Wan, who conducted e-beam patterning for me. I also would like to acknowledge the Willson group and the Ellison group (University of Texas at Austin) for the collaboration.

I could not have survived without the Bates group members who offered me assistance, feedbacks, and friendships. I also benefited greatly from having interactions with other polymer group members in the University of Minnesota. I am indebted to many people at Wisconsin who welcomed me as a friend and helped my research.

I should thank Prof. John B. Goodenough, my previous academic advisor at the University of Texas at Austin. He has been always willing to give me his kind advice

even after I left Austin. His ardor for research at his age will always be a role model for me.

Finally, I would like to thank my parents and sister for love and support.

* Acknowledgements specific to each chapter:

(Chapter 4) The crosslinkable brush material was provided by Chris Thode (Nealey group, Univ. Wisconsin).

(Chapter 5) SMG was synthesized by Chris Thode (Nealey group, Univ. Wisconsin). The PTMSS-PLA and tBSMA results were provided by C. M. Bates, A. Thio, and J. D. Cushen (the Willson group and the Ellison group, Univ. Texas).

(Chapter 6) Crosslinked mat and graft brush materials have been provided by Chris Thode (SMG0, SMG28, SMG57, SMG76, SMG94) and Eungnak Han (SMG60, SMOH25, SMOH45) at the University of Wisconsin − Madison. The e-beam exposure for chemical pattern fabrication has been conducted by Lei Wan (Hitachi Global Storage Technologies).

(Chapter 7) SMG60, SMOH43, and SMOH50 mat/brush materials have been provided by Eungnak Han (Gopalan group, Univ. Wisconsin). One TEM micrograph of SIM18 has been taken by Hanseung Lee (McCormick group, Univ. Minnesota) using FEI Tecnai G2 F30. Paulina Rincon (Nealey group, Univ. Wisconsin) fabricated the chemical pattern and used it to direct the self-assembly of SIM18 thin films. Chris Thode (Nealey group, Univ. Wisconsin) synthesized SMG94 materials.

To my parents.

Abstract

The self-assembly of block copolymers in thin films has been a subject of recent studies from both academic and industrial perspectives. One of its potential applications is nanolithography; block copolymers can function as novel mask materials intended for fabrication of small features, not easily realizable by current optical lithography. This dissertation addresses several fundamental issues associated with thin-film block copolymers.

The bulk and interfacial wetting properties of partially epoxidized poly(styrene-*b*-isoprene) diblock copolymers, denoted as PS-PEI, were studied while varying the degree of the chemical modification. The incorporation of the random copolymer architecture induced decoupling between the bulk and the thin-film thermodynamics. The tunable surface wetting, a consequence of the partial modification, permitted control over the orientation of the domains in thin films.

The morphologies of thin-film block copolymers were investigated using two different boundary conditions that involve one neutral interface and one preferential interface. The neutralities at the free surface and the underlying substrate were attained independently by the partial epoxidation in PS-PEI and the composition adjustment of random copolymer mats, respectively. For both boundary conditions, thin-film block copolymers formed an island/hole motif, characterized by 0.5 L_0 step heights (L_0: bulk lamellar periodicity).

The thin-film behavior of PS-PEI block copolymers with random copolymer architecture was examined as the segregation strength (χN) was adjusted systematically across the order-disorder transition. Unlike in the bulk, the random copolymer architecture did not generate abnormal behavior in thin-film thermodynamics compared to plain linear architecture. With decreasing segregation strength, the thin-film system

exhibited fluctuation-pervaded morphologies prior to reaching a disordered state. An agreement was found between the order-disorder transition temperatures in three dimensions (bulk) and in two dimensions (thin film).

Lastly, the bulk properties and the thin-film structures of lamellae-forming poly(styrene-*b*-isoprene-*b*-methyl methacrylate) (SIM) triblock copolymers were studied. The thin-film morphology exhibited the dependence on the size of the poly(isoprene) (PI) middle block. While perpendicular lamellae were observed for the thin-film SIM block copolymer with a small PI volume fraction, complex behavior was observed for the sample with a large PI volume fraction.

Table of Contents

List of Tables ix

List of Figures x

Chapter 1 Introduction 1

- 1.1 Self-Assembly of Block Copolymers in Thin Films....1
- 1.2 Thesis Outline 3

Chapter 2 Background 5

- 2.1 General Background 5
  - 2.1.1 Bulk Block Copolymers and Long-Range Ordering....5
  - 2.1.2 Thin-Film Polymers and Blends: Consequences of Confinements ...10
- 2.2 Thin-Film Block Copolymers: Nanolithography....12
  - 2.2.1 Conventional Optical Lithography and Its Limitation....18
  - 2.2.2 Morphology Orientation Control in Thin-Film Block Copolymers...20
    - 2.2.2.1 Interface Modification....20
    - 2.2.2.2 Solvent Annealing....22
    - 2.2.2.3 Electric Fields 24
  - 2.2.3 Long Range Ordering in Thin-Film Block Copolymers....27
    - 2.2.3.1 Chemical Patterns and Density Multiplication 27
    - 2.2.3.2 Graphoepitaxy....31
- 2.3 Random Copolymers and Chemical Modification....34
  - 2.3.1 Solubility Parameter Formalism 35
  - 2.3.2 Binary Interaction Model....37
  - 2.3.3 Epoxidation 39

Chapter 3 Experimental Methods 43

- 3.1 Synthesis of Block Copolymers....44
  - 3.1.1 Controlled Anionic Polymerization 44
  - 3.1.2 Synthetic Procedures....45
  - 3.1.3 Selective Partial Epoxidation....48
- 3.2 Characterization Techniques in Bulk....49

3.2.1 Size Exclusion Chromatography (SEC)....49
3.2.2 Nuclear Magnetic Resonance Spectrometry (^{1}H-NMR)....50
3.2.3 Small Angle X-ray Scattering (SAXS)....51
3.2.4 Differential Scanning Calorimetry (DSC)....54
3.2.5 Dynamic Mechanical Spectroscopy (DMS)....54
3.3 Thin Film Characterization and Chemical Pattern Fabrication....56
3.3.1 Scanning Electron Microscopy (SEM)....57
3.3.2 Atomic Force Microscopy (AFM)....59
3.3.3 Chemical Pattern Fabrication....59
3.3.4 Plasma Treatment....61
Chapter 4 Decoupling Bulk Thermodynamics and Wetting Characteristics of Block Copolymer Thin Films....65
4.1 Introduction....65
4.2 Experimental....67
4.3 Results....69
4.4 Discussion....82
Chapter 5 Consequences of Surface Neutralization in Diblock Copolymer Thin Films....89
5.1 Introduction....89
5.2 Experimental Methods....92
5.3 Results....96
5.4 Discussion....118
5.5 Conclusion....126
Chapter 6 Block Copolymer Self-Assembly in Thin Films: Segregation Strength Variations....128
6.1 Introduction....128
6.2 Experimental....131
6.3 Results....134
6.4 Discussion....157
Chapter 7 Self-Assembly of ABC Triblock Copolymers in Thin Films....168
7.1 Introduction....168

7.2 Experimental Methods 171
7.3 Results and Discussion 173
Bibliography 191
Appendix A. ABA Triblock Copolymers 209
A.1 Experimental 209
A.2 Preliminary Results 210

List of Tables

Table 2.1 Issues and corresponding targets set for directed self-assembly. Reprinted with permission from Herr.[50] Copyright 2011 CUP. 17

Table 4.1 Molecular characterization...70

Table 4.2 Characterization of PS-PIxn..71

Table 5.1 Characterization data of three diblock block copolymers utilized in the present study: PS-PI (preferential free surface), PS-PEI78 (non-preferential free surface), and PTMSS-PLA (preferential free surface)...96

Table 5.2 Characterization data of substrate surfaces utilized in the present study. PS-OH and SMG (57/37/6 mole % PS:PMMA:PGMA) were used with PS-PI and PS-PEI78. tBSMA's (mole % PtBS:PMMA:PVBzAz) were used with PTMSS-PLA block copolymers: tBSMA-15 (15/77/8); tBSMA-23 (23/71/6); tBSMA-25 (25/69/6); tBSMA-34 (34/59/7)..102

Table 6.1 Molecular characterization..135

Table 6.2 The χN estimations for SI21E, SI14E, and SI10E. 159

Table 7.1 Molecular characterization of poly(styrene-*b*-isoprene-*b*-methyl methacrylate) (SIM) triblock copolymers. f, M_n, PDI, and L_0 denote the volume fraction, the molecular weight, the polydispersity index, and the bulk periodicity..174

Table A.1 Molecular characterization..210

List of Figures

Figure 2.1 Schematic diagram of a linear AB diblock copolymer. Poly(styrene) and poly(dimethylsiloxane) are given as examples of A and B blocks. 5

Figure 2.2 Phase diagram for linear poly(styrene-*b*-isoprene) diblock copolymers. χ, N, and f_{PI} denote the interaction parameter, the degree of polymerization, and the volume fraction of the poly(isoprene) block, respectively. Reprinted with permission from Khanpur *et al.*[2] Copyright 1995 ACS. 7

Figure 2.3 Schematics of possible lamella formations in sheared diblock copolymers. Arrows indicate the direction of the shear. Reprinted with permission from Gupta *et al.*[13] Copyright 1996 ACS. 9

Figure 2.4 Schematic illustrations of block copolymer lithography. Thin films of sphere-forming poly(styrene-*b*-butadiene) (PS-PB) block copolymers are used as masks to fabricate features in underlying layers of silicon nitride. *RIE* stands for reactive ion etching. Reprinted with permission from Park *et al.*[35] Copyright 1997 AAAS. 13

Figure 2.5 Dependence of a lamellar morphology formed by block copolymer thin films on the interfacial boundary conditions: (a) the preferential free surface and the preferential underlying substrate; (b) the neutral free surface and the neutral substrate; and (c) the preferential free surface and the neutral substrate. (a-1) and (a-2) correspond to commensurate and incommensurate film thickness for the scenario (a), respectively. <L>, n, and L_0 refer to the average film thickness, an integer, and the lamellar microdomain periodicity, respectively. 15

Figure 2.6 Schematic illustration of conventional optical lithography. Adapted from Plummer *et al.*[51] 19

Figure 2.7 Top-down TEM image of a cylindrical morphology formed by PS-PMMA diblock copolymers adjacent to electrodes. The light lines are PMMA cylinders while the dark regions are PS. (a) With the applied electric fields, domains are aligned parallel to the applied electric field (in-plane alignment). (b) In the absence of electric fields, the domains are randomly oriented. The scale bar corresponds to 500 nm. Reprinted with permission from Morkved *et al.*[73] Copyright 1996 AAAS.. 25

Figure 2.8 Schematic illustrations of (a) cylindrical domains of PS-PMMA diblock copolymers aligned parallel to the applied electric field (perpendicular to the substrate) and (b) the formation of a nanoporous PS template by removal of the PMMA domains. This structure was used to grow nanowires within the pores. Reprinted with permission from Thurn-Albrecht *et al.*[37] Copyright 2000 AAAS.. 27

Figure 2.9 Schematic illustrations of chemical pattern fabrication and directed self-assembly of thin-film block copolymers: (a-b) PET and photoresist deposition; (c) EUV-IL exposure and development; (d) chemical modification of PET SAM's using irradiation; (e) photoresist removal; (f-g) block copolymer thin film deposition and thermal annealing. Reprinted with permission from Kim *et al.*[85] Copyright 2003 NPG. 28

Figure 2.10 Top-down SEM images of non-stripe elements realized using (a-d) PS-PMMA ternary blends and (e) PS-PMMA diblock copolymers. Reprinted with permission from Stoykovich *et al.*[92] and Wilmes *et al.*[93] Copyright 2007 ACS. Copyright 2006 ACS. 30

Figure 2.11 1X and 4X density multiplications. (a-d) Schematic illustrations of chemical pattern fabrication with different densities and directed self-assembly of thin-film block copolymers. Two chemical patterns have periodicities (L_S) of L_0 and 2 L_0, respectively, where L_0 is the periodicity of the thin-film block copolymers. (e-f) Top-down SEM images of the developed e-beam resists, used to make chemical patterns of different periodicities. (g-h) Top-down SEM images of perpendicularly oriented PS-PMMA cylinders, whose self-assembly was guided by the underlying chemical patterns derived from (e-f). Reprinted with permission from Ruiz *et al.*[94] Copyright 2008 AAAS. ...31

Figure 2.12 Schematic illustrations and corresponding microscopy images of aligned morphologies of block copolymers implementing graphoepitaxy (reprinted with permission from the references, as indicated): (a) AFM height image of sphere forming PS-P2VP;[99] (b) AFM height image of PS-PEP;[104] (c) top-down SEM image of PS-PMMA.[107] Copyright 2001 Wiley-VCH. Copyright 2004 ACS. Copyright 2007 Wiley-VCH. 33

Figure 3.1 Schematic representation of procedures required for the synthesis of poly(styrene-*b*-isoprene-*b*-methyl methacrylate) triblock copolymers. DPE and THF denote 1,1-diphenylethylene and tetrahydrofuran, respectively. 46

Figure 3.2 Schematic representation of scattered waves from multiple scattering sources. The parameters $\mathbf{q_i}$, $\mathbf{q_0}$, 2θ, and $\mathbf{r_j}$ denote the wavevectors of incident and scattered waves, the angle between the waves, and the position of the jth scatterer, respectively. **q** (scattering vector) = $\mathbf{q_o} - \mathbf{q_i}$. Bold characters are used to denote vectors. Adapted from Roe.[200] 51

Figure 3.3 Schematic illustration showing the process of chemical pattern fabrication. Adapted from Liu *et al*.[96] 61

Figure 4.1 Epoxidation of PS-PI diblock copolymers. The partially epoxidized PS-PI is denoted as PS-PIxn while f and xn (%) represent the mole fraction and degree of epoxidation, respectively. 68

Figure 4.2 SEC traces for PS-PIxn diblock copolymers (with xn indicated in %). ..72

Figure 4.3 SEC traces for hPIxn (with xn indicated in %). 72

Figure 4.4 ^{1}H-NMR spectra of PS-PIxn. The intensities are normalized to the most intense peak associated with the poly(styrene) block, and spectra are shifted vertically for clarity 73

Figure 4.5 DSC traces for hPIxn as a function of percent epoxidation. Arrows indicate the glass transition temperature. Data except hPI (0% epoxidation) have been shifted vertically for clarity. 74

Figure 4.6 DSC obtained from PS-PIxn as a function of % epoxidation. Arrows indicate the glass transition temperatures. Data except PS-PI (0% epoxidation) have been shifted vertically for clarity. 75

Figure 4.7 Variation in the glass transition temperature (T_g) for hPIxn (filled symbols) and PS-PIxn (open symbols) as a function of percent epoxidation based on DSC measurements. The dashed lines illustrate linear dependences. 76

Figure 4.8 Temperature dependence of the dynamic elastic modulus G′(1 rad/sec) for PS-PIxn diblock copolymers determined during heating (0.2 − 10 °C/min). Arrows indicate the order-disorder transitions signaled by an abrupt change in G′. Data have been shifted vertically as indicated. 77

Figure 4.9 Frequency (ω) dependence of the dynamic elastic modulus G′ (filled symbols) and loss modulus G″ (open symbols) for (a) PS-PI at 110 °C, (b) PS-PI14 at 105 °C, (c) PS-PI14 at 120 °C and (d) PS-PI41 at 105 °C. Data have been shifted vertically as indicated for clarity. 78

Figure 4.10 Small angle x-ray scattering (SAXS) obtained from PS-PIxn (with xn indicated in percentages) at room temperature. Arrows identify discernible Bragg reflections, which are consistent with a lamellar morphology. Data have been shifted vertically for clarity 79

Figure 4.11 Static contact angle (θ) of water droplets (1 μL) on thin films of hPIxn (filled symbols) and poly(styrene) (solid line). Error bars identify standard deviations and the dashed line illustrates a linear fit to the data. 80

Figure 4.12 (a-f) Top-down SEM images of PS-PIxn thin films above a crosslinked SMG mat. With one exception, these images contain island and hole textures indicative of a parallel lamellar morphology. A perpendicular lamellar orientation characterizes the panel (e). 81

Figure 4.13 Effective interaction parameter (χ_{eff}) between poly(styrene) and partially epoxidized poly(isoprene) blocks in PS-PIxn diblock copolymers, determined at 100 °C based on d_1 (SAXS data) (filled symbols) and T_{ODT} (DMS data) (empty symbols). The curves were fit to these points using the binary interaction parameter model (Eq. 4.2). The solid line identifies the mean-field ODT condition for N = 259, above and below which the system is ordered and disordered, respectively. 83

Figure 5.1 Schematic illustrations of lamella-forming block copolymer thin films, confined between one neutral and one preferential interface, characterized by 0.5 L_0 step heights............ 92

Figure 5.2 SEC traces for PS-PI, PS-PEI78, and PS-PEI78 after 6-hour thermal annealing. 97

Figure 5.3 DSC traces for PS-PI and PS-PEI78 diblock copolymers. Arrows indicate the glass transition temperatures. Data for PS-PEI78 have been shifted vertically for clarity. 98

Figure 5.4 Small angle x-ray scattering (SAXS) obtained from PS-PI and PS-PEI78 at room temperature. Arrows identify discernible Bragg reflections, which are consistent with a lamellar morphology. Data for PS-PEI78 have been shifted vertically for clarity. 99

Figure 5.5 SEC traces for PTMSS-OH parent homopolymers (right) and PTMSS-PLA diblock copolymers (left). Courtesy of collaborators at Univ. Texas. 100

Figure 5.6 SAXS data (collected for 1 hour) of PTMSS-PLA annealed at 160 °C for 5 minutes. Courtesy of collaborators at Univ. Texas. 100

Figure 5.7 DSC data for PTMSS-PLA. Courtesy of collaborators at Univ. Texas. 101

Figure 5.8 SEC traces of the tBSMA crosslinkable materials. Courtesy of collaborators at Univ. Texas. 101

Figure 5.9 Top-down SEM images of thin-film block copolymers with various film thicknesses on PS brushes. (a-f) PS-PI with <L>/L_0 = 1.5, 1.7, 2.0, 2.2, 2.3, 2.5. (g-l) PS-PEI78 with <L>/L_0 = 1.5, 1.8, 2.0, 2.1, 2.3, 2.6. The thin films were annealed at 105 °C for 6 − 12 h. 103

Figure 5.10 Top-down AFM height image, phase image, thickness profile, and SEM image of PS-PI thin films (<L> = 2.3 L_0) on (a-d) the PS brush and (e-h) the SMG mat. Step heights obtained from the thickness profiles equal to 19.1 nm and 19.6 nm, respectively (≈ 1.0 L_0). The thin films were annealed at 105 °C/12h. 104

Figure 5.11 (a-d) Top-down SEM images of PS-PEI78 thin films of various film thicknesses (<L>/L_0 = 1.5, 1.9, 2.1, 2.5) on the SMG mats. Scale bars correspond to 100 nm. (e-f) AFM height and phase images of PS-PEI78 on the SMG mat (<L> = 2.5 L_0). The thin films were annealed at 105 °C for 6 h. 105

Figure 5.12 AFM height images, phase images, and height profiles of thin-film PS-PEI78 above the PS brushes. (a-c) Short annealing (<L> = 1.9 L_0). (d-f) Long annealing (12 hours) (<L> = 1.8 L_0). The thin films were annealed at 105 °C. Step heights equal to (c) 10.0 nm and (f) 11.5 nm, respectively. 107

Figure 5.13 AFM height images, phase images, and height profiles of thin-film PS-PEI78 above the PS brushes. (a-c) Short annealing (<L> = 1.6 L_0). (d-f) Long annealing (12 hours) (<L> = 2.1 L_0). The thin films were annealed at 105 °C. Step heights equal to (c) 10.8 nm and (f) 9.9 nm, respectively. 108

Figure 5.14 AFM height images, phase images, and height profiles of PS-PEI78 (annealed at 105 °C/12h) on the PS brushes. (a-c) <L> = 2.3 L_0. (d-f) <L> = 2.6 L_0. Height differences equal to (c) 9.2 nm and (f) 19.1 nm (two steps), respectively. 109

Figure 5.15 (a-c) Top-down AFM height image, phase image, and topographic profile, and (d) SEM image of thin films of poly(styrene-*b*-isoprene) diblock copolymer (12.3 kg/mol-10.5 kg/mol) with 65% degrees of epoxidation (<L> = 1.3 L_0) on the PS brush. Thin films were annealed at 105 °C/6h. The step height from the thickness profile equals to 19.3 nm (≈ 1.0 L_0). 109

Figure 5.16 Optical micrograph, AFM height image, and height profile of PTMSS-PLA (<L>/L_0 ≈ 1.68, annealed at 150 °C/10 min.) on two surfaces: (a-c) tBSMA-15 (PLA preferential, asymmetric wetting) and (d-f) tBSMA-34 (PTMSS preferential, symmetric wetting). All color ranges in AFM represent 40 nm. Courtesy of collaborators at Univ. Texas. 111

Figure 5.17 AFM height, phase, and height profile data of PTMSS-PLA with various thicknesses on near-neutral tBSMA-25. (a-c) $\langle L \rangle / L_0 = 1.20$. (d-f) $\langle L \rangle / L_0 = 1.42$. The thin films were annealed at 150 °C for 10 min. The scale bars represent 5 μm. All height color scales range from 0 to 40 nm, and all phase color scales range from 0 to 3 °. Courtesy of collaborators at Univ. Texas..112

Figure 5.18 Thickness dependence of PTMSS-PLA structures with 0.5 L_0 step heights on near-neutral tBSMA-23. (a-d) AFM height data and (e-h) corresponding AFM height trace. The thin films were annealed at 150 °C for 10 min. All scale bars represent 5 μm. Courtesy of collaborators at Univ. Texas. 113

Figure 5.19 (a-b) AFM height and phase images of a PS-PMMA diblock copolymer ($\langle L \rangle / L_0 = 1.7$) above the SMG mat. The thin film was annealed at 230 °C for 6 h. The lamellar periodicity L_0 is extrapolated ($L_0 \approx 60$ nm). 115

Figure 5.20 Top-down SEM images of PS-PMMA thin films of various film thicknesses ($\langle L \rangle / L_0 = 1.4, 1.5, 1.7, 2.0, 2.3, 2.5$) on the SMG mats. Thin films were annealed at 230 °C/6h. The scale bars correspond to 200 nm..115

Figure 5.21 Top-down SEM images of PS-PMMA thin films of various film thicknesses ($\langle L \rangle / L_0 = 1.4, 1.5, 1.7, 2.0, 2.3, 2.5$) on the PS brushes. Thin films were annealed at 230 °C/6h. The scale bars correspond to 10 μm. 116

Figure 5.22 AFM height, phase, and height profile images of thin-film PS-PMMA above the PS brushes for various film thicknesses: (a-c) <L> = 1.4 L_0, (d-f) <L> = 1.7 L_0, (g-i) <L> = 2.3 L_0, and (j-l) <L> = 2.5 L_0. Step heights equal to (c) 30.9 nm, (f) 29.5 nm, (i) 34.5 nm, and (l) 33.1 nm, respectively. Thin films were annealed at 230 °C/6h.. 117

Figure 5.23 Cross-sectional schematic illustration of parallel lamellae with ½ L_o step heights. The step height profile at the edge is characterized by a broad “transition zone.” 123

Figure 5.24 Step height profiles. (a-b) PS-PI (<L>/L_0 = 2.3) on PS and SMG brush/mats. (c-e) PS-PEI78 on PS brushes with varying <L> (<L>/L_0 = 1.8, 2.3, 2.6). 123

Figure 5.25 AFM height, phase, and height profile images of (a-c) PS-PEI78 and (d-f) PS-PMMA above the PS brushes. <L> = 1.7 L_0. Step heights equal to (c) 10.3 nm and (f) 26.5 nm, respectively. 125

Figure 6.1 SEC traces for SI26, SI26E, and SI26E after 6-hour thermal annealing. 135

Figure 6.2 SEC traces for SI14, SI14E, and SI14E after 6-hour thermal annealing. 136

Figure 6.3 SEC traces for SI10, SI10E, and SI10E after 6-hour thermal annealing. 136

Figure 6.4 DSC traces for SI26, SI26E, SI14, SI14E, SI10, and SI10E diblock copolymers taken at ramping rates of +10 °C/min. Arrows indicate the inflections. Data except SI26 have been shifted vertically for clarity. 137

Figure 6.5 Small angle x-ray scattering (SAXS) obtained from SI26, SI26E, SI14, SI14E, SI10, and SI10E at room temperature. Arrows identify discernible Bragg reflections. Data except SI26 have been shifted vertically for clarity. 138

Figure 6.6 Magnified view of small angle x-ray scattering (SAXS) obtained from SI14E. The arrow identifies a broad "peak." 139

Figure 6.7 Temperature dependence of the dynamic elastic modulus G′(1 rad/sec) for SI26, SI21, SI14, and SI10 during heating (0.5 − 1 °C/min). Arrows indicate the order-disorder transition, signaled by an abrupt change in G′. Data for SI21 have been shifted upward for clarity ($G'_{shifted} = 50 \times G'$). 139

Figure 6.8 Temperature dependence of the dynamic elastic modulus G′(ω = 1 rad/sec) for SI14E on heating (+0.5 °C/min) with 1% strain. 140

Figure 6.9 Reduced frequency (a_T ω) plot for (a) dynamic storage modulus (G′) and (b) loss modulus (G″) for SI14E. The shift factors are shown in Figure 6.10. 141

Figure 6.10 Logarithmic shift factors as a function of temperature for SI14E. The fit to Williams-Landel-Ferry (WLF) (solid line) leads to C_1 = 7.6 and C_2 = 120. 142

Figure 6.11 (a) Temperature dependence of G′(1 rad/sec) for SI10E and SI21E on heating (1.0 − 10 °C/min) with 1% strain. (b) Frequency (ω) dependence of G′ (closed symbols) and G″ (open symbols) for SI10E (at 60 °C) and SI21E (at 105 °C). In (b), data for SI21E have been shifted upward for clarity ($G_{shifted} = 10^3 \times G$). 143

Figure 6.12 Top-down AFM height, phase, topographic profile, and SEM data of thin-film block copolymers above SMG94. (a-d) SI26 (<L>/L_0 = 1.0, annealed at 105 °C/6h). (e-h) SI21 (<L>/L_0 = 2.3, annealed at 105 °C/6h). (i-l) SI14 (<L>/L_0 = 2.3, annealed at 80 °C/6h). The step heights are 19.5 nm, 19.6 nm, and 16.0 nm, respectively. 145

Figure 6.13 Top-down SEM images of SI21E annealed at 105 °C/6h while the film thickness (<L>) and the composition of the underlying mat are adjusted. (<L>/L_0 = 1.5, 1.7, 1.9, 2.1, 2.3, 2.5) (SMG00, SMG28, SMG57, SMG76) Images with perpendicular ordering are highlighted while mixed lamellae are denoted as such. Refer to the scale bar at bottom left of the figure. Images with stars have been reproduced from Fig. 5.11 (Chapter 5). 146

Figure 6.14 SEM image of the SI21E thin film (<L>/L_0 = 2.5) on SMG57 taken at a tilt angle of 45 °. 147

Figure 6.15 Top-down SEM image of thin-film SI21E (<L>/L_0 = 1.3) on SMOH45. 147

Figure 6.16 (a-f) Top-down SEM of thin-film SI26E (<L>/L_0 = 0.9) on the SMG crosslinkable mats with varying compositions. The thin films have been annealed at 122 °C/24h and etched slightly using oxygen plasma (except for panel (e)) prior to SEM measurement. 148

Figure 6.17 Top-down SEM image of the SI26E thin film (<L> = 0.9 L_0), annealed at 140 °C/6h, on SMG60. The inset shows its Fast Fourier Transform, used to estimate the periodicity of the thin-film perpendicular cylinders (21.1 nm). The film has been slightly etched with oxygen plasma for image contrast. 149

Figure 6.18 (a-e) Top-down SEM of thin-film SI14E ($<L>/L_0 = 1.6 – 1.7$) above SMG mats with varying compositions. (f-h) AFM height, phase, and topographic profile data of SI14E above SMG94 ($<L>/L_0 = 1.6$). The step height is equal to 8.5 nm (≈ 0.6 L_0). The films were annealed at 80 °C for 6 hours. For (a-d), SEM images were taken after a small degree of plasma etching..151

Figure 6.19 (a-b) Top-down SEM images of thin-film SI14E ($<L>/L_0 = 1.6$) (annealed at 80 °C for 6 h) above SMG28 and SMG57 mats prior to plasma etching...151

Figure 6.20 SEM image of thin-film SI14E ($<L>/L_0 = 1.5$) (80 °C/6h) on SMOH45 taken at a tilt angle of 45 °..152

Figure 6.21 Top-down SEM image of (a) photoresist patterns after e-beam exposure and development and (b) trim-etched patterns (7 seconds etching). The pattern period is 38 nm. Corresponding schematic illustrations are shown above. The scale bars correspond to 100 nm....152

Figure 6.22 (a-c) Top-down SEM images of the directed self-assembly of SI21E ($<L>/L_0 = 1.5$) above chemical patterns with a periodicity of 38 nm (≈ 2 L_o) as the width (w) of the SMG94 guiding stripe in the chemical patterns was varied by controlling trim etching duration (5 − 7 seconds). The panel (d) corresponds to a larger area scan of the thin film with 6 seconds of etching. The white arrows indicate the regions of incomplete alignment in (d). The schematic illustrates block copolymer thin films above chemical patterns. Scale bars correspond to 100 nm..153

Figure 6.23 Top-down SEM image of SI14E (<L>/L_0 = 2.0) aligned by underlying chemical patterns with a periodicity of 44.1 nm (≈ 3 L_o). Scale bars correspond to 100 nm. A small degree of plasma etching was implemented before SEM imaging. 154

Figure 6.24 (a-d) Top-down SEM images of thin-film SI14E (<L>/L_0 = 0.8 − 1.5) above SMOH45 with varying thermal annealing conditions. The SEM images were taken after a small degree of plasma etching. Scale bars correspond to 100 nm. 155

Figure 6.25 SEM image of thin-film SI14E (<L> = 0.8 L_0) on SMOH45 (100 °C/3h) taken at a tilt angle of 45 °. 156

Figure 6.26 (a-b) Top-down SEM images of SI10E (<L> = 10 − 30 nm), annealed at various conditions (as indicated), on non-preferential interfaces (SMOH45, SMG60). 157

Figure 6.27 Top-down SEM images of (a) SI21E, (b-c) SI14E, and (d) SI10E thin films (<L>/L_0 = 1.7 − 2.0) on non-preferential mats (SMG28, SMG57) with estimated χN as denoted.. 165

Figure 7.1 Schematic illustrations on directed self-assembly of AB diblock copolymers and ABC triblock copolymers. Selective etching leaves features of size d and d’, respectively. L_0 and L_s denote the bulk lamellar periodicity of block copolymers and the pitch of underlying chemical patterns, respectively. 169

Figure 7.2 ^{1}H-NMR spectra of SIM18. 175

Figure 7.3 SEC traces of SIM03 before and after rinsing in cyclohexane. 176

Figure 7.4 SEC traces of SIM18 prior to and after thermal annealing at 160 °C for 6 hours. 176

Figure 7.5 SEC traces of SIM28 prior to and after thermal annealing at 160 °C for 6 hours. 177

Figure 7.6 SAXS of SIM03 taken at room temperature. 178

Figure 7.7 SAXS of SIM18 taken at room temperature. 178

Figure 7.8 SAXS of SIM28 taken at room temperature. 179

Figure 7.9 (a) DSC trace of SIM03 and (b) its derivative (Δ(Heat Flow)/Δ(Temp.)). T_g stands for the glass transition temperature for each domain. 180

Figure 7.10 (a) DSC trace of SIM18 and (b) its derivative (Δ(Heat Flow)/Δ(Temp.)). T_g stands for the glass transition temperature for each domain. 181

Figure 7.11 (a) DSC trace of SIM28 and (b) its derivative (Δ(Heat Flow)/Δ(Temp.)). T_g stands for the glass transition temperature. 181

Figure 7.12 (a) TEM image of SIM18. Stained with OsO_4 for 5 minutes. (b) Corresponding schematic illustrating PI domains (dark) and PS and PMMA domains (white). L_0 denotes the lamellar periodicity. Courtesy of Hanseung Lee. 182

Figure 7.13 (a) TEM image of SIM18. Stained with RuO_4 for 5 minutes. (b) Corresponding schematic illustrating PI (dark), PS (gray), and PMMA domains (white). L_0 denotes the lamellar periodicity. 183

Figure 7.14 (a) TEM micrograph of SIM28. Stained with OsO_4 for 5 minutes. (b) Corresponding schematic identifying PI domains (dark) and PS and PMMA domains (white). L_0 denotes the lamellar periodicity. 183

Figure 7.15 Top-down SEM images of thin-film SIM18 ($\langle L\rangle/L_0$ = 0.8) above SMOH50: (a) prior to and (b) after PMMA development. The thin films were thermally annealed for 178 °C for 24 hours........................184

Figure 7.16 Top-down SEM image of self-assembly of SIM18 triblock copolymers, guided by chemical patterns. The periodicity of chemical pattern (L_s) is approximately 2 L_0, where L_0 denotes the lamellar periodicity of SIM18 ("2X density multiplication"). Courtesy of Paulina Rincon. 185

Figure 7.17 Top-down SEM images of thin-film SIM28 ($\langle L\rangle/L_0$ = 0.8) above SMG60: (a) prior to and (b) after PMMA development. The thin films were thermally annealed for 160 °C for 24 hours. R1 – R3 refer to different characteristic regions in the micrographs...........................186

Figure 7.18 Schematic illustrating the structure of SIM28 thin films at the region R2. 186

Figure 7.19 Top-down SEM images of thin-film SIM28 ($\langle L\rangle/L_0$ = 0.8) with various degrees of partial epoxidation above SMG60: (a) 10%, (b) 29%, and (c-d) 57%. The thin films were thermally annealed for 178 °C for 24 hours. 189

Figure A.1 SEC traces of MSM1 and its poly(styrene) aliquot. 211

Figure A.2 ^{1}H-NMR spectrum for MSM1. 211

Figure A.3 DSC trace of MSM1. 212

Figure A.4 SAXS of MSM1 taken at room temperature..213

Figure A.5 Temperature dependence of the dynamic elastic modulus G′(ω = 1 rad/sec) for SI14E on heating (+10 °C/min) with 1% strain.................213

Figure A.6 (a) Reduced frequency (a_T ω) plot for dynamic storage modulus (G′) and loss modulus (G″) for MSM1. (b) The shift factors as a function of temperature. The fit to the Williams-Landel-Ferry (WLF) equation (solid line) leads to C_1 = 9.57 and C_2 = 358.2 (T_{ref} = 260 °C). 214

Chapter 1 Introduction

1.1 Self-Assembly of Block Copolymers in Thin Films

The need for new lithographic techniques has arisen as technical advances approached the practical limitations of the smallest feature realizable by conventional optical lithography. The self-assembly of block copolymers has been investigated as one of future lithographic processes. Previous studies on bulk block copolymers have shown that they exhibit characteristic microphase segregation into periodic morphologies with length scales of 10 – 100 nm, as described in Chapter 2 of this dissertation. This lies in the range of feature sizes that conventional lithographic tools have had difficulties in fabricating. Taking advantage of such small length scales, the implementation of thin-film block copolymers as lithographic mask materials has had promising successes. Chapter 2 further provides a brief literature survey on (1) physical properties of thin-film polymers and blends and (2) various research efforts conducted in thin-film block copolymers. However, despite a long history of investigations, the current understanding of many thin-film properties is not complete due to complications arising from surface interactions at the interface. There still remain many improvements to be made before the technique may actually be implemented into the lithography process.

One of the critical issues in the self-assembly of block copolymers in thin films is the orientation of the thin-film morphologies. The dimensionality reduction entails symmetry breaking of microdomains, and the domain orientation with respect to the interfaces dictate the possible application of the structures. A variety of methods have been devised to control the orientation. They include the manipulation of the boundary conditions at the confining interfaces and the application of external fields. This

dissertation (Chapter 4) reports a novel method that involves partial chemical modification of existing block copolymers, and this allows one to tune the surface energy of thin-film block copolymers and to control the orientation of the thin-film morphologies.

For thin films of lamella-forming block copolymers, preferential boundary conditions at both confining interfaces induce parallel structures with L_0 step heights (L_0: bulk periodicity), commonly referred to as islands and holes. On the other hand, non-preferential wetting at both interfaces leads to the formation of perpendicular morphologies, which are a technologically more useful orientation. However, each individual block copolymer system has a different neutral condition, and it has not been a trivial task to attain the neutrality at neighboring interfaces and observe perpendicular ordering for a given system. The difficulty originates, in part, from the challenging task of analyzing thin-film morphologies. Chapter 5 offers a simple method to test the neutral wetting condition by associating a novel thin-film structure with boundary conditions that involve only one neutral interface.

In accordance with Moore's Law, the resolution enhancement in feature sizes has been pursued persistently for thin-film block copolymers. Such effort involves a reduction in the periodicity of the block copolymers until the system reaches the order-disorder transition and becomes disordered. While various chemistries have been implemented to maximize the interaction parameter in block copolymer systems, little investigation on the thin-film morphologies has been conducted at the limit near the order-disorder transition. This results from the difficulty and the complexity in attaining neutral boundary conditions, without which the preferential interfaces overwhelm the thin-film thermodynamics and preclude one from studying the sole consequence of dimensionality reduction. Chapter 6 of this dissertation focuses on thin-film block

copolymers with partial chemical modification that generates neutralized interfaces. The thin-film morphology is monitored while the segregation strength is varied across the order-disorder transition.

Triblock copolymer architecture exhibits a larger “parameter space” and forms more diverse morphologies compared to diblock copolymers. Even for simple lamellar morphologies, variation in the volume fractions of the blocks offers the immediate prospect of tuning feature sizes for triblock copolymers. However, the thin-film implementation of triblock copolymers has encountered the complex interplay among bulk thermodynamics, interfacial interactions, and chain conformations. In Chapter 7, the dependence of a thin-film morphology on the size of the middle block, characterized by a low surface energy, is examined using poly(styrene-*b*-isoprene-*b*-methyl methacrylate) (SIM) triblock copolymers.

1.2 Thesis Outline

Chapter 2 first provides a general background on the properties of bulk block copolymers and the consequences of dimensionality reduction (bulk → thin film) on various polymer properties. This is followed by a discussion on self-assembly of block copolymers in thin films and its potential application to nanolithography while some challenges faced by current optical lithography are also listed. Successful implementation of block copolymer thin films to lithography requires control over domain orientation, long-range ordering, and registration, and a literature survey addressing these factors is provided. At the end of Chapter 2, epoxidation methods and resulting random copolymer architecture are discussed. In Chapter 3, a synthetic procedure on controlled anionic polymerization and bulk characterization techniques, such as size exclusion chromatography and small angle x-ray scattering, are explained.

Procedures employed for the fabrication of block copolymer thin films and chemical patterns are also provided.

The bulk and thin-film characterization of partially epoxidized poly(styrene-*b*-isoprene) block copolymers are provided for various degrees of epoxidation in Chapter 4. The difference in the role that the random architecture plays in the bulk and thin-film block copolymers is investigated. Two boundary conditions of thin films are addressed in Chapter 5: (1) a free surface neutralized block copolymer above a preferential interface and (2) a block copolymer characterized by a disparate surface energy above a neutral interface. The similarity and difference in the thin-film structures regarding these scenarios is provided. Chapter 6 examines the thin-film behavior of a block copolymer characterized by a neutral free surface as the segregation strength is varied in a controlled manner across the order-disorder transition. The implication of incorporating random architecture in thin films is addressed, followed by a discussion on the consequence of dimensionality reduction for thin-film block copolymers. In Chapter 7, the bulk and thin-film properties of poly(styrene-*b*-isoprene-*b*-methyl methacrylate) triblock copolymers are studied while the volume fraction of the middle block is varied systematically.

Chapter 2 Background

2.1 General Background

2.1.1 Bulk Block Copolymers and Long-Range Ordering

Block copolymers are macromolecules formed by covalent end-to-end unions of different homopolymers. A linear AB diblock copolymer is shown in Figure 2.1. A and B represent different homopolymers, such as poly(styrene), poly(dimethylsiloxane), and poly(isoprene).

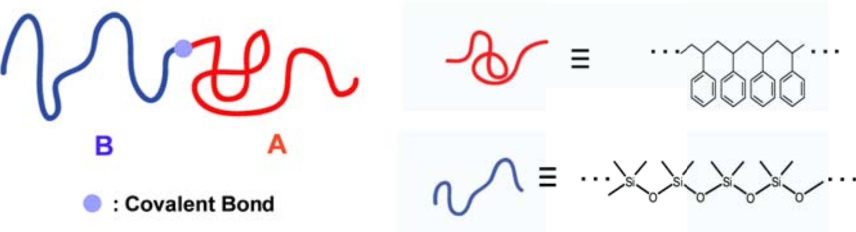

Figure 2.1 Schematic diagram of a linear AB diblock copolymer. Poly(styrene) and poly(dimethylsiloxane) are given as examples of A and B blocks.

With advances in knowledge of block copolymer synthesis, block copolymers have been made into various architectures, such as ABA, ABC, star block, and graft, in addition to the simplest form of the linear diblock copolymer, AB. While many applications, such as pressure sensitive adhesives, surfactants, and footwear, have been put into commercial use by taking advantage of different properties originating from alterations in chemical structures, the work in this dissertation is mainly concerned with linear diblock copolymers and triblock copolymers.

Two or more disparate components in polymer mixtures generally go through *macrophase segregation* while they tend to mix at high temperatures. This trend can be explained based on Flory-Huggins regular solution theory,[1]

$$\frac{\Delta G_m}{kT} = \frac{f_A}{N_A}\ln(f_A) + \frac{f_B}{N_B}\ln(f_B) + f_A f_B \chi_{AB} \qquad \text{(Eq. 2.1)}$$

where the change in the Gibbs free energy for a mixture of A and B polymers (ΔG_m) is expressed in terms of the volume fractions (f_A, f_B), the degrees of polymerization (N_A, N_B), and the Flory-Huggins interaction parameter, χ_{AB}. The first two terms on the right side of the equation represent the change in entropy of mixing while the last term denotes the energetic penalty for placing polymers adjacent to each other. A few general predictions can be made based on this equation. Molecules with high N_A would have more of a tendency to phase separate instead of forming a mixed state. Considering that χ_{AB} is generally a function of temperature, the temperature can be changed to affect the miscibility of polymers in the blends. In the case of block copolymers, on the other hand, the covalent bond connecting two polymers imposes constraints on the extent that one block can move away from the other during phase segregation, rendering complete segregation impossible. The system accommodates both the tendency to phase separate and the connectivity between polymers by going through *microphase segregation*, resulting in a periodic morphology with the domain size restricted to a molecular scale, *i.e.*, a few tens of nanometers.

Linear diblock copolymers have been studied for over 30 years, and various structures have been identified depending on the volume fractions of each component and $\chi_{AB}N$, as shown in Figure 2.2. A close agreement between the theoretical predictions and the experimental results has been observed over the years.

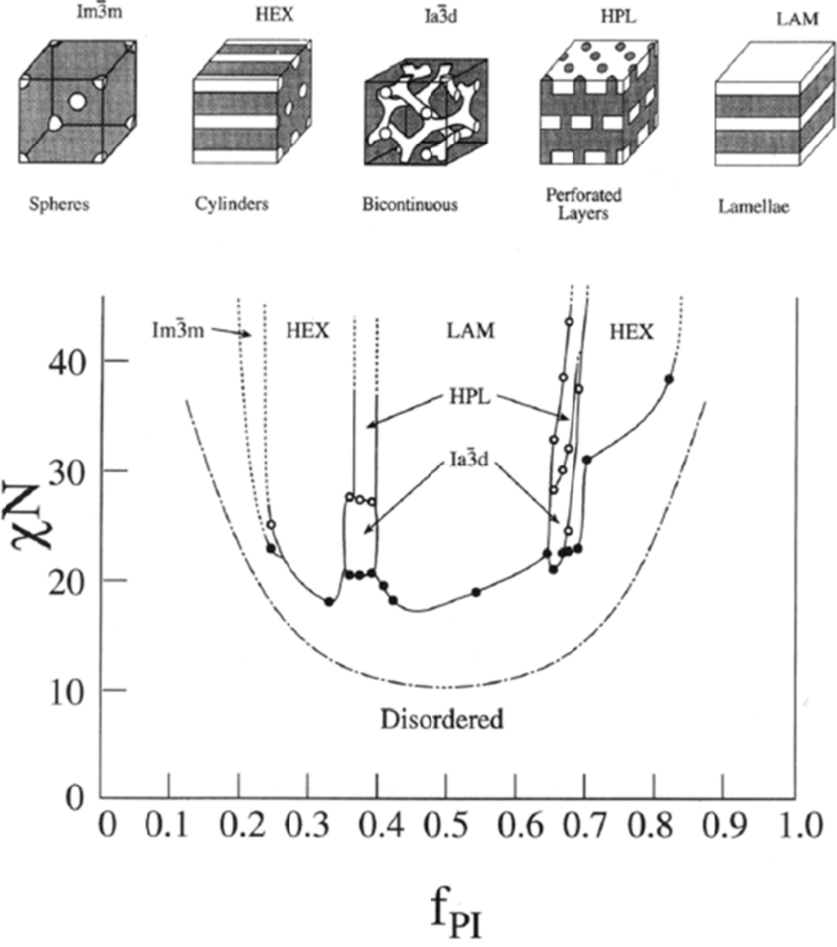

Figure 2.2 Phase diagram for linear poly(styrene-*b*-isoprene) diblock copolymers. χ, N, and f_{PI} denote the interaction parameter, the degree of polymerization, and the volume fraction of the poly(isoprene) block, respectively. Reprinted with permission from Khanpur *et al.*[2] Copyright 1995 ACS.

As shown in the diagram, symmetric diblock copolymers form a self-assembled microphase for $\chi N > 10.5$ and become disordered when χN is less than 10.5. This transition is called the *order-disorder transition* (ODT).[3] While the mean field theory predicts a second-order transition for the ODT at the symmetric composition, fluctuation

effects instead induce a weakly first-order transition. As a result, a correction term is added to the mean field theory criterion for the ODT:[4] $(\chi N)_{ODT} = 10.5 + 41.0\ \bar{N}^{-1/3}$. $\bar{N} = N\ a^6\ \upsilon^{-2}$, where a and υ are the statistical segment length and the segment volume, respectively.

Three different regimes are used to describe the phase behavior of block copolymers with varying χN: *weak* (WSL), *intermediate* (ISL), and *strong* (SSL) *segregation limits*. In the WSL (low χN), the length scales in the system exhibit the $N^{1/2}$ dependence as polymer chains are undisturbed or only weakly perturbed. On the other hand, the domain spacing (L_0) of the lamellar morphology for strongly segregated symmetric AB diblock copolymers (high χN) obeys the following relationship:[5]

$$L_0 \approx 1.03\, a\, \chi_{AB}^{1/6} N^{2/3} \qquad \text{(Eq. 2.2)}$$

where a corresponds to a monomer size. The $N^{2/3}$ dependence of L_0 in Eq. 2.2 has been verified by a number of research groups.[6, 7] ISL refers to the behavior that deviates from general features for WSL and SSL.

Different methods have been implemented in the past to attain the macroscopic alignment for bulk block copolymers. For example, Keller *et al.*[8] achieved alignment of cylinder-forming poly(styrene-*b*-butadiene-*b*-styrene) (PS-PB-PS) triblock copolymers by bulk extrusion of the melt. The low angle x-ray diffraction pattern was consistent with a hexagonal symmetry with the cylinder axes aligned parallel to the extrusion direction. Similarly, oscillatory shear strain was used to attain the alignment of poly(styrene-*b*-isoprene) (PS-PI) diblock copolymers.[9] Using in-situ rheo-optical measurements, Chen *et al.*[10] confirmed the long-range alignment of microphases in PS-PI diblock copolymers after applying oscillatory shear. Electric fields also have been used to induce long-range ordering in microphases of block copolymers.[11] As poly(styrene-*b*-methyl methacrylate) (PS-PMMA) symmetric diblock copolymers were

slowly cooled from temperatures above the order-disorder transition temperature, an electric field from two parallel electrodes was applied to the sample, resulting in the alignment of the lamellar microphase as confirmed by SAXS.

In addition, research has been done to control the microphase orientations of block copolymers in the bulk state. Possible orientations of a lamellar morphology are shown in Figure 2.3. Koppi *et al.*[12] found with poly([ethylene-*alt*-propylene]-*b*-ethylethylene) (PEP-PEE) diblock copolymers that the orientation of sheared lamellar microphases varied depending on the shearing frequencies and the temperature at which the oscillatory shear strain was applied.

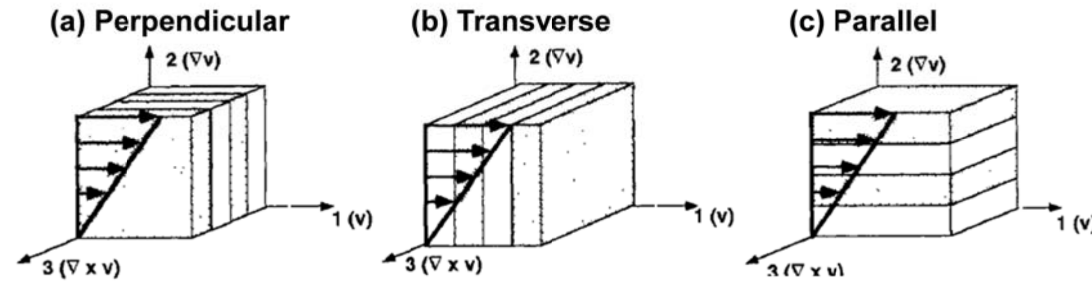

Figure 2.3 Schematics of possible lamella formations in sheared diblock copolymers. Arrows indicate the direction of the shear. Reprinted with permission from Gupta *et al.*[13] Copyright 1996 ACS.

Using PS-PI diblock copolymers, Zhang *et al.*[14] found an additional parallel lamellar orientation in the high shearing-frequency regime, identifying a total of three frequency regimes that led to different orientations. The large difference in viscoelastic properties between the poly(styrene) block and the poly(isoprene) block was considered as one of reasons behind the formation of the parallel microphase in the high frequency region.

After monitoring the alignment process with time, Chen *et al.*[10] suggested a two-step mechanism for the morphology formation in sheared block copolymers. In the early stage, the grains of different phases quickly developed from randomly oriented phases. Then, one of the phases slowly grew at the expense of the other phases until it pervaded throughout the sample. Such a two-step process has also been observed by Gupta *et al.*,[13] who also showed that the orientation of lamellar phases depended on the magnitude of the oscillatory shear as well.

2.1.2 Thin-Film Polymers and Blends: Consequences of Confinements

Dimensionality reduction from the bulk to the thin-film state inevitably involves modifications to the fundamental physical properties of polymers and their blends. Due to a relatively large increase in the surface area compared to the total volume, the total Gibbs free energy of the polymers must account for the energy penalty resulting from interface interactions. The entropic contributions are also affected by the presence of a free surface and an impenetrable interface.

Past investigations have found that the polymer dynamics near an interface may be different from that in a bulk state. For example, studies have shown that the diffusion coefficient (D) of polymers in thin films depended on the degree of attraction of the polymers to the substrate.[15] D of poly(styrene) (PS) decreased as the substrate surfaces were chemically modified to exhibit a stronger interaction with PS. Zheng *et al.*[16] further investigated the dependence of D on the distance of polymers from the substrate interface. They found that the diffusion coefficient of PS located close to the silicon substrate (as close as one radius of gyration (R_g)) was smaller than the bulk value by a few orders of magnitude. The suppression of the diffusion coefficient persisted until the distance of PS from the interface reached approximately 10 R_g, beyond which the bulk

diffusion coefficient was recovered. It was suggested that the lower mobility resulted from the entanglement of mobile chains with the "adsorbed" chains at the interface. On the other hand, chain ends have been found to segregate preferentially to the free surface,[17] creating more free volume. Indeed, the smaller density for thinner films and the resulting enhancement in the mobility have been observed for dewetting films.[18] The influence of confinement on the glass transition temperature of polymer thin films has also been investigated.[19, 20]

The perturbations to the chain conformations have been studied for polymers in confined geometries. Jones *et al.*[21] found that thin-film polymer blends retained a Gaussian chain conformation within the experimental uncertainty. Based on diffuse neutron scattering results, Kraus *et al.*[22] observed that the in-plane component of the radius of gyration ($R_{g\,\parallel}$) of PS and deuterated PS blends increased as the film thickness was reduced below 6 R_{g_bulk}, where R_{g_bulk} is the radius of gyration of an unperturbed Gaussian chain. At the film thickness of R_{g_bulk}, $R_{g\,\parallel}$ was as large as 1.5 R_{g_bulk}. The increase in the in-plane component would be equivalent to the chain elongation parallel to the substrate plane. The chain conformations of semicrystalline poly(di-*n*-hexylsilane) (PD6S) also became disrupted as the film thickness decreased.[23, 24] As a result, the degree of crystallization within as-cast films decreased for thinner films, and the crystallization was effectively suppressed (*i.e.*, a complete amorphous state) below a threshold thickness (= 150 Å).

Spinodal decomposition in thin-film polymer blends has been explored. Jones *et al.*[25] found that the interfacial interaction of polymers in blends below the critical temperature induced anisotropic spinodal decomposition. During the process, the wavevectors representative of the composition fluctuation propagated normal to the surface. Krausch *et al.*[26] were able to collapse the composition profiles into one master

curve (the scaling behavior) and found that the thickness of the wetting layer increased proportional to (time)$^{1/3}$. The coarsening exponent of 1/3 corresponds to the intermediate stage in the phase separation of binary mixtures.[27] The constructive and the destructive interferences of the spinodal decomposition waves from two confining interfaces were studied for the blend.[28] A damped sinusoidal functional form was used to represent the spinodal decomposition propagating from one interface, and the sum of the two decaying sinusoidal functions from both interfaces was fit to the composition profile in the confined film. The experimental profile was in qualitative agreement with the simulation. However, when the film thickness was smaller than the wavelength of the spinodal decomposition wavevectors in the bulk, the composition profile could no longer be described using the same functional form.

The phase transition temperature of polymer blends is also affected by the dimensionality reduction imposed on the system. Reich and Cohen[29] studied the cloud point of thin-film polymer blends using laser light scattering and found that the system exhibited a temperature shift in the cloud point as a function of film thickness. While the bulk values were recovered for the film thickness > 1 μm, the upward shift was as large as ~60 °C for 100 Å thick films. A similar trend was also found in other polymer blend systems.[30]

2.2 THIN-FILM BLOCK COPOLYMERS: NANOLITHOGRAPHY

While block copolymer self-assembly in thin films is investigated for various reasons, such as composite confinement,[31, 32] photonic crystals,[33] and cell separation in biomedical applications,[34] one of the most exciting applications is nanolithography.

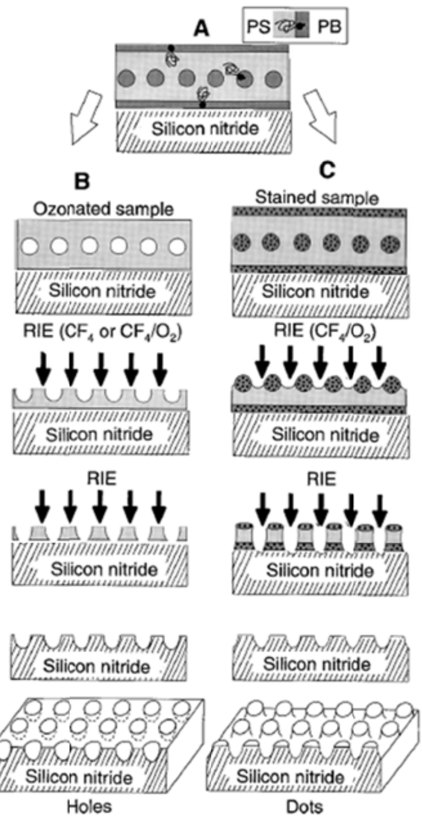

Figure 2.4 Schematic illustrations of block copolymer lithography. Thin films of sphere-forming poly(styrene-*b*-butadiene) (PS-PB) block copolymers are used as masks to fabricate features in underlying layers of silicon nitride. *RIE* stands for reactive ion etching. Reprinted with permission from Park *et al.*[35] Copyright 1997 AAAS.

The morphologies exhibited by block copolymers have typical dimensions of a few tens of nanometers. Conventional lithographic process implemented by the semiconductor industry does not have easy access to this length scale, making the self-assembled block copolymers potentially useful as mask materials in the lithographic process. Components in thin films can be removed selectively, and the remaining films can be used as a mask for underlying layers. A simple illustration of block copolymer lithography is provided

in Figure 2.4. In this example, using thin films of sphere-forming block copolymers as masks, either dots or holes are fabricated in the silicon nitride underlying layers depending on the selective etching process implemented. Block copolymer lithography has been applied to the fabrication of quantum dots,[35, 36] nanowires,[37, 38] capacitors,[39] magnetic dot arrays for storage media,[40, 41] and membranes.[42]

Two important considerations concerning the implementation of thin-film block copolymers into the lithographic process are (1) the control of the microdomain orientations and (2) the long-range ordering over a large area, combined with registration. First, the successful implementation of block copolymer lithography requires a control over the morphology orientation of thin-film block copolymers. For example, the orientation of a cylindrical morphology formed by block copolymer thin films needs to be parallel in order to create stripe patterns while the perpendicular orientation would be required for fabricating porous membranes. In the absence of an external field, the interfacial boundary conditions dictate the orientation of the thin-film morphologies. Figure 2.5 illustrates commonly observed structures exhibited by a lamellar morphology depending on the boundary conditions at the free surface and the underlying substrate.

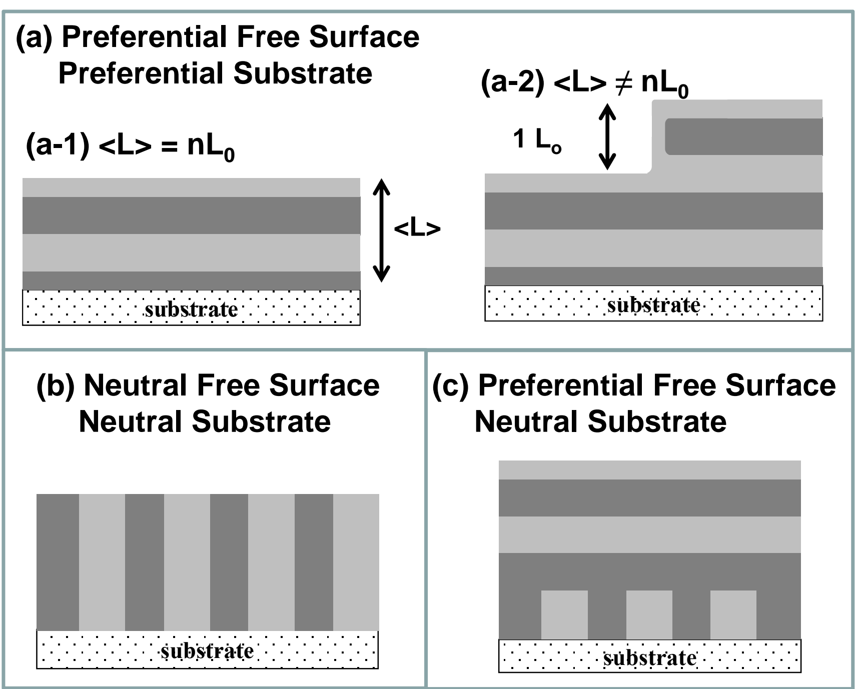

Figure 2.5 Dependence of a lamellar morphology formed by block copolymer thin films on the interfacial boundary conditions: (a) the preferential free surface and the preferential underlying substrate; (b) the neutral free surface and the neutral substrate; and (c) the preferential free surface and the neutral substrate. (a-1) and (a-2) correspond to commensurate and incommensurate film thickness for the scenario (a), respectively. $\langle L \rangle$, n, and L_0 refer to the average film thickness, an integer, and the lamellar microdomain periodicity, respectively.

"Preferential" interactions at the interface indicate that the boundary prefers to be in contact with one of the components of the block copolymers over another component. As shown in Figure 2.5a, preferential interactions at both interfaces produce parallel lamellar morphologies. Due to the incompressible nature of the block copolymers, the thin films of parallel lamellae may be either featureless or topographical depending on

the film thickness. The featureless regions are observed when the average film thickness (<L>) equals the integral multiples of the lamellar periodicity (nL_0, n: integer) for asymmetric wetting (Figure 2.5a-1). For the case $<L> \neq n\ L_0$, the structures referred to as islands and holes form with quantized step heights (= L_0), as demonstrated in Figure 2.5a-2.

On the other hand, neutral wetting conditions refer to the case when the interactions at the interface are balanced such that the boundary favors both components of the block copolymers equally. Neutral interactions at both interfaces can produce perpendicular orientation of the lamellae morphology (Figure 2.5b). While the perpendicular structures are harder to achieve experimentally, they are technologically more useful. While various measures have also been devised to attain perpendicular ordering, selected methods (*e.g.*, *interface modification*, *solvent annealing*, and *electrical field application*) will be discussed later in this chapter. A mixed wetting condition (*i.e.*, one preferential interface and one neutral interface) can result in the coexistence of parallel and perpendicular lamellar structures in the thin films, as illustrated in Figure 2.5c.

Achieving both long-range ordering and controlled registration of thin-film domains is also critical for block copolymer lithography. For example, a single layout fault in integrated circuits, resulting from the failure to attain both, can cause malfunctioning of the whole circuit. However, only short-range ordering is generally observed in as-cast films of block copolymers, possibly due to residual stress present in the films.[43] Various approaches taken in order to attain long-range ordering include microwave annealing,[44] corrugation,[45] zone annealing,[46, 47] shearing,[48] and directional solidification.[49] Methods known as *chemical patterning* and *graphoepitaxy* have proven effective in achieving long-range ordering and, at the same time, controlling precise

translational registration of the block copolymer morphologies. These two methodologies will be discussed in greater details later.

Table 2.1 Issues and corresponding targets set for directed self-assembly. Reprinted with permission from Herr.[50] Copyright 2011 CUP.

Metric	Research targets
Defects	≤0.01 10 nm defects cm^{-2}
Low-frequency LER	≤1.8 nm 3 σ
Gate critical dimension (CD) control	≤1.7 nm 3 σ
Resolution	≤16 nm * (2018)
Essential shapes	Dense/isolated L/S, circles, hexagonal arrays, jogs, T-junctions
Overlay and registration	≤3.8 nm* 3 σ (2018)
Effective throughput	≥1.7 × 300 mm wafers/min [≥100 × 300 mm wafers/h]
Etch and pattern transfer	Competitive with current resist materials
Placement/orientation	20% of the critical dimension
Multiple sizes/layer	≥2 sizes/layer
Ease of integration	Compatible with complementary metal–oxide semiconductor (CMOS) processing
Overall performance	Competitive with chemically amplified resist processing
Other	Environment, safety, and health (ESH) impact, functional materials, etc.

Several other issues need to be addressed prior to the implementation of block copolymer lithography in the manufacturing process. Two dominant methods, mentioned in the previous paragraph, that enable both long-range ordering and registration of block copolymers (*i.e.*, chemical patterning and graphoepitaxy) require

top-down optical lithography as part of the process. In this regard, a hybrid form that combines both block copolymer lithography (bottom-up) and typical optical lithography (top-down) is anticipated in the future, and the integration between two technologies will be an important issue. In addition, there is the need to incorporate multiple morphologies and periodicities into a single layer of thin films. Despite the strong tendency for a given block copolymer system to retain a morphology with one length scale, the layouts in the typical semiconductor process involve the complex geometries with multiple length scales. A strict control over parameters such as defect density, line edge roughness, and registration is required. A comprehensive list of issues and corresponding targets is provided in Table 2.1.

2.2.1 Conventional Optical Lithography and Its Limitation

The semiconductor technology has developed rapidly since 1960s. The rate of development has generally been expressed using Moore's Law, which predicts the trend that the number of transistors integrated in a microchip doubles roughly every two years. While advances in different disciplines have enabled the fulfillment of the Moore's Law prediction, optical lithography played a major role in determining the smallest feature that could be fabricated. The process of optical lithography can be schematically depicted as in Figure 2.6. First, a film is deposited above a silicon substrate, and a light-sensitive photoresist (PR) material is spin-coated above the film. Then, the PR is selectively exposed to light sources by using a mask that has specified patterns. After the reacted PR is removed, the remaining PR is used as a mask for further processing such as etching and doping. These steps may be performed repetitively in order to transfer the pattern in the mask to underlying layers. A few steps have been omitted for the

simplistic understanding, and in reality much more complexity is involved in minimizing the amount of defects and increasing throughputs.

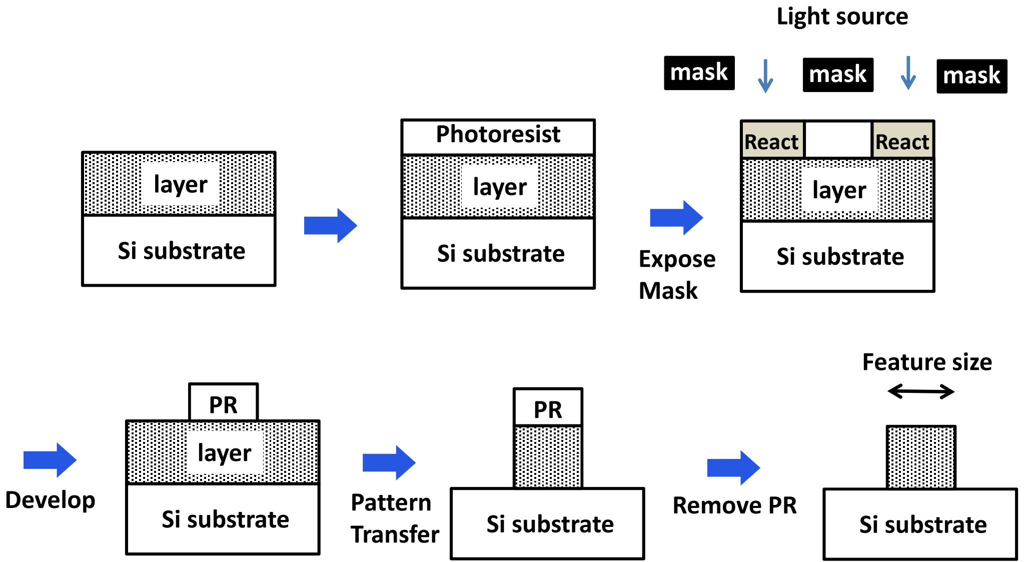

Figure 2.6 Schematic illustration of conventional optical lithography. Adapted from Plummer *et al.*[51]

While the predictions of the end of miniaturization have persisted in the semiconductor industry for many years, technological advancements have consistently eclipsed such predictions. However, in recent years there has been a serious doubt regarding whether current state-of-art optical lithography may be used to make features as small as 40 − 50 nm or less in mass manufacturing, let alone other problems, such as the need for high-k materials. The challenges associated with optical lithography include the following limitations:[52-54]

(1) the fundamental diffraction limit for a given wavelength,

(2) the requirement of light sources with shorter optical wavelengths,

(3) the strict limitation on the transmission mask materials due to their absorption and deformation at shorter wavelengths,

(4) the development of projection lenses compatible with shorter wavelengths,

(5) species diffusion in the catalytic reaction at the photoresist, leading to blurring and roughness,

(6) the restriction on topography due to the depth of focus, which decreases as resolution increases.

Due to these limitations with conventional optical lithography, much attention is given to a group of relatively promising, alternative techniques, such as extreme ultraviolet lithography, electron beam lithography, and nanoimprint lithography. They are generally called *next-generation lithographies* (NGL).

2.2.2 Morphology Orientation Control in Thin-Film Block Copolymers

2.2.2.1 Interface Modification

The interfacial modification at the boundaries has turned out to be a useful method to control the domain orientation in thin-film block copolymers. Not only the surface energy of block copolymers at the free surface, but also the interaction of the polymers with the substrate affects the behavior of the block copolymer thin films. An energetically favorable (repulsive) interaction of one of the blocks with the underlying interface causes its preferential segregation towards (away from) the substrate interface. The relative interaction strength between the polymer and the substrate may be controlled by interface modification (*e.g.*, the chemical composition variation at interfaces). For example, while early thin-film research mostly involved thin-film fabrication on a Si substrate, the polymer-substrate interaction was altered by coating the Si substrate with gold.[55] With thin-film poly(styrene-*b*-methyl methacrylate) (PS-

PMMA) block copolymers, bare Si substrates favor the selective segregation of the poly(methyl methacrylate) (PMMA) block to the polymer-substrate interface. On the other hand, the poly(styrene) (PS) block adsorbs to the underlying interface covered with gold coatings.

Tunable interfacial interactions were accomplished by utilizing substrates with random copolymer coatings and changing the fractions of components in the random copolymers. Kellogg *et al*.[56] used poly(styrene-*ran*-methyl methacrylate) (PS-*r*-PMMA) random copolymers as confining walls. The "unbiased" (also called "neutral" or "non-preferential") substrates were created by adjusting the relative amounts of the components in the random copolymers. With these neutral confining walls, a perpendicular morphology of poly(styrene-*b*-methyl methacrylate) (PS-PMMA) block copolymers was observed. The relative stability of perpendicular ordering with respect to parallel ordering has been explained in terms of the film thickness commensurability and the resulting frustration. On the contrary, they could not find any sign of perpendicular morphologies when preferential substrates were used.

In the previous results,[56] the random copolymer coatings were not chemically bound to the substrates. Therefore, they were susceptible to diffusion during the annealing process, potentially disrupting the balanced surface energies at the interfaces. This issue was addressed by grafting random copolymers with terminated hydroxyl functionalities onto the silicon oxide layer, forming brushes.[57] As the chemical compositions of the random copolymers varied, the systematic change in the contact angles above the random copolymer films was observed, suggestive of the surface interaction variation. The wetting condition at an interface with a random copolymer brush was investigated by Mansky *et al*.,[58] who measured the concentration of block copolymer components at the interface as the random copolymer composition changed.

The random copolymer composition that led to non-preferential wetting was intermediate between the separate compositions that favored the preferential segregation of each block copolymer component. A slight deviation in the non-preferential condition from the calculated value was attributed to the penetration of the thin-film block copolymers into the brush. A top neutral "brush" was created by attaching surface active functional groups to a random copolymer, which as a consequence segregated to the free surface in thin films.[59, 60] Using this method, a thin-film block copolymer was confined between neutral interfaces at both the free surface and the underlying substrate, and perpendicular lamellae formed throughout the entire film. The necessary condition for non-preferential wetting was investigated for the case where the components of a random copolymer brush were chemically different from thin-film block copolymers.[61]

A versatile method has been developed by Ryu *et al.*[62] to create a random copolymer interface on various types of materials without relying on the specific grafting reaction. The benzocyclobutene (BCB) functionality, randomly added to the styrene block in PS-*r*-PMMA, enabled thermal crosslinking of the random copolymers deposited above a variety of substrates (*e.g.*, metals, oxides, and polymers). The surface energies of the crosslinked brush were not affected by the substrate types. Different chemistries have been considered for the crosslinking reaction of random copolymers in thin films.[63, 64]

2.2.2.2 Solvent Annealing

Solvent annealing has been implemented widely in thin-film block copolymers to attain perpendicular ordering for block copolymers with disparate surface energies. The process involves solvent evaporation that creates a concentration gradient perpendicular to the film surface and kinetic trapping of the system in the metastable states. Kim *et*

al.[65] suggested that the morphology ordering propagated from the free surface into the film, presumably at a high evaporation rate. According to Lin *et al.*,[66] the solvent concentration would be lowest at the substrate interface for slow evaporation, and the phase formation propagated from the underlying interface to the free surface. Using such directionality, they were able to attain a long-ranged perpendicular ordering of a cylindrical morphology in thin-film poly(styrene-*b*-ethylene oxide) (PS-PEO) diblock copolymers. The perpendicular ordering disappeared after subsequent thermal annealing above the glass transition temperature, indicating that the morphology obtained through solvent evaporation was not thermodynamically stable, but metastable. Crosslinked samples were able to maintain the perpendicular cylindrical morphology even after being exposed to the same thermal treatment.

Kim and Libera[67] investigated the issue of solvent evaporation further by controlling the solvent evaporation rate of solvent-cast poly(styrene-*b*-butadiene-*b*-styrene) (PS-PB-PS) block copolymers. They found that slow and medium evaporation rates led to parallel and perpendicular cylindrical morphologies, respectively, while fast evaporation resulted in a disordered state. According to them, the solvent evaporation primarily favored the perpendicular orientation, which provides a faster pathway for the solvent within the film to diffuse to the free surface. However, the duration of the evaporation process also put a kinetic constraint on the ongoing movement of polymers to form the thermodynamically stable morphology. Thus, depending on a solvent evaporation rate, the final morphology would not necessarily be the most stable morphology. Similar results have been also reported with symmetric poly(styrene-*b*-butadiene) (PS-PB) diblock copolymers;[68] faster solvent evaporation produced a perpendicular lamellar morphology while slow evaporation resulted in a parallel morphology near the surface.

The morphology of a solvent annealed thin-film block copolymer depends on the type of solvent used. Bosworth *et al.*[69] found that the solvent selectivity of block copolymers led to different degrees of swelling in the domains, inducing two different morphologies depending on the solvent type. In a study by Peng *et al.*,[70] symmetric PS-PMMA thin films were solvent annealed with vapors of different selectivities (neutral, PS selective, and PMMA selective). The variation in the solvent type and the degree of swelling led to a number of morphologies: parallel lamellae, micellar structures, perpendicular cylinders, and spheres. Ross and coworkers[71] carefully implemented the morphology dependence on the solvent types and the swelling ratios and were able to tune the periodicity and the line width of single block copolymer thin films using solvent annealing.

2.2.2.3 Electric Fields

External electric fields have been employed to control the domain orientation of thin-film block copolymers. The tendency for the features to follow the trace of applied electric fields was explained in terms of the energetic stability of specific configurations.[72] For thin-film block copolymers, it has been demonstrated that in-plane cylinders oriented along the direction of electric fields as the fields were applied through planar electrodes (Fig. 2.7).[73] In the absence of the electric field, the parallel cylinders oriented randomly. A threshold value in electric fields, required for complete alignment of the domains, has been found. Below this value, the electric fields induced only partial alignment.

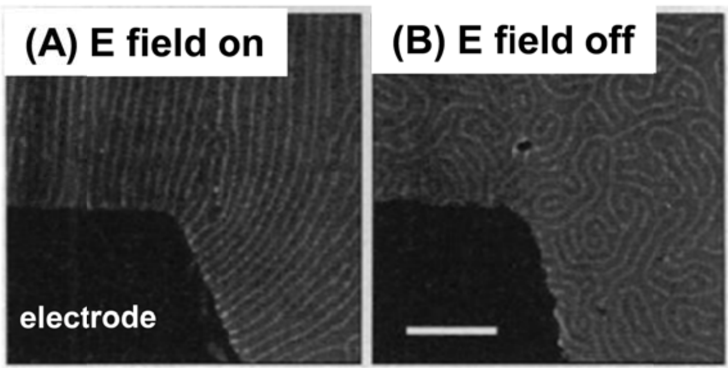

Figure 2.7 Top-down TEM image of a cylindrical morphology formed by PS-PMMA diblock copolymers adjacent to electrodes. The light lines are PMMA cylinders while the dark regions are PS. (a) With the applied electric fields, domains are aligned parallel to the applied electric field (in-plane alignment). (b) In the absence of electric fields, the domains are randomly oriented. The scale bar corresponds to 500 nm. Reprinted with permission from Morkved *et al.*[73] Copyright 1996 AAAS.

Contrary to the in-plane alignment,[73] out-of-plane orientation of domains (Fig. 2.8) can be achieved only when the electric fields that drive the alignment overcome the interfacial energy contributions (*i.e.*, polymer-substrate interaction) that tend to oppose the alignment. Accordingly, the electric field threshold for complete alignment normal to the substrate has been found to be larger than the threshold for the in-plane alignment.[74] Due to this interfacial interaction that favored parallel orientation of domains with respect to the substrates, Xu *et al.*[75] found a critical thickness below which the electric fields were not effective in orienting lamellar morphologies perpendicular to the substrate. Only for films thicker than the critical thickness were the domains at the interior of the film able to orient in the direction of the applied electric fields (perpendicular to the substrates). The interfacial interaction has been tuned by

controlling the composition of random copolymer brushes, and its effect on the alignment of domains using electric fields has been examined.[76] Based on the cross-sectional TEM measurement results, the complete alignment with the electric fields was achieved only when the neutral brush was used at the interface. The study by Wang *et al*.[77] indicated that the threshold field strength could be reduced by adding salts (LiCl) to polymers, presumably due to the increase in the dielectric constant difference between the domains in the block copolymers.

The mechanisms responsible for the alignment of domains in response to external electric fields have been studied. Two possible mechanisms were first suggested by Amundson *et al*.:[78] (1) the disordering and subsequent reformation of morphologies and (2) the movement of defects. Using in-situ small angle x-ray scattering, DeRouchey *et al*.[79] found an intermediate state, characterized by small grains of reduced order, during the alignment. The complete alignment would be then achieved by the rotation of these small grains. Two independent mechanisms were also observed in aligning block copolymer solutions; the defect movement dominated for the system near the order-disorder transition while the grain rotation became more prevalent for the more strongly segregated system.[80] On the other hand, simulations by Zvelindovsky and Sevink[81] resulted in a different microscopic interpretation for the weakly segregated systems; small undulations disrupted the existing domains leading to the formation of intermediate phases. Wang *et al*.[82] varied the effective interaction in the block copolymer system by incorporating salts. They found that with increasing the interaction parameter the main mechanism of rearrangement went through a transition from disruption followed by reformation to grain rotation.

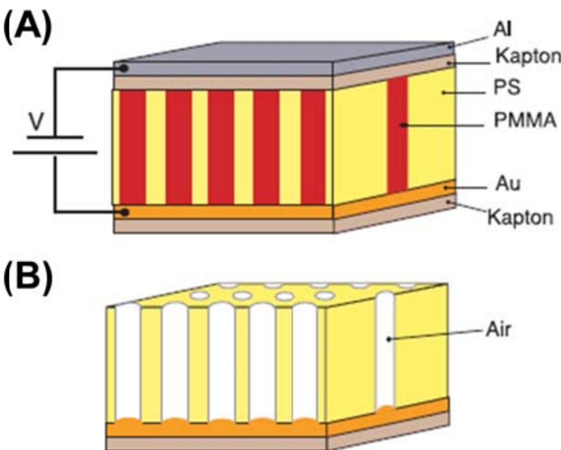

Figure 2.8 Schematic illustrations of (a) cylindrical domains of PS-PMMA diblock copolymers aligned parallel to the applied electric field (perpendicular to the substrate) and (b) the formation of a nanoporous PS template by removal of the PMMA domains. This structure was used to grow nanowires within the pores. Reprinted with permission from Thurn-Albrecht *et al*.[37] Copyright 2000 AAAS.

2.2.3 Long Range Ordering in Thin-Film Block Copolymers

2.2.3.1 Chemical Patterns and Density Multiplication

Periodic patterns present at interfaces that selectively wet different components of block copolymers have been used to guide the alignments of thin-film block copolymers. Rockford *et al*.[83] prepared underlying patterns that consist of alternating stripes of gold (poly(styrene) preferential) and silicon oxide (poly(methyl methacrylate) preferential). When the lamellar spacing of poly(styrene-*b*-methyl methacrylate) (PS-PMMA) diblock copolymers was roughly commensurate (within 25% mismatch) with the periodical spacing in the gold-SiO_x patterns, an incomplete but notable degree of directed self-assembly was observed for the PS-PMMA thin films above the chemical

patterns. The ability of these patterns to induce the alignment of the thin-film block copolymers was further investigated by studying the morphology within thick films.[84] It was found that the underlying pattern could guide the self-assembly as far as 0.5 μm away from the substrate.

Kim *et al.*[85] fabricated chemical patterns with high precision and controlled chemistry using advanced lithographic techniques and obtained defect-free long-range ordering of thin-film PS-PMMA (Fig. 2.9). The "epitaxial" self-assembly of the block copolymers, registered with the chemical patterns, persisted over a region of 8 μm × 5 μm, a significant improvement compared to the previous study that had taken similar approaches.[86]

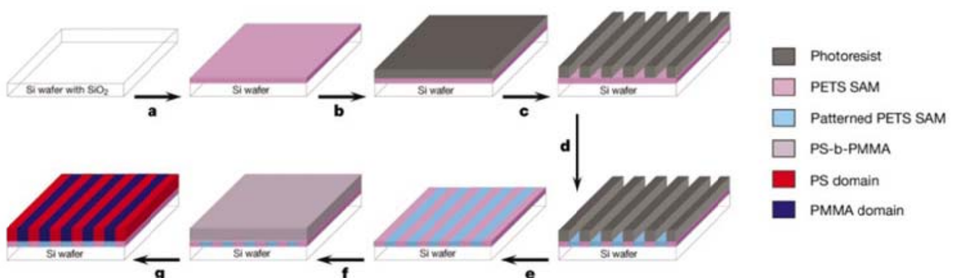

Figure 2.9 Schematic illustrations of chemical pattern fabrication and directed self-assembly of thin-film block copolymers: (a-b) PET and photoresist deposition; (c) EUV-IL exposure and development; (d) chemical modification of PET SAM's using irradiation; (e) photoresist removal; (f-g) block copolymer thin film deposition and thermal annealing. Reprinted with permission from Kim *et al.*[85] Copyright 2003 NPG.

Extreme ultraviolet radiation was used (1) to make patterns on photoresists through interferometric lithography (EUV-IL)[87] and (2) to modify self-assembled monolayers (SAM) of phenylethyltrichlorosilane (PET) chemically. The stripe chemical patterns

consisted of alternating regions of modified (polar) and unmodified (nonpolar) PET SAM's. The self-assembly of PS-PMMA was guided by the selective interaction between the chemical patterns and the block copolymer constituents. As the mismatch between the bulk spacing of the block copolymer and the chemical pattern spacing increased by more than a few percent, misregistration and other types of defects appeared. Using poly(styrene-*ran*-methyl methacrylate) random copolymer brushes, the effective interaction between chemical patterns and block copolymer components has been controlled by Edwards *et al*.[88] The study revealed that the directed self-assembly of PS-PMMA thin films could tolerate a larger mismatch between the chemical pattern period and the bulk polymer spacing before forming defects when the selective interaction of the chemical patterns with the polymers became stronger. The influence of the relative width of the chemical patterns on the directed self-assembly also has been studied.[89]

Much effort has been made to create elements that break the symmetry of bulk morphologies (Fig. 2.10). Bent lines (45 °, 90 °, and 135 °) have been realized with ternary blends of lamellar-forming PS-PMMA, PS homopolymers, and PMMA homopolymers.[90] According to simulation results, the suppression of defect formation around irregular shapes was explained by the segregation of the homopolymers to the corners of the bends. Burgaz and Gido[91] described how defect-like structures could be energetically stabilized by either segregation or depletion of homopolymers near these structures. More complicated shapes such as T-junctions, jogs, isolated lines, and concentric circles have been realized in thin-film block copolymers.[92, 93]

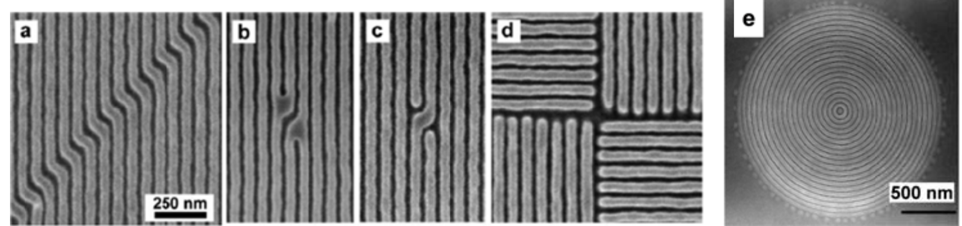

Figure 2.10 Top-down SEM images of non-stripe elements realized using (a-d) PS-PMMA ternary blends and (e) PS-PMMA diblock copolymers. Reprinted with permission from Stoykovich *et al.*[92] and Wilmes *et al.*[93] Copyright 2007 ACS. Copyright 2006 ACS.

The scheme of *density multiplication* enables directed self-assembly of block copolymers using chemical patterns whose periodicity is larger than that of the block copolymers. The major limitation of implementing chemically patterned substrates, discussed in the previous paragraphs, was the requirement that advanced lithographic tools had to be used to make chemical patterns that had comparable periodicities as block copolymers. This issue with the chemical patterning methodology was addressed by Ruiz *et al.*,[94] who were able to achieve alignment of cylindrical morphologies using chemical patterns with lower resolution than the block copolymers (Fig. 2.11). Using e-beam patterning, they prepared two hexagonal chemical patterns with periodicities of L_0 and $2L_0$, where L_0 was the bulk spacing of cylinder-forming PS-PMMA block copolymers (Fig. 2.11e-f). As shown in Figure 2.11g-h, both chemical patterns were able to guide the self-assembly of the PS-PMMA block copolymers, independent of the chemical pattern periodicities (L_S). Density multiplication has also been demonstrated for lamellar morphologies of thin-film block copolymers.[95] The effects of the background chemistry and the relative width of the guiding stripes on the quality of alignment have been investigated independently while implementing density multiplication.[96, 97]

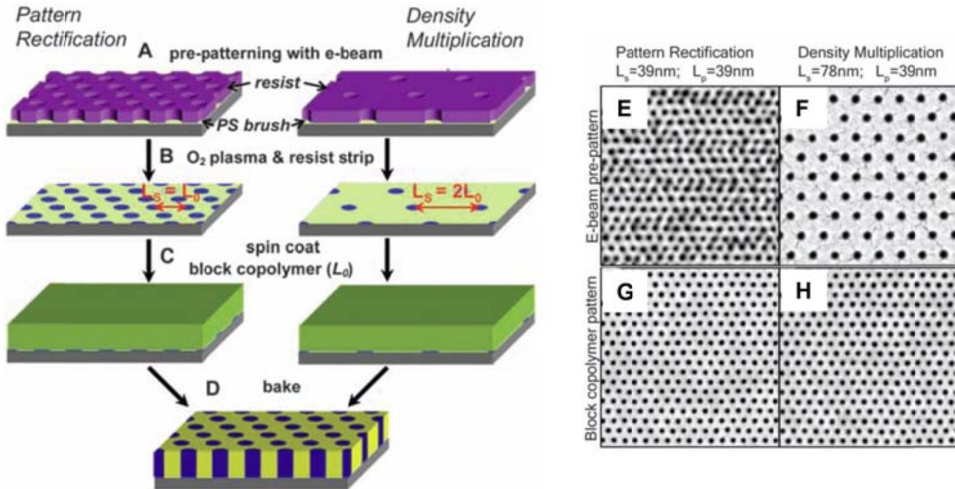

Figure 2.11 1X and 4X density multiplications. (a-d) Schematic illustrations of chemical pattern fabrication with different densities and directed self-assembly of thin-film block copolymers. Two chemical patterns have periodicities (L_S) of L_0 and 2 L_0, respectively, where L_0 is the periodicity of the thin-film block copolymers. (e-f) Top-down SEM images of the developed e-beam resists, used to make chemical patterns of different periodicities. (g-h) Top-down SEM images of perpendicularly oriented PS-PMMA cylinders, whose self-assembly was guided by the underlying chemical patterns derived from (e-f). Reprinted with permission from Ruiz *et al*.[94] Copyright 2008 AAAS.

2.2.3.2 Graphoepitaxy

In graphoepitaxy, topographic constraints are used to create lateral ordering of block copolymers over a large region. The concept of graphoepitaxy was first applied to direct the growth orientations of KCl crystals by the use of Cr gratings.[98] Segalman *et*

al.[99] found that the periodic mesas, fabricated using conventional lithography, induced long-range ordering of spherical morphologies of thin-film poly(styrene-*b*-2-vinylpyridine) (PS-P2VP) diblock copolymers over a large region (~ 5 μm). This was attributed to translational and orientation order imposed by the substrate topography.[100, 101] Both types of order decreased as the regions farther away from the topography were probed, which supported the confinement effect at the boundary on the ordering.

This methodology has also been demonstrated for different block copolymers with various morphologies. Cheng *et al*.[102] used the topographically patterned substrates, fabricated using interference lithography, to register a spherical morphology of poly(styrene-*b*-ferrocenyldimethylsilane) (PS-PFS) diblock copolymers. As the organometallic PFS block was highly resistant to oxygen plasma treatment, an array of PFS posts was obtained after plasma etching. The sidewalls needed to be flat and vertical (not tapered) for good alignment. The effect of line edge roughness of topography on the registration of features formed by thin-film block copolymers has been studied, and it has been shown that the regions farther away from the edges were more tolerant to the roughness.[103] Using substrate topographies, Sibener and his coworkers[104] were able to achieve defect-free alignment of multiple layers of cylinder-forming poly(styrene-*b*-[ethylene-*alt*-propylene]) (PS-PEP) block copolymers. They monitored the alignment process during annealing and found that the alignment started at the sidewall with the preferential interaction. For both spherical and cylindrical morphologies,[105, 106] the block copolymer systems tried to adjust the domain sizes, by either expanding or contracting, in order to be commensurate with the varying well width.

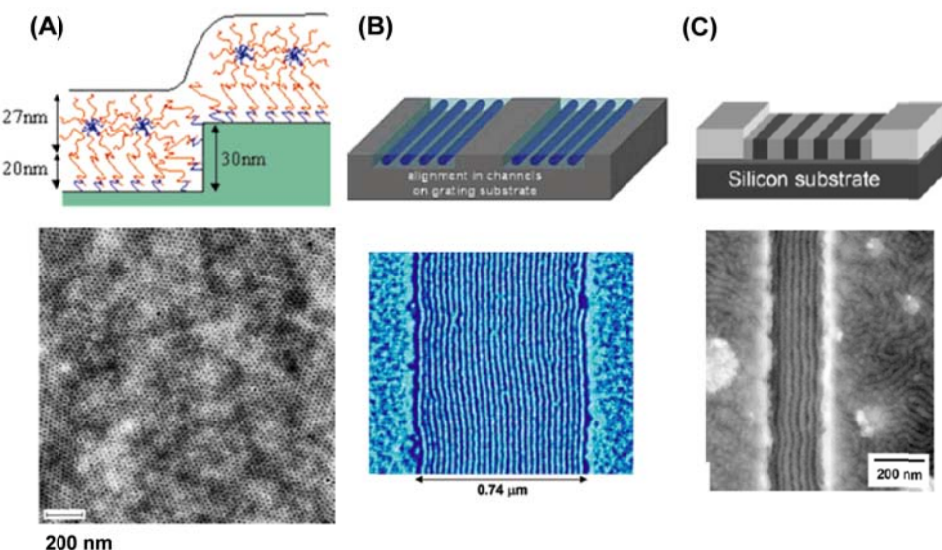

Figure 2.12 Schematic illustrations and corresponding microscopy images of aligned morphologies of block copolymers implementing graphoepitaxy (reprinted with permission from the references, as indicated): (a) AFM height image of sphere forming PS-P2VP;[99] (b) AFM height image of PS-PEP;[104] (c) top-down SEM image of PS-PMMA.[107] Copyright 2001 Wiley-VCH. Copyright 2004 ACS. Copyright 2007 Wiley-VCH.

Park *et al*.[107] combined graphoepitaxy with non-preferential random copolymer brushes to attain directed self-assembly of lamella-forming poly(styrene-*b*-methyl methacrylate) (PS-PMMA) block copolymers. They grafted a poly(styrene-*ran*-methyl methacrylate) random copolymer brush to the bottom interface of the wells while gold sidewalls (PS preferential) were used. Contrary to the previous results mentioned above, the long-range ordering of PS-PMMA induced by the graphoepitaxy only persisted 3 – 4 lamellar periodicities, possibly due to the relatively weak preferential interaction between the gold sidewalls and the PS block. The neutral random copolymer brush also had to be used in conjunction with graphoepitaxy in order to induce long-range order of

cylindrical morphologies of PS-PMMA, oriented perpendicular to the substrate.[108] Other complex patterns have also been achieved using graphoepitaxy.[109]

2.3 Random Copolymers and Chemical Modification

The strategy of incorporating random chemical entities into polymer chains, accomplished either through post-polymerization modification or copolymerization, has been used to attain desired physical properties of polymers.[110] For polymer blends and block copolymers that consist of random copolymer architectures, it has been suggested that various bulk properties are influenced greatly by the composition and the distribution of the random copolymers.[111-115] The interfacial properties of polymer thin films (*e.g.*, adhesion, wetting) may be modified through flame treatment, oxygen plasma, or brush grafting, and such changes are often interpreted as attributable to the variations in the compositions or the degree of random modification at the polymer interfaces.[116-119] With regards to the thin-film applications of block copolymers, random copolymers immobilized at substrate surfaces are implemented to change the interfacial interaction at the boundaries and, thereby, to control the orientation of the thin-film block copolymers supported on the substrates.[57, 62 120] Much of this dissertation deals with partially epoxidized poly(styrene-*b*-isoprene) block copolymers. The random copolymer architecture is anticipated for the partially epoxidized poly(isoprene) block as a result of the chemical modification.

Various methods have been implemented to chemically modify polydienes, such as sulfonation,[121, 122] fluorination,[123-125] hydrogenation,[126] and epoxidation.[127] Other types of modification for polydienes may be found in some review articles.[128, 129] Siddiqui and Cais[130] showed that the addition of difluorocarbene to poly(butadiene) occurred randomly throughout the chain. The NMR studies found that the distribution of

epoxidation on natural rubber or poly(isoprene) was random for numerous epoxidizing agents.[131-133]

Chemical modification of block copolymers proved effective in altering the Flory-Huggins interaction parameter (χ) of the systems. For example, Davidock *et al.*[134] added controlled amounts of difluorocarbene[135] to the poly(isoprene) (PI) block of poly(isoprene-*b*-ethylethylene) (PI-PEE) diblock copolymers. They found that χ between partially fluorinated PI and PEE varied systematically with the degree of modification for lamellar and cylindrical morphologies. Kimishima *et al.*[126] varied the degree of the PI block hydrogenation for PS-PI diblock copolymers. In their study, the periodicity of the microphase segregated lamellae increased with the extent of hydrogenation, presumably due to the change in the interaction parameter.

2.3.1 Solubility Parameter Formalism

The solubility parameter formalism states that the pair-wise interaction parameter between components A and B can be approximated as a function of the difference in solubility parameters of the components (δ_A, δ_B),

$$\chi_{AB} \approx \frac{V}{k_B T}\left(\delta_A - \delta_B\right)^2 \qquad \text{(Eq. 2.3)}$$

where V, k_B, and T represent the molar volume, the Boltzmann constant, and temperature in Kelvin, respectively.[136] Solubility parameters are defined as $\delta = (\Delta E^V/V)^{1/2}$, where the cohesive energy density ($\Delta E^V/V$) represents the energy of evaporation per unit volume for a pure component.[136] Several assumptions are made in the derivation of Eq. 2.3: (1) the Berthelot relation, which states that the interaction between two separate components may be expressed as the geometric mean of the interaction within each pure component, (2) no change in volume upon mixing, and (3)

regular solution mixing. The limitations of the solubility parameter argument would include the failure to incorporate conformational asymmetry into the interaction parameter,[137] negative interaction parameters (*e.g.*, due to hydrogen bonding) and lower critical solution temperatures (LCST) in blends, and the change in volume that leads to an entropic contribution to the interaction parameter. Despite its simplicity to account for all the details, it still provides useful approach for qualitative modeling of the interaction parameters between many pairs of polymers.

Various methods are available to estimate the solubility parameter of polymers, such as turbidimetry,[138] swelling measurements,[139] or viscosity measurements.[140] For example, in the turbidimetry measurement, two different non-solvents are added to polymer solution until the cloud point is reached. Then, the solubility parameter of the polymer may be calculated using the solubility parameter formalism. The viscosity measurements using various solvents give the relationship between Flory-Huggins interaction parameters and the solubility parameters of the solvents. The solubility parameter formalism is again applied, and the solubility parameter of the polymer is calculated from the slope and the intercept of the relationship.

The solubility argument was often implemented in order to explain the changes in physical properties that could be traced to the change in interaction parameters. Notably, the thermodynamics of protonated, hydrogenated, and deuterated polyolefin blends, within which dispersive interactions are dominant, have been studied from the solubility parameter perspective.[141-143] For example, the change in the interaction parameter with deuteration within polymer blends and its influence on the miscibility was explained by the smaller solubility parameter for the deuterated polymers compared to the protonated.[144] Interaction parameters were calculated from small angle neutron scattering (SANS) results from blends, and the solubility parameters extrapolated based

on the formalism agreed well with the solubility parameters obtained from the PVT measurements on pure components.[145, 146] The assignment of unique solubility parameters for protonated, hydrogenated, and deuterated polyolefins has been found to be self-consistent.[145]

The solubility parameter of a random copolymer is generally expressed as $\bar{\delta} = \sum \varphi_i \delta_i$, where φ_i and δ_i are the volume fraction and the solubility parameter of a component *i* in the random copolymer, respectively.[147, 148] The linear relationship between the copolymer solubility parameter and the fractions of constituents has been verified experimentally.[149, 150] Using turbidimetry, Ng *et al.*[151] calculated solubility parameters of epoxidized natural rubber for 20%, 50%, 60% epoxidation and found a linear dependence of the solubility parameter on the degree of epoxidation. Based on the linear dependence, they made an estimate for the solubility parameter of 100% epoxidized natural rubber to be 20.7 $J^{0.5}/cm^{1.5}$.

2.3.2 Binary Interaction Model

The binary interaction model incorporates the concept of intramolecular interactions in calculating effective interaction parameters and is used to explain the miscibility of copolymer blends. According to the model, the effective interaction parameter for the simplest case of blending homopolymers (A) with copolymers (B-*ran*-C) may be expressed as the following:

$$\chi_{eff} = \varphi_B \chi_{AB} + (1 - \varphi_B) \chi_{AC} - \varphi_B (1 - \varphi_B) \chi_{BC} \qquad \text{(Eq. 2.4)}$$

where φ_B and $(1 - \varphi_B)$ represent the fractions of B and C components within the copolymers, respectively.[112, 152, 153] Notably, the effective interaction parameter of blends does not have a dependence on the volume fractions of polymers (homopolymers and

copolymers) in the blend. The first two terms on the right represent the intermolecular interactions experienced by the homopolymers and the copolymers, and the last term on the right defines the intramolecular interactions within the copolymers. According to the equation, strong intramolecular interactions ($\chi_{BC} >> 0$) would induce miscibility between the homopolymers and the copolymers even when the homopolymers are not miscible with each component of the copolymers ($\chi_{AB} > 0$, $\chi_{AC} > 0$).[111] One example is the miscibility of styrene-acrylonitrile (SAN) copolymers with poly(ethyl methacrylate) (PEMA) homopolymers while individual poly(styrene) and poly(acrylonitrile) are not miscible with PEMA.[154]

Several assumptions are made in deriving the binary interaction model.[155] The mixing of components is assumed random such that the frequency of interaction by two species A and B is proportional to the product of their volume fractions. In addition, the interaction is assumed to involve only two units; the effect of the components that are adjacent to unit *i* within the same polymer chain (*i.e.*, units *i*+1 and *i*-1) is not taken into account in considering the interaction of unit *i*. The dependence of the binary interaction model on the sequencing distribution of copolymers was more carefully investigated.[156] Experiments showed deviation from the model on a number of occasions.[115, 141]

The application of the solubility parameter formalism to the binary interaction model results in

$$\chi_{eff} = \frac{V}{k_B T} [\, \varphi_B (\delta_A - \delta_B)^2 + (1 - \varphi_B)(\delta_A - \delta_C)^2 - \varphi_B (1 - \varphi_B)(\delta_B - \delta_C)^2 \,] \quad \text{(Eq. 2.5)}$$

Simple algebraic arrangements of this equation lead to

$$\chi_{eff} = \frac{V}{k_B T} (\delta_A - \bar{\delta})^2 \quad \text{(Eq. 2.6)}$$

where the effective solubility parameter of the copolymer, $\bar{\delta}$, equals $\varphi_B \delta_B + \varphi_C \delta_C$, recovering the linear dependence of the solubility parameter on the fractions of the constituents.

2.3.3 Epoxidation

Among a plethora of modification methods, epoxidation of polymers in various forms, most notably polydienes, has been explored consistently in the past for desirable changes in properties, such as low gas permeability and large oil resistance. For example, Mooney scorch time, defined as a period of time before scorching causes vulcanization of natural rubber (NR), was found to decrease significantly with the degree of epoxidation of NR.[157] The activation of double bonds for vulcanization triggered by the presence of epoxide was suggested in the past.[158] Changes in the rheological behavior and the relaxation modes of epoxidized poly(isoprene) homopolymers were studied while varying the degrees of epoxidation.[159] The correlation between the high tensile strength of epoxidized natural rubber (ENR) vulcanisate and the strain-induced crystallization was studied.[160] In comparison to NR, the higher adhesion to glass substrates and the increase in resistance to swelling and oil permeation were observed for ENR and its vulcanisates.[161, 162] A small difference in the degree of epoxidation, as little as 10%, in the blends of ENR's led to the immiscibility, indicative of non-trivial interaction between NR and ENR units.[163] ENR was blended with epoxy resins in order to attain rubbery toughening, and the effect of the modifier on mechanical properties after curing was studied.[164, 165] Additional modification has been implemented to the epoxide functional groups of epoxidized polydienes. For example, the amine groups were incorporated into epoxidized poly(isoprene) homopolymers for their use as an antioxidant.[166] Photocrosslinkable functional groups were grafted to ENR so that the

polymer films would crosslink upon ultraviolet radiation (UV), and phosphorus-containing functional groups were added to make the polymers more resistant to fire hazard.[128]

An increase in the solubility parameter of natural rubbers with epoxidation has been observed. While the solubility parameter of poly(isoprene) is 16.6 $J^{0.5}/cm^{1.5}$,[167] Grubbs *et al.*[127] extrapolated the solubility parameter of epoxidized isoprene units to be 18.7 $cal^{1/2}/cm^{3/2}$. Based on the relationship between the intrinsic viscosity and the solubility parameter, the solubility parameter of epoxidized polybutadiene (PB) has been estimated to be 19.8 $J^{0.5}/cm^{1.5}$.[168] As mentioned previously, the solubility parameter of ENR changed linearly with the degree of epoxidation,[150, 151] and the linear relation would translate to δ = 19.1 – 20.7 $J^{0.5}/cm^{1.5}$ for completely epoxidized natural rubbers.

Various reagents were implemented to epoxidize olefins and polydienes in the past, and they include peracid, *meta*-chlorobenzoic acid, and dioxirane. ^{1}H-NMR or ^{13}C-NMR are generally used to calculate the degree of epoxidation.[169] Peracid may be generated in-situ when peroxide reacts with acids (*e.g.*, acetic acid, formic acid, phthalic acid). The agent has been used to epoxidize natural rubbers[162, 170] and poly(butadiene) (PB).[168] Block copolymers also have been epoxidized using the oxidizing agents generated in-situ; peracetic acid,[171] performic acid,[172, 173] and monoperoxyphthalic acids[174] were used to incorporate epoxide groups onto the polydiene block in block copolymers. The higher reactivity of double bonds on the polymer backbone chain in comparison to those on the side groups has been frequently observed.[168, 173]

The acidic environment in this in-situ generation method causes the ring opening of the epoxide. The acid-catalyzed hydration of epoxide within the polymer chain leads to the formation of alcohol, ketone, and diol. The ketone may react with epoxide in other chains and form ether (“polymer crosslinking”).[158] The chain scission in epoxidized

poly(butadiene) occurred with long reaction times depending on the types of solvents.[175] The intramolecular reaction of the hydroxyl group with the neighboring epoxide could result in the formation of cyclic ether.[176, 177] Furanized natural rubber, the most likely product (cyclic ether) from the intramolecular reaction, exhibited a stress versus strain curve similar to poly(styrene).[176] Perera *et al.*[177] found that such furanization of epoxidized natural rubber could be minimized when (1) the degree of chemical modification was less than 60%, (2) the acid concentration was low, or (3) the reaction temperature was low. The hydroxyl group from the ring opening of epoxides could also react with the neighboring unreacted diene units, leading to cyclizations.[177, 178]

With relative stability and accessibility in comparison to perbenzoic acid, *m*-chlorobenzoic acid (MCPBA) was first used to estimate the total degree of unsaturation in organic compounds, including natural rubbers, using titration.[179, 180] MCPBA was also used to add epoxide groups to PI and PB homopolymers.[169, 181] Antonietti *et al.* [182] epoxidized PS-PB diblock copolymers and used ring-opening reaction of epoxide in order to obtain amphiphiles. Bailey *et al.*[183] epoxidized the PI block in poly(styrene-*b*-isoprene-*b*-lactide) triblock copolymers. In this study, the chemical modification was implemented in order to make the inner surface of the pores more hydrophilic and to allow an easier passage for an aqueous solution through the pores. The side reaction of epoxide commonly observed with the peracid was not observed when MCPBA was used for the epoxidation.

In the process of decomposition of potassium peroxymonosulfate ($KHSO_5$, or also known as caroate), the oxidation of small molecules has been observed with ketone present as catalysts, and it was suggested that the intermediate, known as dimethyl dioxirane (DMD), was involved in the oxidation.[184] DMD was finally isolated, and its properties were studied by Murray and Jeyaraman.[185] PB homopolymers were

epoxidized using DMD and phase transfer catalysts, and no significant side reaction was observed.[186, 187] Grubbs *et al*. used DMD without any phase transfer catalyst to selectively epoxidize the PI block in poly(isoprene-*b*-butadiene) (PI-PB) diblock copolymers. Based on small angle x-ray scattering results, they suggested that the disordered PI-PB became ordered as the degree of epoxidation was raised higher than 87%.

Chapter 3 Experimental Methods

This chapter discusses experimental methods used to (1) synthesize and characterize bulk block copolymers and (2) fabricate and study thin-film samples. Anionic polymerization was used to synthesize poly(styrene) (PS) and poly(isoprene) (PI) homopolymers, poly(styrene-*b*-isoprene) (PS-PI) diblock copolymers, and poly(styrene-*b*-isoprene-*b*-methyl methacrylate) (PS-PI-PMMA) triblock copolymers. Size exclusion chromatography (SEC) was used to analyze the molecular weight (M_n) and polydispersity index (PDI) of the polymers. Partial epoxidation of poly(isoprene) blocks in the PS-PI and PS-PI-PMMA block copolymers was achieved using dimethyl dioxirane (DMD). The measurement of neutron magnetic resonance (^{1}H-NMR) on the samples gave information about the volume fractions of components and the degrees of chemical modifications in the samples. While the microphase segregated morphologies of the bulk specimens were analyzed using small angle x-ray scattering (SAXS), the glass transition temperature (T_g) was identified using differential scanning calorimetry (DSC) and the rheological behaviors of the block copolymers were investigated through dynamical mechanical spectroscopy (DMS). Thin-film block copolymers were prepared at the University of Wisconsin at Madison by spin-coating, followed by thermal annealing in vacuum. Ellipsometry was employed to measure the film thickness. The thin films were characterized using scanning electron microscopy (SEM) and atomic force microscopy (AFM). The stripe chemical patterns were fabricated and used to direct the self-assembly of thin-film block copolymers. Oxygen plasma treatment was implemented either to increase the contrast during SEM imaging or to control the width of the guiding stripes in the chemical patterns.

3.1 SYNTHESIS OF BLOCK COPOLYMERS

3.1.1 Controlled Anionic Polymerization

In comparison to other types of polymerizations, such as free-radical polymerization, controlled polymerization generally results in much narrower molecular-weight distributions (low polydispersity index (PDI)). The controlled polymerization consists generally of three steps as shown in the following:

Initiation: $I + M \xrightarrow{k_i} P_1^*$ (Eq. 3.1)

Propagation: $P_1^* + M \xrightarrow{kp} P_2^*$ (Eq. 3.2)

$P_N^* + M \xrightarrow{kp} P_{N+1}^*$ (Eq. 3.3)

Termination: $P_{N+1}^* + T \xrightarrow{kt} P_{N+1}T$ (Eq. 3.4)

where I, M, P_N, T, and * stand for initiators, monomers, polymers with N degrees of polymerization, termination agents, and reactive ends, respectively. Once initiation occurs, the chains with active centers start to add monomers to the chains. Without the introduction of terminating agents, these chains remain "active" even after consumption of all the monomers under a controlled environment. For the synthesis of block copolymers, a different type of monomer can be added after the complete polymerization of previously added monomers. Factors such as the relative stability of anions will determine the order of sequential anionic polymerization of the blocks. In experiments, much care is put into assuring the minimal introduction of non-intentional termination or chain transfer agents. For example, anions play the role of active centers in the case of controlled anionic polymerization, and the presence of water or oxygen in the reaction can lead to termination or coupling of living chains. The number of active chains is ideally equal to that of the initiators introduced into the reactor, and this allows precise control over the molecular weight of resulting polymers. In order to attain low

PDI, both the dissociation of initiators and the first monomer addition need to be quick compared to the sequential propagation step so that all chains start polymerization effectively at the same time. It has been found that a Poisson molecular-weight distribution results from controlled anionic polymerization, and its PDI may be expressed as PDI = 1 + 1/N, where N is the degree of polymerization. Typical PDI values observed in experiments are 1.02 − 1.20. A more detailed explanation of controlled anionic polymerization can be found in the literature.[1]

3.1.2 Synthetic Procedures

Styrene (Aldrich), isoprene (Acros), and methyl methacrylate (Fluka) monomers were repeatedly (1) frozen in a liquid N_2 bath, (2) degassed while in a frozen state, and (3) thawed. This "freeze-pump-thaw" process removed dissolved oxygen. Other impurities and inhibitors in styrene and isoprene monomers were removed by stirring them in a controlled environment for 30 − 60 minutes with appropriate purifying agents: di-butyl magnesium (Aldrich) for styrene at room temperature and *n*-butyl lithium (Aldrich) for isoprene in an ice bath. These monomers were distilled to empty flasks and treated one more time with the same purification process. They were finally collected into glass burettes. Methyl methacrylate monomers were stirred with calcium hydride (CaH_2) overnight in order to remove water, then distilled to another flask containing a tri-ethyl aluminum solution in heptane (Aldrich) to remove alcohol and moisture.[188] After the monomers turned yellow-ish, representative of well purified methyl methacrylate monomers, they were transferred by short path vacuum distillation to empty burettes. 1,1-Diphenylethylene (DPE) (Aldrich) was dried by overnight stirring with potassium hydroxide (KOH) and subsequently with calcium hydride (CaH_2). Then, DPE was distilled to an empty flask. Solvents such as cyclohexane (CHX) and

tetrahydrofuran (THF) were primarily purified using purification columns containing copper catalyst and activated alumina to remove oxygen and proton contaminants, respectively.[189] For THF, an additional step was taken, which involved stirring over *sec*-butyl lithium for 30 minutes followed by distillation to empty solvent flasks.

A schematic diagram of the synthetic procedure for PS-PI-PMMA is shown in Figure 3.1. All reactions occurred in a tightly sealed reactor (Pyrex) that was treated with several cycles of torching, applying vacuum, and purging with argon. Much care was taken to minimize the introduction of oxygen or humidity during these steps.

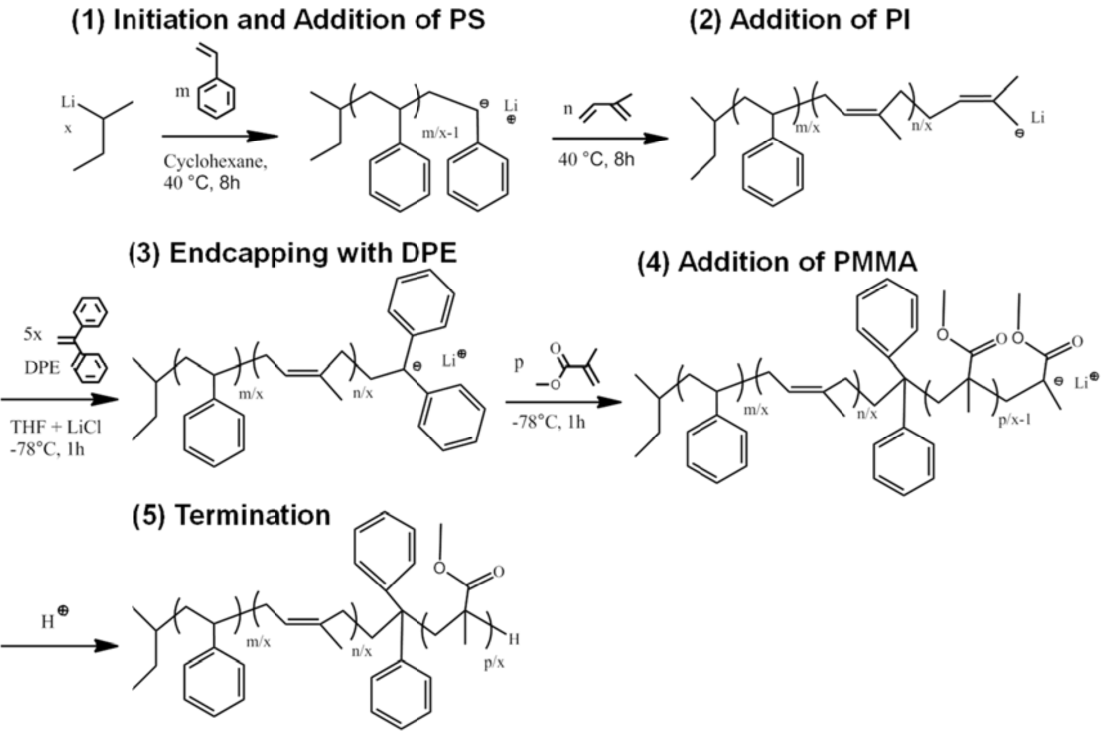

Figure 3.1 Schematic representation of procedures required for the synthesis of poly(styrene-*b*-isoprene-*b*-methyl methacrylate) triblock copolymers. DPE and THF denote 1,1-diphenylethylene and tetrahydrofuran, respectively.

Purified cyclohexane was added to a sealed reactor containing argon. The temperature of the solvent was controlled to reach 40 °C by placing the reactor in contact with a water bath. Then, *sec*-butyl lithium (1.3 M solution in cyclohexane, Aldrich) was added into the reactor as the initiator for anionic polymerization. Purified monomers of styrene and isoprene were added sequentially. Polymerization was conducted at 40 °C for 8 hours per block. For the synthesis of PS-PI block copolymers, degassed methanol was added into the reactor following the completion of the isoprene polymerization in order to terminate the reaction at this stage. For PS-PI-PMMA synthesis, the reactor was cooled to ~ 0 °C and purified tetrahydrofuran (THF) with predissolved lithium chloride (LiCl) and DPE was added. Once the reactor temperature reached -78 °C using a dry ice bath, purified methyl methacrylate monomers were added to the reactor. The reaction was terminated by injecting degassed methanol after 1 hour of polymerization. Finally, the polymers were recovered by precipitation in methanol and dried under vacuum prior to characterization.

Poly(methyl methacrylate) (PMMA) polymerization requires additional experimental steps to minimize side reactions. It has been found that carbanions at the chain ends often attack the carbonyl carbon on the methacrylate monomer. End-capping with bulky side-groups, either at the chain end or the initiator, gives steric hindrance and suppresses such a side reaction. Wiles and Bywater[190] used 1,1-diphenylhexyl lithium, prepared by mixing DPE with butyl lithium, as initiators for the polymerization of methyl methacrylate (MMA). Zune *et al.*[191] were successful in the synthesis of poly(isoprene-*b*-methyl methacrylate) block copolymers by endcapping the living chain ends of PI with DPE, followed by the sequential polymerization of MMA. Polymerization of MMA can also terminate during the ongoing polymerization process. The carbanions at the chains ends may either back-attack the carbonyl groups in the

previously polymerized chains or choose to form ketone, releasing methoxide.[192] To some degree, these side reactions may be prevented by decreasing the reactor temperature (-78 °C). However, THF is generally added to the reactor in order to prevent the CHX solution from freezing at the low temperature, and this addition inevitably leads to an increased reactivity of the chain ends and makes them more susceptible to the side reactions. Varshney and his coworkers[193, 194] have found that the coordination of lithium salts with methyl methacrylate and *tert*-butyl acrylate carbanions results in a much sharper molecular weight distribution, suggesting that the coordination inhibits the chain termination. Similarly, the role of diethyl zinc in the anionic polymerization of MMA has been investigated by Ozaki *et al*.[195] They found that the coordination of diethyl zinc with the enolate anion in methyl methacrylate made the anion more stable and lowered the rate of polymerization, resulting in a lower PDI value.

3.1.3 Selective Partial Epoxidation

The controlled degrees of epoxidations of poly(isoprene) blocks in PI, PS-PI, and PS-PI-PMMA precursors were achieved using dimethyl dioxirane (DMD). This agent appears as an intermediate during the decomposition of potassium peroxymonosulfate ($KHSO_5$) and has been used widely in epoxidation of small molecules[196] and polydienes.[186, 197] Partial epoxidation of the poly(isoprene) block with varying degrees of modification was attained by stirring a polymer solution in dichloromethane along with acetone, an aqueous buffer solution ($NaHCO_3$, Aldrich), and an aqueous solution of potassium monosulfate triple salt (Sigma Aldrich) at room temperature for 16 − 48 hours. The polymer solution was extracted and dried in vacuum.

3.2 CHARACTERIZATION TECHNIQUES IN BULK

3.2.1 Size Exclusion Chromatography (SEC)

Size exclusion chromatography (SEC) is a tool used to measure the molecular weight distribution of polymer samples and is also commonly called gel permeation chromatography (GPC). SEC is made up of a series of columns packed with particles containing pores of various sizes. As the polymer solution is pumped through the column, typically at the flow rate of 1 mL/min, the polymers with larger "hydrodynamic" volume spend less time in the columns and elute first. While various detectors are available, the refractive index detector was mainly used in this study to monitor the quantity of eluted polymers. Standards provided by vendors are used to relate the elution time with the molecular weight.

Three different SEC instruments with either tetrahydrofuran (THF) or chloroform ($CHCl_3$) as mobile phases have been employed: (1) Waters 717 plus Autosampler, columns with 5 μm pore size (Phenomenex Phenogel 5 μm, 300 × 7.8 mm), and Waters 2410 refractive index detector (THF, Univ. of Minnesota); (2) Hewlett-Packard 1100 HPLC, HP 1047A refractive index detector, and poly(divinyl benzene) columns (Gel Organic columns, Jordi) ($CHCl_3$, Univ. of Minnesota); (3) Viscotek VE2001 with 302-050 tetra detector array (THF, Univ. of Wisconsin). The first instrument suffered from broadening of peaks when polymers contained poly(ethylene oxide) or poly(methyl methacrylate) blocks. Such broadening is generally attributed to polymer adsorption to the packing, causing the polymers to stay longer in the columns.[198]

3.2.2 Nuclear Magnetic Resonance Spectrometry (^{1}H-NMR)

Proton nuclear magnetic resonance (^{1}H-NMR) of polymer samples was measured in order to find the compositions of blocks and the degrees of epoxidation on poly(isoprene) blocks in block copolymers. Considering a nucleus has ($2I+1$) spin states in an applied magnetic field B_a (I: nuclear angular momentum number), isolated ^{1}H ($I = 1/2$) has two states separated by $\gamma\hbar B_a$. $\hbar$ is the reduced Planck constant, and γ is called the magnetogyric ratio, which varies depending on the types of atoms. The excitation of a nucleus to the higher (more unstable) spin state can occur when radiated with electromagnetic (EM) waves with the Larmor precession frequency $\omega_0 = \gamma B_a$. The excited nucleus decays back to the stable state, emitting EM waves with ω_0. This research used pulsed NMR, or also known as Fourier Transform (FT) NMR. A pulse of EM waves was applied to samples in order excite all the hydrogen atoms. The decay of excited nucleus, known as *free induction decay* (FID), was detected and recorded. Fourier transform was used to extrapolate the frequency components of FID.

The frequency of EM waves that hydrogen atoms absorb shifts depending on the "environment" surrounding the atoms. The effective magnetic field strength is affected by the diamagnetic contributions from electrons around a nucleus, and this effect is called *shielding*. There are numerous factors that influence the degree of shielding, including electronegativity of the nearby atoms and orientations of molecules to the static magnetic field. This characteristic shift enables the identification of different frequency components in FID with different components in block copolymer samples. For example, the hydrogen atoms in poly(styrene) would absorb waves of different frequencies compared to the hydrogen atoms in poly(isoprene). The area under the peak is proportional to the number of hydrogen atoms giving rise to the signal, and this is used to estimate the compositions or the degrees of chemical modification in samples.[199]

In this research, VAC-300 Autosampler (IBM Instruments) at the NMR laboratory (Univ. of Minnesota) was used.

3.2.3 Small Angle X-ray Scattering (SAXS)

Small angle x-ray scattering (SAXS) was used to characterize the morphology and its periodicity in block copolymer samples. The fundamental principle of SAXS involves the interaction of x-rays with electrons in samples, which leads to the scattering of the incident waves. The scattered waves radiate from the scatterer outward in a spherical form. Assuming the scattering is coherent with no phase change, the phase difference between waves scattered from different positions relies only on the path difference.

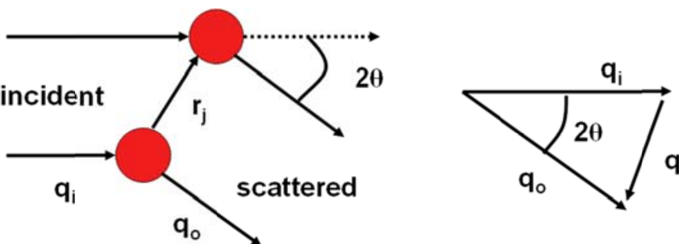

Figure 3.2 Schematic representation of scattered waves from multiple scattering sources. The parameters $\mathbf{q_i}$, $\mathbf{q_0}$, 2θ, and $\mathbf{r_j}$ denote the wavevectors of incident and scattered waves, the angle between the waves, and the position of the jth scatterer, respectively. $\mathbf{q}$ (scattering vector) = $\mathbf{q_o} - \mathbf{q_i}$. Bold characters are used to denote vectors. Adapted from Roe.[200]

For elastic scattering, $|\mathbf{q_i}| = |\mathbf{q_o}|$, and $|\mathbf{q}| = |\mathbf{q_o} - \mathbf{q_i}| = 4\pi \sin(\theta)\, \lambda^{-1}$, where λ stands for the wavelength of the incident waves. The total amplitude A(**q**) and the intensity I(**q**) of two scattered waves would correspond to

$$A(\mathbf{q}) = A_0 \exp(i\mathbf{q_0}\bullet\mathbf{r} - i\omega t))\ (1+\exp(-i\mathbf{q}\bullet\mathbf{r_j})\ ) \quad \text{(Eq. 3.5)}$$

$$I(\mathbf{q}) = A(\mathbf{q})\ A(\mathbf{q})^* = A_0^2\ (1+\exp(-i\mathbf{q}\bullet\mathbf{r_j})\ )\ (1+\exp(+i\mathbf{q}\bullet\mathbf{r_j})\ ) \quad \text{(Eq. 3.6)}$$

The equation may be written to account for all the scatterers. The exponential $\exp(i\mathbf{q_0}\bullet\mathbf{r} - i\omega t)$ in the wave equation is omitted in the rest of this section since it would be cancelled during the calculation for the intensity,

$$A(\mathbf{q}) = \textstyle\sum_j A_0 \exp(-i\mathbf{q} \bullet\mathbf{r_j}) \quad \text{(Eq. 3.7)}$$

Without loss of generality, this may be written as

$$A(\mathbf{q}) = \int_V A_0\, n(\mathbf{r}) \exp(-i\mathbf{q}\bullet\mathbf{r})\, d\mathbf{r} \quad \text{(Eq. 3.8)}$$

where V, **r**, and n(**r**) represent the volume occupied by scatterers, the position of scatterers, and the density of scatterers, respectively. Simple quantum mechanical treatment also results in a similar relationship, assuming the Born approximation.[201] The total amplitude may divided into separate contributions from electrons associated with each unit cell,

$$A(\mathbf{q}) = \sum_{unit\ cells} \int_{V\ unit\ cell} A_0\, n_{unit}(\mathbf{r}) \exp(-i\mathbf{q}\bullet(\mathbf{r}_{unit} + \mathbf{r}_k\ )\, d\mathbf{r}_k$$

$$= \sum_{unit\ cells} A_0 \exp(-i\mathbf{q}\bullet\mathbf{r}_{unit}\ ) \int_{V\ unit\ cell} n_{unit}(\mathbf{r}) \exp(-i\mathbf{q}\bullet\mathbf{r}_k)\, d\mathbf{r}_k$$

$$= S(\mathbf{q})\ F(\mathbf{q}) \quad \text{(Eq. 3.9)}$$

where $n_{unit}(\mathbf{r})$, $\mathbf{r_{unit}}$, and $\mathbf{r_k}$ represent the electron densities in a unit cell, the lattice vector, and the relative position of electrons within a unit cell. S(**q**) (structure factor) and

F(**q**) (form factor) correspond to the Fourier transforms of the Bravais lattice in real space and the electron densities in a unit cell, respectively.

The scattering occurs to a significant degree (S(**q**) ≠ 0) only when **q** is equal to the reciprocal lattice **G**,

$$\mathbf{q} = \mathbf{G} \qquad \text{(Eq. 3.10)}$$

It can be shown that the shortest length of **G** is equal to $2\pi/d$, where d is the spacing between parallel planes in real space perpendicular to **G**.[202] Including reciprocal lattice vectors with higher orders (n: integers > 1),

$$|\mathbf{q}| = \frac{4\pi \sin(\theta)}{\lambda} = |\mathbf{G}| = \frac{2\pi\, n}{d} \qquad \text{(Eq. 3.11)}$$

$$2d \sin(\theta) = n\, \lambda \qquad \text{(Eq. 3.12)}$$

which is known as Bragg's Law.

Ordered morphologies of block copolymers consist of periodic domains of distinct scattering length densities (ρ). For the simplest case of diblock copolymers, the scattering intensity may be expressed as

$$I(\mathbf{q}) \propto (\Delta\rho)^2\, |\, F'(\mathbf{q})\, S(\mathbf{q})\, |^2 \qquad \text{(Eq. 3.13)}$$

where Δρ denotes the difference in the scattering density. The morphologies correspond to different crystallography groups, and the associated symmetries dictate the values of **q** at which peaks are allowed. For example, the allowed peaks in the lamellar morphology appear at the integer multiples of the primary peak position $q^* = 2\pi/d$.[203]

SAXS instruments at three facilities were used: (1) Characterization Facility (Univ. of Minnesota), (2) Materials Science Center (Univ. of Wisconsin), and (3) Argonne National Laboratory. The instrument at the Characterization Facility consists of

a Rigaku Ultrex 18kW generator that produces copper K_α x-rays (λ = 1.54 Å) and a Bruker Hi-Star 2-dimensional detector. The SAXS measurement at Argonne National Laboratory was conducted using the 5-ID-D station at Advanced Photon Source. The scattering of incident x-rays (λ = 0.73 Å) was collected at Mar 165 mm CCD detector. The one-dimensional form of I(q) was obtained by integrating the two-dimensional data using the FIT2D software.

3.2.4 Differential Scanning Calorimetry (DSC)

Differential scanning calorimetry (Q1000 DSC, TA Instruments) was used to find the glass transition temperature (T_g) of block copolymers. In a typical DSC instrument, one reference pan with a known heat capacity (C_p) and another pan containing polymer samples are heated simultaneously. The amount of heat flow to the polymer pan, required to keep the temperature equal in both pans, is monitored as the temperature is varied. Deviations from the linear relationship of the heat flow with varying temperature, $\Delta(\text{Heat}) = C_p\ \Delta T$, are attributed to the thermal transitions in the polymer samples. A step-like function indicates glass transition while exothermic and endothermic peaks suggest crystallization and melting, respectively.

3.2.5 Dynamic Mechanical Spectroscopy (DMS)

Dynamic mechanical spectroscopy (DMS) (ARES, Rheometric Scientific) was used to determine order-disorder transition temperatures (T_{ODT}) of block copolymers and to study thermal fluctuations in systems near T_{ODT}. The basic principles of DMS are based on the viscoelasticity of polymers, which means that the materials exhibit both liquid-like and solid-like behaviors. Viscoelasticity is observed in numerous materials (*e.g.*, silly putty). These phenomena may be understood in terms of whether components

in materials are given enough time to move and relax in response to perturbations. When the rate of the perturbation is fast enough such that the time allowed is less than the typical relaxation time of the components, the material behavior would resemble the elastic response of typical solids to an external stress. On the contrary, when the rate is slow, the components would have enough time to relax in response to the perturbation and the materials would behave viscously as liquid. Generally, the distinction between viscoelastic solids and liquids is made by the question of whether the stress may be relieved completely given an infinite amount of time.[204] In this research, strain $\gamma = \gamma_0 \sin(\omega t)$ was applied to polymer samples as a perturbation, and the shear stress was measured. In this case, the rate of the perturbation would be the frequency ω of the strain sinusoidal wave.

The concepts of elasticity and viscosity arise while establishing relationships between shear stress σ and shear strain γ, as shown in following equations.

$$\sigma = G \gamma \qquad \text{(Eq. 3.13)}$$

$$\sigma = \eta \, (d\gamma/dt) \qquad \text{(Eq. 3.14)}$$

where G and η denote shear modulus and viscosity, respectively. Complex notations are used to denote the applied oscillatory shear strain $\gamma^* = \gamma_0 \exp(i\omega t)$ and the measured shear stress $\sigma^* = \sigma_0 \exp(i\omega t + i\delta)$ with the phase difference δ. If a material property can be described solely by either elastic or viscous components, the phase of the shear stress would be either in phase or out of phase by 90° ($\delta = \pi/2$) with respect to the oscillatory strain. Generally, the phase of polymer samples lies between 0° and 90°, indicating the presence of viscoelasticity. The complex dynamic modulus G* is defined as

$$G^* = \sigma^* / \gamma^* = G' + i\, G'' \qquad \text{(Eq. 3.15)}$$

where G' and G'' are known as elastic (or storage) modulus and viscous (or loss) modulus, respectively. For polymer samples, the viscous characters originate from the friction of the polymers as they move past one another in order to relieve external stress and to attain the most probable conformation. The elastic components come from the distortion in the Gaussian distribution of the chains.

As the oscillatory frequency (ω) of the strain is varied in a controlled manner, different length scales within a polymer chain that can relax in response to the strain are probed. There is an inevitable time lapse between responses of a short segment and a longer segment, causing them to respond differently to a common source of stress. At high ω (*i.e.*, short relaxation time), only small segments in a chain may relax while the whole chain would be able to relax at much lower ω (long relaxation time). Therefore, in order to investigate block copolymer morphologies of finite periodic dimensions, a frequency regime below the critical frequency (ω_c) needs to be studied.

The coupling between a sample morphology and its mechanical properties induce morphology-specific frequency dependence of $G'(\omega)$ and $G''(\omega)$ at low ω. For example, $G'(\omega)$ and $G''(\omega)$ of diblock copolymers with a lamellar morphology were found to exhibit $\omega^{0.5}$ dependence for $\omega < \omega_c$ while they are proportional to ω^2 and ω^1 at the terminal region in the disordered melt state.[205] The dependences of $G'(\omega)$ and $G''(\omega)$ on ω for other morphologies may be found elsewhere.[206, 207] The abrupt change in the magnitude of $G'(\omega)$ during isochronal temperature sweep has been widely used to identify T_{ODT}, which separates a ordered morphology from a disordered melt state.

3.3 Thin Film Characterization and Chemical Pattern Fabrication

Thin-film fabrication and characterization were conducted at the University of Wisconsin, Madison. Polymer solutions in toluene (0.2 – 4.0 wt. %) were prepared and

stirred for at least 2 hours prior to the use. Uniform polymer thin films were prepared through the process of spin coating on Si substrates, and the ellipsometry instrument (AutoEL-II, Rudolph Research) was used to measure the film thickness. Then, the polymer films were thermally annealed in vacuum. For selected samples, the static contact angles of water drops (1 μL) were measured (OCA15, Data Physics).

3.3.1 Scanning Electron Microscopy (SEM)

Scanning electron microscopy (SEM) detects and displays the interaction between specimens and a narrow coherent beam of electrons that travels in vacuum. Two main forms of the interaction are elastic and inelastic scattering. While the beam does not lose its kinetic energy and only changes its direction upon elastic scattering, the energy transfer occurs during inelastic scattering. The aftermath of the beam-specimen interaction takes place over a region called *interaction volume*, and the interaction volume increases for a beam with larger energies, which lead to deeper penetration into samples.

Electrons that escape the specimens after elastic scatterings are called backscattered electrons (BSE). On the other hand, various components are generated as consequences of inelastic scattering. Secondary electrons are the electrons ejected from the outer-shells of atoms when the energy transferred is large enough to ionize the atoms. Bremsstrahlung refers to a continuous spectrum of electromagnetic radiation generated as a result of the beam deceleration. When the transferred energy ejects electrons from the inner-shell of atoms, the vacancies are filled by outer-shell electrons, leading to either x-ray or Auger electron generation.

Generally, SEM instruments detect backscattered electrons and secondary electrons. A small fraction of backscattered electrons are scattered backwards from the

impact area; they contain high resolution information and are called BSE_I. The rest (BSE_{II}) experience a series of elastic scattering, travelling away from the initial impact area, before they depart from the samples. There are three types of secondary electrons generated as a result of inelastic beam-specimen interactions: SE_I, SE_{II}, and SE_{III}. SE_I forms as a result of direct interaction between the beam and the specimen at the beam impact area and is known to carry high resolution information about the specimen. The SE_{II} signal is generated away from the beam impact area by backscattered electrons that have returned to the surface. Lastly, the SE_{III} component is generated as the backscattered electrons that have escaped specimens strike other components in SEM, *e.g.*, the inner chamber. The ratio of the signals, SE_I/SE_{II}, may be raised by implementing smaller accelerating voltages. Based on these BSE and SE signals, the contrast in SEM images arises as a result of various factors, such as the atomic number difference, the topography, and the thickness difference of the specimens. SEM equipped with an energy-dispersive spectrometer (EDS) may be used to analyze the chemical composition of specimens through the detection of the generated x-rays. More detailed information about SEM may be found in the reference.[208]

SEM (LEO 1550 VP FESEM) (previously located at the Synchtron Radiation Center, Stoughton, WI) at the Soft Materials Laboratory (Univ. of Wisconsin) was used in this study with the following experimental setup during imaging: 1 kV (top-down) and 10 kV (cross-sectional) accelerating voltage, 3 mm working distance, and 30 μm aperture size. The polymer thin films were not treated with any conductive coating for imaging. The in-lens SE detector, which has been known to collect SE_I efficiently, was mainly used for imaging. SEM was also used to create patterns on PMMA photoresists by controlling the regions of e-beam exposure.

3.3.2 Atomic Force Microscopy (AFM)

Atomic force microscopy (AFM) is generally used to characterize the surface of materials by measuring the force between its probe tip and the surface. The interaction causes the tip to bend, and the degree of deflection is monitored by measuring laser reflection from the end of the tip. Different regimes of forces are probed depending on the distance between the tip and the sample surface, leading to three modes of operations for AFM: (1) contact, (2) non-contact, and (3) intermittent contact (commonly called "tapping"). In contact mode AFM, the cantilever-surface distance is a few angstroms (Å), and the tip experiences repulsive van der Waals forces. Due to the proximity of the tip and the amount of forces applied, the contact mode operation can damage soft materials during scanning. In non-contact mode AFM, the tip is a few tens to hundreds of angstroms away from the surface and feels attractive van der Waals forces. The resonant frequency and amplitude of the tip are monitored during scanning. In intermittent contact mode, the resonating tip comes into a temporary contact with, or "taps", the surface. The height and phase of the resonant tip may be obtained in tapping mode. The phase information is known to be sensitive to the adhesion, friction, and chemical composition of the surface.

In this work, atomic force microscopy (Nanoscope III Multimode AFM, Digital Instruments) at the Materials Science Center (University of Wisconsin) was implemented in tapping mode (1) to measure topographic profiles and (2) to distinguish domains of block copolymer thin films at the free surface using phase images.

3.3.3 Chemical Pattern Fabrication

The schematic on pattern fabrication procedures is provided in Figure 3.3. A solution (0.2 wt. %, toluene) of crosslinkable materials (*e.g.*, random copolymers

containing 94 mol. % styrene and 6 mol. % glycidyl methacrylate) was spin coated above a silicon wafer covered with a thin SiO_2 layer, followed by thermal treatment in vacuum at 190 °C for 24 hours that created the mat (thickness ≈ 5 − 8 nm). The mat was sonicated in toluene repeatedly (5 minutes × 3 times) in order to remove any unreacted materials. Then, exposure method specific photoresist materials (PR) were deposited on the top of the mat by spin coating. For extreme ultraviolet lithography (EUV) exposure (Synchrotron Radiation Center, Stoughton, WI), a 50 nm thick layer of poly(methyl methacrylate) (PMMA, 950 kg/mol, in anisole solution) was used while a 35 nm thick ZEP layer was used for electron beam patterning (Hitachi Global Storage Technologies, San Jose, CA). The main advantage of EUV above e-beam patterning is that it takes much less time to make multiple patterns while e-beam patterning enables fabrication of small features. In addition, while a prefabricated mask is required for EUV, any shape can virtually be programmed for e-beam patterning. The adjustable PR exposure time to the beamline determines the relative width of the exposed area with respect to the screened area. The remaining PR patterns after exposure and development were used as a mask during the sequential oxygen plasma treatment (Unaxis 790, Univ. of Wisconsin). The top-down SEM images of the stripe patterns after the development process and after the plasma treatment are shown in Figure 6.21 (Chapter 6). The remaining photoresist layer was removed by sonication in *n*-methyl-2-pyrrolidone (NMP) and chlorobenzene. The subsequent process of solution spin coating and thermal annealing was implemented in order to graft hydroxyl-terminated brushes (“backfill brush”) onto the SiO_x regions, exposed as a consequence of the oxygen plasma. The wafers were sonicated in toluene 3 times for 5 minutes each in order to remove unreacted brush materials.

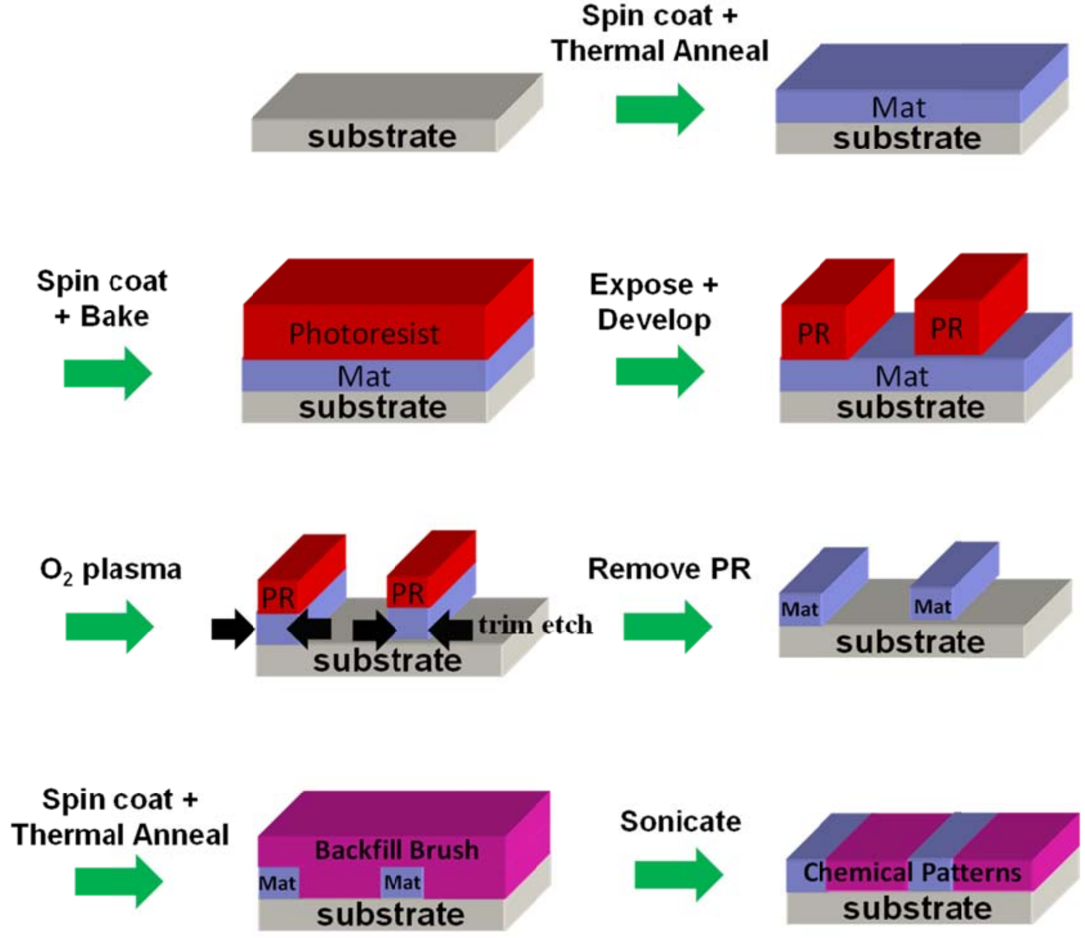

Figure 3.3 Schematic illustration showing the process of chemical pattern fabrication. Adapted from Liu *et al*.[96]

3.3.4 Plasma Treatment

While plasma treatment can be used to change surface energies and wettability of polymers,[116] plasma treatment was implemented in this research to etch thin-film structures. Plasma etching has been used widely in the semiconductor industry for two reasons: (1) to pursue more active etching compared to wet etching and (2) to gain anisotropy in the etching process.[51] A simplified experimental setup consists of two

parallel electrodes with voltage bias, samples placed above one of the electrodes, and gases that fill the chamber. Depending on the types of dominant species in the gases, the plasma etching can occur in two different ways: chemical radical etching (isotropic) and physical ion bombardment (anisotropic). Often both methods are used in conjunction with each other, and this process is known as *ion-enhanced etching*. In chemical etching, radicals move in random directions ("isotropic arriving angles") and have to strike surfaces several times before they react ("low sticking coefficient"), making the process isotropic.[51] However, the radicals in the chemical etching process usually react and etch materials selectively. On the contrary, the physical etching due to ion bombardment is nonselective on the chemical species of the surfaces, but it is anisotropic due to the directionality of electric fields that accelerate ions. The ion-enhanced etching involves both mechanisms (chemical and physical etching) and accomplishes anisotropy and etching selectivity at the same time. The total etching rate in ion-enhanced etching may be higher than the sum of etching rates for each individual mechanism as the ion bombardment sometimes assists the chemical etching processes.

Polymer resistance to plasma treatment has been a vital part in microelectronic processing for transferring pattern in a polymer film to the underlying layers. This aspect will remain as one of the important considerations for the implementations of block copolymer self-assembly to conventional lithographic process; the relative etch resistance will determine the component of the block copolymers that would remain and function as a mask for subsequent process. The oxygen plasma etching rates have been investigated by Taylor and Wolf[209] for various polymers at 35 °C. The removal rate for poly(styrene) (PS) was found to be 270 Å/min while poly(methyl methacrylate) (PMMA) was etched 2.37 times faster than PS. The significantly higher etching rate of poly(isoprene) (5.6 times compared to PS) is of consequence in this research, which

deals with PS-PI diblock copolymers and PS-PI-PMMA triblock copolymers. Based on their experiments with a variety of polymers, they found a close linear relationship between the cleavage of the backbone and the etching rate. While the presence of weak side-chains next to the main polymer chain facilitates the backbone cleavage for some cases, the presence of aromatic groups may increase the stability of polymers to oxygen plasma treatments. Organosilicon polymers, such as poly(dimethylsiloxane) (PDMS), and other organometallic polymers can exhibit very high etch resistance due to the formation of etch resistant oxides on the surface.

Atomic oxygen free radicals are generally considered to be the most important constituent in oxygen plasma while other components, such as other radicals, excited neutrals, electrons, and ions, can work in synergic ways with the oxygen radicals.[210] Though the detailed etching mechanisms can become complex in the presence of supplemental gases, frequently added to enhance the etching rate, a simplified mechanism on how oxygen radicals react with and cleave polymer backbone chains is provided by the following reaction scheme:[211]

$$\sim\!C{-}C\!\sim \; + \; :O \longrightarrow \; \sim\!\dot{C}{-}C\!\sim \; + \; {}^{\cdot}OH \qquad (1)$$

$$\sim\!\dot{C}{-}C\!\sim \; + \; :O \longrightarrow \; \sim\!C(O^{\cdot}){-}C\!\sim \qquad (2)$$

$$\sim\!C(O^{\cdot}){-}C\!\sim \; \longrightarrow \; \sim\!C{=}O \; + \; {}^{\cdot}C\!\sim \qquad (3)$$

Chain scission may also occur through “depolymerization” due to the radical at the chain end in the product of step 3. The end products of depolymerization consist of monomers and short chains. The degree of depropagation depends on the stability of the radical and the thermal energy imparted by ion bombardments.

As shown above, chain scission leads to the formation of not only volatile components, but also –C=O and –COOH within chains that are expected to cause changes in the surface energies of the remaining polymers. X-ray photoelectron spectroscopy for chemical analysis (ESCA or XPS) has been widely used to investigate properties at film surfaces after plasma treatment. Clark and Wilson[212] used ESCA on polymer films after treatment with an oxygen plasma and confirmed a sign of oxidation at the surface. The depth of the polymer films that are susceptible to degradation, oxidation, and even crosslinking from plasma treatment can be as large as 500 Å from the film surface.[116] Surface treatment of PS with an oxygen plasma was conducted by Hall *et al.*,[213] and a huge increase in adhesion was observed for the treated polymer films. Similarly, the water contact angles on polymers drop significantly after oxygen plasma treatment on the polymers.[214] Notably, Occhiello *et al.*[215] found that the increase in the wettability of PS as a result of plasma treatment is temporary and becomes faint with aging. In addition to the attachment of the polar groups, the increase in the interdiffusion of polymers, facilitated by smaller chain size after the cleavage, may also be responsible for the increase in the bondability of plasma-treated polymers.[116]

Chapter 4 Decoupling Bulk Thermodynamics and Wetting Characteristics of Block Copolymer Thin Films[1]

* Reproduced in part with permission from Kim, S.; Nealey, P. F.; Bates, F. S. *ACS Macro Letters* **2012**, 1, 11 – 14. Copyright 2011 American Chemical Society.

4.1 INTRODUCTION

Seemingly small differences in the chemical structure of polymers are known to induce non-negligible changes in various physical properties, a phenomenon which in some cases results in significant commercial implications.[216] For example, finite positive Flory-Huggins interactions characterize blends of deuterated and protonated poly(styrene) (dPS and PS) homopolymers that are otherwise chemically identical,[217] leading to phase separation and upper critical solution temperatures at sufficiently high molecular weights. The segregation of dPS to the free surface in thin-film blends of dPS and PS derives from the same isotope effect, where the surface energy of dPS is slightly lower than that of PS.[218] The miscibility window for polymer blends modified partially with bromination and fluorination has been known to depend on the degree of the chemical modification.[111, 112] Changes in various properties of polydienes upon epoxidation have been investigated in the past for multiple reasons, as described in section 2.3.3 of this dissertation.

Block copolymers form myriad morphologies depending on the volume fractions of the constituent blocks, the associated interaction parameters, the overall degree of polymerization, and the molecular architecture (*e.g.*, linear versus branched). Impressive agreement between the experimental and the theoretical studies has been found for linear diblock copolymers.[5] Partial modification of polydienes in multiblock

[1] Refer to Acknowledgements for contributions made by other people.

copolymers such as sulfonation,[121, 122] fluorination,[123, 134] hydrogenation,[126] epoxidation,[197] and liquid crystal attachment[114] has shown that the certain physical properties can be "tuned" by chemical modification. As with the miscibility of blends involving statistical copolymers, the binary interaction model has been employed (*e.g.*, by Ren *et al.*[123] and Davidock *et al.*[134]) to rationalize changes in the effective interaction parameters between block copolymer constituents with fluorination.

Epoxidation of block copolymers has been studied for a host of practical purposes including the oil resistance improvement,[172] the functionalization,[182] and the hydrophilicity control.[183] In this chapter, the effect of the epoxidation of poly(isoprene) blocks is studied by monitoring the physical properties of epoxidized poly(isoprene) (hPIxn) homopolymers and epoxidized poly(styrene-*b*-isoprene) (PS-PIxn) diblock copolymers with varying degrees of epoxidation (xn). The following are reported here: (1) measurements of the glass transition temperatures and the water contact angles of hPIxn, (2) the rheological behavior and the morphology of bulk PS-PIxn, and (3) a preliminary analysis of the thin-film morphology of PS-PIxn, supported on a tailored polymer brush substrate. The segment-segment interaction parameters χ_{ij} governing PIxn, PS, and PI are estimated by fitting a binary interaction model to the effective interaction parameters χ_{eff} obtained for the PS-PIxn diblock copolymers by small-angle x-ray scattering (SAXS) and dynamic mechanical spectroscopy. A decoupling of bulk and surface interaction energies due to the incorporation of the PIxn random copolymer is demonstrated. Non-preferential wetting at the substrate interface and the free surface of films may be realized at an intermediate level of epoxidation, while maintaining a state of order in the bulk. These findings point to a new strategy for imposing a perpendicular domain orientation in block copolymer films with a relatively small domain periodicity.

4.2 EXPERIMENTAL

Anionic polymerization was used to synthesize poly(styrene) (hPS) homopolymers, poly(isoprene) (hPI) homopolymers, and poly(styrene-*b*-isoprene) (PS-PI) diblock copolymers. Styrene (Aldrich) and isoprene (Acros) monomers were first treated with the repetitive cycles of freezing with liquid nitrogen, pumping in vacuum, and thawing. The purification of styrene and isoprene monomers involved stirring for 30 – 60 minutes with di-butyl magnesium (1.0 M solution in heptane, Aldrich) and *n*-butyl lithium (2.5 M solution in hexane, Aldrich), respectively. Polymerizations of hPS, hPI, and PS-PI were initiated with *sec*-butyl lithium (1.4 M solution in cyclohexane, Aldrich). The purified monomers of styrene and isoprene were added (sequentially for PS-PI) to the sealed reactor containing purified cyclohexane, and polymerization was conducted at 40 °C for 8 hours per each block. The reaction was terminated with methanol, degassed with argon gas for 1 hour. Finally, the polymers were precipitated in methanol and dried prior to their characterization and utilization.

Controlled epoxidation of hPI and PS-PI was carried out using dimethyl dioxirane (DMD) (Fig. 4.1). This agent appears as an intermediate during the decomposition of potassium peroxymonosulfate ($KHSO_5$) and has been used widely in epoxidation of small molecules[196] and polydienes.[186, 197] Partially reacted PS-PI and hPI with varying degrees of epoxidation (xn), denoted PS-PIxn and hPIxn, were prepared by stirring the polymer in dichloromethane (2 – 5 wt. %) along with acetone, an aqueous buffer solution ($NaHCO_3$, Aldrich), and an aqueous solution of potassium monosulfate triple salt (Sigma Aldrich) at room temperature for 16 – 48 hours. The polymer solution was extracted with separation funnels and dried under vacuum. It is assumed that the

epoxidation occurs at random positions along the polymer chains based on previous studies.[131, 133, 219]

Figure 4.1 Epoxidation of PS-PI diblock copolymers. The partially epoxidized PS-PI is denoted as PS-PIxn while f and xn (%) represent the mole fraction and degree of epoxidation, respectively.

Size exclusion chromatography (SEC) was used to determine the number average molecular weight (M_n) and polydispersity index (PDI) of the synthesized polymers. A Waters 717 instrument fitted with an Autosampler, columns with 5 μm pore size (Phenomenex Phenogel 5 μm, 300 x 7.8 mm) and a Waters 2410 Refractive Index Detector was operated with tetrahydrofuran (THF) as the mobile phase. Proton nuclear magnetic resonance (^{1}H-NMR) (VAC-300 Autosampler, IBM Instruments) was utilized to establish the composition of the polymers and to estimate the degree of epoxidation in hPIxn and PS-PIxn.

Random copolymers ($M_n \approx 28.5$ kg/mol, PDI ≈ 1.5) containing styrene (57 mole %), methyl methacrylate (37 mole %), and crosslinkable functional units (6 mole % glycidyl methacrylate), denoted SMG, were synthesized using nitroxide-mediated living free radical polymerization (NMP).[120] Spin-coating a solution (0.2 wt. % in toluene) at 4000 rpm resulted in the formation of a mat, which was crosslinked during 24 hours of annealing under vacuum at 190 °C.

Differential scanning calorimetry (DSC) (Q1000, TA Instruments) was employed to identify the glass transition temperature (T_g) of polymers at a ramping rate of ± 10 °C/min. Rheological measurements were conducted on pressed PS-PIxn samples with an ARES rheometer (Rheometric Scientific) in two modes: isochronal experiments while heating (0.2 – 10 °C/min) and isothermal frequency sweep measurements. In order to investigate the bulk morphology, small-angle x-ray scattering (SAXS) experiments were conducted at room temperature on PS-PIxn specimens at Argonne National Laboratory and on a laboratory source (Materials Science Center (MSC) at the University of Wisconsin − Madison) after annealing in vacuum at 105 °C for 6 hours. Data collected on an area detector were reduced to the one-dimensional form of the intensity versus the scattering wavevector magnitude $q = 4\pi\lambda^{-1}\sin(\theta/2)$.

Solutions of PS-PIxn (1.0 wt. %, in toluene) were deposited on the crosslinked SMG substrates in the form of uniform thin films. Average film thicknesses ranging from $1.7d_1$ to $1.9d_1$ ($d_1 = 2\pi/q_1$ where q_1 is the principle Bragg reflection measured by SAXS) were determined with an ellipsometry instrument (AutoEL-II, Rudolph Research). The thin films were annealed at 107 °C for 6 hours in vacuum, and characterized by scanning electron microscopy (SEM) (LEO 1550-VP FESEM). The same procedure was employed to produce 22 – 30 nm thick films of hPS and hPIxn above bare Si wafers from 1.0 wt. % solutions in toluene. Static contact angles formed by a drop of water (1 μL) at the thin film surface (averaged over 5 to 10 measurements) were established using a goniometer (Data Physics OCA15).

4.3 RESULTS

Molecular characterization data for the poly(styrene) (hPS) and poly(isoprene) (hPI) homopolymers, and the PS-PI diblock copolymers are shown in Table 4.1; the

consistency with the targeted molecular weights and compositions and relatively low PDI's confirm successful polymerizations.

Table 4.1 Molecular characterization.

	M_n (kg/mol)	f_S [b]	f_I [b]	PDI	T_g (°C)
PS-PI	22.8 [a]	0.50	0.50	1.05	-61, 84
hPI	20.1	0	1	1.05	-65
hPS	21.6	1	0	1.05	103

[a] The SEC measurement of the poly(styrene) block aliquots gave the result of 12.3 kg/mol. M_n of PS-PI was calculated by comparing the molecular weight of the poly(styrene) aliquot with the ratio between the poly(styrene) and the poly(isoprene) blocks estimated from the NMR measurement.

[b] Densities at 140 °C were used to calculate the volume fractions.

Characterization results for the partially epoxidized diblock copolymers, denoted PS-PIxn, are shown in Table 4.2. SEC traces for the PS-PIxn compounds (Figure 4.2) indicate that the functionalized polymers retain monodisperse molecular weight distributions with all levels chemical modification; slight broadening of the SEC peaks may occur due to adsorption of polymers to the column.[198] Similar results were obtained with hPIxn (xn = 15%, 27%, 33%, 79%, 99%) including retention of the monodisperse PDI (1.09 – 1.13), except for minor broadening in hPI27 (PDI ≈ 1.27) (Figure 4.3). ^{1}H-NMR data from PS-PIxn, shown in Figure 4.4, demonstrate that resonances corresponding to 1,4-poly(isoprene) repeat units vanish and those for epoxidized 1,4-poly(isoprene) units (δ ≈ 2.75 ppm) grow as the extent of epoxidation, xn, increases. The

peaks corresponding to epoxidized 3,4-poly(isoprene) units ($\delta \approx 2.60$ ppm) become apparent only with 99% epoxidation (PS-PI99); lower reactivity of 3,4 units relative to 1,4 units has been reported previously with other epoxidation methods for poly(styrene-*b*-isoprene-*b*-styrene) (PS-PI-PS) triblock copolymers[173] and poly(butadiene) homopolymers.[168]

Table 4.2 Characterization of PS-PIxn.

Percent epoxidation (xn) in PS-PIxn	0%	14%	41%	65%	75%	99%
PDI [a]	1.05	1.07	1.09	1.09	1.09	1.08
T_{ODT} (°C) [b]	182	112	< 85	167	> 200	> 200
d_1 (nm) [c]	20.1 (LAM)	18.5 (LAM)	Not Ordered	20.0 (LAM)	20.3 (LAM)	22.0 (LAM)

[a] Polydispersity index measured using SEC.

[b] Order-disorder transition temperature based on rheological measurements.

[c] The lattice spacing was calculated based on the primary peak position in the SAXS profiles measured at room temperature. LAM denotes the lamellar morphology.

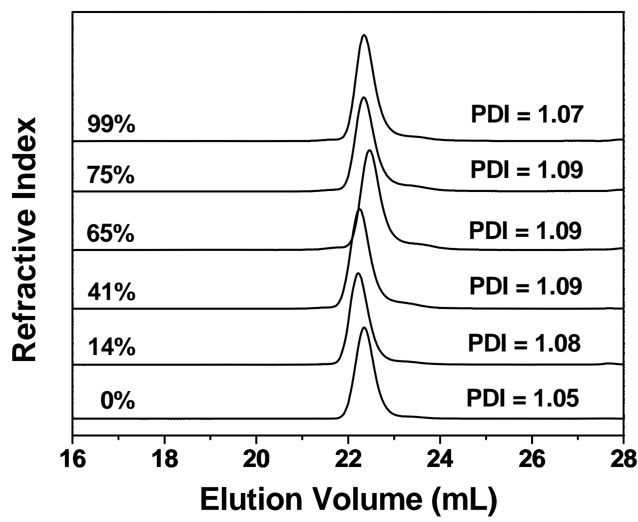

Figure 4.2 SEC traces for PS-PIxn diblock copolymers (with xn indicated in %).

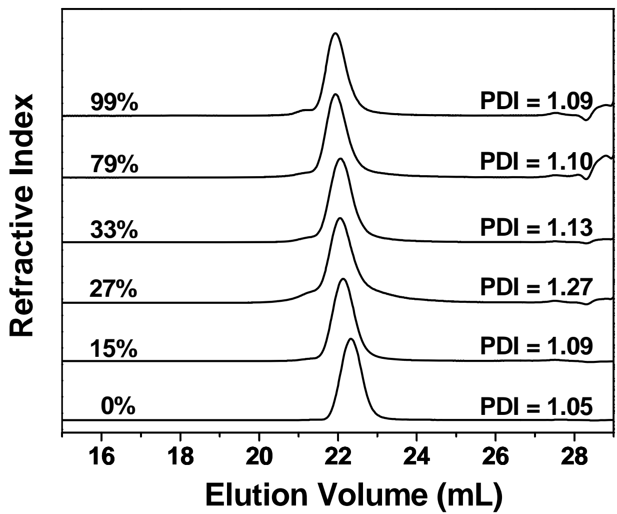

Figure 4.3 SEC traces for hPIxn (with xn indicated in %).

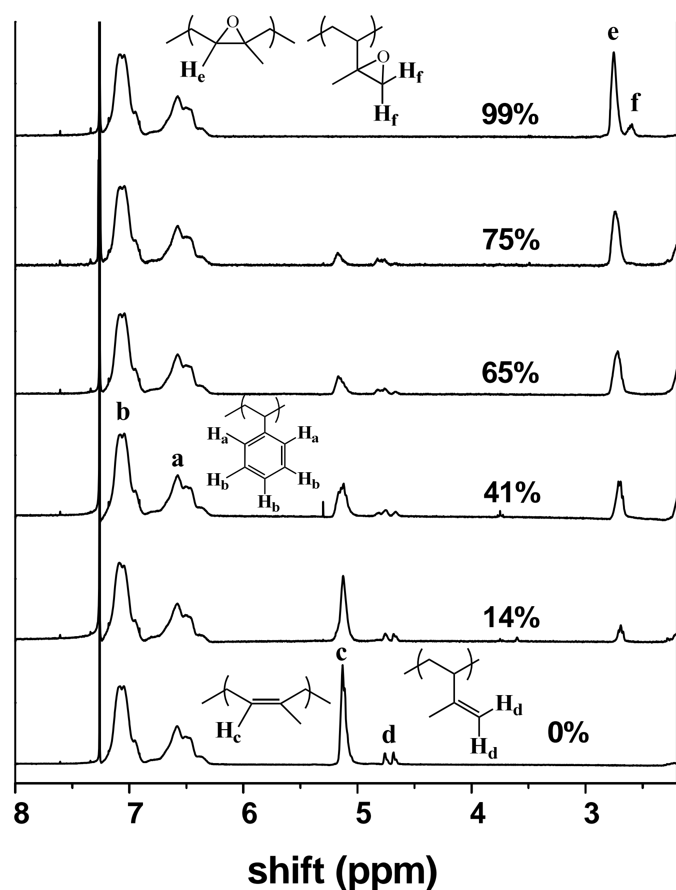

Figure 4.4 ^{1}H-NMR spectra of PS-PIxn. The intensities are normalized to the most intense peak associated with the poly(styrene) block, and spectra are shifted vertically for clarity.

Figures 4.5 and 4.6 show DSC traces that establish the temperature dependence of the glass transition temperatures (T_g) as a function of xn in hPIxn and PS-PIxn. Attaching bulky groups to the polymer backbone reduces local segment rotation, leading to an 80 °C increase in T_g with full epoxidation. A linear increase in $T_{g,hPIxn}$ and $T_{g,PIxn}$

with the extent of epoxidation in both systems is demonstrated in Figure 4.7, consistent with previous reports on epoxidized natural rubbers (ENR).[170, 176] The linearity indicates that unreacted and epoxidized isoprene units within the blocks are uniformly mixed. DSC traces taken with the PS-PIxn diblock copolymers (Figure 4.6) show two distinct glass transitions, suggestive of microphase segregation. However, the signature of T_g for poly(styrene) in PS-PI41 is less obvious due to broadening of the transition. A subtle but noticeable deviation in the PS and PIxn block T_g's suggests some degree of block compatibility at intermediate levels (*e.g.*, 14 and 41%) of epoxidation.

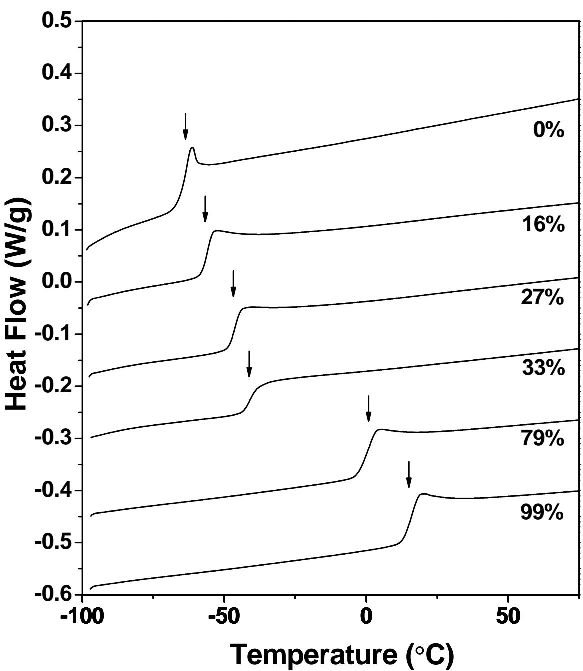

Figure 4.5 DSC traces for hPIxn as a function of percent epoxidation. Arrows indicate the glass transition temperature. Data except hPI (0% epoxidation) have been shifted vertically for clarity.

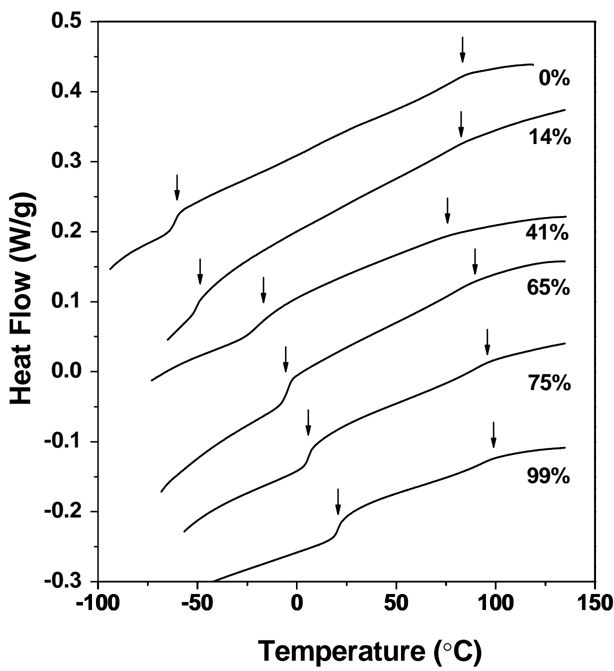

Figure 4.6 DSC obtained from PS-PIxn as a function of % epoxidation. Arrows indicate the glass transition temperatures. Data except PS-PI (0% epoxidation) have been shifted vertically for clarity.

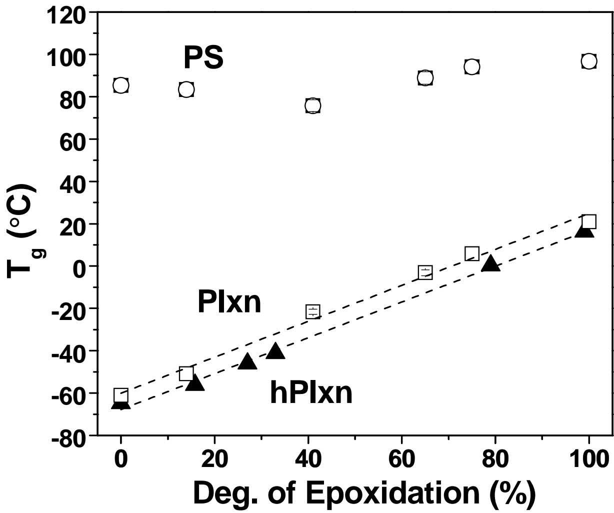

Figure 4.7 Variation in the glass transition temperature (T_g) for hPIxn (filled symbols) and PS-PIxn (open symbols) as a function of percent epoxidation based on DSC measurements. The dashed lines illustrate linear dependences.

The rheological behavior of the PS-PIxn materials was monitored for a temperature range between 85 and 200 °C. Abrupt changes in G′ and G″ with increasing (or decreasing) temperature provide a convenient way to identify the order-disorder transition temperature (T_{ODT}). Clear evidence of ODT's can be found in the isochronal (ω = 1 rad/s) linear dynamic mechanical spectroscopy (DMS) results for PS-PI, PS-PI14, and PS-PI65 as presented in Figure 4.8, where T_{ODT} = 182 °C, 112 °C, and 167 °C, respectively. The other samples show no sign of an ODT over the range of temperatures probed. Isothermal frequency experiments (0.1 rad/sec < ω < 100 rad/sec) have been conducted in order to establish whether specimens are ordered or disordered, and several representative results are presented in Figure 4.9 for PS-PI, PS-PI14, and PS-PI41. Diblock copolymer PS-PI14 exhibits terminal behavior ($G' \sim \omega^2$ and $G'' \sim \omega^1$) at 120 °C

and decidedly non-terminal behavior ($G' \sim G'' \sim \omega^{0.6}$) at 105 °C. Both results are consistent with the assignment of $T_{ODT} \approx 112$ °C (Fig. 4.8). Similarly, PS-PI is ordered at 110 °C ($T_{ODT} \approx 182$ °C from Fig. 4.8) and PS-PI41 is disordered at 105 °C. Based on the isochronal temperature scan for PS-PI41, it is concluded that $T_{ODT} < 85$ °C for this material. The values of T_{ODT} for PS-PIxn are summarized in Table 4.2.

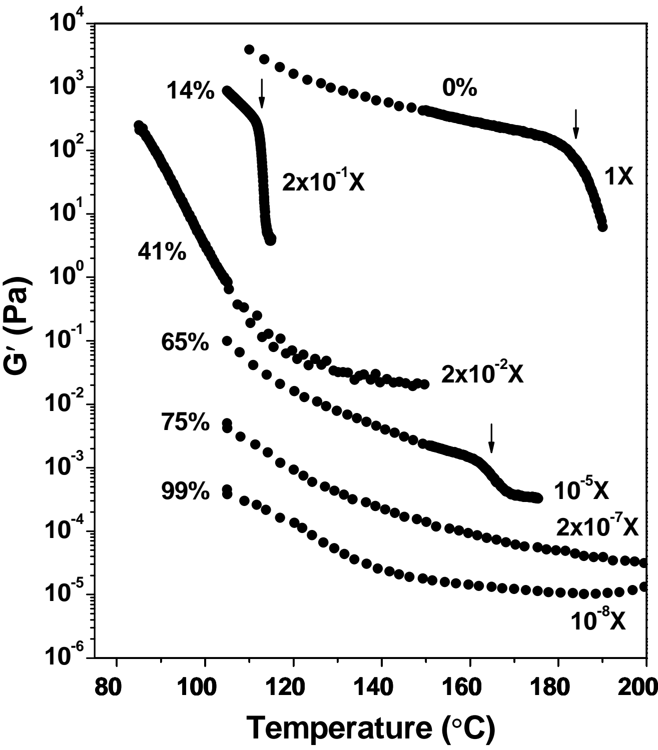

Figure 4.8 Temperature dependence of the dynamic elastic modulus G′(1 rad/sec) for PS-PIxn diblock copolymers determined during heating (0.2 − 10 °C/min). Arrows indicate the order-disorder transitions signaled by an abrupt change in G′. Data have been shifted vertically as indicated.

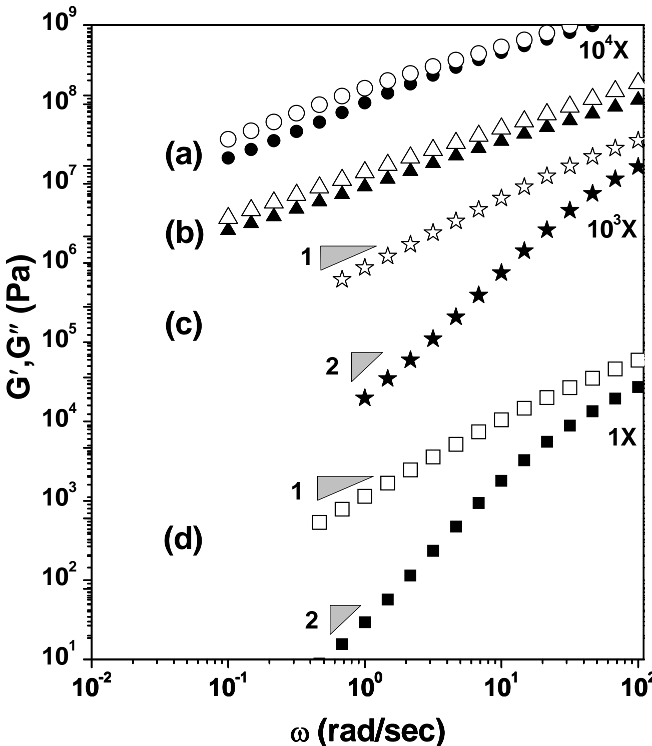

Figure 4.9 Frequency (ω) dependence of the dynamic elastic modulus G′ (filled symbols) and loss modulus G″ (open symbols) for (a) PS-PI at 110 °C, (b) PS-PI14 at 105 °C, (c) PS-PI14 at 120 °C and (d) PS-PI41 at 105 °C. Data have been shifted vertically as indicated for clarity.

Small-angle x-ray scattering (SAXS) was employed at room temperature to determine the bulk morphology and the domain dimensions for the PS-PIxn materials. Figure 4.10 shows results for all six specimens, each of which displays a principle reflection at scattering wavevector q_1 and higher-order peaks at $q_2 = 2q_1$ (and $3q_1$ for PS-PI), except for PS-PI14 and PS-PI41. The q_1 peak for PS-PI41 is distinctly broader than those for the other samples, consistent with a state of disorder as deduced from the DMS

measurements (Fig. 4.8 and 4.9); a relatively high peak intensity suggest this specimen is close to ordering. Also evident is the near extinction of the scattering intensity from PS-PI65, which is attributed to a contrast matching condition at an intermediate level of epoxidation; the electron density (ρ) of PIxn matches that of PS (*i.e.*, $\rho_{PI} < \rho_{PS} \approx \rho_{PI65} < \rho_{PI99}$). Overall, the SAXS results demonstrate that the ordered specimens contain a lamellar morphology as anticipated based on the symmetric compositions.

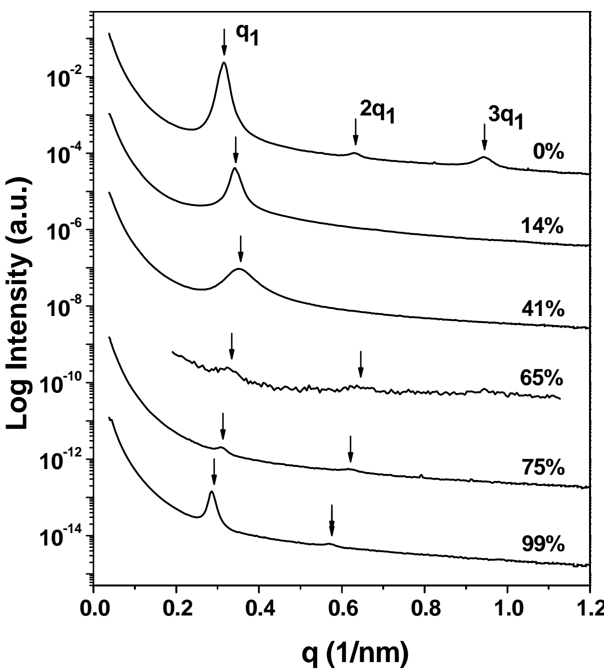

Figure 4.10 Small angle x-ray scattering (SAXS) obtained from PS-PIxn (with xn indicated in percentages) at room temperature. Arrows identify discernible Bragg reflections, which are consistent with a lamellar morphology. Data have been shifted vertically for clarity.

To estimate the changes in interfacial properties of the PIxn domains in the block copolymer as a function of xn, the wetting properties of hPIxn homopolymer films were investigated. The dependence of the static contact angle of water (θ_{water}) above cast films of hPIxn (xn = 0%, 15%, 27%, 33%, 79%, 99%) are shown in Figure 4.11. Measurements of θ_{water} for hPI (108°) and hPS (92°) agree with previous reports.[220, 221] Increasing the extent of epoxidation reduces θ_{water} for the hPIxn thin films, a trend generally associated with increasing surface energies.[118] Figure 4.11 suggests that the surface energy of hPIxn is lower than hPS at low degrees of epoxidation, higher than hPS at high degrees of epoxidation, and equals the surface energy of hPS at an intermediate degree of epoxidation. As with many simple liquid mixtures,[222] the surface energy of most copolymers is proportional to the bulk composition (minor deviations from linearity may be explained in terms of sequence distributions and block sizes)[118, 119] consistent with the θ_{water} data for hPIxn.

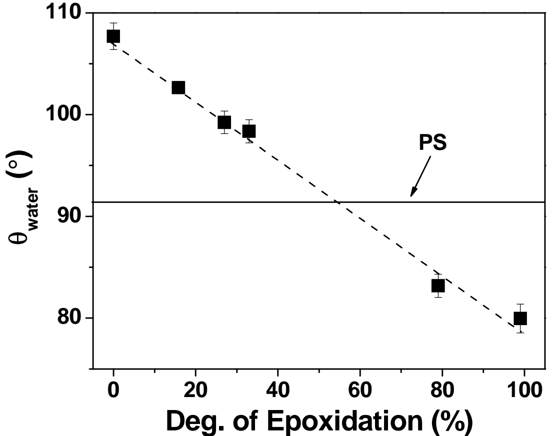

Figure 4.11 Static contact angle (θ) of water droplets (1 μL) on thin films of hPIxn (filled symbols) and poly(styrene) (solid line). Error bars identify standard deviations and the dashed line illustrates a linear fit to the data.

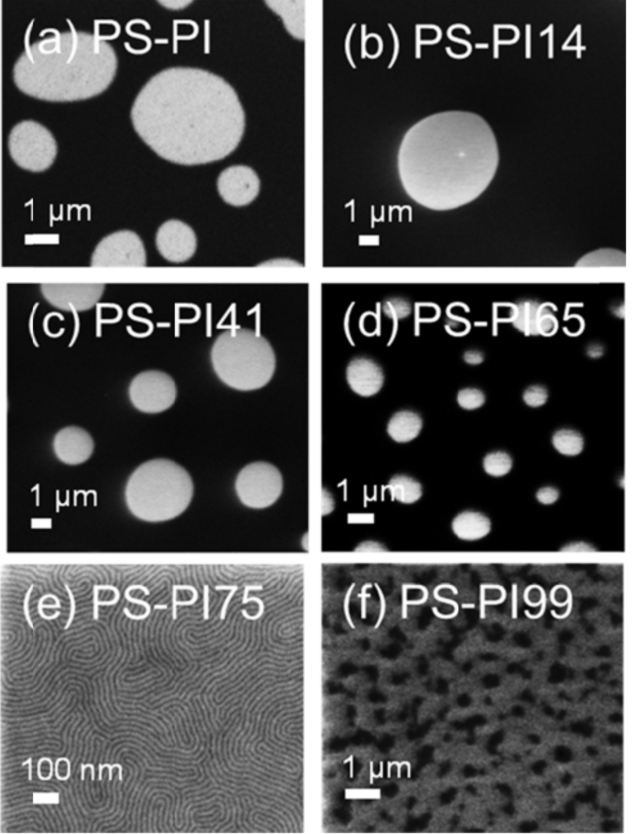

Figure 4.12 (a-f) Top-down SEM images of PS-PIxn thin films above a crosslinked SMG mat. With one exception, these images contain island and hole textures indicative of a parallel lamellar morphology. A perpendicular lamellar orientation characterizes the panel (e).

Representative SEM images taken from thin films of PS-PIxn supported on crosslinked SMG mats are shown in Figure 4.12. These specimens were prepared with average film thickness $1.7\ d_1 \leq L \leq 1.9\ d_1$, where $d_1 = 2\pi/q_1$. Except for PS-PI75, these films contain an "island and hole" texture indicative of lamellae oriented parallel to the substrate. This type of stepped surface topology occurs with incommensurate films, driven by preferred wetting conditions at the substrate and the unconstrained air

interfaces. There is a free-energy penalty associated with the step defects at the boundary regions while this term vanishes with coarsening of islands and holes in size.[223] In sharp contrast, the PS-PI75 film displays a “fingerprint” pattern, characteristic of lamellae oriented perpendicular to the substrate. These images all support the lamellar phase assignment established by SAXS, except for sample PS-PI41, which is disordered in the bulk state at the annealing temperature, 107 °C. Preferential interfacial wetting at an interface has been shown to induce lamellar order in symmetric diblock copolymers that are disordered in the bulk state,[224, 225] particularly near T_{ODT},[226] which explains this result for PS-PI41.

4.4 DISCUSSION

The results presented in the previous section provide clear evidence that controlled epoxidation of PS-PI diblock copolymers offers an attractive strategy for preparing materials with precisely tailored segment-segment interaction parameters. Our experimental results demonstrate that the effective interaction parameter χ_{eff} between PS and the random copolymer PIxn varies systematically with temperature T and xn. Two methods have been used to estimate $\chi_{eff}(T,xn)$.

In the strong segregation limit, the self-consistent field theory anticipates the periodic lamellar spacing,[227]

$$d_l = 1.10\, a\, N^{2/3}\, \chi_{eff}^{1/6} \qquad \text{(Eq. 4.1)}$$

in which χ_{eff} and the degrees of polymerization N are defined based on a common segment volume v. The statistical segment length $a = R_g(N/6)^{-1/2}$ is related to the unperturbed coil radius-of-gyration R_g, also governed by the choice of v. The molar volumes of the PS and PI repeat units have been estimated based on published densities and thermal expansivities (ρ_{PS} = 1.03 g/cm^3 and ρ_{PI} = 0.86 g/cm^3 at 105 °C).[228] The

density of fully epoxidized poly(isoprene) was estimated using the group contribution method (1.067 g/cm^3),[228] yielding a value roughly comparable to that reported for completely epoxidized natural rubber (1.032 g/cm^3).[163] The segment volume v = 144 Å^3 was used to calculate N = 259 resulting in an effective segment length a = 6.53 Å (a_{PS} = 6.26Å and it is assumed that a_{PIxn} = a_{PI} = 6.83 Å, both corrected for the indicated segment volume).[229] With these parameters, χ_{eff} for xn = 0%, 14%, 65%, 75%, and 99% has been calculated using Eq. 4.1, and the results are plotted in Figure 4.13 (solid symbols).

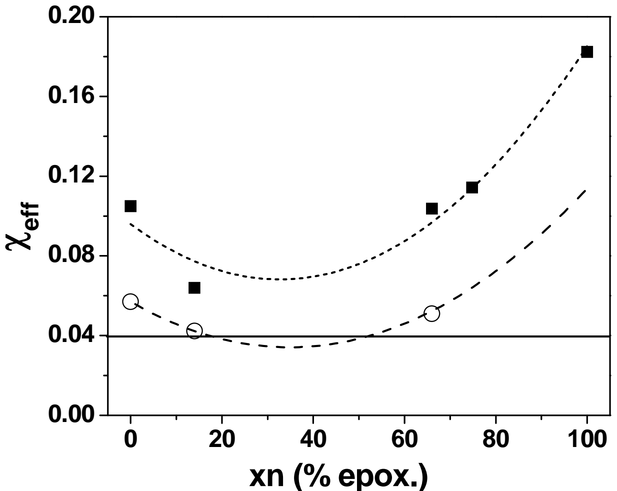

Figure 4.13 Effective interaction parameter (χ_{eff}) between poly(styrene) and partially epoxidized poly(isoprene) blocks in PS-PIxn diblock copolymers, determined at 100 °C based on d_1 (SAXS data) (filled symbols) and T_{ODT} (DMS data) (empty symbols). The curves were fit to these points using the binary interaction parameter model (Eq. 4.2). The solid line identifies the mean-field ODT condition for N = 259, above and below which the system is ordered and disordered, respectively.

Since these calculations are based on room temperature SAXS data (Fig. 4.10), the χ_{eff} values in Figure 4.13 are associated with roughly T = 100 °C, approximately the temperature where the structure is arrested during cooling. Here it is noted that this is a rather crude treatment since Eq. 4.1 is rigorously valid only in the limit of strong segregation. Nevertheless, prior studies[123, 230] have shown that this approach yields plausible estimates even close to the ODT, presumably due to the fluctuation induced first-order character of the transition.[231]

The binary interaction model[152, 232] has been used successfully to describe the mixing behavior of simple homopolymers and random copolymers.[111, 112, 233] For the present case this treatment reduces to,

$$\chi_{eff} = \frac{xn}{100}\chi_{SEI} + (1-\frac{xn}{100})\chi_{SI} - \frac{xn}{100}(1-\frac{xn}{100})\chi_{IEI} \qquad \text{(Eq. 4.2)}$$

where S, I, EI refer to poly(styrene), poly(isoprene) and epoxidized poly(isoprene) repeat units, respectively, and xn is the degree of epoxidation. The best fit to Eq. 4.2 with the SAXS based χ_{eff} values yields $\chi_{SI} \approx 0.096$, $\chi_{SEI} \approx 0.19$, and $\chi_{IEI} \approx 0.26$. The upper (dotted) curve in Figure 4.13 shows Eq. 4.2, computed using these three interaction parameters, demonstrating a minimum at xn ≈ 33%. This conclusion is consistent with a report of improved miscibility of poly(styrene) and natural rubber following partial epoxidation (25%, 35%, and 50%)[234] and closely resembles the composition dependence of χ_{eff} for partially fluorinated PS-PI diblock copolymers also determined using Eq. 4.1 and 4.2.[123]

According to the mean-field theory, the order-disorder transition for symmetric diblock copolymers is governed by,[3]

$$(\chi_{eff}N)_{ODT} = 10.5 \qquad \text{(Eq. 4.3)}$$

where χ_{eff} is given by Eq. 4.2. Application of Eq. 4.2 and 4.3 requires information regarding the temperature dependence of the interaction parameters χ_{SI}, χ_{SEI}, and χ_{IEI}. Generally, the interaction parameter can be expressed as a sum of enthalpic and entropic contributions, $\chi_{ij} = AT^{-1} + B$. For PS-PI diblock copolymer (with $v = 144$ Å^3),[235]

$$\chi_{SI} = 28.6T^{-1} - 0.0198 \qquad \text{(Eq. 4.4)}$$

which gives $\chi_{SI} = 0.057$ at 100 °C, close to what is shown in Figure 4.13 based on the SAXS analysis. There are four unknown constants associated with χ_{SEI} (= A_{SEI} T^{-1} + B_{SEI}) and χ_{IEI} (= A_{IEI} T^{-1} + B_{IEI}). These have been reduced to two unknowns by assuming χ_{SEI} and χ_{IEI} exhibit the same dependence on temperature as χ_{SI},

$$\chi_{SEI} = k_1\ \chi_{SI} = k_1\left(\frac{A_{SI}}{T} + B_{SI}\right) \qquad \text{(Eq. 4.5)}$$

$$\chi_{IEI} = k_2\ \chi_{SI} = k_2\left(\frac{A_{SI}}{T} + B_{SI}\right) \qquad \text{(Eq. 4.6)}$$

where k_1 and k_2 are simple proportionality constants. Substitution of Eq. 4.5 and 4.6 into the binary interaction model yields

$$\chi_{eff}(xn,T) = \chi_{SI}(T)\left[\frac{xn}{100}k_1 + (1-\frac{xn}{100}) - \frac{xn}{100}(1-\frac{xn}{100})k_2\right]. \qquad \text{(Eq. 4.7)}$$

Solving Eq. 4.3 and 4.7 with T_{ODT} = 112 °C (xn = 14%) and T_{ODT} = 167 °C (xn = 65%) leads to k_1 = 1.99 and k_2 = 3.30. $\chi_{eff}(xn)$ is plotted in Figure 4.13 (lower dashed curve) using Equation 4.7 with these constants. The agreement with the previous estimate (Eq. 4.1 and 4.2) is quite good considering the assumptions and the experimental uncertainties associated with both treatments. Also shown in Figure 4.13 is the ODT criterion $\chi_{eff,ODT}$ = 10.5/N (solid line); when $\chi_{eff} > \chi_{eff,ODT}$ the system is predicted to be ordered. Solving Equations 4.3 and 4.7 with xn = 41% results in T_{ODT} = 59 °C, which is consistent with the rheological (Fig. 4.8 and 4.9) and the SAXS (Fig. 4.10) results

discussed previously. The T_{ODT}-based model is adopted for the remainder of this discussion.

The concave form of χ_{eff}(xn) resembles the thermodynamic behavior of certain binary systems comprised of a statistical copolymer (A-*ran*-B) and a homopolymer (C).[154, 236, 237] For example, blends of poly(ethyl methacrylate) (PEMA) and styrene-acrylonitrile copolymer (SAN) have been reported to be miscible at intermediate compositions while neither poly(styrene) nor poly(acrylonitrile) alone is miscible with PEMA.[154] This can be rationalized based on the effects of strongly unfavorable intramolecular interactions within the statistical copolymer relative to intermolecular interactions (*i.e.*, $\chi_{AB} >> \chi_{AC} \approx \chi_{BC}$), which drives miscibility. The binary interaction model accounts for this mechanism through the last term in Eq. 4.2.

The presentation of PS and PIxn domains in a "fingerprint" pattern at the free surface of a PS-PIxn film (see Fig. 4.12e) confirmed that at an intermediate degree of epoxidation (xn = 75 %), the surface energies of the PS and PI75 blocks are nearly equal at the temperature of annealing. The increase in the surface energy with epoxidation of the random copolymer from γ_{PI} (32.0 mJ/m^2)[167] to the condition that both blocks have nearly equal surface energies, $\gamma_{PI75} \approx \gamma_{PS}$ (40.7 mJ/m^2),[167] agrees with the contact angle measurement. Notably, the fundamental domain period of the perpendicular lamellae, d_1 = 20.3 nm, which is comparable to the smallest dimension feasible with poly(styrene-*b*-methyl methacrylate) diblock copolymers,[95, 238] can be reduced roughly 30% for PS-PI75 without inducing disorder based on strong segregation scaling ($d_1 \sim N^{2/3}$) and the results shown in Figure 4.13.

The results of Figure 4.12 demonstrate that the interfacial wetting properties of PS-PIxn are also a function of xn. To realize perpendicularly oriented lamellar domains in the PS-PI75 film (Fig. 4.12e), nearly non-preferential wetting of the blocks of the

copolymer at the substrate is required in addition to the condition of nearly equal surface energies. Previously the wetting behavior of substrates towards overlying block copolymer films has been controlled using random copolymer brushes or crosslinked mats of the same[57, 120] or different[95, 239] combinations of monomers as the block copolymer. Here it is empirically found that substrates treated with crosslinked poly(styrene-*ran*-methyl methacrylate) (57 mole % styrene, 37 mole % methyl methacrylate, and 6 mole % glycidyl methacrylate (crosslinker)) mats satisfy the non-preferential wetting condition at the substrate interface for PS-PI75. Representative SEM images taken from thin films of PS-PIxn (xn = 0, 14, 41, 65, 99) supported on the same composition mats are shown in Figures 4.12a-d,f. In contrast to PS-PI75, these films contain an "island and hole" texture, indicative of preferred wetting conditions for one of the block copolymer constituent either at the underlying substrate or at the free surface that orient lamellae parallel to the plane of the film.

Apparently, incorporation of a random copolymer molecular architecture in one block of a diblock copolymer (A-*b*-[B-*ran*-C]) decouples the mechanisms that govern bulk phase behavior and interfacial phenomena, a strategy not available to simple (A-*b*-B) diblock copolymers. The parameter χ_{eff}, which governs the bulk (3-dimensional) interactions, depends on χ_{AB}, χ_{AC}, and χ_{BC} interactions and may exhibit a minimum value at intermediate levels of compositions of the random copolymer block. The surface energy of the random copolymer block, in contrast, varies approximately linearly with its composition between values for pure B and pure C. These different functional forms decouple the bulk and surface thermodynamics, allowing neutralization of differences in surface energies of the block copolymer components without disordering the material. For the system studied here, $\chi_{eff}(xn = 75\%) \approx 0.063$ while $\gamma_{PI75} \approx \gamma_{PS}$. This decoupling mechanism is believed to be a direct consequence of the different roles that a random

copolymer molecular architecture plays in the thermodynamics of 3-dimensional mixing and demixing versus 2-dimensional surface and interfacial phenomena.

Our results show that PS-PIxn phase behavior is quantitatively accounted for by the binary interaction model (Eq. 4.2), and the miscibility between PIxn and PS at intermediate compositions is driven by the minimization of strongly unfavorable intramolecular interactions within the statistical copolymer relative to intermolecular interactions, *i.e.*, $\chi_{IEI} > \chi_{SI}$, χ_{SEI}. This model assumes that the probability of the segment-segment contact in a completely disordered state is directly proportional to the segment volume fractions. However, "diluting" unfavorable interactions at the 2-dimensional surface of a microphase separated block copolymer film may be more restricted than in the 3-dimensional bulk state due to the combined effects of polymer chain connectivity and conformational constraints imposed by the microstructure. The concept of controlling the bulk and the interfacial properties of block copolymers using random copolymer blocks is believed to be applicable to other monomer combinations, notably those that permit the formation of microphase separated and perpendicularly oriented lamellae (or cylinders) characterized by even smaller domain periods.

Chapter 5 Consequences of Surface Neutralization in Diblock Copolymer Thin Films[2]

* This work has been conducted in collaboration with the Willson group and the Ellison group at the University of Texas – Austin.

5.1 INTRODUCTION

Boundary conditions and the associated symmetries dictate physical phenomena in many scientifically interesting as well as practical engineering systems. For example, quantum confinement in nanocrystals[240-242] and precise 3-dimensional spatial arrangements of nanostructures in photonic crystals[243] have led to a host of unconventional physics, generating questions from both academic and industrial perspectives. Similarly, interfaces that impose constraints on the density, boundary contours, and energetic interactions of neighboring polymers exert influences on various fundamental properties of the polymers, such as glass transitions, diffusion coefficients, crystallinity, and chain conformations.[15, 19, 22, 24] Any method capable of making changes to the boundary conditions at thin-film interfaces has the prospect for revealing new and potentially useful phenomena.[244]

Control of interfacial properties in polymer thin films has been extensively studied. A variety of modification methods, including flaming, oxygen plasma treatment, crosslinking, brush grafting, and other chemical surface modifications, have been implemented to tailor thin-film properties of polymers, such as adhesion, membrane permeability, and wetting.[116] Another crucial need for the control of polymer interfacial properties arises with thin-film block polymers, potentially useful as membranes and for lithographic templating.[245, 246] Block copolymers self-assemble into

[2] Refer to Acknowledgements for contributions made by other people.

various ordered morphologies that depend on molecular architecture, molecular weight, polydispersity, segment-segment interactions, and the volume fractions of the constituent blocks.[5] The morphology and the domain orientation in block copolymer thin films, essential parameters in any application, can be controlled by tuning the interfacial properties and the boundary conditions.

Incorporation of random chemical entities into polymer chains is a classical approach to manipulating macromolecular physical properties.[110] The dependence of bulk properties on the distributions and compositions of random copolymers has been studied for polymer blends and block copolymers of various chemistries.[111-114, 123, 126, 197] Interfacial properties in polymer thin films are strongly influenced by the degrees of random modification, or an overall composition.[57, 116-119] Recently, it has been shown that certain combinations of random copolymer and homopolymer blocks lead to a decoupling of the thermodynamics that govern bulk and surface segregation, affording control over domain orientations, *e.g.*, perpendicular versus parallel lamellae.[247]

A lamellar morphology of an incompressible block copolymer responds differently to confinement conditions depending on the nature of the interactions at each interface. Affinity of chemically distinct blocks towards the substrate and/or the free surface results in a parallel arrangement of lamellae, as demonstrated using a variety of measurement techniques including secondary ion mass spectroscopy (SIMS)[55, 248] and neutron reflectivity (NR).[249] Incommensurate film thicknesses are defined as $\langle L \rangle \neq (n - \frac{1}{2})L_0$ for asymmetric wetting and $\langle L \rangle \neq nL_0$ for symmetric wetting, where $\langle L \rangle$, L_0, and n are the average film thickness, the bulk periodicity, and the number of periodic layers, respectively. Film thickness quantization results in the formation of surface topography, referred to as "islands" and "holes," with 1.0 L_0 step heights for incommensurate thin films.[250-252] In contrast, neutral boundary conditions, *i.e.*, no wetting preference, at both

interfaces lead to a perpendicular arrangement.[253, 254] Intermediate wetting conditions (*e.g.*, preferential wetting at the free surface and a neutral condition at the substrate or vice versa) can produce mixed orientations.[255-257] Concerted efforts to create perpendicular arrangements of lamellae for the aforementioned applications make neutral boundary conditions extremely important.

This chapter addresses three possible combinations of neutral boundary conditions in block copolymer thin films: (1) both non-preferential free and substrate surfaces, (2) a non-preferential free surface and a preferential substrate surface, and (3) a preferential free surface and a non-preferential substrate surface. Figure 5.1 illustrates two possible configurations of lamellar-forming block copolymers addressed herein for scenarios (2) and (3) when confined as sufficiently thin films. Neutralization of the free surface in scenarios (1) and (2) is made possible by utilizing a partially epoxidized poly(styrene-*b*-isoprene) (PS-PI) diblock copolymer, referred to as PS-PEI78 (78 mole % of the repeat units in the unsaturated PI block are epoxidized). In a recent letter,[247] it has been demonstrated that this combination of homopolymer and random copolymer blocks leads to a neutral free surface wetting condition without compromising bulk microphase separation. The scenario (3) leverages poly(4-trimethylsilylstyrene-*b*-$_{\text{D,L}}$-lactide) (PTMSS-PLA) diblock copolymers,[258] characterized by the strong preferential interaction between the silicon-containing block and the free surface.[259, 260] The underlying substrate surfaces for PTMSS-PLA utilizes crosslinkable random copolymers of varying compositions to enable access to various PTMSS-PLA wetting conditions, including near neutral conditions. Arguments previously applied to the phase separation of bulk (3-dimensional) binary mixtures are implemented to explain the formation of free surface topographies with 0.5 L_0 height differences that are observed with a singly neutral boundary condition (Figure 5.1).

(a) Neutral Free Surface
Preferential Substrate

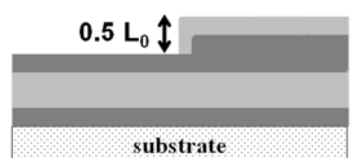

(b) Preferential Free Surface
Neutral Substrate

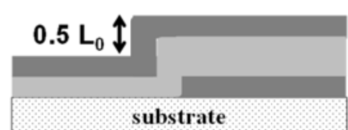

Figure 5.1 Schematic illustrations of lamella-forming block copolymer thin films, confined between one neutral and one preferential interface, characterized by 0.5 L_0 step heights.

5.2 EXPERIMENTAL METHODS

Material Synthesis and Bulk Characterization. (1) PS-PI and PS-PEI78: A poly(styrene-*b*-isoprene) (PS-PI) diblock copolymer was synthesized using anionic polymerization, followed by controlled epoxidation of the PI block using dimethyl dioxirane (DMD),[247] resulting in a diblock copolymer referred to as PS-PEI78. Size exclusion chromatography (SEC) (Waters 717 Autosampler with Waters 2410 Refractive Index Detector; Viscotek VE2001 with 302-050 Tetra Detector Array; THF mobile phase) was used to determine the number average molecular weight (M_n = 21.3 kg/mol) and polydispersity index (PDI = 1.06) of PS-PI. The composition f_I = 0.51 (volume fraction of PI) of PS-PI and the extent of epoxidation in PS-PEI78 (78 mole %) were determined using proton nuclear magnetic resonance (^{1}H-NMR) (VAC-300 Autosampler, IBM Instruments). Differential scanning calorimetry (Q1000 DSC, TA Instruments) was utilized (heating rate of ±10 °C/min) to determine the glass transition temperatures (T_g) of the polymers. The order-disorder transition temperature (T_{ODT}) of PS-PI was identified by dynamic mechanical spectroscopy (Ares 2, Rheometrics) based

on the steep drop in the linear dynamic elastic shear modulus (G′) obtained while heating at 1 °C/min. Small angle x-ray scattering (SAXS) experiments (Argonne National Laboratory) were performed on bulk specimens at room temperature after annealing in vacuum at 105 °C for 3 – 6 hours. The one-dimensional form of the scattering intensity, I(q) ($q = 4\pi\lambda^{-1}\sin(\theta/2)$ is the scattering wavevector), was obtained by reducing the data recorded on a two-dimensional area detector. *(2) PTMSS-PLA*: 4-trimethylstyrene monomers and symmetric poly(4-trimethylsilylstyrene-*b*-$_{D,L}$-lactide) block copolymers were prepared at the University of Texas, as reported previously.[258]

Mat/Brush Preparation: Random copolymers (28.5 kg/mol, PDI = 1.50) containing styrene (m_S = 0.57), methyl methacrylate (m_{MMA} = 0.37), and crosslinkable functional groups (glycidyl methacrylate) (m_{GMA} = 0.06), were synthesized using nitroxide-mediated living free radical polymerization (NMP),[120] where *m* represents the mole fraction. The mat (denoted SMG) was fabricated by spin coating a solution (0.2 – 0.5 wt. % in toluene) at 3000 rpm and a subsequent crosslinking reaction, achieved by thermal annealing under vacuum at 160 – 190 °C for 24 hours. Hydroxyl-terminated poly(styrene) homopolymers (PS-OH, 3.7 and 6.0 kg/mol) were purchased from Polymer Source, Inc., (sample #: P7499-SOH, P7590-SOH) and used as brush materials without any further purification. The polymer brushes were grafted onto bare silicon wafers (as received) by spin-coating a solution (1.0 wt. % in toluene) at 3000 rpm and annealing at 190 °C for 24 hours in vacuum. Unreacted materials were removed by post sonication (5 minutes) of the PS modified wafers in toluene for three times. Poly(4-*tert*-butylstyrene-*ran*-methyl methacrylate-*ran*-4-vinylbenzylazide) surfaces were prepared by conventional free radical copolymerization in a two-step process analogous to previous reports.[63, 239] The materials are denoted tBSMA-*yy*, where *yy* refers to the mole % of 4-*tert*-butylstyrene (*i.e.*, tBSMA-15, tBSMA-23, tBSMA-25, tBSMA-28, and

tBSMA-34) (Table 5.2). 4-*tert*-butylstyrene, methyl methacrylate, and 4-vinylbenzyl chloride were copolymerized to low conversion (< 10 %) to minimize monomer drift. Upon isolation, the copolymers were post-polymerization functionalized with sodium azide. The two principal components, poly(4-*tert*-butylstyrene) and poly(methyl methacrylate), were selected due to their large interaction parameter.[261] Low quantities (*ca*. 6 − 8 mole %) of poly(4-vinylbenzyl azide) were included for crosslinking. The tBSMA crosslinkable materials were dissolved as 0.5 wt. % solutions in toluene and spin coated at 3500 rpm to afford uniform films with ≈ 14 nm thickness. Films were crosslinked at 250 °C for 5 minutes on a hot plate in air, cooled to room temperature, and washed three times with toluene. Combustion analysis performed by Midwest Microlab LLC was used to calculate the relative compositions of the substrate surface treatments tBSMA.

Thin Film Preparation and Characterization of PS-PI and PS-PEI78: Uniform thin films were obtained by spin coating solutions of PS-PI and PS-PEI78 (1.0 − 1.5 wt. %, in toluene) on crosslinked SMG mats and PS brushes. Average film thicknesses (<L>) ranging from 1.5 L_0 to 2.6 L_0 ($L_0 = 2\pi/q_1$ where q_1 is the principle Bragg reflection measured by SAXS) were determined by ellipsometry (AutoEL-II, Rudolph Research). The spin-cast thin films were first placed in an oven chamber under vacuum (< 10 mtorr), then N_2 gas was constantly flowed into the chamber so that the pressure within the chamber remained at ≈ 1.0 torr throughout the thermal annealing process. The oven chamber was heated at the rate of 1.0 °C/min to the set temperature and cooled down slowly (< 0.25 °C/min) to room temperature once the heater was turned off. The annealing temperatures reported in this paper were read from a thermocouple attached to a bare Si wafer, placed in the chamber during thermal annealing. The annealing time refers to the period that the sample temperature was maintained at 105 °C, excluding the

time required for ramping up and down. The expression "*short-time annealing*," referred to later in this paper, corresponds to a thermal annealing procedure in which the heater is turned off as soon as the temperature of the annealing chamber reaches 105 °C.

Thin films were characterized by scanning electron microscopy (SEM) (LEO 1550-VP FESEM) and atomic force microscopy (AFM) (Nanoscope III Multimode AFM, Digital Instruments) (Materials Science Center, Univ. of Wisconsin). AFM was employed in tapping mode, with tips of resonant frequencies in the range of 170 kHz − 310 kHz, to measure the height profiles and the phase images of thin-film block copolymers. The largest scanned area in AFM was restricted to ≈ 11 × 11 μm^2 due to the availability of headers with recent calibrations, and samples of a known topography were measured to check the calibrations. AFM phase images generally are sensitive to near-surface properties, such as adhesion, viscoelasticity, and hardness, and the contrast in a phase image often permits discrimination of the block copolymer domain type at the top surface.[262] The difference in glass transition temperatures between PS and epoxidized PI (PEI) blocks (Figure 5.3) was expected to enhance the phase contrast at the measurement condition (room temperature) since the PS block is glassy and the PEI block is rubbery.[263] While the topography extracted from AFM height profiles was quantitatively reproducible, the phase contrast showed some variability but nonetheless allowed us to discriminate the surface chemistry.

PTMSS-PLA Thin Film Preparation and Characterization: A Brewer CEE 100CB Spincoater was used to coat thin films of PTMSS-PLA onto tBSMA mats. Film thicknesses were characterized by ellipsometry (J.A. Woollam Co, Inc. VB 400 VASE Ellipsometer) with 65 ° angle of incidence and wavelengths from 382 to 984 nm. Uniform PTMSS-PLA films were applied from variable solution concentrations (0.5 − 1.2 wt. %) in toluene at various spin speeds. Samples were annealed on a hot plate

(Heraeus Vacutherm Type VT 6060 P from Kendro) and quickly cooled to room temperature on a metal block. Optical microscope data were collected with Olympus BX60 at 100X magnification. Tapping-mode atomic force microscopy was performed with Asylum MFP-3D utilizing tips with resonant frequencies 170 kHz − 310 kHz.

5.3 RESULTS

Table 5.1 Characterization data of three diblock block copolymers utilized in the present study: PS-PI (preferential free surface), PS-PEI78 (non-preferential free surface), and PTMSS-PLA (preferential free surface).

Block Copolymers	Structure	M_n (kg/mol)	Đ	f_{PS} or f_{PTMSS}	T_g (°C)	T_{ODT}
PS-PI	m, n	21.3	1.06	0.49	82, -62	182
PS-PEI78	O, m, 0.22n, 0.78n, n	23.1	1.09	0.49	78, 3	N/A
PTMSS-PLA	O, o, O, O, p, $SiMe_3$	12.1	1.06	0.50	104, 48	N/A

Table 5.1 shows molecular characterization results for three block copolymers utilized herein. Symmetric PS-PI, PS-PEI78, and PTMSS-PLA diblock copolymers were prepared for this study. SEC traces of PS-PI, PS-PEI78, and thermally annealed PS-PEI78, are shown in Figure 5.2. Annealing PS-PEI78 at 105 °C for 6 hours does not

produce discernible degradation of the material. However, annealing at higher temperatures, *e.g.*, > 160 °C for 6 hours, led to the presence of some amount of swollen gel when the polymer was immersed in THF, suggestive of thermal crosslinking through the epoxides.[157] For this reason T_{ODT} for PS-PEI78 could not be determined; T_{ODT} = 182 °C for PS-PI.

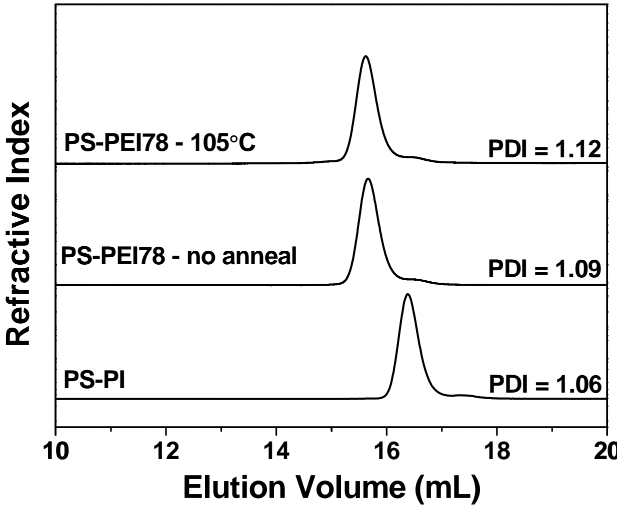

Figure 5.2 SEC traces for PS-PI, PS-PEI78, and PS-PEI78 after 6-hour thermal annealing.

Two distinct glass transitions are evident in the DSC traces for both PS-PI and PS-PEI78 diblock copolymers (Figure 5.3); $T_{g\text{-}PS} \approx$ 82 °C and $T_{g\text{-}PI} \approx$ -62 °C for PS-PI and $T_{g\text{-}PS} \approx$ 78 °C and $T_{g\text{-}PEI78} \approx$ 3 °C for PS-PEI78. An increase in the glass transition temperature of the rubbery block with the chemical modification is expected based on previous reports dealing with epoxidized natural rubbers.[170, 176]

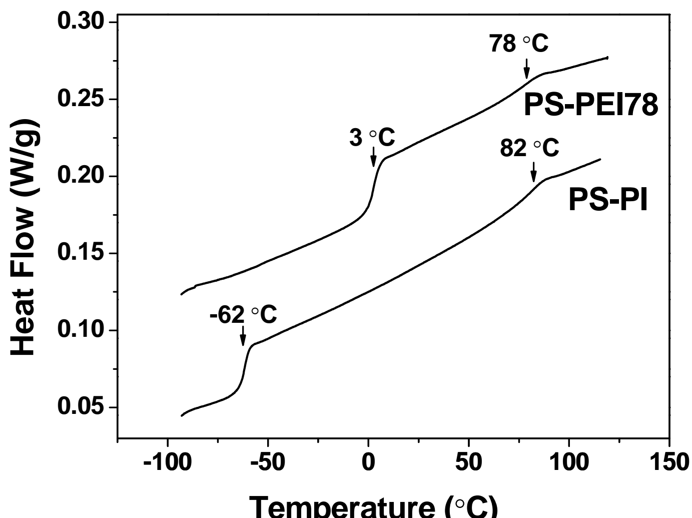

Figure 5.3 DSC traces for PS-PI and PS-PEI78 diblock copolymers. Arrows indicate the glass transition temperatures. Data for PS-PEI78 have been shifted vertically for clarity.

Diffraction peaks evident in the SAXS patterns (Figure 5.4) are consistent with lamellar morphologies for bulk PS-PI and PS-PEI78, as expected based on the symmetric compositions of these block copolymers. The bulk periodicities (L_0) of PS-PI and PS-PEI78 estimated from the primary peak positions of the SAXS patterns are 18.9 nm and 19.1 nm, respectively. A substantial decrease in the scattered intensity associated with PS-PEI78 relative to PS-PI is attributed to the near electron-density matching created by the presence of oxygen in the epoxidized compound.[247]

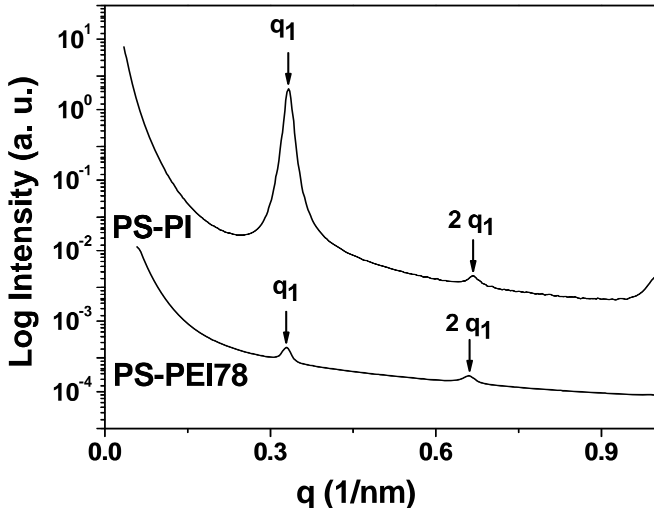

Figure 5.4 Small angle x-ray scattering (SAXS) obtained from PS-PI and PS-PEI78 at room temperature. Arrows identify discernible Bragg reflections, which are consistent with a lamellar morphology. Data for PS-PEI78 have been shifted vertically for clarity.

SEC traces of PTMSS homopolymers and PTMSS-PLA (Figure 5.5) are consistent with complete and monodisperse block growth. SAXS data on a PTMSS-PLA sample annealed at 160 °C (Figure 5.6) verify a lamellar morphology with L_0 = 14.6 nm. DSC traces (Figure 5.7) are consistent with two glass transition temperatures ($T_{g\text{-}PTMSS}$ = 104 °C, $T_{g\text{-}PLA}$ = 49 °C), similar to those previously reported for PTMSS-PLA of a similar molecular weight.[258]

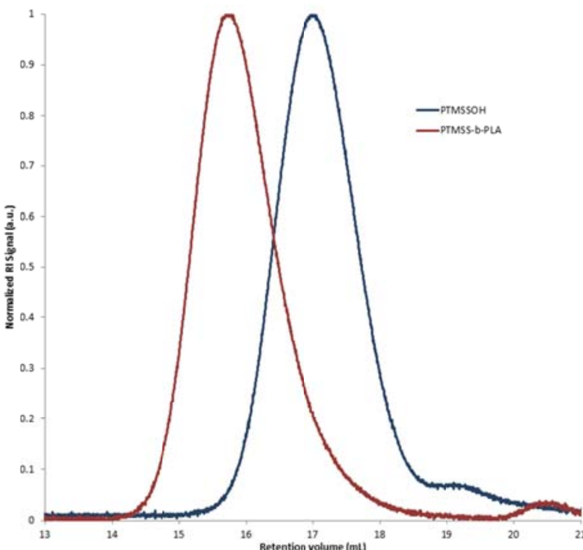

Figure 5.5 SEC traces for PTMSS-OH parent homopolymers (right) and PTMSS-PLA diblock copolymers (left). Courtesy of collaborators at Univ. Texas.

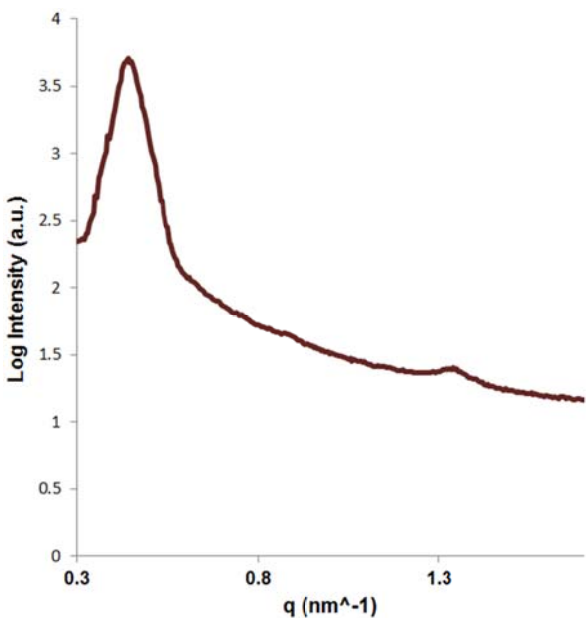

Figure 5.6 SAXS data (collected for 1 hour) of PTMSS-PLA annealed at 160 °C for 5 minutes. Courtesy of collaborators at Univ. Texas.

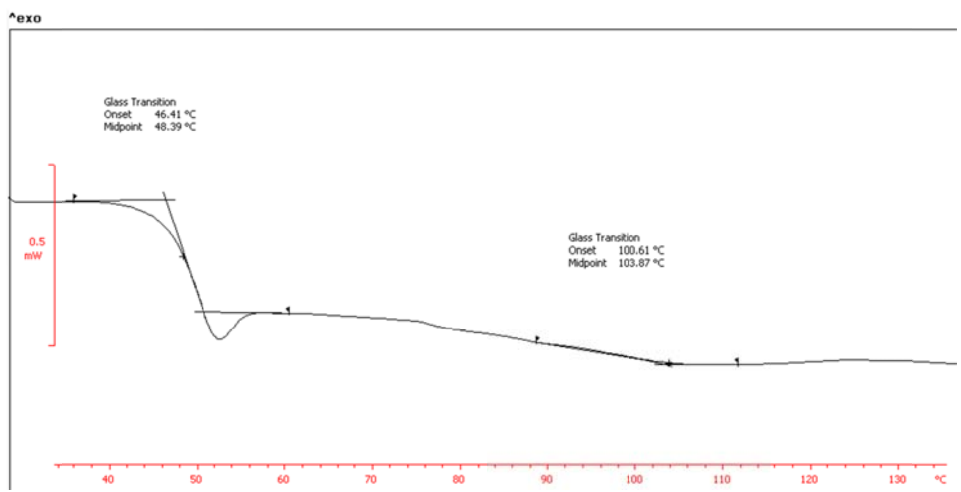

Figure 5.7 DSC data for PTMSS-PLA. Courtesy of collaborators at Univ. Texas.

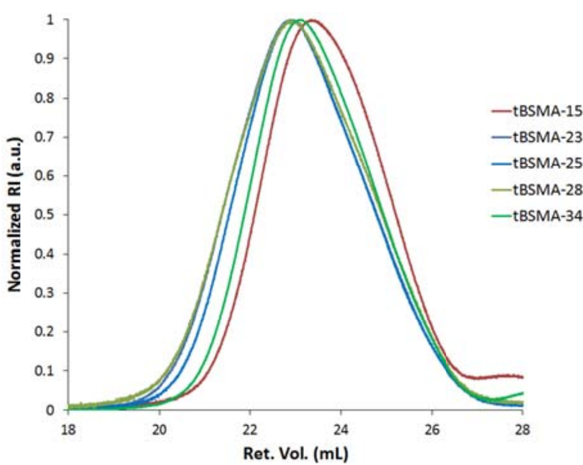

Figure 5.8 SEC traces of the tBSMA crosslinkable materials. Courtesy of collaborators at Univ. Texas.

Table 5.2 Characterization data of substrate surfaces utilized in the present study. PS-OH and SMG (57/37/6 mole % PS:PMMA:PGMA) were used with PS-PI and PS-PEI78. tBSMA's (mole % PtBS:PMMA:PVBzAz) were used with PTMSS-PLA block copolymers: tBSMA-15 (15/77/8); tBSMA-23 (23/71/6); tBSMA-25 (25/69/6); tBSMA-34 (34/59/7).

Substrate Surface Treatments	Structure	M_n (kg/mol)	Đ	Substrate Surface Interaction
PS-OH		3.7, 6.0	1.06	PS Preferential
SMG		28.5	1.50	Neutral for PS-PEI78
tBSMA-15		31.6	1.38	PLA Preferential
tBSMA-23, 25, 28		38.5, 35.9, 37.2	1.70, 1.66, 1.82	Near Neutral for PTMSS-PLA
tBSMA-34		34.2	1.44	PTMSS Preferential

Table 5.2 shows the chemical structures and characterization data for substrate surfaces utilized to produce different substrate wetting conditions for the three block copolymers in thin films. SEC data (Figure 5.8) of the five poly(4-*tert*-butylstyrene-*ran*-methyl methacrylate-*ran*-4-vinylbenzylazide) surfaces (tBSMA, referred to by the mole % PtBS content) are consistent with monomodal molecular weight distributions.

PS-PI behaves in a predictable manner[264] when cast as thin films on PS brushes, preferentially wet by the PS blocks. As illustrated in Figure 5.9a-f, a gradual variation in the average film thickness (<L>/L_0 = 1.5, 1.7, 2.0, 2.2, 2.3, and 2.5) leads to a sequential change in the top-down motifs [featureless → islands (light colored by SEM) → bicontinuous → holes (dark colored by SEM) → featureless] in agreement with the literature.[264]

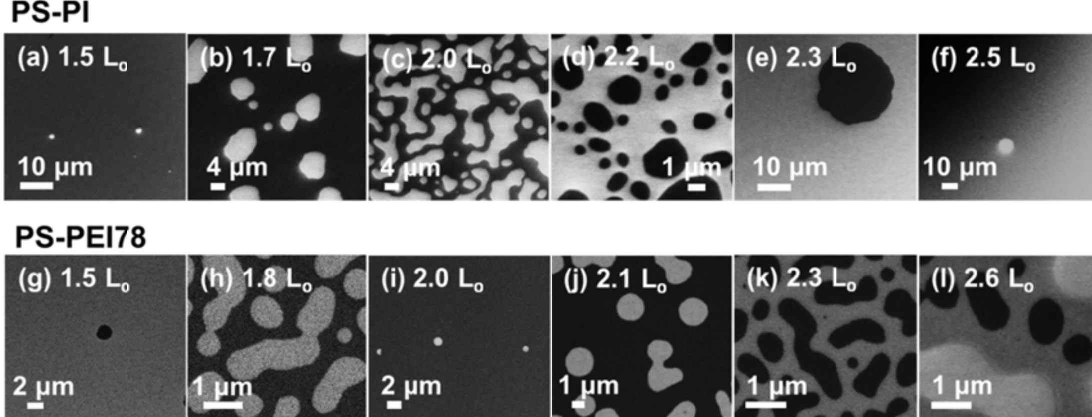

Figure 5.9 Top-down SEM images of thin-film block copolymers with various film thicknesses on PS brushes. (a-f) PS-PI with <L>/L_0 = 1.5, 1.7, 2.0, 2.2, 2.3, 2.5. (g-l) PS-PEI78 with <L>/L_0 = 1.5, 1.8, 2.0, 2.1, 2.3, 2.6. The thin films were annealed at 105 °C for 6 − 12 h.

AFM height (Figure 5.10a) and phase (Figure 5.10b) images from the <L> = 2.3 L_0 thick film (supported by SEM data, Figure 5.10d) confirm holes with a step height h = 19.1 nm (≅ L_0, *i.e.* the bulk period, Figure 5.10c). The absence of AFM phase contrast between the hole and the surrounding regions (mesas) indicates that the lower surface energy PI is expressed everywhere at the air interface, as shown in previous studies.[265] PS-PI behaves similarly when cast on the SMG mat (Figure 5.10e-h), also with <L> =

2.3 L_0, implying that SMG has a greater affinity for PS over PI. Hence, PS-PI forms asymmetric thin-film morphologies when supported on either substrate.

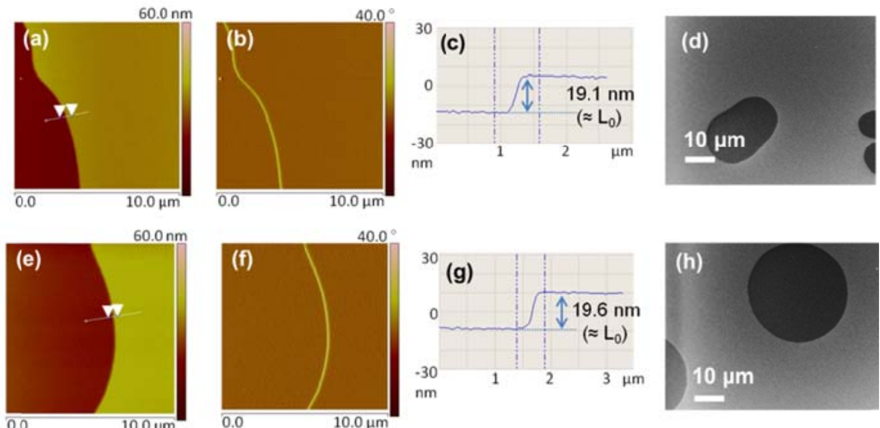

Figure 5.10 Top-down AFM height image, phase image, thickness profile, and SEM image of PS-PI thin films (<L> = 2.3 L_0) on (a-d) the PS brush and (e-h) the SMG mat. Step heights obtained from the thickness profiles equal to 19.1 nm and 19.6 nm, respectively (≈ 1.0 L_0). The thin films were annealed at 105 °C/12h.

Non-preferential wetting is attained at both substrate and free surfaces when PS-PEI78 is cast on the SMG mat and annealed. Top-down SEM images (Figure 5.11a-d) demonstrate a perpendicular lamellae morphology independent of film thickness for <L>/L_0 = 1.5, 1.9, 2.1, 2.5. Figure 5.11e-f demonstrates that the "fingerprint" pattern in the <L> = 2.5 L_0 film can be visualized by AFM using either the height or the phase contrast mode, confirming that the expression of the constituent blocks of PS-PEI78 at the film surface can be discriminated using this technique. These data provide proof that PS-PEI78 is neutral at the free surface.

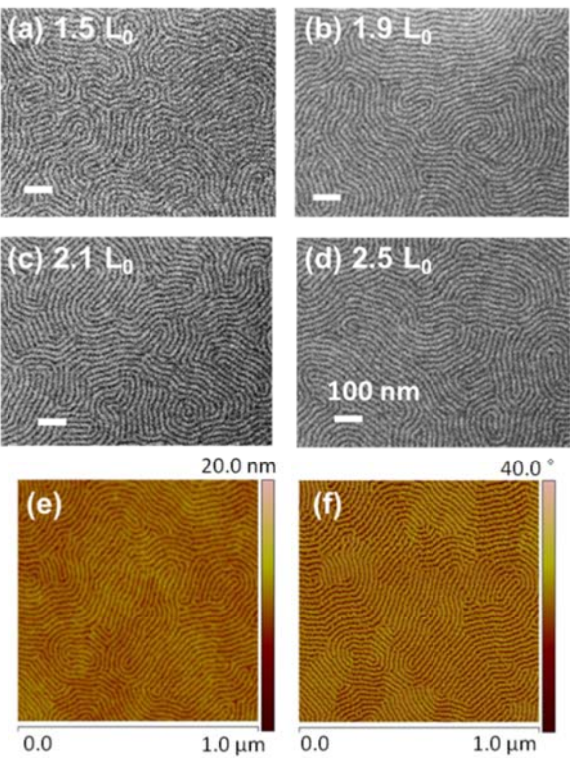

Figure 5.11 (a-d) Top-down SEM images of PS-PEI78 thin films of various film thicknesses (<L>/L_0 = 1.5, 1.9, 2.1, 2.5) on the SMG mats. Scale bars correspond to 100 nm. (e-f) AFM height and phase images of PS-PEI78 on the SMG mat (<L> = 2.5 L_0). The thin films were annealed at 105 °C for 6 h.

The two scenarios that involve a single neutral interface are now addressed. First, when PS-PEI78 (with a neutral free surface) is deposited on the PS brush (preferential to the PS block of PS-PEI78), the thickness dependence of its surface topology differs qualitatively from the patterns produced by PS-PI. The top-down SEM images of the PS-PEI78 films shown in Figure 5.9g-l exhibit island and hole structures as the average film thickness (<L>) is varied between 1.5 L_0 and 2.6 L_0. The film surfaces of <L> = 1.5

L_0 (Figure 5.9g) and <L> = 2.0 L_o (Figure 5.9i) samples are nearly featureless while the elongated motifs exhibited by the samples with <L> = 1.8 L_0 (Figure 5.9h) and <L> = 2.3 L_0 (Figure 5.9k) indicate proximity to the spinodal morphology that occurs at the most incommensurate film thickness (*e.g.*, see Figure 5.9c).[264] This behavior is in sharp contrast with simple asymmetric wetting, obeyed by PS-PI, in which the geometry of the surface motifs is repeated at intervals of 1.0 L_0 in the film thickness[264] as seen in Figure 5.9a-f. In the thickest PS-PEI78 film, <L> = 2.6 L_0, three distinct levels of contrast (bright gray, dark gray, and black) are apparent in the SEM image (Figure 5.9l), implying that the film topography contains more than two heights. Although the exact origins of this multi-tiered structure are unknown, its presence provides additional insight into the underlying symmetry of the PS-PEI78 films. (The hierarchical surface morphology may result from the proximity of the solvent boiling point (toluene, 111 °C) to the annealing temperature (105 °C) used in preparing the PS-PEI78 films, which leads to the relatively slow release of the residual solvent.)[266]

AFM experiments with PS-PEI78 supported on the PS modified substrate (Figures 5.12 – 5.14) demonstrate a parallel lamellar structure, characterized by non-integral step heights ($h \neq nL_0$) and the expression of both block components at the free surface. Both short-time and long-time annealed samples with <L_0> = 1.8 – 1.9 L_0 exhibit topographic profiles characterized by $h \cong 0.5\ L_o$ (Figure 5.12c,f); longer annealing times lead to larger scale structures, *e.g.*, increasing from 100 – 400 nm (Figure 5.12a,b) to 1 – 3 μm (Figure 5.12d,e). Contrasts in phase images recorded from the same surface regions (Figure 5.12b,e) reveal that the two surface features (holes and mesas) are covered with chemically different materials. Step heights determined from multiple measurements on long-time annealed samples are distributed narrowly around

the mean value 0.5 L_0 with a standard deviation of less than 0.03 L_0 (= 0.6 nm), which lies within the experimental uncertainty associated with the AFM instrument.

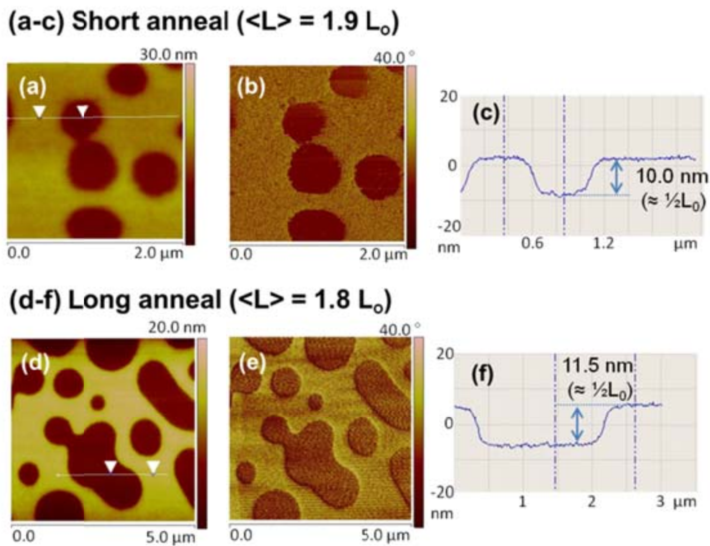

Figure 5.12 AFM height images, phase images, and height profiles of thin-film PS-PEI78 above the PS brushes. (a-c) Short annealing (<L> = 1.9 L_0). (d-f) Long annealing (12 hours) (<L> = 1.8 L_0). The thin films were annealed at 105 °C. Step heights equal to (c) 10.0 nm and (f) 11.5 nm, respectively.

Remarkably, all the PS-PEI78 thin films cast on PS brushes generated half-integral step height features ($h \cong 0.5\ L_0$) characterized by different phase contrasts, as demonstrated by representative AFM images in Figures 5.13 and 5.14. Even the hierarchically complex structure (<L> = 2.6 L_0) conforms to this behavior (Figure 5.14d-f). These AFM results, reinforced by the top-down SEM results, of PS-PEI78 are consistent with the parallel lamellar structure with 0.5 L_0 step heights, as depicted in Figure 5.1a. In this thin-film structure, which has been proposed for the combination of the neutral free surface and the preferential substrate, the most incommensurate film thickness would

correspond to <L> = (n ± 0.25) L_0. Significantly, reducing the degree of epoxidation to 65% (done with a different symmetric PS-PI diblock copolymer precursor) leads to island and hole formation with h = 1.0 L_o and no phase contrast between topographical features (Figure 5.15).

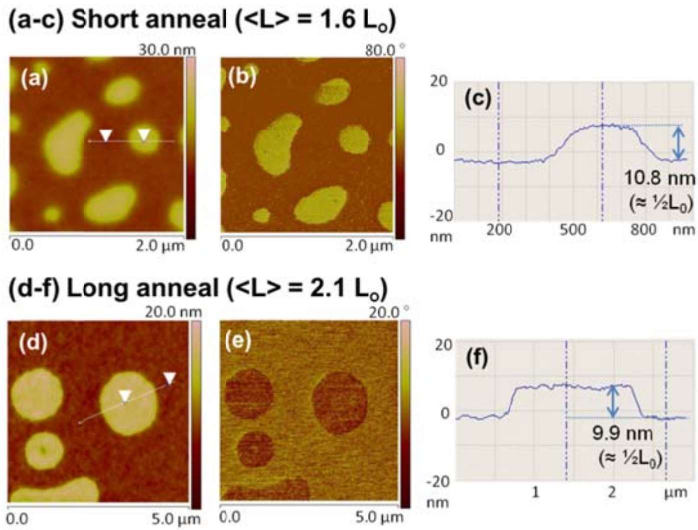

Figure 5.13 AFM height images, phase images, and height profiles of thin-film PS-PEI78 above the PS brushes. (a-c) Short annealing (<L> = 1.6 L_0). (d-f) Long annealing (12 hours) (<L> = 2.1 L_0). The thin films were annealed at 105 °C. Step heights equal to (c) 10.8 nm and (f) 9.9 nm, respectively.

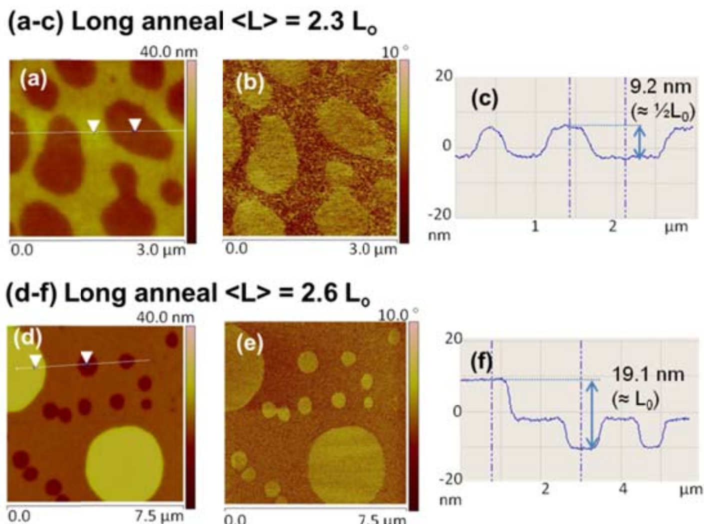

Figure 5.14 AFM height images, phase images, and height profiles of PS-PEI78 (annealed at 105 °C/12h) on the PS brushes. (a-c) <L> = 2.3 L_0. (d-f) <L> = 2.6 L_0. Height differences equal to (c) 9.2 nm and (f) 19.1 nm (two steps), respectively.

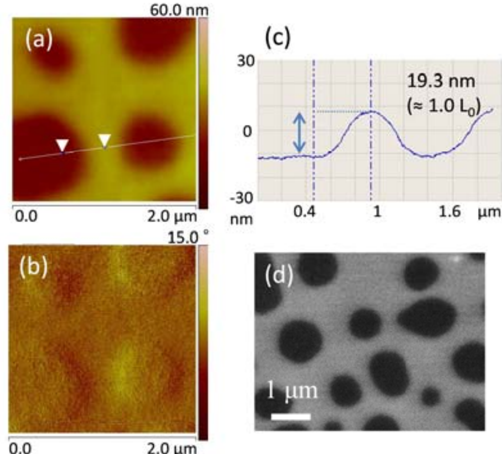

Figure 5.15 (a-c) Top-down AFM height image, phase image, and topographic profile, and (d) SEM image of thin films of poly(styrene-*b*-isoprene) diblock copolymer (12.3 kg/mol-10.5 kg/mol) with 65% degrees of epoxidation (<L> = 1.3 L_0) on the PS brush. Thin films were annealed at 105 °C/6h. The step height from the thickness profile equals to 19.3 nm (≈ 1.0 L_0).

PTMSS-PLA enables access to highly preferential free surfaces with variable substrate surface wetting, which is controlled by the tBSMA substrate composition. Figure 5.16 shows thin-film PTMSS-PLA samples annealed on two substrate surfaces, tBSMA-15 and tBSMA-34. Note that light colors are thinner and dark colors are thicker with the optical micrographs reported herein, as opposed to the contrast in AFM height results. Atomic force microscopy (Figures 5.16c,f) demonstrates that the quantized height or depth of surface topographies produced on tBSMA-15 and tBSMA-34 is $h \cong 1.0\ L_0$. Asymmetric wetting is achieved with PTMSS-PLA annealed on a surface with 15 mole % PtBS (tBSMA-15); thin-film samples with $1.50\ L_0 < \langle L \rangle < 2.00\ L_0$ form islands (Figure 5.16a-b). Since the PTMSS block preferentially wets the free surface due to its lower surface energy, PLA must wet tBSMA-15. In contrast, the same thickness range of $1.50\ L_0 < \langle L \rangle < 2.00\ L_0$ produces holes on tBSMA-34 (Figure 5.16d-e). These results are consistent with symmetric wetting of PTMSS-PLA on tBSMA-34, and PTMSS wetting is expected at the tBSMA-34 interface. Control of substrate surface wetting with random copolymer surface treatments is well established.[57, 267] The non-preferential random copolymer composition exists intermediate to compositions that induce symmetric and asymmetric wetting of block copolymers.[255] The change of PTMSS-PLA wetting on tBSMA-15 and tBSMA-34 thus implies the presence of a neutral surface composition between 15 and 34 mole % PtBS for tBSMA crosslinkable mats.

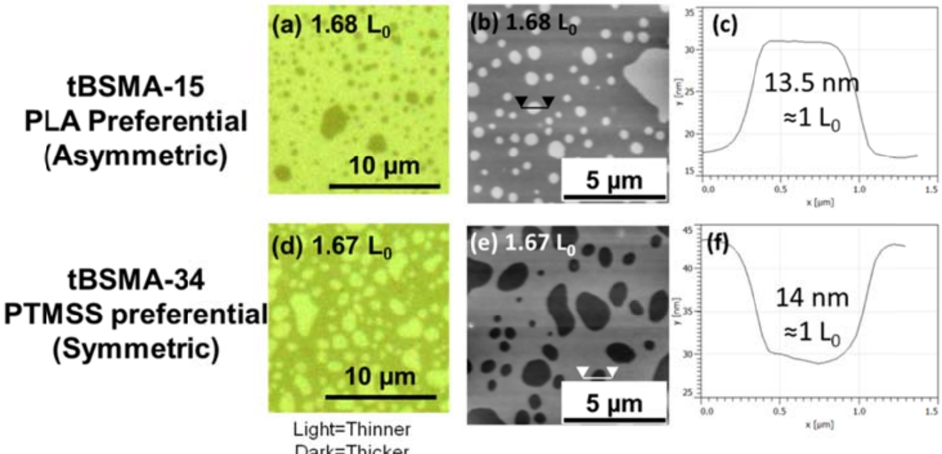

Figure 5.16 Optical micrograph, AFM height image, and height profile of PTMSS-PLA ($\langle L \rangle / L_0 \approx 1.68$, annealed at 150 °C/10 min.) on two surfaces: (a-c) tBSMA-15 (PLA preferential, asymmetric wetting) and (d-f) tBSMA-34 (PTMSS preferential, symmetric wetting). All color ranges in AFM represent 40 nm. Courtesy of collaborators at Univ. Texas.

PTMSS-PLA films annealed on tBSMA crosslinkable mats with compositions intermediate to 15 and 34 mole % PtBS produce surface topography with step heights h $\cong 0.5\ L_0$. For PTMSS-PLA films on tBSMA-25, "half islands" form at $\langle L \rangle = 1.20\ L_0$ (Figure 5.17a-c) and "half holes" at $\langle L \rangle = 1.42\ L_0$ (Figure 5.17d-f). In both cases, the topography and surrounding regions are characterized by the expression of a single material at the free surface, as evidenced by a lack of contrast in AFM phase measurements (Figure 5.17b,e). These data are consistent with a highly preferential free surface that is wet exclusively by the PTMSS block. PTMSS-PLA thin films of various film thicknesses on tBSMA-23 also produce the $h = 0.5\ L_0$ topography (Figure 5.18). The "half step" structures generated on tBSMA-25 are stable to extended annealing times, implying that the topography is not metastable. The formation of the uncommon

structures indicates the interfacial boundary condition at tBSMA-23 and tBSMA-25 must be different from simple preferential wetting exhibited by tBSMA-15 and tBSMA-34; tBSMA-23 and tBSMA-25 are inferred to be near non-preferential for PTMSS-PLA.

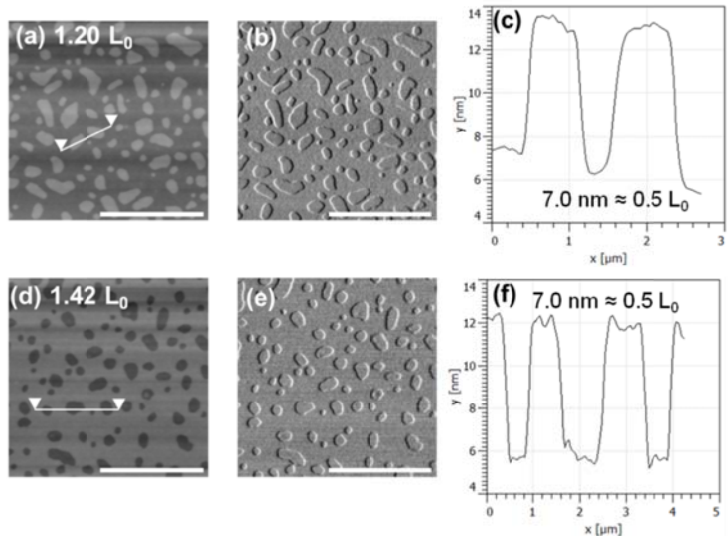

Figure 5.17 AFM height, phase, and height profile data of PTMSS-PLA with various thicknesses on near-neutral tBSMA-25. (a-c) $<L>/L_0 = 1.20$. (d-f) $<L>/L_0 = 1.42$. The thin films were annealed at 150 °C for 10 min. The scale bars represent 5 μm. All height color scales range from 0 to 40 nm, and all phase color scales range from 0 to 3 °. Courtesy of collaborators at Univ. Texas.

The film thickness dependence of h = 0.5 L_0 topography was elucidated with PTMSS-PLA on tBSMA-23 (Figure 5.18). All four film thicknesses tested ($<L>/L_0$ = 1.14, 1.36, 1.68, and 1.93) form half islands or half holes as confirmed by AFM (Figure 5.18e-h). Significantly, thicknesses $<L>$ = 1.14 L_0 (half islands) and 1.36 L_0 (half holes) unexpectedly generate opposite 0.5 L_0 surface topography. Analogously, $<L>$ = 1.68 L_0

generates half islands while $\langle L \rangle = 1.93\ L_0$ produces half holes. A similar thickness dependence of $0.5\ L_0$ topography is found for PTMSS-PLA on tBSMA-25 (Figures 5.17).

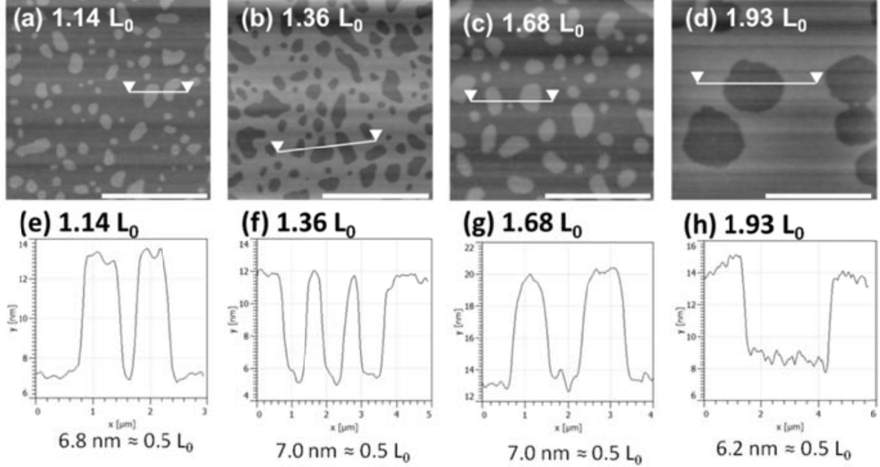

Figure 5.18 Thickness dependence of PTMSS-PLA structures with $0.5\ L_0$ step heights on near-neutral tBSMA-23. (a-d) AFM height data and (e-h) corresponding AFM height trace. The thin films were annealed at 150 °C for 10 min. All scale bars represent 5 µm. Courtesy of collaborators at Univ. Texas.

This behavior contrasts with the topographical thickness dependence observed for the well-established parallel lamellar structure with $h = 1.0\ L_0$; for simple asymmetric and symmetric wetting, thicknesses $1.0\ L_0 < \langle L \rangle < 1.5\ L_0$ should result in uniform topographical features (either islands or holes) while the range $1.5\ L_0 < \langle L \rangle < 2.0\ L_0$ will also result in uniform (but opposite) topography. The same abnormal thickness dependence is also observed with the $h = 0.5\ L_0$ structures formed by PS-PEI78 on the PS brush; $\langle L \rangle = 1.6\ L_0$ and $1.9\ L_0$ generate opposite topographical features (Figures 5.12a and 5.13a). A similar inversion in the topography is observed with PS-PEI78 for

<L> = 2.1 L_0 and 2.3 L_0 (Figures 5.13d and 5.14a). These results for PTMSS-PLA and PS-PEI78 are consistent with the most incommensurate film thickness at <L> = (n ± 0.25) L_0, surrounding which the inversion in topography (*i.e.*, holes ↔ islands) occurs. Based on the results, the unusual thickness dependence of the h = 0.5 L_0 topography is believed to be uniquely associated with thin-film samples confined between a non-preferential interface and a preferential interface. Implications and applicability are discussed below.

The universal nature of this behavior is further established by annealing thin films of a poly(styrene-*b*-methyl methacrylate) (PS-PMMA) diblock copolymer (66 kg/mol-63.5 kg/mol, Polymer Source, Inc.) at 230°C, where the surface wetting tendencies of the two blocks are reported to become equivalent.[58] While the different domains of perpendicular lamellae formed by PS-PMMA can be distinguished by AFM measurements (Fig. 5.19), the PS-PMMA thin films above the SMG mats exhibit perpendicular ordering independent of the film thickness (Fig. 5.20). The thickness independence confirms the surface neutrality achieved at both interfaces. Figures 5.21 – 5.22 demonstrate islands and holes with h = 0.5 L_0 for PS-PMMA on the PS brushes.

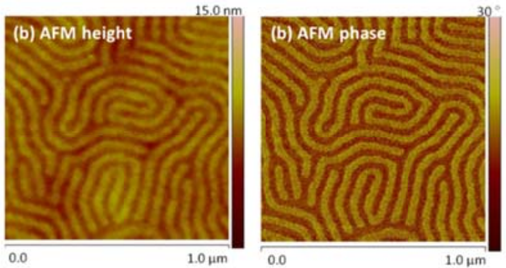

Figure 5.19 (a-b) AFM height and phase images of a PS-PMMA diblock copolymer (<L>/L_0 = 1.7) above the SMG mat. The thin film was annealed at 230 °C for 6 h. The lamellar periodicity L_0 is extrapolated ($L_0 \approx 60$ nm).

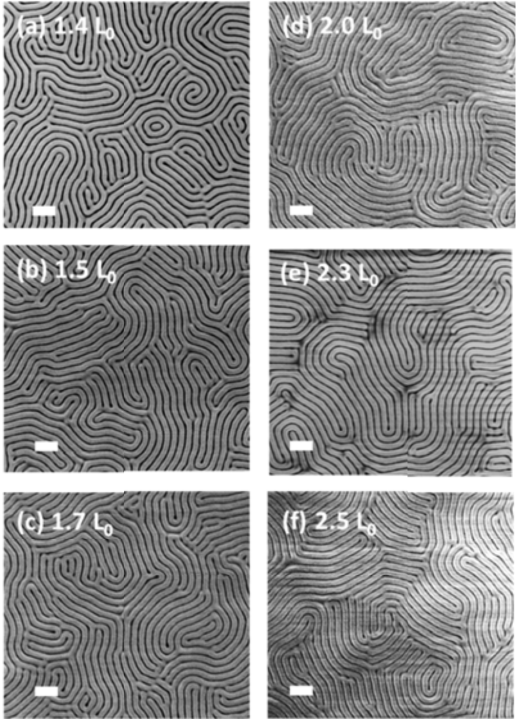

Figure 5.20 Top-down SEM images of PS-PMMA thin films of various film thicknesses (<L>/L_0 = 1.4, 1.5, 1.7, 2.0, 2.3, 2.5) on the SMG mats. Thin films were annealed at 230 °C/6h. The scale bars correspond to 200 nm.

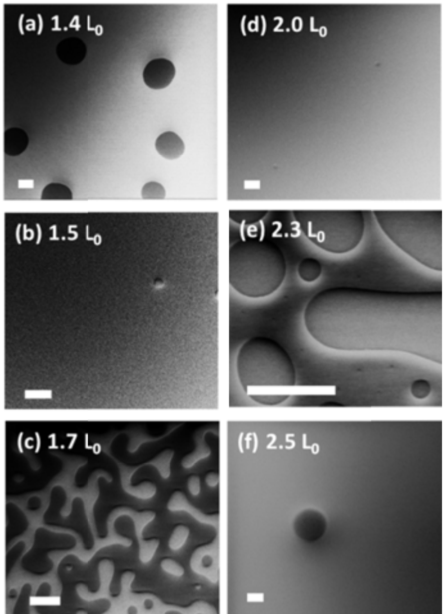

Figure 5.21 Top-down SEM images of PS-PMMA thin films of various film thicknesses ($\langle L \rangle / L_0$ = 1.4, 1.5, 1.7, 2.0, 2.3, 2.5) on the PS brushes. Thin films were annealed at 230 °C/6h. The scale bars correspond to 10 μm.

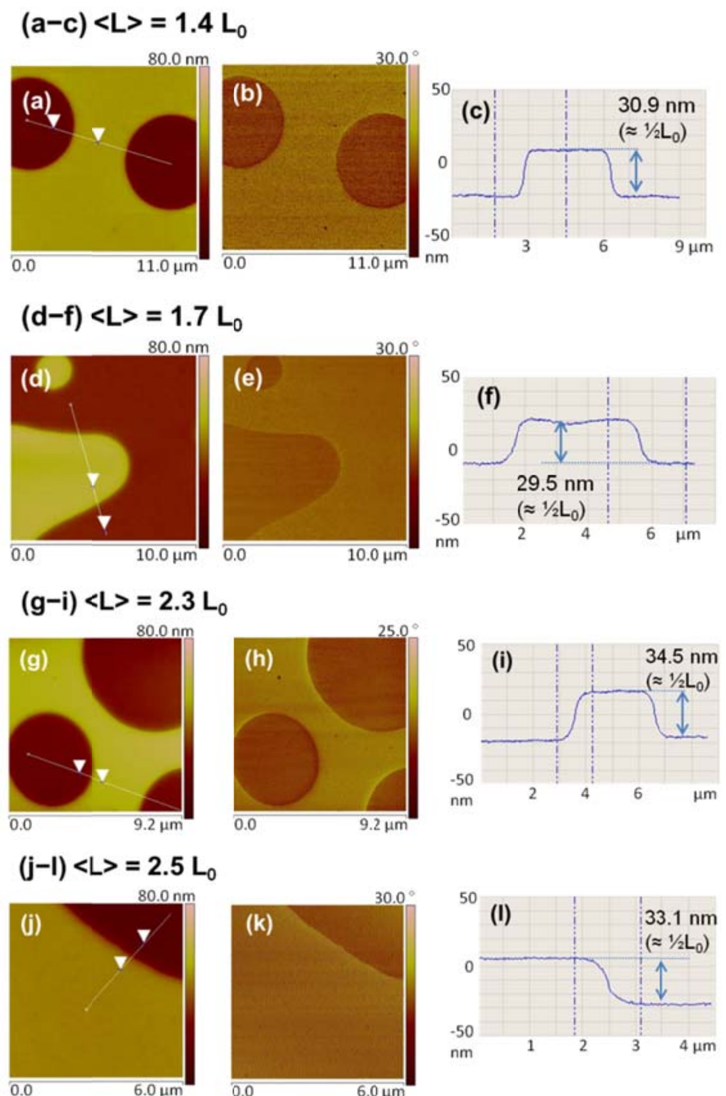

Figure 5.22 AFM height, phase, and height profile images of thin-film PS-PMMA above the PS brushes for various film thicknesses: (a-c) <L> = 1.4 L_0, (d-f) <L> = 1.7 L_0, (g-i) <L> = 2.3 L_0, and (j-l) <L> = 2.5 L_0. Step heights equal to (c) 30.9 nm, (f) 29.5 nm, (i) 34.5 nm, and (l) 33.1 nm, respectively. Thin films were annealed at 230 °C/6h.

5.4 DISCUSSION

Combining appropriately designed homopolymer and random copolymer blocks offers unique advantages in producing thin films with remarkable morphological control. “Decoupling” the thermodynamic driving forces that govern bulk segregation and interfacial wetting through the random chemical modification of preformed polymers, such as PS-PI, provides a facile method for tuning the surface energies of block copolymers, virtually independent of microphase segregation in the bulk material.[247] The persistence of perpendicular ordering in thin films of PS-PEI78 when supported on the SMG mats (Figure 5.11), independent of the film thickness, provides incontrovertible evidence that both the free and substrate interfaces have been neutralized.[253, 254] This indeed demonstrates that the surface energy of the PI block has changed through the partial chemical modification and become comparable to that of the PS block.

Island and hole formation with h = 0.5 L_0 is found for both PS-PEI78 on a PS brush and PTMSS-PLA on near neutral tBSMA mats. PS-PEI78 on the PS brush produces AFM phase contrast between topographical features since the two blocks compete to wet the free surface in the layered lamellar structure. The h = 0.5 L_0 island/hole structures observed with PTMSS-PLA are analogous to those observed with PS-PEI78. However, a lack of AFM phase contrast between the topography and the surrounding highlights the primary difference: a single block (PTMSS) is expressed at the free surface. To the best of our knowledge, the unusual h = 0.5 L_0 finding has not been described previously. In general, island/hole topologies are characterized by h = 1.0 L_0,[248, 250-252] although several instances of metastable structures with smaller step heights (h < 1.0 L_0) have been reported at the early stage of relief formation; examples include a broad distribution of step heights (h < 1.0 L_0) that eventually sharpen into discrete h = 1.0 L_0 features upon further annealing[268, 269] and regions with h ≈ 0.5 L_0 that appear transiently along with L_0 steps.[270] The results for both PS-PEI78 and PTMSS-PLA are

qualitatively different then these anecdotal examples of non-equilibrium surface motifs. PS-PEI78 and PTMSS-PLA both produce $h = 0.5\ L_0$ features that are stable to long-term annealing and persist as the surface morphology coarsens to lateral dimensions beyond several microns.

The observations with both PS-PEI78 on the PS brush and PTMSS-PLA on tBSMA-23 and tBSMA-25 are consistent with the schematics shown in Figure 5.1. The illustrations show two possible ways that structures with step heights $h = 0.5\ L_0$ can arise in thin films. In each case, a single block exclusively wets the preferential interface, and the neutral interface contacts both blocks. PS-PEI78 on the PS brush facilitates the direct observation of the neutral interface since AFM is intrinsically a top-surface measurement technique. AFM phase contrast demonstrates that surface topography is characterized by separate regions of contact between each block and the free surface (Figure 5.1a). These conclusions presumably translate to the opposite interfacial neutralization, PTMSS-PLA on tBSMA-23 and tBSMA-25, but the neutral interface wetting is difficult to observe directly in this case. Due to the strongly preferential interaction of PTMSS with the free surface, proving unequivocally that tBSMA-23 and tBSMA-25 are indeed neutral for PTMSS-PLA (*e.g.*, thickness independent perpendicular orientation) is challenging without additional top surface neutralization, a topic of ongoing research. However, PTMSS-PLA provides confirmation that a single block wets the preferential interface when $0.5\ L_0$ topography is formed, insight that complements the data obtained with PS-PEI78 on the PS brush. Coupled with the PS-PEI78 results, the generation of $h = 0.5\ L_0$ topography for PTMSS-PLA only on surfaces that must be compositionally near neutral strongly implicates non-preferential substrate interactions as the cause, as depicted in Figure 5.1b.

The inversion of the $h = 0.5\ L_0$ topographic features surrounding $<L> = (n \pm 0.25)\ L_0$ provides powerful methodology that can be used to evaluate the neutrality of block copolymers and interfacial modifiers. The results for both PS-PEI78 on the PS brush and PTMSS-PLA on tBSMA-23 and tBSMA-25 suggest that the formation of $h = 0.5\ L_0$ features in either case is indicative of successful neutralization at a single interface. Therefore, block copolymers designed to neutralize free surface interactions can be screened on highly preferential substrate surfaces, or block copolymers with highly preferential free surface interactions can be analyzed to find non-preferential substrates. Both possibilities were presented herein. In principle, the analysis need not even quantify the height profile for $h = 0.5\ L_0$. If there is a single neutral surface, a change in topographical features (*i.e.*, islands ↔ holes) will occur between thickness ranges of $(n - 0.5)\ L_0 < <L> < (n - 0.25)\ L_0$ and $(n - 0.25)\ L_0 < <L> < nL_0$. The topography will remain unchanged if no neutral interface is present. The analysis can be performed entirely with an optical microscope rather than for instance AFM. Even extremely small thickness differences (*ca*. 7 nm) between the “half” structures and the surrounding matrix can be resolved optically.

Phase separation of initially homogeneous binary mixtures of polymers (and many other condensed systems)[271, 272] in 3 dimensions (bulk) generally proceeds by two distinct kinetically controlled mechanisms: nucleation and growth (NG) and spinodal decomposition (SD).[273] Factors, such as the mixture composition and the quench depth relative to the equilibrium (bimodal) and stability (spinodal) limits, control the rate of structural evolution and the morphology of the resulting two-phase system. Symmetry breaking surfaces can modify blends that are homogeneous in the bulk state, leading to two dimensional layered structures in the thin film limit.[25, 274] Numerous studies

conducted over the past two and a half decades have dealt with the formation of two-phase morphologies in thin layers of homopolymer blends.

The initial formation and subsequent coarsening of relief structures in thin-film block copolymers bear some resemblance to the transient morphologies that develop during the phase separation of unstable bulk binary mixtures. Incommensurability between the initial average film thickness $\langle L \rangle$ and the natural microdomain period L_0, combined with the incompressible nature of polymer melts, leads to the formation of terraces on the free surface, and the mechanisms that describe the transition from an initially smooth to textured interface have been studied both theoretically and experimentally.[275-278] The island/holes formation proceeds by either kinetic mode (NG or SD) depending on various factors, such as the thermal ramping rate[279] and the initial film thickness.[280] Shull[275] adapted an analytical approach originally developed for the early stages of spinodal decomposition in binary mixtures in modeling the formation of hole/island motifs in thin-film block copolymers. Similar to the development of directed spinodal waves in thin-film polymer blends,[25, 274] composition waves propagate from interfaces and interfere with each other in block copolymer thin films during annealing.[55, 281] The critical domain size required for the hole/island structures to survive the action of thermal fluctuations during the initial stage was estimated,[282] and a number of growth mechanisms were proposed.[269, 282-284]

The free energy of formation associated with nuclei of heights $h = 0.5\ L_0$ and $h = 1.0\ L_0$ can be used to explain the formation of the relief structures obtained in the PS-PEI78 thin films. Slow thermal ramping rates (≈ 1 °C/min, similar to what was implemented in annealing PS-PEI78) have been found to favor the NG mechanism in island/hole formation.[279] Achieving a critical nucleus size is the principle barrier that must be overcome for subsequent growth of the surface morphology. The free energy of

a nucleus is controlled by three factors: (1) the interfacial energy at the free surface; (2) the elastic strain energy that originates from the thickness incommensurability; (3) the line tension that results from the defects formed at the boundaries of the topographic structures. Roughening of films inherently occurs upon annealing a mixed, solvent-cast state.[285, 286] During the formation of non-uniform variations in the film thickness, the smaller thickness gradient associated with h = 0.5 L_0 relative to h = 1.0 L_0 should favor the formation of half step nuclei. Of course the large difference in the surface energy between the blocks in PS-PI overwhelms any such advantage leading to the formation of structures with h = 1.0 L_0.

A transition zone separates regions of parallel lamellae regardless of the value of h. Experiments have shown that the free energy penalty associated with features containing a small radius of curvature causes the transition zone to broaden considerably as illustrated in Figure 5.23,[287] necessitating a reconstruction of the underlying morphology. For example, perpendicular lamellae can accommodate a continuously varying transition zone thickness but require splicing onto the parallel layers at the transition boundaries; this can be accommodated by an interfacial arrangement such as Scherk's surface.[288, 289] Figure 5.24 shows the edge profiles of structures for h = 1.0 L_0 (PS-PI) and h = 0.5 L_0 (PS-PEI78) obtained using AFM measurements. The transition width (Δx) has been estimated as the difference in the lateral positions that correspond vertically to 20% and 80% of the step heights ($\Delta x = x|_{y=0.8h} - x|_{y=0.2h}$). Based on the profiles in Figure 5.24, $\Delta x/h$ ranges 5 – 6 and 6 – 8 for h = 1.0 L_0 and h = 0.5 L_0, respectively. Previous studies report significantly larger step widths for structures with h = 1.0 L_0.[251, 288] Normalized transition widths $\Delta x/h$ for PTMSS-PLA with h = 1.0 L_0 (Figure 5.16c,f) fall roughly in the range 18 − 27. Some roundness to the peaks in the height traces for h = 0.5 L_0 (Figures 5.17c,f, 5.18e-h) makes exact calculations of Δx

somewhat arbitrary. The range of $\Delta x/h \sim 55 - 65$ for $h = 0.5\ L_0$ in PTMSS-PLA is significantly larger than the range for $h = 1.0\ L_0$ and the measured PS-PEI78 transition widths.

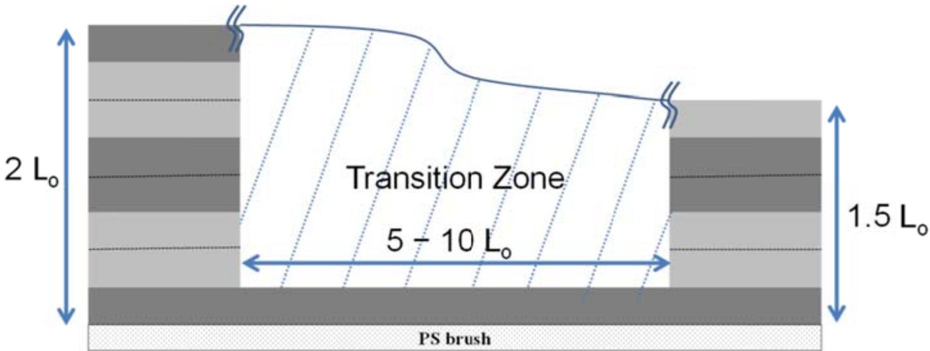

Figure 5.23 Cross-sectional schematic illustration of parallel lamellae with ½ L_o step heights. The step height profile at the edge is characterized by a broad "transition zone."

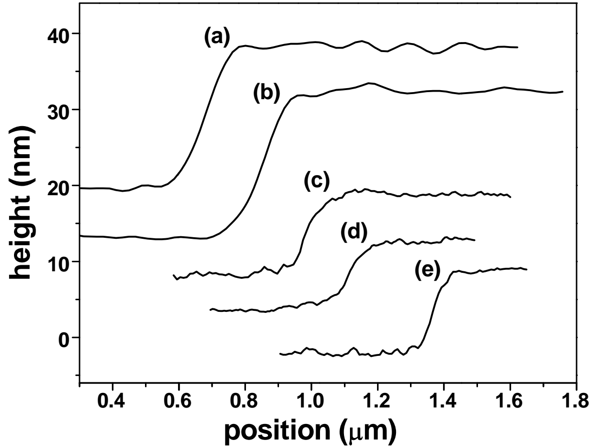

Figure 5.24 Step height profiles. (a-b) PS-PI ($\langle L\rangle/L_0 = 2.3$) on PS and SMG brush/mats. (c-e) PS-PEI78 on PS brushes with varying $\langle L\rangle$ ($\langle L\rangle/L_0 = 1.8$, 2.3, 2.6).

The morphology of the transition zone is expected to be established soon after the initially formed topological features begin to coarsen, analogous to the establishment of an equilibrium interfacial thickness following either nucleation or the initial stages of spinodal decomposition in phase separating polymer blends.[290, 291] The exact structure of the transition zone likely depends on many factors, including the exact copolymer composition, molecular weight, polydispersity, statistical segment lengths, and possibly whether the free surface or the substrate is preferentially wet. These differences could contribute to the significantly larger transition zones measured for PTMSS-PLA compared to PS-PEI78. Intuitively, microdomain structures with negative Gauss interfacial curvature are anticipated, by analogy with the microdomain structures found adjacent to lamellae in bulk specimens, *i.e.*, gyroid and perforated lamellae[2] and Scherk's surface found at the boundary between orthogonally arranged lamellar grains.[289] Another way to relieve the local strain is to embed cylindrical domains underneath the edges of island and hole structures for symmetric block copolymers.[292] Evidence of such intermediate morphologies in the transition zone at the edges surrounding the island and hole structures of PS-PEI78 and PS-PMMA has been recorded in AFM images (Figure 5.25). These features are difficult to resolve and are not always visible in the AFM measurements. Alternatively, the block copolymer could partially disorder in portions of the transition zone, although this should become prohibitively expensive in the free energy as the segregation strength increases. Liu *et al.*[292] documented reconstructed island edges for large molecular weight (M_n > 100 kg/mol) but not for low molecular weight (M_n < 40 kg/mol) poly(styrene-*b*-2-vinylpyridine) (PS-P2VP) block copolymers. The absence of well-described microphase segregation in highly constrained block copolymer systems also has been reported.[55, 293]

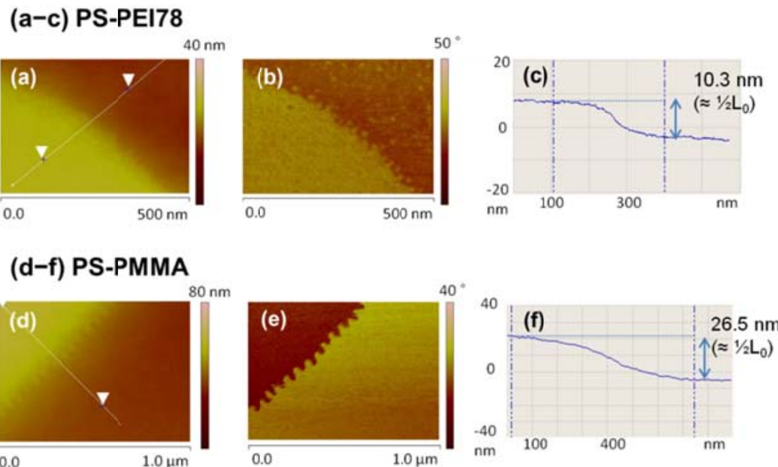

Figure 5.25 AFM height, phase, and height profile images of (a-c) PS-PEI78 and (d-f) PS-PMMA above the PS brushes. $\langle L \rangle = 1.7\ L_0$. Step heights equal to (c) 10.3 nm and (f) 26.5 nm, respectively.

The relief structures of $h = 0.5\ L_0$, which initially form as a result of surface neutralization, may face energetic barriers in transforming into structures of $h = 1.0\ L_0$. Such a transformation would involve a transport of polymers that already constitute well-built structures of large domains (~ μm) (Figures 5.12 − 5.14, 5.17 – 5.18). The possibility of "pinning" should not be dismissed in explaining the observation of step heights solely of 0.5 L_0 even after 12 hours of annealing PS-PEI78 or 6 hours of annealing PTMSS-PLA. The persistence of intermediate morphologies, or "pinning" of stages, due to kinetic traps that prevent a system from reaching its thermodynamic equilibrium has been commonly observed in various systems that go through phase separations. Examples include development of microstructures in metal alloys, spinodal decomposition of off-critical polymer blends,[294] coarsening of phase-separated polymer blends in thin films,[27] path-dependent morphologies in micelles[295] or ternary mixtures of

oil/water/block copolymer surfactant,[296] the formation of spherical morphologies of bulk block copolymers with solvent annealing,[297] and the growth of hole/island structures in thin-film block copolymers that form parallel lamellae.[298, 299] Sometimes, the specific kinetically-frozen states are sought after for their desirable properties, such as perpendicular domain orientations in the case of solvent annealing of block copolymer thin films.[66, 67] Various mechanisms have been suggested as responsible for such pinning, including surface curvature elasticity,[264] loss of interfacial continuity when a percolating morphology breaks up into clusters,[294] glassy cores[300] or the incompatibility between cores and solvents[295] that suppress a chain exchange in micelles. All these examples display kinetic barriers that must be overcome before reaching the true thermodynamic equilibrium. Similarly, the local transformation of structures from h = 0.5 L_0 into h = 1.0 L_0 would be inhibited by unfavorable diffusion normal to the microdomain interfaces[301, 302] and suppressed by the requirement for long-range lateral transport of materials.

5.5 Conclusion

Three possible combinations involving at least one non-preferential interface have been demonstrated. Surface neutralization at both the free and substrate surfaces was accomplished with PS-PEI78 thin films on SMG mats, based on SEM measurements that show a perpendicular arrangement of lamellae independent of the overall film thickness. Topographical step heights with half the bulk periodicity (0.5 L_0) are generated when a block copolymer is confined between a single neutral interface and a single preferential interface. PS-PEI78 (neutral free interface) exhibits such behavior when supported on a preferential PS brush. Both constituents of the block copolymer are expressed at the free surface, as demonstrated by AFM phase contrast images. In

contrast, PTMSS-PLA has a strongly preferential free surface and produces 0.5 L_0 step heights only when supported on a near neutral substrate. AFM phase contrast measurements demonstrate that PTMSS-PLA expresses a single block over the entire free surface. The most incommensurate film thickness associated with 0.5 L_0 step heights is $<L> = (n \pm 0.25) L_0$, distinctly different than simple asymmetric (nL_0) and symmetric [$(n - 0.5) L_0$] wetting. These results provide a simple and powerful method for determining surface neutrality of block copolymers or substrate surface treatments.

Chapter 6 Block Copolymer Self-Assembly in Thin Films: Segregation Strength Variations[3]

6.1 INTRODUCTION

Among diverse interests,[303] self-assembly has received much attention as a bottom-up scheme to attain small features. The microlithography has played an important role in the development of the semiconductor industry, generally expressed in terms of Moore's Law, by enabling the fabrication of features in small dimensions. Recently, the industry faces challenges in overcoming the theoretical limit of the optical lithography at 22 nm half-pitch, and uncertainty remains as to what technique would emerge as the next generation lithography (NGL) and replace the optical lithography. While a few critical issues have not been completely resolved with several candidates for NGL, such as extreme ultraviolet lithography (EUVL), the International Technology Roadmap for Semiconductors (ITRS) has started to list directed self-assembly since 2007 as one of potential solutions that would enable sub-22 nm half-pitch.[304]

The self-assembly of bulk block copolymers leads to the formation of ordered, periodic structures whose dimensions lie in the range of a few tens of nanometers.[5] Such nature of block copolymers has been implemented in thin films for a wide range of applications, such as photonics,[33] membranes,[42] and capacitors.[39] Features that need to be manipulated for successful application of thin-film block copolymers include (1) the domain orientation, (2) the periodic dimension of the morphology, and (3) the etch resistance contrast for pattern transfer.

For thin-film block copolymers in thermodynamic equilibrium, the interfacial boundary conditions determine the domain orientations. The system with comparable

[3] Refer to Acknowledgements for contributions made by other people.

interfacial energies exhibits perpendicular ordering, which is technologically more useful than other morphologies. The early extensive investigation of poly(styrene-*b*-methyl methacrylate) (PS-PMMA) diblock copolymer thin films stems in part from the comparable surface energies of the blocks.[58] Various measures have been taken to compensate for the surface energy difference in other block copolymers.[59, 60, 305] One example is solvent annealing that allows one to effectively "neutralize" or nullify the interfacial energy difference between constituents by kinetic trapping of the system.[66] However, the thin-film morphology after solvent annealing is affected by numerous factors, such as solvent selectivity,[70] annealing duration,[65, 306] evaporation rates,[67, 68, 307] humidity,[308] and temperature.[309] The intricate interplay among these factors in solvent annealing has not been fully understood, making it difficult to predict the resulting morphology. While a random copolymer brush has been devised to control the interaction between thin-film block copolymers and underlying interfaces,[57] the incorporation of random architecture into thin-film block copolymers offers an alternative in attaining free surface neutralization. The random modification of block copolymers and blends has not been studied in thin-film forms as extensively as in a bulk state.[111, 112, 123, 126, 127] The previous reports on the partially epoxidized poly(styrene-*b*-isoprene) diblock copolymers suggested that the surface energies of the two constituting blocks could be tuned almost independent of the bulk microphase segregation.[247] This methodology would allow one to attain perpendicular ordering of the thin-film block copolymers, which initially exhibit disparate surface energies prior to the chemical modification.

The application of block copolymer self-assembly to lithography, which inherently aims towards resolution enhancement, requires minimizing the degree of polymerization (N) in thin-film block copolymers. This effort inevitably involves

monitoring the behavior of the system as the segregation strength decreases, and the primary prediction for thin films may be made based on the bulk characterization results. For example, the order-disorder transition (ODT) (χN = 10.5 in mean field theory)[3] is expected to place a fundamental limit on the smallest features in thin films attainable for a given system with a measurable interaction parameter χ (*e.g.*, 20 – 25 nm feature size for PS-PMMA).[95, 238] However, studies suggest that the translation in behavior from the bulk to the thin film may not be straightforward as a consequence of dimensionality reduction. Not much work has been done in looking at the dependence of thin-film block copolymers on segregation strength variation. One difficulty associated with the thin-film investigation originates from the strong influences exerted by interfacial interactions that disrupt the thin-film behaviors. For the case of bulk, on the other hand, an extensive work has been done on looking at different aspects of block copolymers for various ranges of χN, encompassing the ODT. For example, at $\chi N \sim 6$ a crossover in the conformation of polymer chains occurs, signaling the change in the power dependence of chain extensions.[230] Though negligible in strong segregation limit ($\chi N >> 10.5$), the effect of fluctuation becomes prominent near the ODT for block copolymers of small N.[4] Fluctuations cause deviation in behaviors from mean field predictions; the ODT occurs at a higher χN and the weakly first-order ODT is induced in symmetric block copolymers in bulk.[231, 310] Though the effects of transitions and fluctuations on thin film block copolymers have received less attention in the past, these matters are expected to be of grave importance in the future as people are interested in attaining smaller features for thin-film block copolymer applications and approach the ODT (*i.e.*, $\chi N \sim 10.5$).

In this chapter, the thin film behavior of partially epoxidized poly(styrene-*b*-isoprene) diblock copolymers is investigated as χN is varied, mostly through adjustments in N. The neutrality of the block copolymers at the interfaces minimizes the

disruption of the thin-film behaviors and allows the inner thin-film morphology to be expressed at the free surface. The values of χN for this investigation range from 8 to 17, and our discussion is arbitrarily divided into two regimes of χN. For moderate segregation strength ($\chi N > 12$), thin-film behavior is studied while the film thickness and the underlying brush compositions are varied in a controlled manner. The thermodynamic equilibrium achieved in the thin-film block copolymers, which consist of random copolymer architecture, is discussed based upon the previous results reported for PS-PMMA. Stripe chemical patterns are also implemented to direct the self-assembly of the block copolymers. For the system in the weaker segregation regime ($\chi N < 12$), the both bulk and thin-film studies on the system are presented, and the comparison allows the investigation about the effect of dimensionality on ODT and fluctuations.

6.2 EXPERIMENTAL

Materials, Synthesis, and Bulk Characterization: Poly(styrene-*b*-isoprene) diblock copolymers of various molecular weights were synthesized using anionic polymerization and are denoted as SI*xx*, where *xx* represents the molecular weights (units in kg/mol). Controlled epoxidation of the precursors was carried out using dimethyl dioxirane (DMD), as done previously,[127] and their products are denoted as SI*xx*E. The synthesis and thin-film characterization of SI21 and SI21E have been presented to some degrees in Chapter 5 of this dissertation, from which selected data will be provided again in this chapter.

Two size exclusion chromatographies (SEC) using tetrahydrofuran (THF) as mobile phases ((1) Waters 717 with Autosampler, Waters 2410 Refractive Index Detector (Amundson Hall, Univ. of Minnesota) and (2) Viscotek VE2001, 302-050

Tetra Detector Array (Soft Materials Laboratory, Univ. of Wisconsin)) were used to determine the number average molecular weight (M_n) and polydispersity index (PDI) of the polymers. Proton nuclear magnetic resonance (^{1}H-NMR) (VAC-300 Autosampler, IBM Instruments) was utilized to establish the composition of SI*xx* and to estimate the degree of epoxidation in SI*xx*E.

Differential scanning calorimetry (DSC) (Q1000 DSC, TA Instruments) was employed to identify the glass transition temperature (T_g) of the polymers while scanning at a ramping rate of ± 10 °C/min. Rheological measurements were conducted on pressed samples with a rheometer (ARES, Rheometric Scientific). Small-angle x-ray scattering (SAXS) experiments were conducted at room temperature at Argonne National Laboratory on the pre-annealed specimens (105 °C for 3 − 6 hours in vacuum).

Brush/Mat Synthesis and Preparation: Two different types of random copolymers that consist mainly of poly(styrene) and poly(methyl methacrylate) were prepared using nitroxide-mediated living free radical polymerization (NMP), as done previously.[120] The first type of the random copolymers incorporates thermally-crosslinkable functional groups (GMA, glycidyl methacrylate). With the fraction of GMA retained at 4 − 6 mol. %, the random copolymers were prepared with various compositions of poly(styrene) and poly(methyl methacrylate) ($M_n \approx 9.5 – 40.1$ kg/mol, PDI ≈ 1.4 – 2.1). They are denoted as SMG*yy*, where *yy* represents the mol. % of styrene units (SMG00, SMG28, SMG57, SMG60, SMG76, SMG94). Thin films were prepared by spin coating a solution (0.2 – 0.5 wt. % in toluene) at 3000 rpm on Si wafers (as received), and the mat formed from a crosslinking reaction within the thin film, achieved by annealing under vacuum at 160 − 190 °C for 24 hours. Another type of random copolymers, represented as SMOH*zz*, contains the terminal hydroxyl functionality (-OH) ($M_n \approx 2.1 – 4.2$ kg/mol, PDI ≈ 1.2 − 2.0) and consists of *zz* mol. % of styrene units and

(100 – *zz*) mol. % of methyl methacrylate units (SMOH25, SMOH45). Uniform thin films were obtained by spin-coating a solution (1.0 – 1.5 wt. % in toluene, 3000 rpm) onto the bare silicon wafer (as received). Hydroxyl-terminated polymers were grafted upon thermal annealing at 190 °C for 24 hours in vacuum. Unreacted brush materials were removed by post sonication in toluene (3 times/5 minutes).

Thin Film Preparation and Characterization: Uniform thin films were obtained by spin-coating solutions of SI*xx*E (0.75, 1.0, 1.25, 1.5 wt. %, in toluene) on crosslinked SMG mats and SMOH brushes. Average film thicknesses (<L>), determined with an ellipsometry instrument (AutoEL-II, Rudolph Research), ranged from 0.8d to 2.5d (d = 2π/q*, where q* is the principle Bragg reflection measured by SAXS). The thin films were thermally annealed in a vacuum chamber with a constant flow of N_2 gas. Thin films were characterized by scanning electron microscopy (SEM) (LEO 1550-VP FESEM). Oxygen plasma (PE-200, Plasma Etch Inc.) was occasionally used to etch thin films prior to SEM imaging in order to enhance the image contrast, and the recipe implemented was designed to etch approximately 0.3 − 0.5 nm of poly(styrene) homopolymer thin films. Atomic force microscopy (AFM) (Nanoscope III Multimode AFM, Digital Instruments) was also employed in tapping mode to measure the height profiles and the phase images of the thin-film block copolymers.

Chemical Pattern Fabrication and Directed Self-Assembly: The chemical pattern was fabricated as previously demonstrated by Liu *et al.*,[96] and the sequential steps for the fabrication are illustrated in Figure 3.3 (Chapter 3) of this dissertation. Thin films of e-beam photoresists (zep520, 35 nm thick) were prepared above SMG94 mats (7 nm thick) using spin-coating. Stripe patterns of the photoresists were fabricated by e-beam exposure and sequential development. The periodicities of the stripe patterns were targeted to 39.0 nm and 44.1 nm, which correspond approximately to the integer

multiples of the lamellar periodicities of the block copolymers (*i.e.*, L_0(SI21E) = 19.1 nm, L_0(SI14E) = 14.7 nm). These patterns, provided by Hitachi Global Storage Technologies, were treated with the oxygen plasma (Unaxis 790 RIE), during which the trim-etched photoresist patterns were transferred to the underlying SMG94 mats. The removal of photoresists left stripe features made up of SMG94. Then, thin films of SMOH25 above the structures were prepared by spin-coating the solution (1.0 wt. %, toluene). The thermal annealing was implemented to graft the brush materials to the exposed SiO_x regions. The unreacted brush materials were removed using sonication in toluene (3 times/5 minutes). Lastly, SI21E and SI14E solutions were spin-coated above the chemical patterns, and the films were thermally annealed in vacuum at 105 °C and 80 °C, respectively, for 6 hours.

6.3 RESULTS

Four poly(styrene-*b*-isoprene) diblock copolymers were prepared: one cylinder-forming block copolymer (SI26) and three symmetric block copolymer with different molecular weights (SI21, SI14, SI10). Table 6.1 shows their molecular characterization and the degrees of modification attained for partially epoxidized samples (SI26E, SI21E, SI14E, SI10E). SEC traces (Figures 6.1 – 6.3) of the samples are characterized by monodisperse profiles with low polydispersity index (PDI), suggestive of the conservation of the sample integrities through chemical modification and thermal annealing implemented in this chapter. The bulk characterization results for SI21 and SI21E that have been already shown in Chapter 5 (denoted as PS-PI and PS-PEI78 in Chapter 5) are omitted here.

Table 6.1 Molecular characterization.

	M_n [a] (kg/mol)	f_S [b]	f_I [b]	PDI	T_g (°C)	T_{ODT} (°C)	Epox. Sample and Deg. (%)
SI26	25.7	0.69	0.31	1.04	-68, 90	170	SI26E, 82
SI21 [c]	21.3	0.49	0.51	1.06	-62, 82	182	SI21E, 78
SI14	13.9	0.48	0.52	1.05	-62, 68	86	SI14E, 78
SI10	9.6	0.49	0.51	1.04	-60, 42	< 50	SI10E, 80

[a] M_n was calculated by comparing the molecular weight of the poly(styrene) aliquots with the ratio between the poly(styrene) and the poly(isoprene) blocks estimated from the NMR measurement.

[b] Densities at 140 °C were used to calculate the volume fractions (f_S, f_I).

[c] Data have been reproduced from Table 5.1. SI21 and SI21E correspond to PS-PI and PS-PEI78, respectively, in Chapter 5.

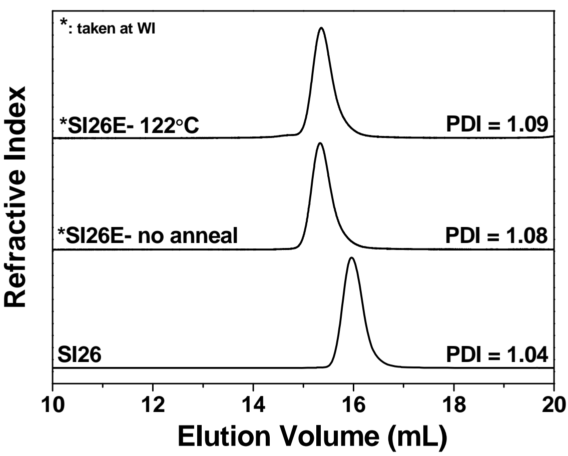

Figure 6.1 SEC traces for SI26, SI26E, and SI26E after 6-hour thermal annealing.

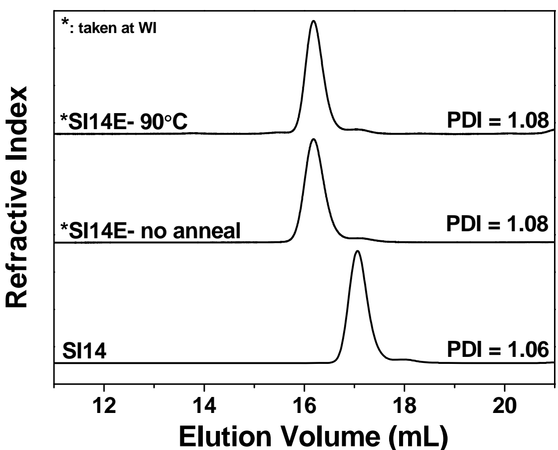

Figure 6.2 SEC traces for SI14, SI14E, and SI14E after 6-hour thermal annealing.

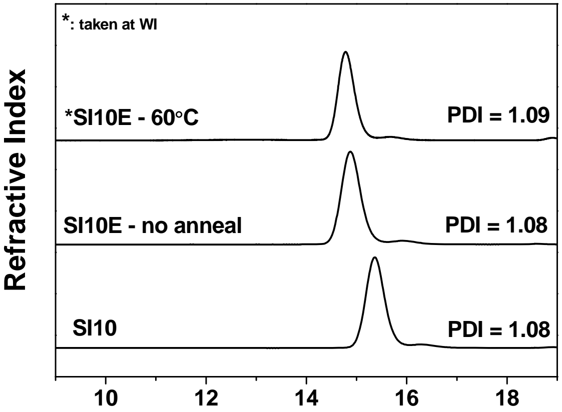

Figure 6.3 SEC traces for SI10, SI10E, and SI10E after 6-hour thermal annealing.

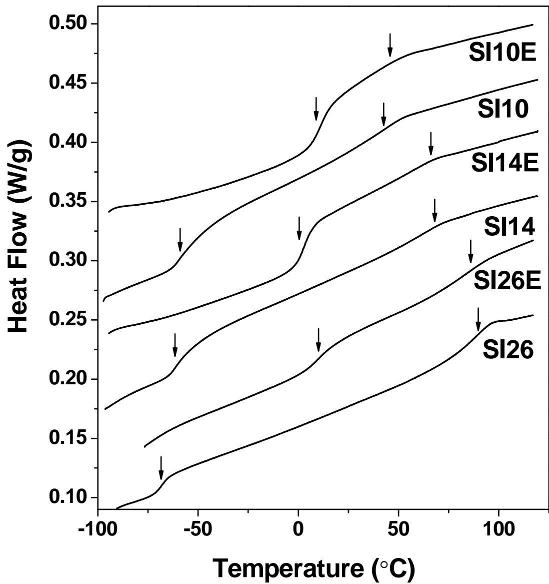

Figure 6.4 DSC traces for SI26, SI26E, SI14, SI14E, SI10, and SI10E diblock copolymers taken at ramping rates of +10 °C/min. Arrows indicate the inflections. Data except SI26 have been shifted vertically for clarity.

Two distinct inflection points in DSC traces are witnessed for both the precursors and the partially modified samples (Fig. 6.4). The bulk morphologies and the periodicities were investigated using SAXS, as shown in Figure 6.5. The relative peak positions for SI26 agree with a cylindrical morphology, as expected from its composition while the rest of the samples in the figure do not exhibit decisive higher order peaks. The proximity to disorder can be inferred for SI10 based on the broad primary peak. The difficulty involved with locating the primary peak for SI14E and SI10E is presumably due to combined effects of the greater mixing of the domains and the electron density matching. The bulk periodicities (L_0), estimated from the primary peak positions (L_0 =

2π / q^*, where q^* is the primary peak position), are 18.9 nm (SI26), 20.0 nm (SI26E), 14.4 nm (SI14), and 14.7 nm (SI14E, see Fig. 6.6), respectively. The results in Chapter 5 corroborated the lamellar morphology for SI21 (L_0 = 18.9 nm) and SI21E (L_0 = 19.1 nm). The order-disorder transition temperatures (T_{ODT}) of the precursors in Table 6.1 are estimated based on the abrupt change in linear elastic dynamic modulus (G′) measured on heating (Fig. 6.7).

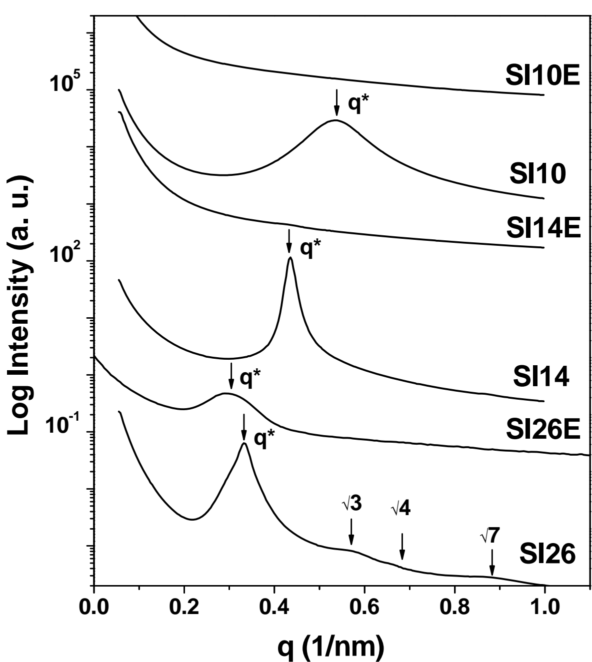

Figure 6.5 Small angle x-ray scattering (SAXS) obtained from SI26, SI26E, SI14, SI14E, SI10, and SI10E at room temperature. Arrows identify discernible Bragg reflections. Data except SI26 have been shifted vertically for clarity.

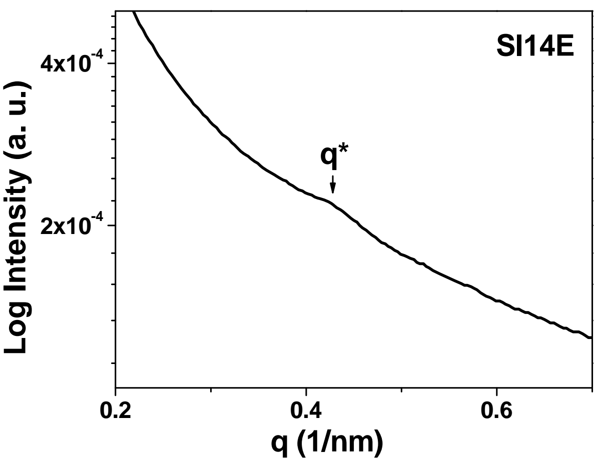

Figure 6.6 Magnified view of small angle x-ray scattering (SAXS) obtained from SI14E. The arrow identifies a broad "peak."

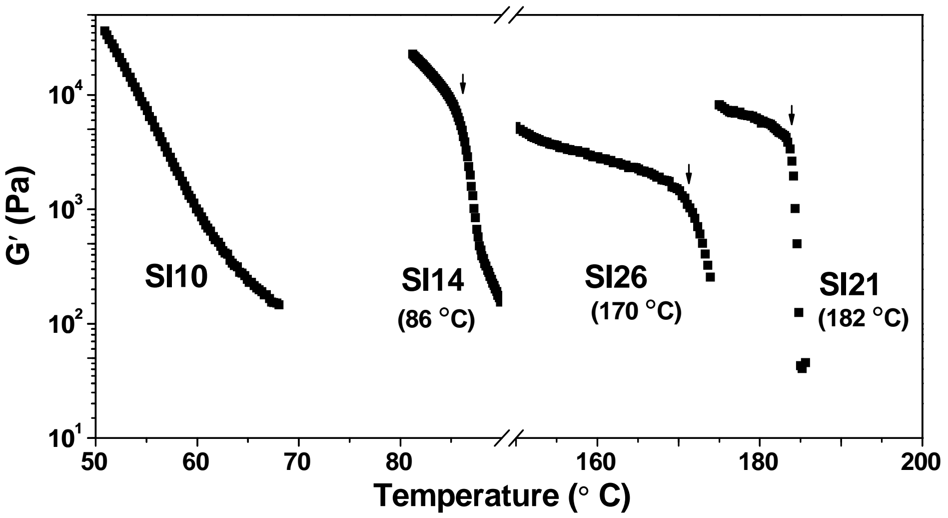

Figure 6.7 Temperature dependence of the dynamic elastic modulus G′(1 rad/sec) for SI26, SI21, SI14, and SI10 during heating (0.5 − 1 °C/min). Arrows indicate the order-disorder transition, signaled by an abrupt change in G′. Data for SI21 have been shifted upward for clarity ($G'_{shifted} = 50 \times G'$).

As a versatile method to characterize block copolymers near the transition,[311] rheological measurements have been conducted for SI14E. While the discrete change in G′ upon heating is less pronounced, it is estimated that $T_{ODT} \approx 91$ °C (Fig. 6.8). The moderate, not abrupt, change in G′ across $T = T_{ODT}$ may have arisen due to the proximity of the shear frequency to the critical frequency (ω_c'), below which the length scale corresponding to the block copolymer domains may be probed.[311]

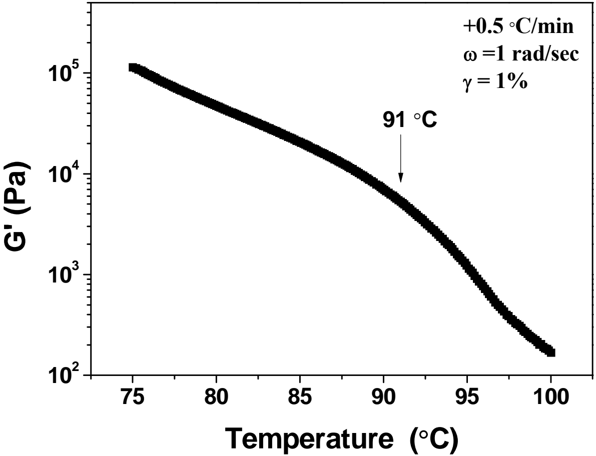

Figure 6.8 Temperature dependence of the dynamic elastic modulus G′(ω = 1 rad/sec) for SI14E on heating (+0.5 °C/min) with 1% strain.

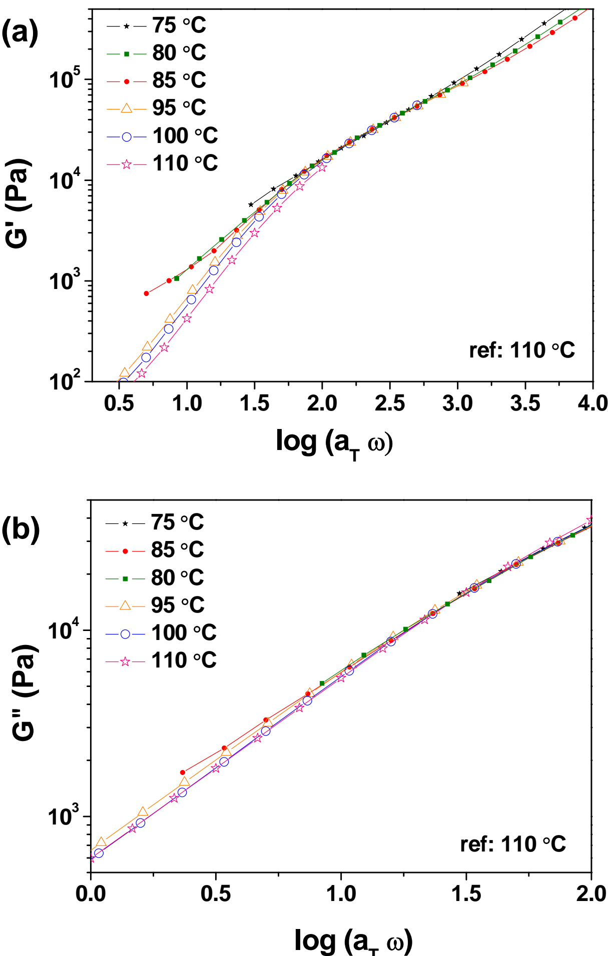

Figure 6.9 Reduced frequency (a_T ω) plot for (a) dynamic storage modulus (G′) and (b) loss modulus (G″) for SI14E. The shift factors are shown in Figure 6.10.

Time-temperature superposition has been applied to frequency sweep data obtained at various temperatures (T), and the master curves for G′ and G″ are shown in Figure 6.9. The shift factor a_T was fit using the Williams-Landel-Ferry (WLF) equation, resulting in C_1 = 7.6 and C_2 = 120 (Fig. 6.10). SI14E exhibits a terminal behavior in G′ at low

frequency for T > 95 °C ($G' \sim \omega^2$) while a non-terminal behavior is observed T < 85 °C ($G' \sim \omega^{1/2}$). This notable difference in the frequency sweep response between T < 85 °C and T > 95 °C confirms that T_{ODT} for SI14E would lie between 85 °C and 95 °C, in agreement with the earlier estimation ($T_{ODT} \approx 91$ °C). It is more difficult to discern the abrupt change in G″ with temperature variations, presumably due to the lower critical frequency for G″ (ω_c'').[311] Notably, G′ for SI14E does not collapse into one curve after the time-temperature superposition for T > 95 °C. The failure of the time-temperature superposition for disordered block copolymers has been attributed in the past to effects of thermal fluctuations.[311, 312]

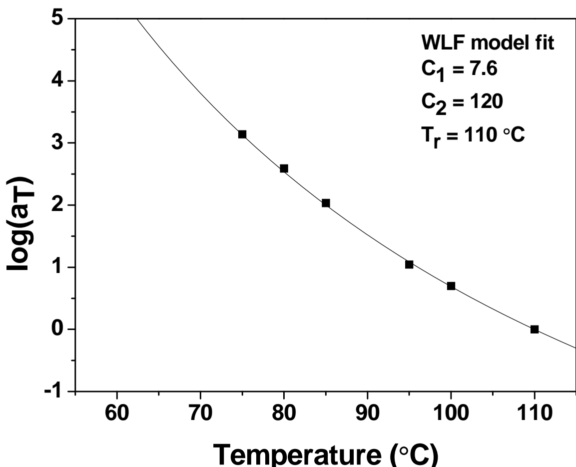

Figure 6.10 Logarithmic shift factors as a function of temperature for SI14E. The fit to Williams-Landel-Ferry (WLF) (solid line) leads to $C_1 = 7.6$ and $C_2 = 120$.

On the other hand, neither SI21E nor SI10E shows abrupt changes in G′ during heating, lacking any sign of the order-disorder transition (Figure 6.11a). While the frequency dependence of SI10E agrees with a disordered melt state, SI21E appears to be ordered

based on the non-terminal frequency dependence (Figure 6.11b). It is concluded from the data that T_{ODT}'s for SI21E and SI10E would lie above 160 °C and below 60 °C, respectively.

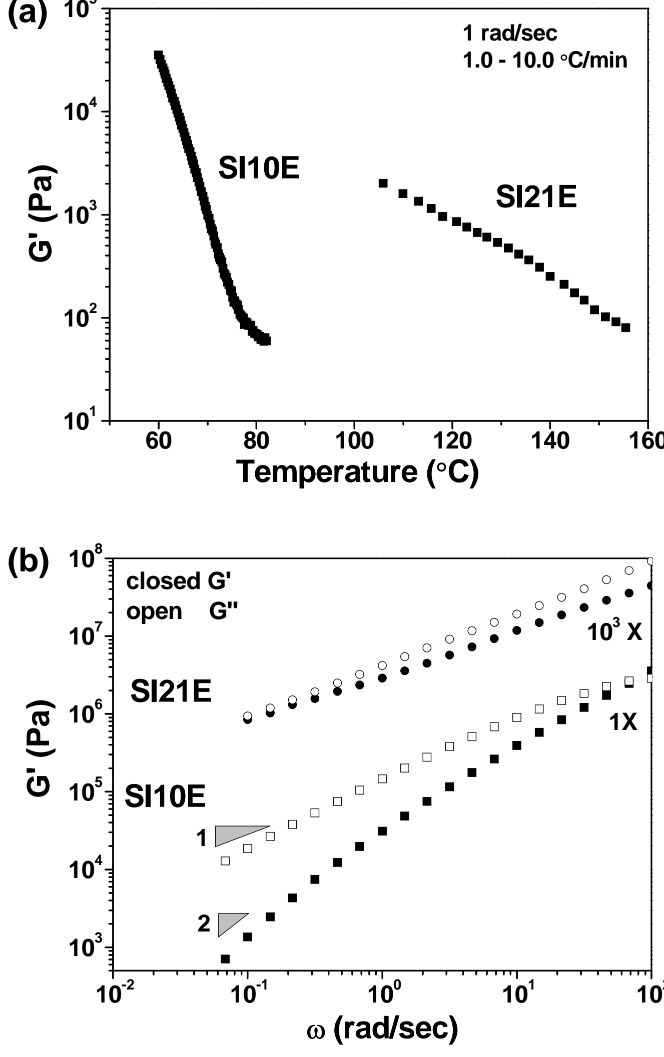

Figure 6.11 (a) Temperature dependence of G′(1 rad/sec) for SI10E and SI21E on heating (1.0 − 10 °C/min) with 1% strain. (b) Frequency (ω) dependence of G′ (closed symbols) and G″ (open symbols) for SI10E (at 60 °C) and SI21E (at 105 °C). In (b), data for SI21E have been shifted upward for clarity ($G_{shifted} = 10^3 \times G$).

The formation of a layered structure is observed for thin films of SI26, SI21, and SI14 poly(styrene-*b*-isoprene) diblock copolymer precursors, independent of variations in the compositions of underlying crosslinked mats. Figure 6.12 reveals representative SEM and AFM results that exhibit hole/island textures with step heights h ≈ 1 L_0. The formation of layered morphologies by thin-film block copolymers that form non-lamellar morphologies in bulk, as observed in the case of SI26, has been reported when a strong preferential interaction (*e.g.*, the lower surface energy of the poly(isoprene) block compared to the poly(styrene) block in SI26) is present at the interfaces.[265, 313] On the other hand, the thin films of SI10 above SMG mats dewetted when annealed at 80 °C for 3 hours (not shown).

Thin-film SI21E exhibits a morphology dependence on its film thickness and the chemistry of the underlying interface, analogous to the behavior observed in the past for PS-PMMA block copolymer thin films.[223, 254] Figure 6.13 shows the top-down SEM images of SI21E films with various film thicknesses ($\langle L \rangle / L_0$ = 1.5, 1.7, 1.9, 2.1, 2.3, 2.5) above the crosslinked mats of controlled compositions (SMG00, SMG28, SMG57, SMG76). Above SMG28 and SMG57, SI21E retains perpendicular lamellar structures for all the film thickness, suggestive of neutrality at both interfaces. The cross-sectional SEM measurement of the film ($\langle L \rangle / L_0$ = 2.5) indicates that the perpendicular ordering persists throughout the film thickness (Fig. 6.14). Above SMG00 and SMG76, SI21E exhibits either perpendicular or mixed lamellae depending on the film thickness. SMG00 induces perpendicular ordering near the half-integral L_0 thickness ($\langle L \rangle = (n + ½) L_0$, where n is an integer) while mixed lamellae (perpendicular + parallel)[256] are observed in the vicinity of the integral L_0 thickness ($\langle L \rangle = n L_0$). The thickness dependence of the morphologies switches for SI21E on SMG76; the mixed lamellae are observed for the

half-integral L_0 thickness and a crossover to perpendicular morphologies occurs at the integral L_0 thickness. Similar thickness dependence was reported previously for PS-PMMA above non-preferential and weakly preferential brushes.[223, 254] SMOH45, a hydroxyl-terminated brush that consists of 45 mol. % styrene units, also induces perpendicular ordering for SI21E (Fig. 6.15).

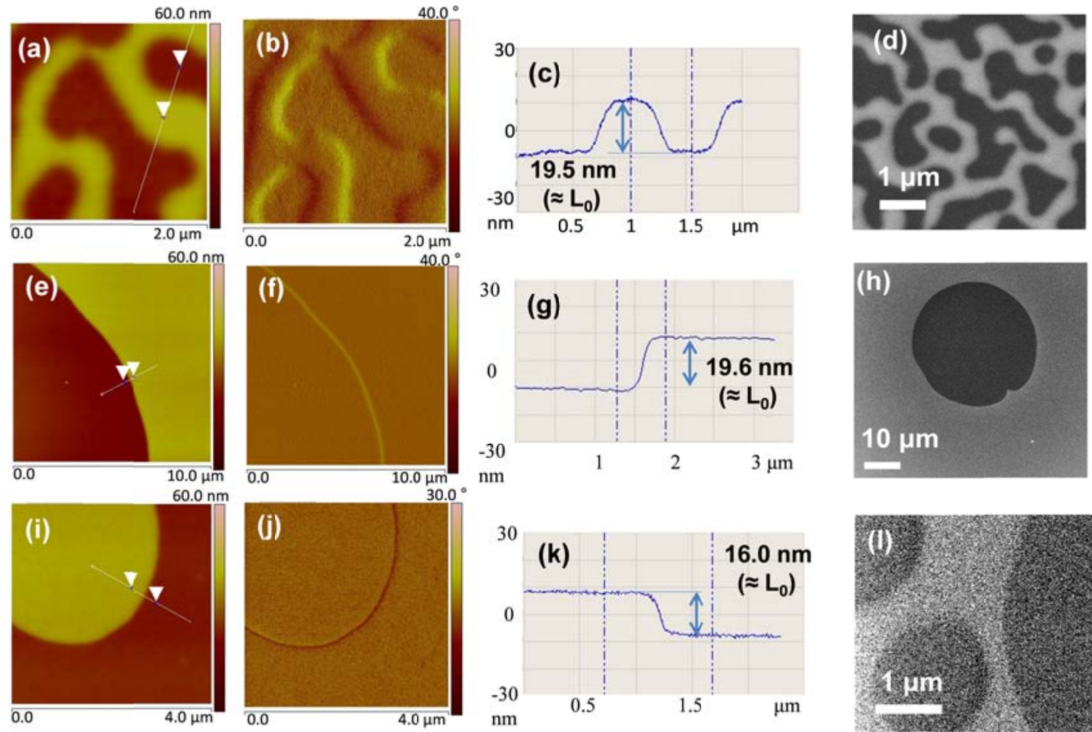

Figure 6.12 Top-down AFM height, phase, topographic profile, and SEM data of thin-film block copolymers above SMG94. (a-d) SI26 ($\langle L \rangle / L_0 = 1.0$, annealed at 105 °C/6h). (e-h) SI21 ($\langle L \rangle / L_0 = 2.3$, annealed at 105 °C/6h). (i-l) SI14 ($\langle L \rangle / L_0 = 2.3$, annealed at 80 °C/6h). The step heights are 19.5 nm, 19.6 nm, and 16.0 nm, respectively.

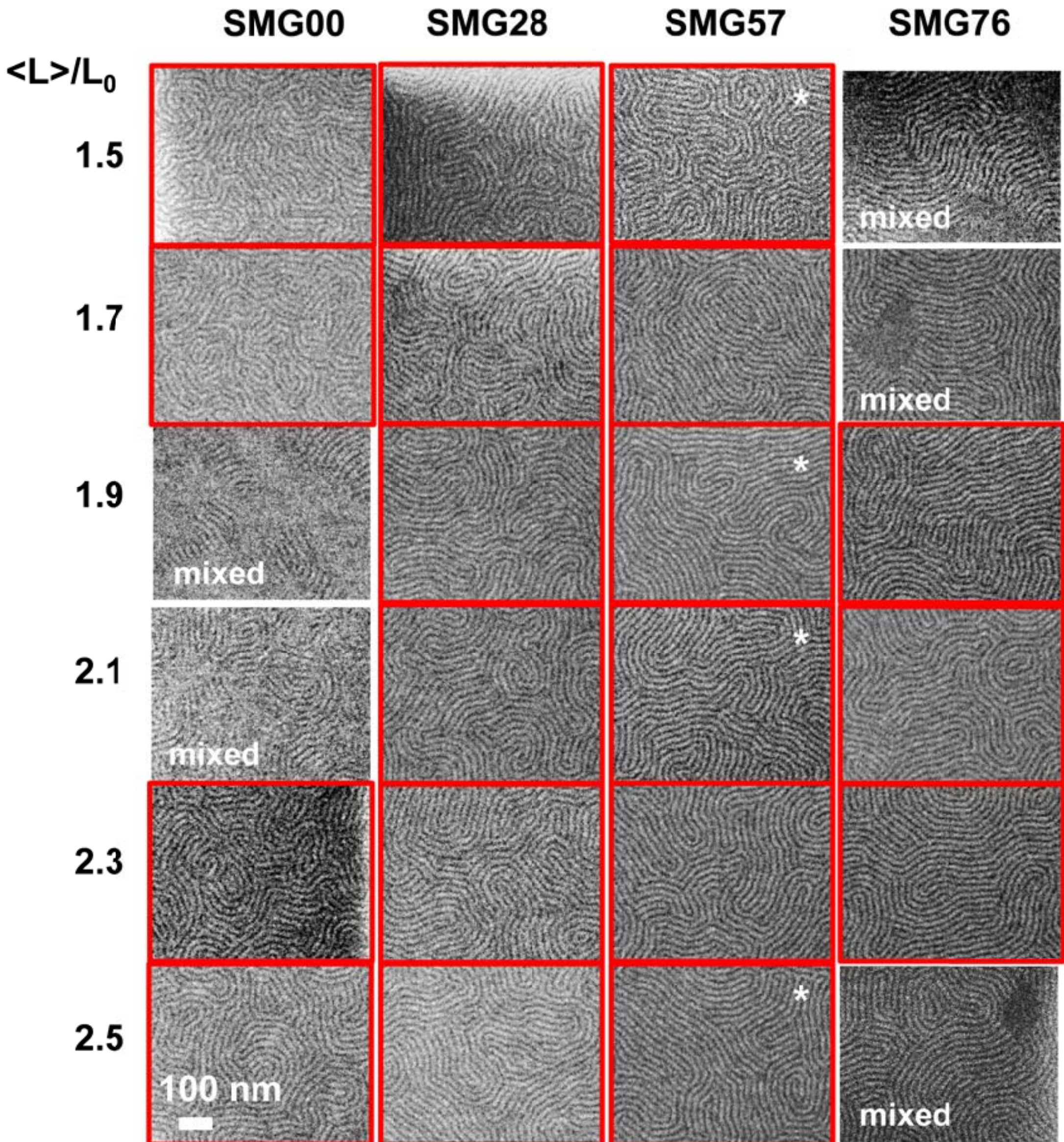

Figure 6.13 Top-down SEM images of SI21E annealed at 105 °C/6h while the film thickness (<L>) and the composition of the underlying mat are adjusted. ($\langle L\rangle/L_0$ = 1.5, 1.7, 1.9, 2.1, 2.3, 2.5) (SMG00, SMG28, SMG57, SMG76) Images with perpendicular ordering are highlighted while mixed lamellae are denoted as such. Refer to the scale bar at bottom left of the figure. Images with stars have been reproduced from Fig. 5.11 (Chapter 5).

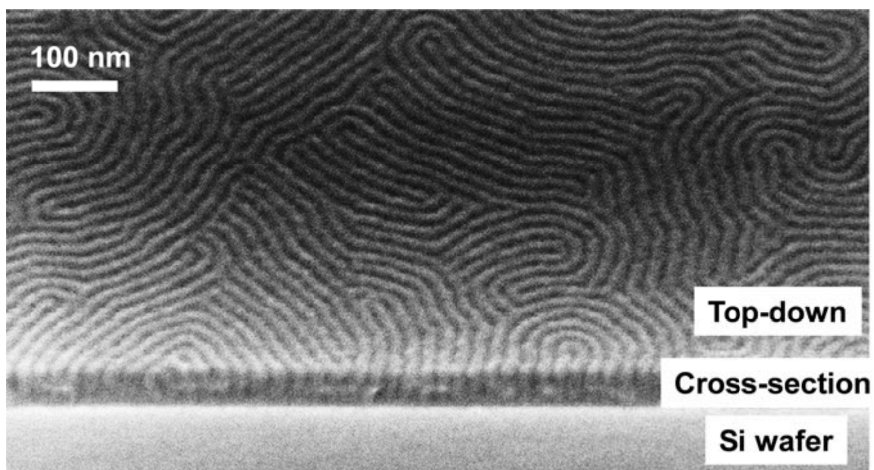

Figure 6.14 SEM image of the SI21E thin film ($\langle L \rangle / L_0 = 2.5$) on SMG57 taken at a tilt angle of 45 °.

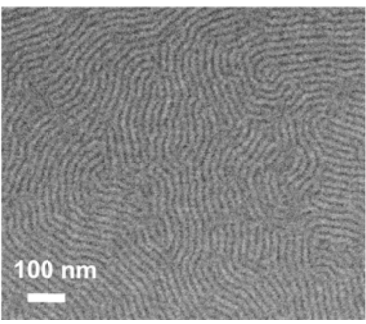

Figure 6.15 Top-down SEM image of thin-film SI21E ($\langle L \rangle / L_0 = 1.3$) on SMOH45.

Figure 6.16 reveals the change in effective orientation of the cylindrical morphology for thin-film SI26E as the interfacial interaction is adjusted by varying compositions in the underlying mat. While mostly parallel cylinders are observed for SI26E on SMG00 and SMG94, a larger fraction of perpendicular cylinders is observed above other mats, most notably SMG57. Comparison between top-down SEM images of

SI26E before and after a small degree of etching (Fig. 6.16d,e) shows the benefits of the etching process in terms of probing inner thin-film morphologies; while perpendicular cylinders are visible regardless of etching, parallel cylinders become clearly apparent after etching. Though the film thickness (<L>/L_0 = 0.9), employed for SI26E in Figure 6.16, has been found to promote perpendicular ordering,[314] a small degree of parallel cylinders is still noted for SI26E on SMG57 (Fig. 6.16c), apparently closest to being neutral. The relatively narrow window in the brush compositions that leads to the perpendicular ordering for a cylindrical morphology, with respect to a lamellar morphology, has been reported in the past.[120] The difference may be attributed to smaller penalty for forming parallel cylinders compared to parallel lamellae.

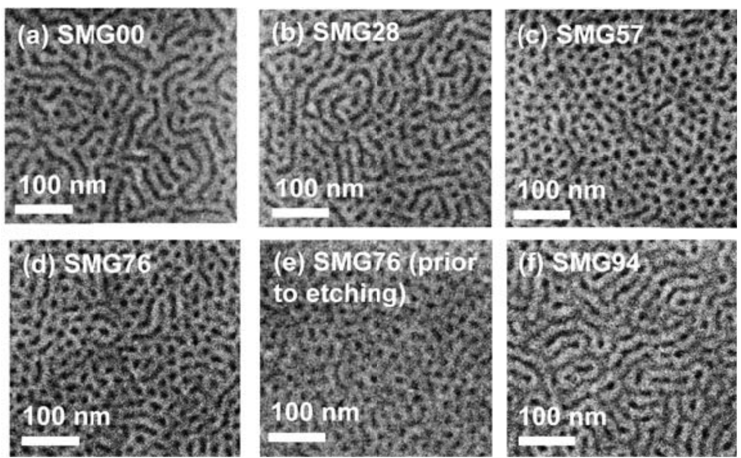

Figure 6.16 (a-f) Top-down SEM of thin-film SI26E (<L>/L_0 = 0.9) on the SMG crosslinkable mats with varying compositions. The thin films have been annealed at 122 °C/24h and etched slightly using oxygen plasma (except for panel (e)) prior to SEM measurement.

Efforts are currently made in finding suitable experimental conditions that lead to perpendicular ordering over a larger region by changing the mat compositions, the film thickness, the degree of epoxidation, and the annealing conditions. One of the preliminary results is shown in Figure 6.17, in which small changes in the mat composition (SMG60) and annealing conditions (140 °C/6h) have led to noticeable reduction in parallel cylinders in SI26E thin films. The periodicity of the cylinders in thin films is estimated to be 21.1 nm based on Fast Fourier Transform of the top-down SEM image, in close agreement with L_0 calculated from the bulk SAXS patterns (20.0 nm).

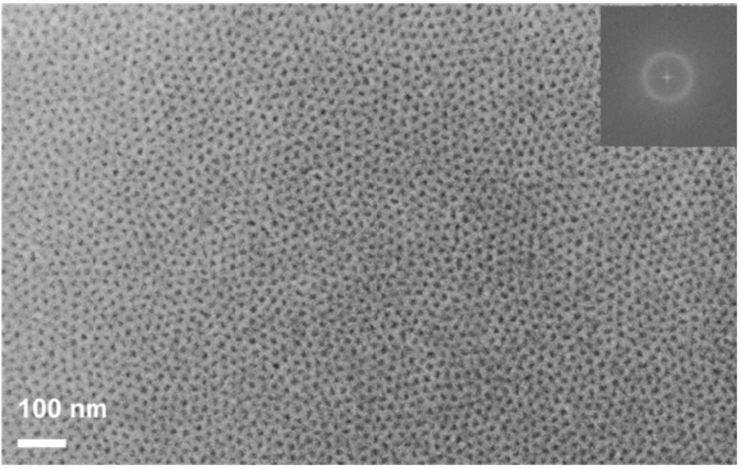

Figure 6.17 Top-down SEM image of the SI26E thin film (<L> = 0.9 L_0), annealed at 140 °C/6h, on SMG60. The inset shows its Fast Fourier Transform, used to estimate the periodicity of the thin-film perpendicular cylinders (21.1 nm). The film has been slightly etched with oxygen plasma for image contrast.

The effect of underlying mat compositions is also studied for SI14E thin films (<L>/L_0 = 1.7). The information gathered from the brush composition dependence of

SI21E and SI14E becomes invaluable later when these polymers are aligned using chemical patterns and appropriate compositions for backfill brushes ("background" regions") in the chemical patterns are chosen.[97] Top-down SEM images in Figure 6.18a-d exhibit fingerprint patterns for SI14E thin films above selected SMG mats (SMG00, SMG28, SMG57, SMG76). Considering higher molecular weight SI21E exhibits mixed lamellae on SMG00 and SMG76, the absence of mixed domains for SI14E may result from the molecular weight dependence of (1) entropic contributions that favor perpendicular ordering or (2) penalties for defect formations at mixed domain interfaces.[315] In comparison to SI21E, the greater difficulty involved in discriminating two domains of SI14E prior to oxygen etching in SEM measurements (Fig. 6.19) may be attributed to a larger degree of domain mixing. A shorter correlation length observed for SI14E above SMG00 and SMG76 (weakly preferential), in comparison to SMG28 and SMG57 (non-preferential), may be associated with the dependence of polymer mobility on interfacial interactions.[316] The cross-sectional SEM image of thin film SI14E on SMOH45, shown in Figure 6.20, indicates perpendicular ordering throughout the film thickness. AFM measurements show that SMG94, a preferential mat, induces hole/island structures with ½ L_0 step heights, accompanied by phase contrasts (Figure 6.18f-h). These features indicate both constituents of SI14E are exposed to the free surface and have previously been attributed to surface neutralization of thin-film block copolymers, as discussed in Chapter 5.

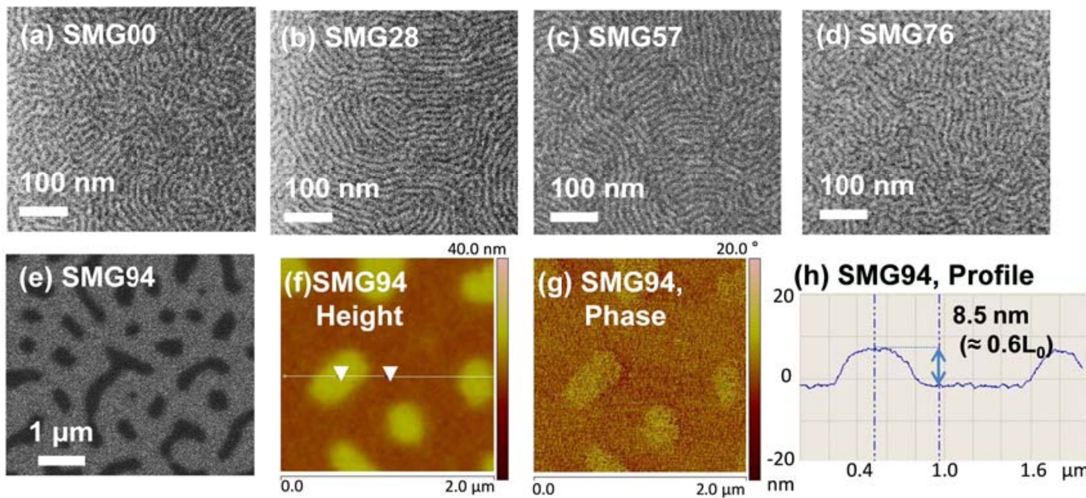

Figure 6.18 (a-e) Top-down SEM of thin-film SI14E (<L>/L_0 = 1.6 – 1.7) above SMG mats with varying compositions. (f-h) AFM height, phase, and topographic profile data of SI14E above SMG94 (<L>/L_0 = 1.6). The step height is equal to 8.5 nm (≈ 0.6 L_0). The films were annealed at 80 °C for 6 hours. For (a-d), SEM images were taken after a small degree of plasma etching.

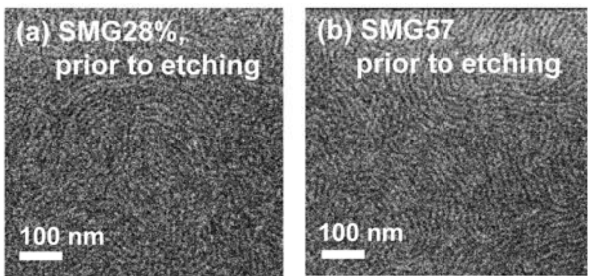

Figure 6.19 (a-b) Top-down SEM images of thin-film SI14E (<L>/L_0 = 1.6) (annealed at 80 °C for 6 h) above SMG28 and SMG57 mats prior to plasma etching.

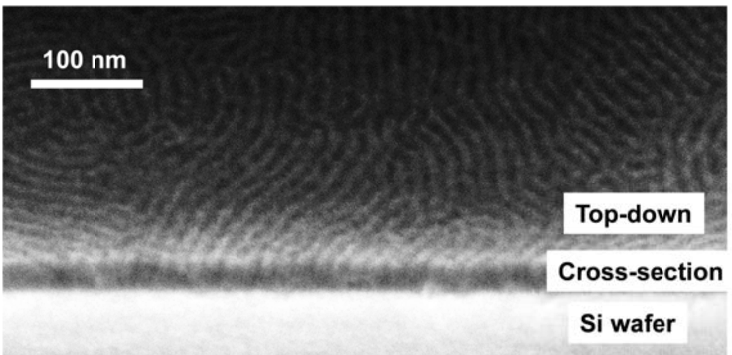

Figure 6.20 SEM image of thin-film SI14E (<L>/L_0 = 1.5) (80 °C/6h) on SMOH45 taken at a tilt angle of 45 °.

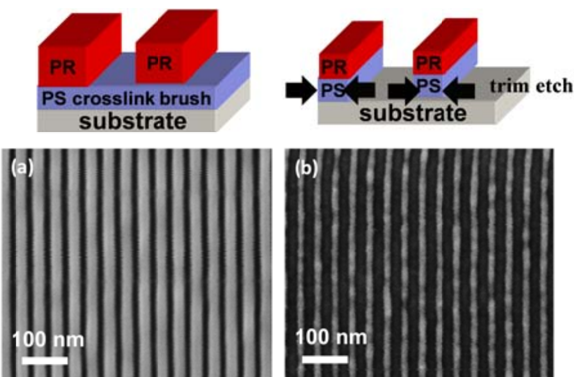

Figure 6.21 Top-down SEM image of (a) photoresist patterns after e-beam exposure and development and (b) trim-etched patterns (7 seconds etching). The pattern period is 38 nm. Corresponding schematic illustrations are shown above. The scale bars correspond to 100 nm.

The directed self-assembly of SI21E and SI14E are achieved using underlying chemical patterns, as implemented for PS-PMMA.[85] The stripe patterns of photoresists generated from the e-beam exposure and development (as received from Hitachi Global Storage Technologies) are shown in Figure 6.21a, and the sequential plasma treatment trim etches the stripes (Figure 6.21b). These patterns are used to align the thin-film

block copolymers after an appropriate background brush is grafted; SMOH25, which consists of 25 mole % of styrene, is used as the backfilling brush. Figure 6.22 shows the self-assembly of SI21E (L_0 = 19.1 nm) aligned using chemical patterns with a periodicity of 38 nm (≈ 2 L_0, "2X density multiplication").

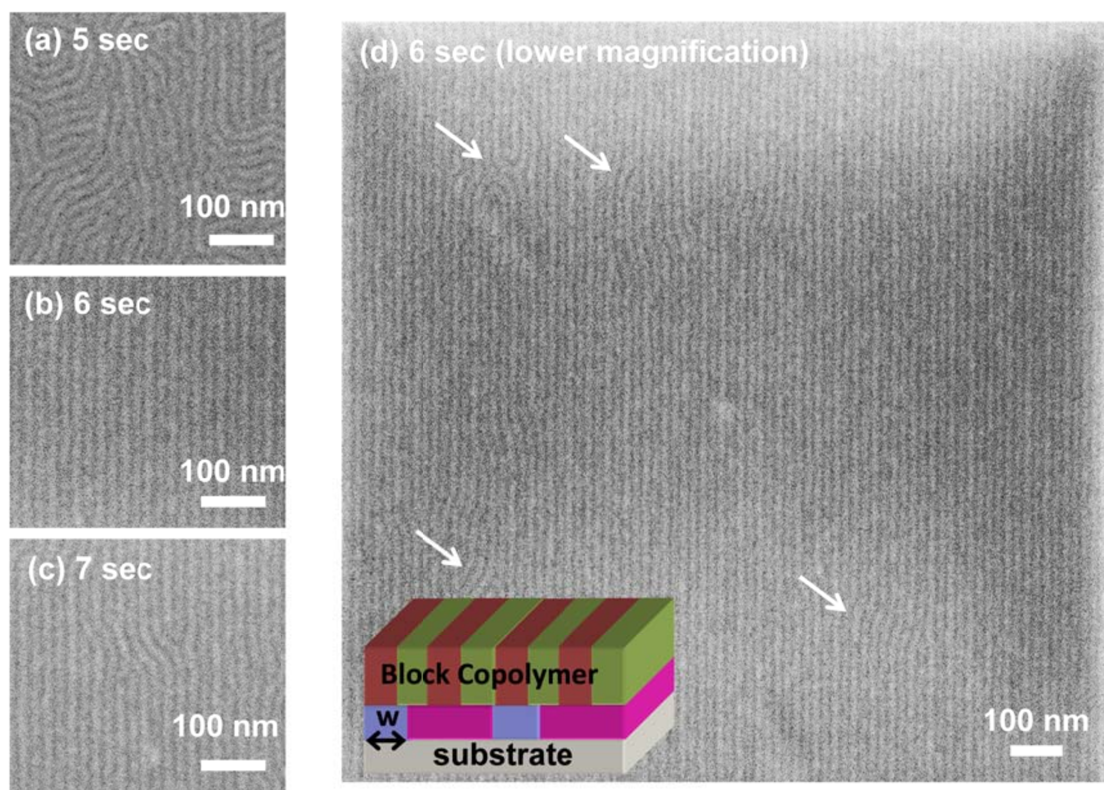

Figure 6.22 (a-c) Top-down SEM images of the directed self-assembly of SI21E ($\langle L \rangle / L_0$ = 1.5) above chemical patterns with a periodicity of 38 nm (≈ 2 L_o) as the width (w) of the SMG94 guiding stripe in the chemical patterns was varied by controlling trim etching duration (5 − 7 seconds). The panel (d) corresponds to a larger area scan of the thin film with 6 seconds of etching. The white arrows indicate the regions of incomplete alignment in (d). The schematic illustrates block copolymer thin films above chemical patterns. Scale bars correspond to 100 nm.

The width (w) of SMG94 guiding stripes, controlled by the extent of trim etching during the plasma treatment, has been found to affect the degree of alignment.[96] Figure 6.22a-c shows such dependence of the directed self-assembly on the plasma exposure time (5, 6, 7 seconds); the highest degree of alignment is observed for samples with 6 second trim etch. The signs of incomplete alignment, expressed as dislocations and other defects, are observed for the same sample over a larger region (Fig. 6.22d). A similar scheme has been implemented to attain the self-assembly of SI14E (L_0 = 14.7 nm) guided by chemical patterns with a periodicity of 44.1 nm (≈ 3 L_0, "3X density multiplication") (Fig. 6.23). Some minor defects are observed over the region of 0.7 μm × 1 μm.

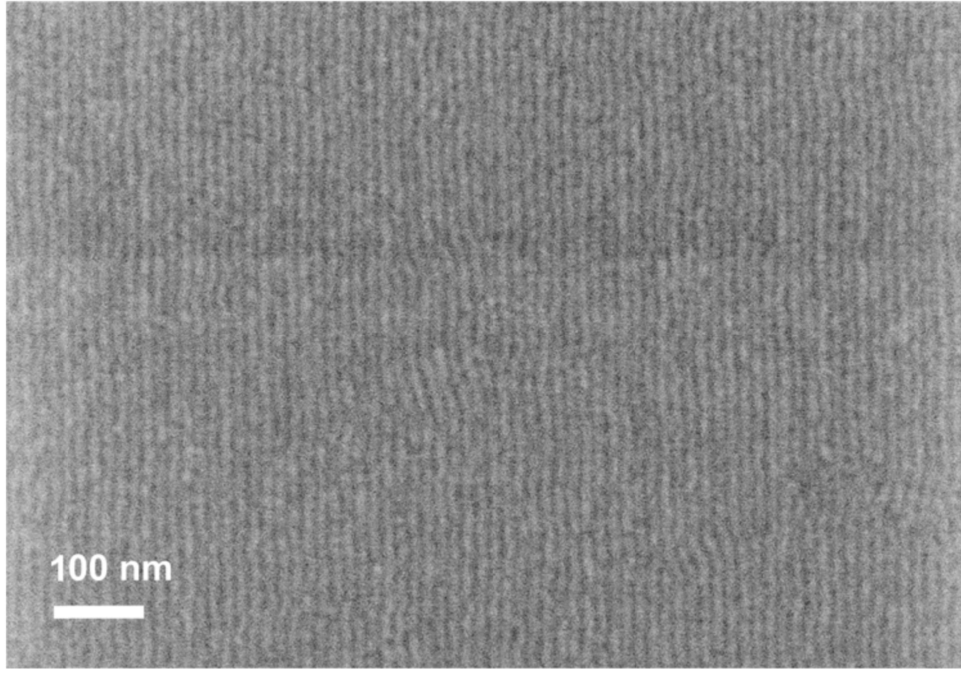

Figure 6.23 Top-down SEM image of SI14E ($\langle L \rangle / L_0$ = 2.0) aligned by underlying chemical patterns with a periodicity of 44.1 nm (≈ 3 L_o). Scale bars correspond to 100 nm. A small degree of plasma etching was implemented before SEM imaging.

Figure 6.24 shows top-down SEM images of SI14E as a function of annealing temperatures (T). For T = 70 °C and 80 °C ($T < T_{ODT}$), sizeable lamellar grains are observed (Fig. 6.24a,b). Even when T is raised to 100 °C and 120 °C ($T > T_{ODT}$), a large enough composition difference is retained such that the lamellar domains, characteristic of different constituents of the block copolymers, are visible (Fig. 6.24c,d). However, for $T > T_{ODT}$ the correlation length characterizing the lamellar domains in the samples almost diminishes, resulting in little grains. These patterns for $T > T_{ODT}$ resemble "fluctuation-induced disordered structures," previously observed in disordered bulk samples.[317]

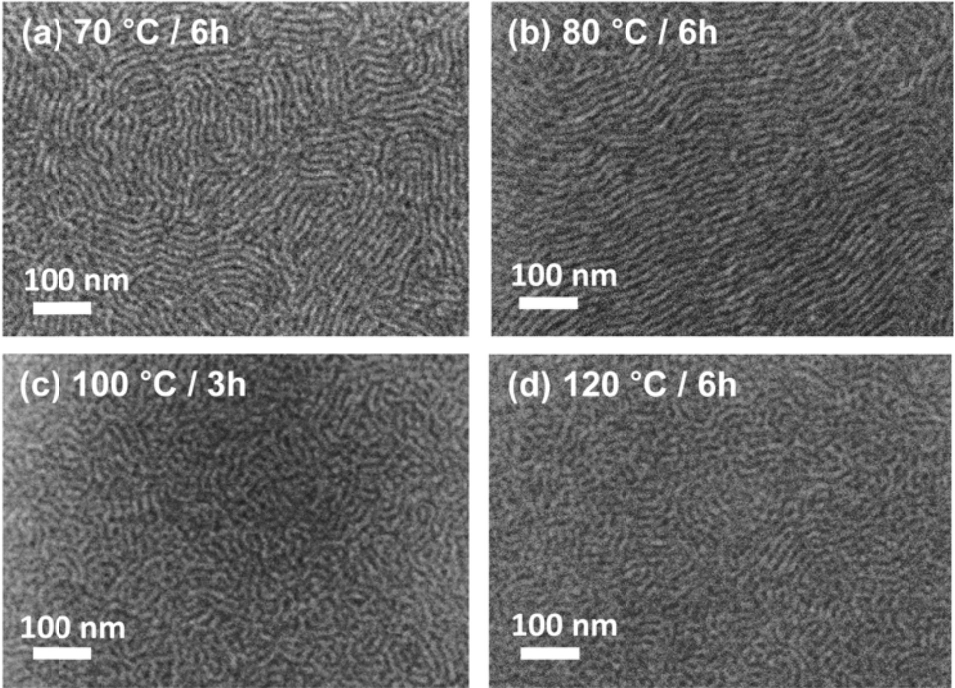

Figure 6.24 (a-d) Top-down SEM images of thin-film SI14E ($\langle L \rangle / L_0 = 0.8 - 1.5$) above SMOH45 with varying thermal annealing conditions. The SEM images were taken after a small degree of plasma etching. Scale bars correspond to 100 nm.

The cross-sectional SEM image of SI14E (<L> = 0.8 L_0) (Fig. 6.25) suggests that even at T > T_{ODT} the sample maintains perpendicular ordering throughout the film thickness. Though Alexander-Katz and Fredrickson[318] have predicted that a degree of composition fluctuations along the z-direction (normal to the film) would appear for thicker block copolymers near the ODT (<L> > 2 R_g), the efforts to take a cross-sectional SEM image for thicker films and to confirm the three-dimensional structure were unsuccessful.

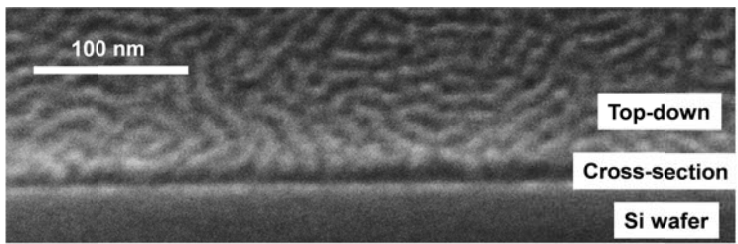

Figure 6.25 SEM image of thin-film SI14E (<L> = 0.8 L_0) on SMOH45 (100 °C/3h) taken at a tilt angle of 45 °.

On contrary to complex behaviors observed with other samples, top-down SEM images of SI10E thin films above non-preferential SMOH45 and SMG60 (Figure 6.26) exhibit featureless regions, lacking any domain contrast. A small degree of plasma etching did not reveal any new feature in this case. This behavior for SI10E is distinctly different compared to SI14E, which retains some degrees of contrast between lamellar domains even for T > T_{ODT} (Fig. 6.24).

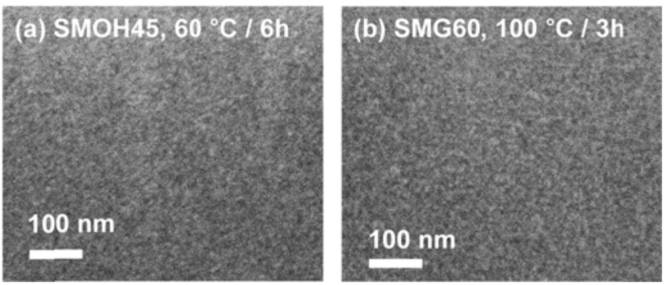

Figure 6.26 (a-b) Top-down SEM images of SI10E (<L> = 10 − 30 nm), annealed at various conditions (as indicated), on non-preferential interfaces (SMOH45, SMG60).

6.4 DISCUSSION

The characteristic behaviors of bulk block copolymers for different ranges of χN have been a topic of interest in the past. For low χN ($\ll 5$), the entropic contributions overwhelm the repulsive enthalpic interactions causing block copolymers to be disordered. This regime is described well by the mean field approximation and lies in the weak segregation regime.[3] In this limit, polymer chains act like unperturbed or only weakly perturbed Gaussian coils; $\delta = 1/2$ where $D \sim N^{\delta}$ (D and N are the length scale and the degree of polymerization, respectively). The terminology called the intermediate segregation regime has been generally used in order to describe behaviors that deviate from the weak and the strong segregation regimes. The exact χN value at the transition from the weak to the intermediate segregation regime also varies depending on the specific behavior of interest though the transition has been commonly suggested to occur at $\chi N \sim 10 - 15$.[319-321] As χN is raised across $\chi N \sim 6$, the coil conformation goes through a transition from being Gaussian to stretched, and the exponent δ changes from 0.5 to 0.8.[230] The mean field theory[3] predicts that the order-disorder transition occurs at χN = 10.5 while thermal fluctuation effects cause the transition to occur at higher χN.[4] The

intermediate segregation regime is characterized by rich and complex morphologies, such as gyroid (G)[322] and perforated lamellae (PL),[323] in addition to classical morphologies observed at high χN. The transition from the intermediate to the strong segregation regime has been suggested to occur at $\chi N \sim 29$, signaled by the change in δ from $\delta \approx 0.8 - 1.0$ to $\delta \approx 2/3$.[275, 324] Numerous groups confirmed both theoretically and experimentally the molecular weight dependence ($\delta \approx 2/3$) in the strong segregation limit.[6, 7] At high χN, the complex morphologies (*e.g.*, G and PL) become unstable[319] as a result of stronger packing frustrations that induce deviations from constant mean curvature of interfaces.[325]

The effective Flory-Huggins interaction parameter (χ_{eff}) for poly(styrene-*b*-isoprene) diblock copolymers with partial epoxidation has been estimated based on the SAXS and rheology results.[247] The χ_{eff} equation based on the rheology result (eq. 4 in the earlier work[247]) would predict T_{ODT} = 110 °C for SI14E, in close agreement with the experimental result shown here ($T_{ODT} \approx 91$ °C, Fig. 6.8). This equation is used to calculate the χN values for the symmetric systems (SI21E, SI14E, SI10E), as shown in Table 6.2. χN has been controlled mostly through adjustments in N as the range of annealing temperature was restricted in order to minimize degradation in the block copolymers. According to the estimated χN values, SI21E and, presumably, SI26E are expected to lie in the regime of moderate segregation strength ($\chi N > 12$). For the temperature range implemented experimentally, SI14E lies in the vicinity of the order-disorder transition (ODT) ($\chi N \approx 11$). While much commercial interest lies in attaining small features, as mentioned previously, SI14 and SI14E have been prepared specifically (1) to attain the smallest periodicity possible with the given system by approaching the limit of the ODT and (2) to find out the viability of the chemical modification method in controlling block copolymer orientations near the ODT. On the other hand, SI10E is

located within the disordered regime ($\chi N \approx 8$). The resemblance between the previous reports for PS-PMMA and our results for the moderate strength regime confirms that the same thermodynamic equilibrium is reached by the self-assembly of thin-film block copolymers independent of the random architecture. In turn, this conclusion allows us to generalize the results obtained for weaker segregation strength as universal characteristics applicable to other block copolymers.

Table 6.2 The χN estimations for SI21E, SI14E, and SI10E.

	N (ref. 144 Å^3)	Deg. Epox (%)	Annealing Temp. (°C)	χ_{eff} [a]	χ_{eff} N
SI21E	259	78	105	0.068	17.5
SI14E	158	78	80	0.074	11.7
SI14E	158	78	100	0.069	10.9
SI10E	111	80	100	0.072	8.0

[a] The equation 4 from the previous publication[247] was used.

Moderate Segregation Strength ($\chi N > 12$): The control of brush/mat compositions has proven effective in tuning the interfacial interactions with overlying thin films of block copolymers, thereby inducing different thin-film morphologies. The perpendicular lamella ordering independent of the film thickness for SI21E on SMG28 and SMG57 suggests both the air-polymer and the polymer-mat interfaces have been effectively neutralized.[253, 254] The perpendicular ordering of SI21E on SMOH45 corroborates that any composition between two neutral compositions in random

copolymer interfaces (mat or brush) also acts as a neutral composition. As the chemical composition of the underlying interface deviates from the neutral composition (*i.e.*, weakly preferential SMG00 and SMG76), SI21E exhibits mixed lamellae (perpendicular + parallel) for a certain range of the film thickness. These results are consistent with the observation of mixed morphologies above weakly preferential interfaces for PS-PMMA and poly(styrene-*b*-2-vinylpyridine) (PS-P2VP) block copolymers.[120, 257] When SMG00 induces perpendicular lamellae for a given film thickness in SI21E, SMG76 favors the formation of mixed lamellae for the same film thickness, and vice versa. This asymmetric relation, also previously reported for PS-PMMA,[223, 254] is believed to arise from the change in the preferential interaction of the mats with the block copolymer constituent. Cylinder-forming SI26E also responds to changes in the compositions of underlying mats and exhibits a gradual transition in the orientation of cylinders, as previously observed for PS-PMMA.[120] On the other hand, the SI21 and SI26 precursors, characterized by a notable surface energy difference between the components, form parallel structures independent of underlying mats. The perpendicular ordering for SI26E suggests that the method of partial chemical modification that permits control over the domain orientation is applicable to non-lamellar morphologies.

The fine control of a film thickness has been found as a viable method to induce perpendicular ordering above weakly preferential surfaces. The change in a film thickness has been known to induce different behaviors in thin-film block copolymers. Examples include the thickness dependence of morphologies and domain orientations,[326, 327] the incorporation of systematic thickness variations, or corrugations, to align block copolymer domains,[328, 329] and the critical thickness below which the disorder is induced.[55] Despite the diversity in the behaviors, the common origin behind the thickness dependence of thin-film block copolymer properties lies on the issue of

commensurability between the bulk microdomain periodicity and the finite dimensions of the film structures. Confinement of thin films has been used both theoretically and experimentally to investigate the effect of commensurability.[56, 253, 276, 277] Above SMG00 and SMG76, the SI21E thin film morphology alternates between perpendicular and mixed morphologies for every 1 L_0 change in the film thickness, resembling the behavior of PS-PMMA thin films on weakly preferential interfaces.[223, 254] Suh *et al.*[223] accounted for the total interfacial energies for each configuration and attributed the periodic change in the thin-film morphology to the incommensurability in the film thickness.

The self-assembly of SI21E and SI14E thin films have been guided using underlying chemical patterns that possess selective affinities to the constituents in the block copolymers. The implementation of block copolymer self-assembly to lithography processes in industries requires the ability to control precisely the registration of thin-film morphologies over a large region. Various methods previously implemented to align the domains of thin-film block copolymers include chemical patterns,[83] graphoepitaxy,[99] shearing,[48] and corrugation.[329] The scheme of chemical patterns involves the fabrication of underlying patterns that have selectively preferential interactions with block copolymers and has proven effective in achieving defect-free, directed self-assembly of PS-PMMA.[85] This methodology also allows the realization of essential layout geometries, required for integrated circuits, with block copolymer self-assembly in thin films.[92] In order to overcome the inherent limit in periodicities that can be realized using established semiconductor processing, the scheme of "density multiplication" has been devised to align thin-film block copolymers of small periodicities with chemical patterns of large periodicities.[94, 96] Despite the thermodynamic driving force exerted by the chemical patterns, misalignments arise

depending on a number of factors, such as the commensurability between the periodicities of chemical patterns and block copolymers,[83] the composition of the backfill brush,[88, 97] and the relative line width of chemical patterns.[89, 96] Despite the minor defects observed with SI21E and SI14E, attributable to those factors, the significant degree of alignment of these block copolymers seems to indicate that the scheme of chemical patterns is general enough to be applicable to block copolymers of various architectures. Considering how a disordered state is described by a random arrangement of domains, the directed self-assembly of SI14E, which is close to being disordered (χN = 11.7 at 80 °C), may be critically dependent upon the degree of interaction of the block copolymers with the chemical patterns. The preferential interaction of SMG94 guiding stripes with the poly(styrene) block of SI14E is expected to enhance the degree of "order" in the system, raising the effective χN.[225, 226]

The thin-film behaviors discussed so far indicate the resemblance between partially modified poly(styrene-*b*-isoprene) block copolymers and PS-PMMA. Such similitude suggests that the random architecture does not induce abnormal behaviors in thin-film thermodynamics compared to other plain block copolymers without random chemical modification. This does not hold true in the bulk state, leading to the decoupling phenomenon.[247] The common thermodynamic driving force in thin films allows facile implementations of the studies previously established for PS-PMMA to partially modified system; this has been demonstrated in this chapter with the directed self-assembly using the chemical patterns. More importantly, based on this analogue it is assumed that the random architecture in the block copolymers would not produce any measurable influence on the thermal fluctuations and the order-disorder transition in reduced dimensions, discussed below for weaker segregation strength.

Weak Segregation Strength ($\chi N < 12$): Fredrickson and Helfand[4] accounted for the effect of fluctuations on block copolymers near the order-disorder transition (ODT). Fluctuations induce the weakly first-order transition for symmetric block copolymers, suppressing the second-order transition predicted by the mean field theory.[330] While the mean field criterion for the ODT (*i.e.*, $(\chi N)_{ODT} = 10.5$)[3] is accurate for large molecular weight block copolymers, a more detailed expression incorporates the additional correction term 41.0 $\bar{N}^{-1/3}$, where $\bar{N} = N a^6 \upsilon^{-2}$ (*a* is the statistical segment length and υ is the segment volume). As a consequence, the ODT occurs at a higher χN value in comparison to the mean field prediction. Even for a disordered sample ($\chi N < (\chi N)_{ODT}$), the composition difference without long-ranged translational and orientation order persists significantly until χN becomes trivial. The existence of composition fluctuations in vicinity of the ODT has been investigated using scattering and rheology. The presence of such structures in a specimen is coupled to its mechanical properties, and the failure of time-temperature superposition in the dynamic modulus (G' and G'') of a disordered melt ($T > T_{ODT}$) at a low shear frequency regime ($\omega < \omega_c$) has been attributed to the fluctuations.[311, 312] With the presence of fluctuations, the ODT is accompanied by a discrete change in the scattering intensity and a continuous variation in the principle Bragg reflection q*.[311, 312, 331, 332] There were a few studies that claimed imaging of fluctuations in bulk samples.[317]

While reduction in dimension (*i.e.*, bulk → thin film) is anticipated to enhance the effect of fluctuations in systems,[333] fluctuations in 2-dimensional block copolymers near the ODT have received little attention in the past. The thin-film confinement has non-trivial effects on various aspects of materials that include phase transformations in metal alloys,[334] phase formations in liquid crystals,[335] sphere packing in block copolymers,[336] coarsening in polymer blends,[27] and macromolecular properties (*e.g.*,

glass transition, chain conformation, and rheology).[19, 21, 337] However, the effect of 2-dimensional confinement on polymers tends to be obscured by interfacial interactions that impose strong fields and dictate the behaviors of the systems. For example, the spinodal decomposition in thin polymer blend films bound by preferential interface is characterized by anisotropic composition waves and slower coarsening of the phases compared to the bulk.[25] Preferential interactions by neighboring interfaces induce order in thin-film block copolymers even at temperature above bulk T_{ODT}.[281, 338] Therefore, the study on the influence of reduced dimensionality requires characterization with neutral boundaries.

High χ exhibited by partially epoxidized poly(styrene-*b*-isoprene) block copolymers leads to stronger fluctuation effects near the ODT while the surface neutralization attained as a result of the random modification allows one to observe fluctuation effects in thin films. In the previous study,[247] the change in the effective χ, estimated from SAXS and T_{ODT} data, was monitored as a function of the degree of partial epoxidation on the system. As a result, $\chi_{eff} = 0.074$ for 78% epoxidation at 80 °C (Table 6.2), in comparison to $\chi = 0.036$ for PS-PMMA at T = 230 °C.[339] The higher value of χ implies stronger fluctuation effects as a result of smaller N near the ODT. Indeed, the rheology data in Figure 6.9 strongly suggest that the fluctuation is present in bulk SI14E. Reduced dimensionality has been known to favor fluctuations that destroy order, as evidenced by Peierls instability in one dimension. Accordingly, the characterization of SI14E thin-film morphology for $T > T_{ODT}$ (Fig. 6.24c-d) matches the earlier description for fluctuation pervaded structures (*i.e.*, sinusoidal fluctuations with random orientations and phases).[312] Based on rheology and scattering experiments, Rosedale *et al.*[311] proposed the possible composition profiles of block copolymer melts as a function of χN. In correspondence to their illustrations in bulk (Fig. 16 in the

reference[311]), top-down SEM images of the partially epoxidized poly(styrene-*b*-isoprene) block copolymer thin films have been assembled in Figure 6.27 for various χN.

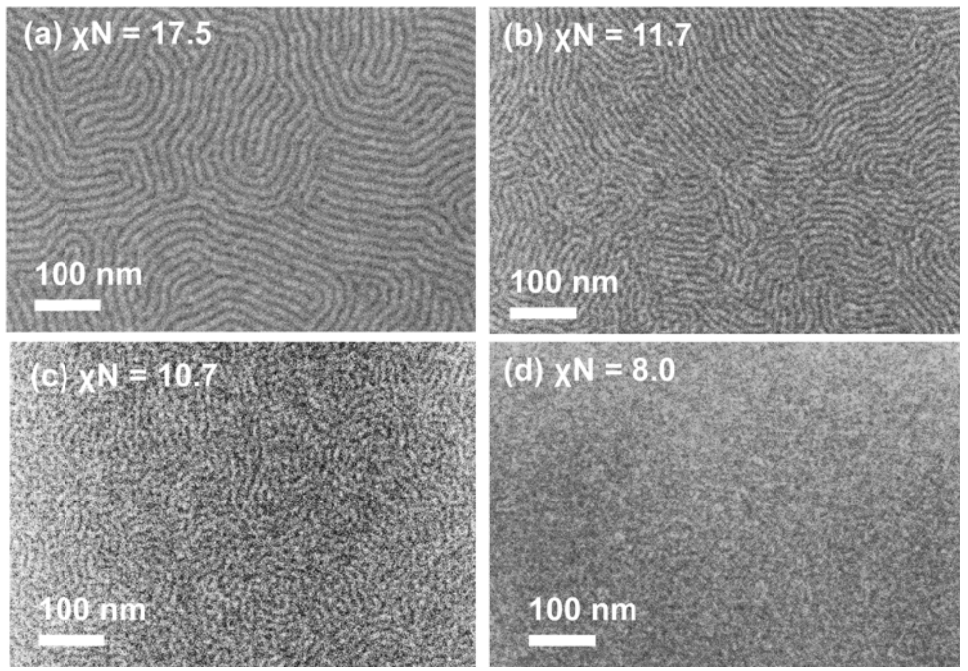

Figure 6.27 Top-down SEM images of (a) SI21E, (b-c) SI14E, and (d) SI10E thin films ($\langle L \rangle / L_0 = 1.7 - 2.0$) on non-preferential mats (SMG28, SMG57) with estimated χN as denoted.

The shift in the critical temperature of a phase separation as a result of dimensionality reduction has been suggested for both polymeric and non-polymeric materials.[340-342] Previous studies on polymer blend thin films have reported the deviation in the cloud point from the bulk value with decreasing the film thickness ($\Delta T_{cloud} \sim 10 - 60$ °C).[29, 30] Similarly, it has been suggested $(\chi N)_{ODT}$ of diblock copolymer films, confined by neutral interfaces, increases rapidly as the film thickness becomes

comparable to R_g, the radius of gyration, which in turn leads to a change in T_{ODT}.[318, 343] Ryu and his coworkers[344] also found using GISAXS that T_{ODT} of PS-PMMA thin films bound by neutral interfaces may be lower than the bulk value by as much as a few tens of degrees depending on the film thickness. Hammond *et al*.[345] associated with the ODT the nematic-isotropic transition of aligned cylinders in thin films and found that the transition temperature for monolayer is ~ 25 °C lower than the bulk T_{ODT}. While the bulk T_{ODT} is estimated to be 91 °C for SI14E, the thermal treatment of SI14E thin films at 80 °C has been implemented to attain sizeable grains of lamellar domains (Fig. 6.24b) and to achieve alignment using underlying chemical patterns (Fig. 6.23). The thin-film morphologies characterized as composition fluctuations were obtained upon thermal annealing at 100 °C (Fig. 6.24c), and this suggests that the thin-film T_{ODT} lies between 80 °C and 100 °C. Considering the earlier studies showing the influence of the confinement on the phase separation temperature, it is notable that in the case of SI14E the bulk and the thin-film T_{ODT} values coincide within ±10 °C. In order to gain more accurate assessment of the T_{ODT} shift in reduced dimensions for SI14E, the grain size may be monitored as the thin-film annealing temperature is carefully controlled.

In conclusion, the partially epoxidized poly(styrene-*b*-isoprene) block copolymers, characterized as a surface-neutralized system, have been investigated for a various range of segregation strength (χN). For high χN, the system exhibits the dependence of the thin-film morphology on the film thickness and the underlying interfacial interactions. The resemblance in the thin-film behaviors to poly(styrene-*b*-methyl methacrylate) (PS-PMMA) block copolymers suggests that the thin-film thermodynamic behavior of block copolymers is dictated by the same guiding principle independent of the incorporation of the random architecture. This is different compared to the bulk behaviors of partially modified systems reported in the past. Perpendicular

ordering observed for non-lamellar morphologies also implies the generality of the "partial modification" scheme in controlling the interaction at the free surface. The directed self-assembly of the block copolymers has been demonstrated for multiple lamellar periodicities using underlying chemical patterns, a well-established method previously implemented for aligning PS-PMMA. In the vicinity of the ODT (lower χN), the partially modified system exhibits fluctuation effects in both bulk and thin films, presumably due to stronger χ. It is believed that the surface neutrality of the system enabled the direct observation of fluctuation pervaded structures in thin films. On the other hand, the system with lowest χN, disordered in the bulk, did not show any composition contrast in thin films. The change in the thin-film block copolymer behaviors with a χN variation, based on the real space observation, agree qualitatively with the earlier prediction for bulk.

Chapter 7 Self-Assembly of ABC Triblock Copolymers in Thin Films[4]

* This work has been conducted in collaboration with the Nealey group and the de Pablo group at the University of Wisconsin − Madison.

7.1 INTRODUCTION

Block copolymer self-assembly in thin films has received much attention due to its ability to fabricate periodic patterns in thin films. One potential application is in the lithographic process employed in the semiconductor industry. Among various thin-film block copolymer systems, poly(styrene-*b*-methyl methacrylate) (PS-PMMA) block copolymers have been studied most thoroughly. PS-PMMA is characterized by (1) comparable surface energies of the poly(styrene) (PS) block and the poly(methyl methacrylate) (PMMA) block and (2) the capability to wet-etch the PMMA block selectively. The first feature allows one to achieve a perpendicular morphology in the block copolymer thin films, a technologically more useful orientation. While there is an incessant effort to attain resolution enhancement, the smallest feature achievable with PS-PMMA lies around 20 – 25 nm.[95, 238] This limit arises from the order-disorder transition; diblock copolymers become disordered for $\chi N < 10.5$ (mean field limit),[3] where χ and N denote the interaction parameter and the degree of polymerization of the block copolymers, respectively. New block copolymer systems that exhibit smaller periodicities while retaining the characteristic features of PS-PMMA would be desirable.

Underlying chemical patterns have been successfully implemented to guide the self-assembly of PS-PMMA.[85] However, advanced optical lithography techniques had to be implemented in order to fabricate chemical patterns whose periodicity was comparable to the block copolymer domain sizes. Figure 7.1a illustrates that the smallest

4 Refer to Acknowledgements for contributions made by other people.

feature (d) attainable for lamellae-forming diblock copolymers is restricted to be approximately half the chemical pattern periodicity (L_s). In this case, there is no benefit of replacing optical lithography with the self-assembly of block copolymers in terms of resolution enhancement. One method to cope with the limitation is *density multiplication*, which allows chemical patterns with large periodicities to guide the self-assembly of thin-film block copolymers of small periodicities.[94]

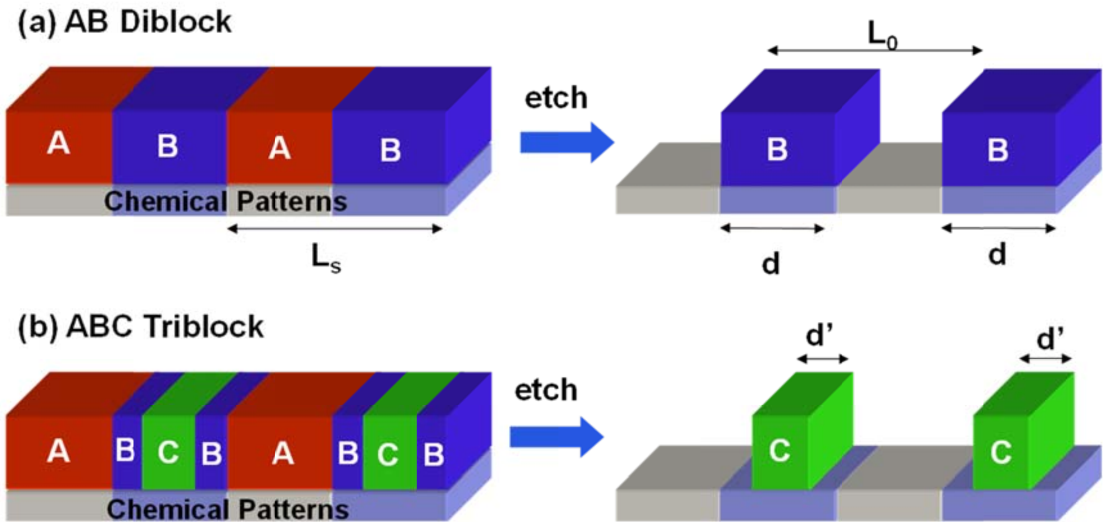

Figure 7.1 Schematic illustrations on directed self-assembly of AB diblock copolymers and ABC triblock copolymers. Selective etching leaves features of size d and d', respectively. L_0 and L_s denote the bulk lamellar periodicity of block copolymers and the pitch of underlying chemical patterns, respectively.

Theoretically, the triblock copolymer architecture offers an alternative solution to both issues, mentioned in the previous paragraphs, for PS-PMMA diblock copolymers. While a "parameter space" refers to the degrees of freedom that can be

varied to control properties of systems, triblock copolymers exhibit a larger parameter space compared to diblock copolymers. As a result, the domain size may be varied to a greater extent in triblock copolymers while retaining a same morphology. Figure 7.1b shows how the variation in the volume fractions allows one to control the feature size (d') independent of the chemical pattern size (L_S) in triblock copolymers. In addition, the interaction parameters of the middle block with respect to the end blocks may be arbitrarily controlled by an appropriate choice of the chemistry. The large interaction parameters between the middle block and the end blocks in triblock copolymers may potentially reduce the smallest feature size attainable by increasing the effective interaction parameter in the systems.

In this chapter, lamella-forming poly(styrene-*b*-isoprene-*b*-methyl methacrylate) (SIM) triblock copolymers are studied. There are several reasons behind the choice of this triblock copolymer system. First, since more complex behavior is anticipated for triblock copolymers compared to diblock copolymers, addition of one new block to the existing PS-PMMA is expected to minimize the complications and allows one to take advantage of previous results obtained for PS-PMMA. Second, it has been suggested that the middle block with a lower surface energy, compared to the end blocks, induce perpendicular ordering of thin-film triblock copolymers.[346] The poly(isoprene) (PI) homopolymers exhibits a lower surface energy (≈ 31 mJ/m^2)[347] compared to PS and PMMA homopolymers (≈ 40 – 41 mJ/m^2).[116, 347] This difference is expected to aid in attaining the perpendicular ordering in thin-film triblock copolymers, the primary target for the lithographic application. Third, the interaction parameters of the middle block with the end blocks are larger than the interaction parameter between the end blocks ($\chi_{PS\text{-}PI} \approx \chi_{PI\text{-}PMMA} > \chi_{PS\text{-}PMMA}$). Based on the previous reports, $\chi_{PS\text{-}PI} = 0.072$ (at 180 °C),[2] $\chi_{PI\text{-}PMMA} = 0.077$ (at 22 °C),[348] and $\chi_{PS\text{-}PMMA} = 0.028$ (at 180 °C).[349] Finally, the anionic

polymerization of poly(styrene-*b*-isoprene) diblock copolymers is well established and offers the versatility of adding either block after another without restriction on the sequence, enabling $(SI)_nM$ multiblock terpolymers.

In this study, three SIM triblock copolymers are prepared with different volume fractions of the PI block (f_{PI} = 0.03, 0.18, 0.28) while exhibiting relatively constant volume fractions of the PMMA block ($f_{PMMA} \approx 0.45$) and retaining a narrow range of microdomain periodicities ($L_0 \approx 33 - 49$ nm). Only two bulk specimens with large PI volume fractions (f_{PI} = 0.18, 0.28) form three phase lamellae, as corroborated from the bulk characterization. They exhibit different behavior in thin films; while one sample (f_{PI} = 0.18) exhibits a perpendicular lamellar morphology, another (f_{PI} = 0.28) shows a complex morphology that presumably incorporates capped chain conformations. This difference is explained in terms of the competition between the energetic driving force to segregate the middle block to the free surface and the entropic contributions that penalize such capped conformations.

7.2 EXPERIMENTAL METHODS

Bulk synthesis and characterization: Poly(styrene-*b*-isoprene-*b*-methyl methacrylate) (SIM) triblock copolymers were synthesized using anionic polymerization, as described in Chapter 3 of this dissertation. The controlled epoxidation of the block copolymer samples was achieved using dimethyl dioxirane (refer to the section 3.1.3 of Chapter 3).[127] Two size exclusion chromatography (SEC) instruments were used to characterize the polymer samples: (1) Hewlett-Packard 1100 HPLC, HP 1047A refractive index detector, poly(divinylbenzene) columns (Gel Organic columns, Jordi), chloroform mobile phase and (2) Viscotek VE2001, 302-050 Tetra Detector Array, tetrahydrofuran mobile phase. The volume fractions of the samples and the

degrees of epoxidation were determined using proton nuclear magnetic resonance (^{1}H-NMR) (VAC-300 Autosampler, IBM instruments). Differential scanning calorimetry (DSC) (Q1000 DSC, TA Instruments) was used to determine thermal transitions of the polymer samples while scanning at the ramping rate of ± 10 °C/min. Small angle x-ray scattering (SAXS) was measured at Argonne National Laboratory after the samples had been thermally annealed at 170 °C for 7 – 8 hours. Thin sections (80 – 120 nm thickness) of block copolymers were prepared using cryo-microtoming (Leica EM UC6). These specimens were exposed to vapors of staining agents (OsO_4 or RuO_4) for 5 – 10 minutes in order to provide imaging contrast. Transmission electron micrographs (JEOL 1210 and FEI Tecnai G2 F30) were employed to establish bulk morphologies.

Mat/brush synthesis and preparation: Both crosslinkable mat and grafting brush materials have been synthesized using nitroxide-mediated living free radical polymerization (NMP).[120] The crosslinkable material, denoted as SMG*xx* (*xx*: mol. % of styrene), is a random copolymer that consists of styrene, methyl methacrylate, and glycidyl methacrylate (GMA). The solutions (0.2 wt. %, toluene) were spin-coated on Si wafers (as received) to produce uniform thin films. Then, the mat was generated by thermal annealing at 180 °C for 24 hours, allowing 4 – 6 mol. % of GMA to undergo a crosslinking reaction. On the other hand, the poly(styrene-*ran*-methyl methacrylate) random copolymers with the hydroxyl functionality at the ends are represented by SMOH*yy*, where *yy* stands for mol. % of styrene. The materials grafted to Si wafers (as received) and formed a brush during thermal annealing treatment (180 °C / 24 hours). The unreacted materials were removed by rinsing in toluene.

Thin film preparation and characterization: Thin-film SIM triblock copolymers were prepared by spin-coating solutions (1.0 wt. %, toluene) above crosslinkable mats or grafted brushes. Then, the thin films were thermally annealed in vacuum at 160 – 180 °C

for 24 hours, well above the glass transition temperatures of SIM. Scanning electron microscopy (SEM) (LEO 1550-VP FESEM) was used to investigate the thin-film morphologies. In certain occasions, the poly(methyl methacrylate) block (PMMA) has been selectively removed from the thin-film SIM triblock copolymers using the typical development method; the thin films were exposed to extreme ultraviolet (EUV) light sources (300 mJ/cm^2) followed by rinsing in a mixed solution (3:1 v/v) of isopropyl alcohol (IPA) and methyl isobutyl ketone (MIBK). The chemical patterns were fabricated using the EUV system, as described in Chapter 3 of this dissertation. While the guiding stripe in the chemical patterns was composed of SMG94, SMOH43 and SMOH50 were used as the background brush materials. Chemical patterns with the 2X density multiplication ($L_s = 2\ L_0$) were used to direct the self-assembly of thin-film SIM triblock copolymers.

7.3 Results and Discussion

The effect of the poly(isoprene) (PI) middle block, characterized by a significantly lower surface energy, on the thin-film morphology of poly(styrene-*b*-isoprene-*b*-methyl methacrylate) (SIM) triblock copolymers was investigated by varying the PI volume fraction. Table 7.1 shows the molecular characterization of SIM triblock copolymers synthesized. The samples are denoted as SIM*zz*, where *zz* represents the volume fractions (%) of the PI block.

Table 7.1 Molecular characterization of poly(styrene-*b*-isoprene-*b*-methyl methacrylate) (SIM) triblock copolymers. f, M_n, PDI, and L_0 denote the volume fraction, the molecular weight, the polydispersity index, and the bulk periodicity.

	f_{PS} [a]	f_{PI} [a]	f_{PMMA} [a]	M_n (kg/mol)	PDI	L_0 (nm)
SIM03	0.51	0.03	0.46	63.0 [c]	1.04	32.7
SIM18 [d]	0.41	0.18	0.41	56.0 [c]	1.07	42.5
SIM28	0.27	0.28	0.45	65.2 [b]	1.12	48.7

[a] The following densities of poly(styrene), poly(isoprene), and poly(methyl methacrylate) at 140 °C were used to calculate the volume fractions: (PS) 0.969 g/cm^3; (PI) 0.830 g/cm^3; (PMMA) 1.13 g/cm^3. Taken from the Ph.D. dissertation of J. Chatterjee (Univ. Minnesota).

[b] The SEC measurement of the poly(styrene) block aliquots gave the result of 17.2 kg/mol. M_n was calculated by comparing the molecular weight of the poly(styrene) aliquot with the weight fractions, estimated from the NMR measurement.

[c] Measured in SEC with eluted SIM relative to poly(styrene) standards.

[d] For the synthesis, diethyl zinc was used instead of lithium chloride.

Figure 7.2 illustrates the ^{1}H-NMR spectra SIM18. While the peaks at 6.5 and 7.1 ppm are associated with PS, those located at 5.1 and 4.7 ppm correspond to signals from the 1,4-addition and other additions (1,2- and 3,4-additions) of PI, respectively. PMMA generates the characteristic peak located at 3.6 ppm.

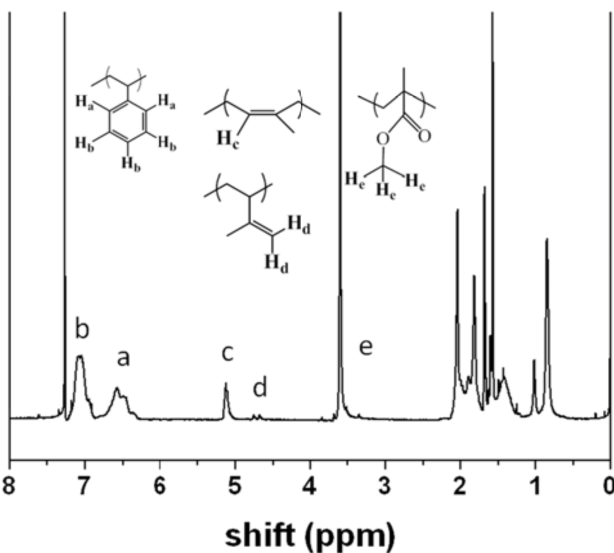

Figure 7.2 ^{1}H-NMR spectra of SIM18.

Figures 7.3 – 7.5 illustrate the SEC traces of the SIM samples. Despite the purification of tetrahydrofuran (THF), early termination of living anions at the introduction of tetrahydrofuran during the synthesis resulted in a fair amount of poly(styrene-*b*-isoprene) diblock copolymers (SI). All the samples after synthesis were cleaned in cyclohexane in order to selectively remove the diblock copolymers. Figure 7.3 compares the SEC traces of SIM03 before and after the cyclohexane rinsing (SEC #1, chloroform). The rinsing effectively removed the lower molecular weight peak, which originated from the SI diblock copolymers. Table 7.1 and other results presented herein reflect only the characterization of triblock copolymers after the cleaning. Figures 7.4 and 7.5 show the SEC traces of SIM18 and SIM28 triblock copolymers before and after thermal treatment (SEC #2, THF). The monodisperse, narrow peaks are retained,

suggestive of minimal side-reactions upon thermal treatments implemented later in the thin-film study.

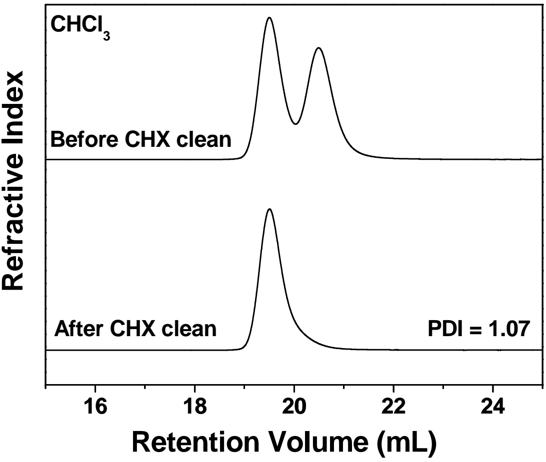

Figure 7.3 SEC traces of SIM03 before and after rinsing in cyclohexane.

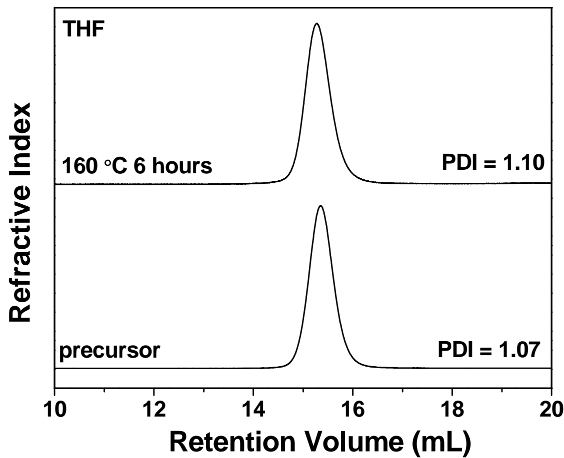

Figure 7.4 SEC traces of SIM18 prior to and after thermal annealing at 160 °C for 6 hours.

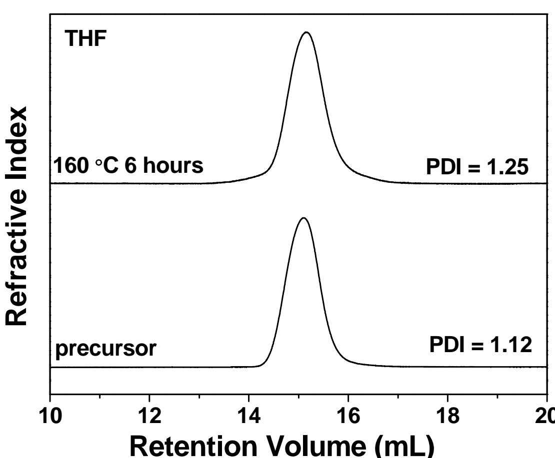

Figure 7.5 SEC traces of SIM28 prior to and after thermal annealing at 160 °C for 6 hours.

SAXS has been employed to determine the bulk morphologies and the corresponding periodicities of the SIM triblock copolymers. Figures 7.6 – 7.8 illustrate SAXS patterns for SIM03, SIM18, and SIM28. All the samples exhibit peaks at integer multiples of the primary peak positions (q*), suggestive of lamellar morphologies. The lamellar periodicities, calculated from the primary peak positions ($L_0 = 2\pi / q^*$), lie in the narrow range from 32.7 nm to 48.7 nm and are listed in Table 7.1.

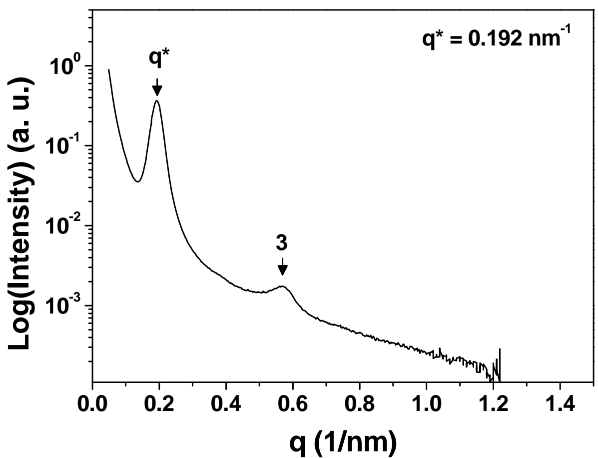

Figure 7.6 SAXS of SIM03 taken at room temperature.

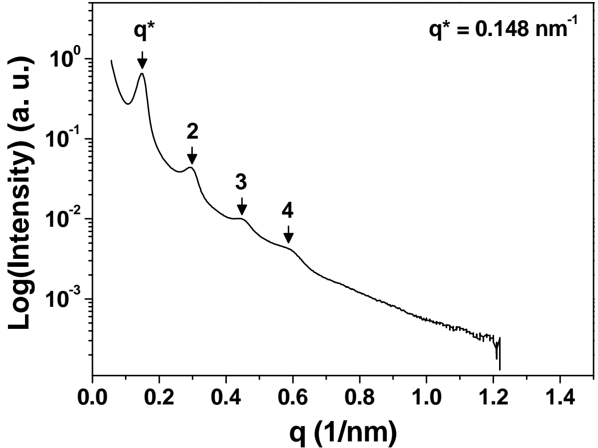

Figure 7.7 SAXS of SIM18 taken at room temperature.

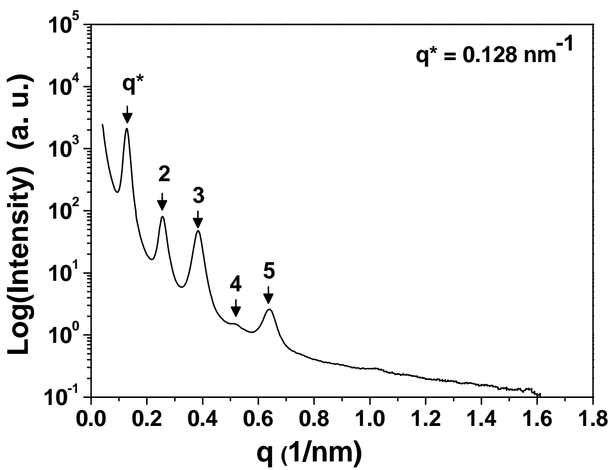

Figure 7.8 SAXS of SIM28 taken at room temperature.

DSC traces may be used to distinguish two phase vs. three phase lamellae in triblock copolymers. Control over the feature size independent of the chemical pattern periodicity, mentioned previously (Fig. 7.1b) as one of potential benefits for implementing triblock copolymers in thin films, requires the microphase segregation into three distinct domains. However, it is non-trivial to determine the number of lamellar domains (two vs. three) using SAXS. On the other hand, DSC detects glass transitions associated with each domain and provides complementary information about the number of domains in the SIM triblock copolymers. Figures 7.9 – 7.11 show the DSC traces and the temperature derivatives of the heat flow for SIM03, SIM18, and SIM28. SIM03 exhibits only two thermal transitions, as shown by the DSC trace and the temperature derivative (Fig. 7.9). Two peaks distinctly observed in the temperature derivative of the heat flow are consistent with the typical glass transitions associated with PS and PMMA blocks. The absence of any transition for the PI domain, generally observed at T ≈ -60 °C, is not surprising considering the small volume fraction (3 %) of

the PI block. These results suggest that SIM03 consists of two lamellar domains. On the other hand, both SIM18 and SIM28, which comprise of larger volume fractions of the PI block, exhibit three thermal transitions, as shown by Figures 7.10 − 7.11. These results suggest that SIM18 and SIM28 form lamellar morphologies with three domains.

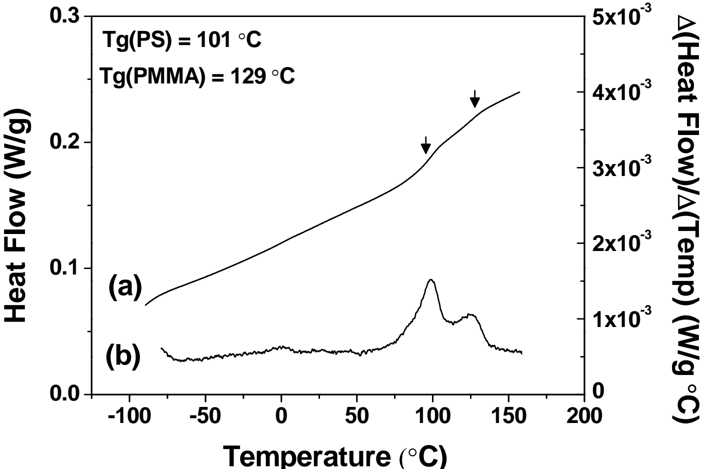

Figure 7.9 (a) DSC trace of SIM03 and (b) its derivative (Δ(Heat Flow)/Δ(Temp.)). T_g stands for the glass transition temperature for each domain.

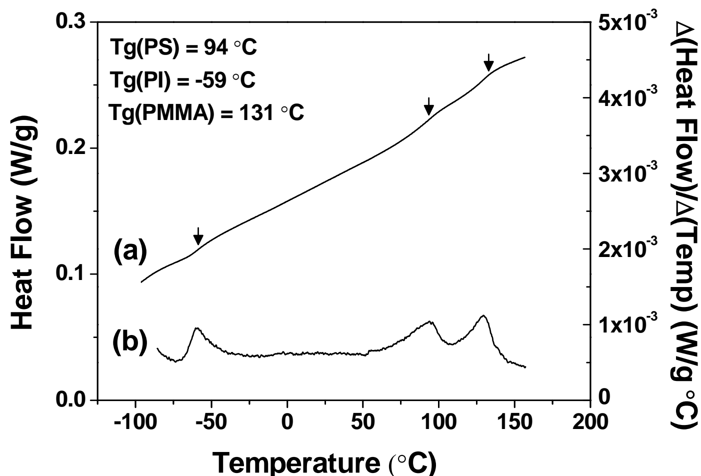

Figure 7.10 (a) DSC trace of SIM18 and (b) its derivative (Δ(Heat Flow)/Δ(Temp.)). T_g stands for the glass transition temperature for each domain.

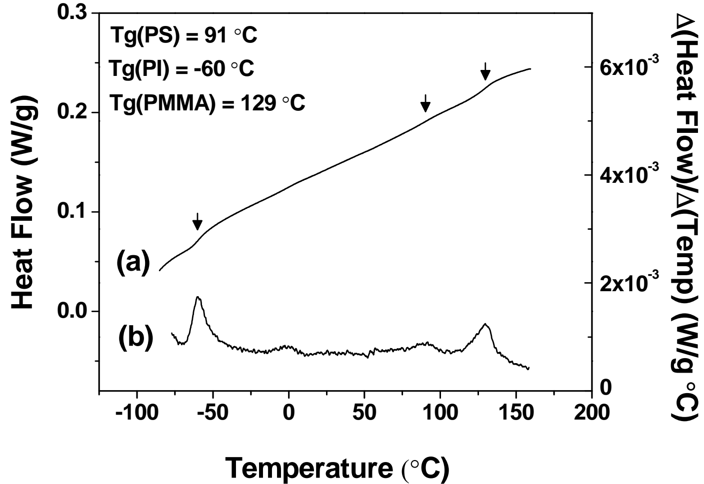

Figure 7.11 (a) DSC trace of SIM28 and (b) its derivative (Δ(Heat Flow)/Δ(Temp.)). T_g stands for the glass transition temperature.

TEM has been implemented for SIM18 and SIM28 in order to establish the bulk morphology. Figure 7.12a illustrates the representative TEM micrograph of SIM18, consistent with the lamellar morphology as estimated from the SAXS results. As the OsO_4 vapor stains PI domains selectively, the dark stripes in the micrograph confirm the presence of segregated PI domains in SIM18. The proposed schematic (Fig. 7.12b) portrays PI domains as dark and both PS and PMMA regions as white. Complementary information may be gathered from the TEM micrograph of SIM18, stained with RuO_4 (Fig. 7.13a). In this case, both PI and PS regions are stained during the exposure to the RuO_4 vapor. Notably, three distinct regions are observed for selected regions (enclosed by a white circle) in the micrograph; PI, PS, and PMMA regions are expected to correspond to dark, gray, and white domains, respectively (Fig. 7.13b). The contrast in the TEM micrograph (Fig. 7.14a) observed for SIM28 (OsO_4 staining) also corroborates the presence of PI domains in the lamellar morphology.

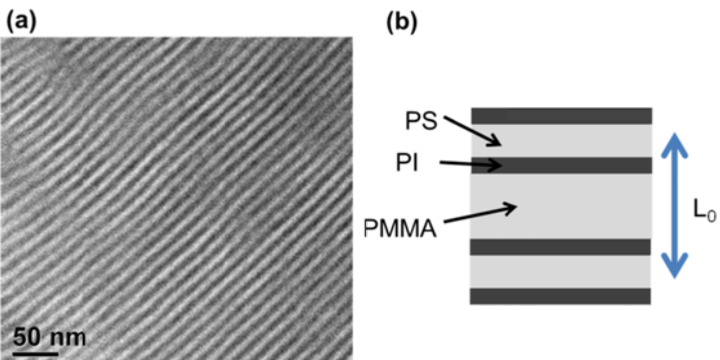

Figure 7.12 (a) TEM image of SIM18. Stained with OsO_4 for 5 minutes. (b) Corresponding schematic illustrating PI domains (dark) and PS and PMMA domains (white). L_0 denotes the lamellar periodicity. Courtesy of Hanseung Lee.

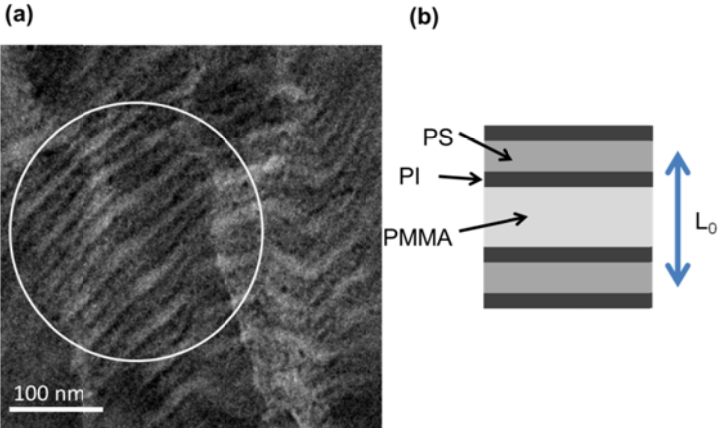

Figure 7.13 (a) TEM image of SIM18. Stained with RuO_4 for 5 minutes. (b) Corresponding schematic illustrating PI (dark), PS (gray), and PMMA domains (white). L_0 denotes the lamellar periodicity.

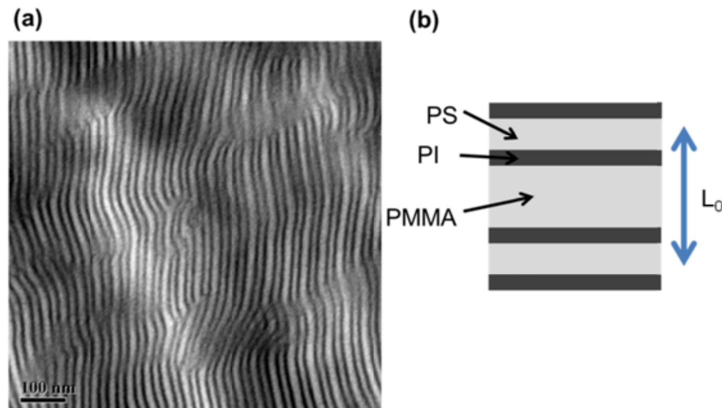

Figure 7.14 (a) TEM micrograph of SIM28. Stained with OsO_4 for 5 minutes. (b) Corresponding schematic identifying PI domains (dark) and PS and PMMA domains (white). L_0 denotes the lamellar periodicity.

Thin film morphologies have been investigated for SIM18 and SIM28, which form three phase lamellae in bulk. It is assumed that these triblock copolymers maintain three distinct domains in the thin-film state. Figure 7.15a exhibits top-down SEM images of thin-film SIM18 (average film thickness $\langle L \rangle = 0.8\ L_0$) above SMOH50. Fingerprint patterns are observed, suggestive of perpendicular lamellar morphologies. The same expression at the top-surface is retained even after the selective removal of the PMMA block (Fig. 7.15b). The directed self-assembly of SIM18 was achieved using underlying chemical patterns, as illustrated in Figure 7.16.

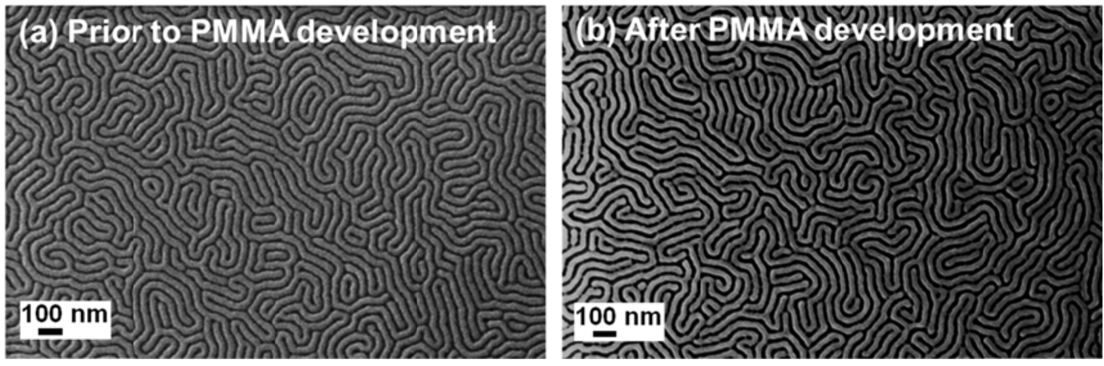

Figure 7.15 Top-down SEM images of thin-film SIM18 ($\langle L \rangle / L_0 = 0.8$) above SMOH50: (a) prior to and (b) after PMMA development. The thin films were thermally annealed for 178 °C for 24 hours.

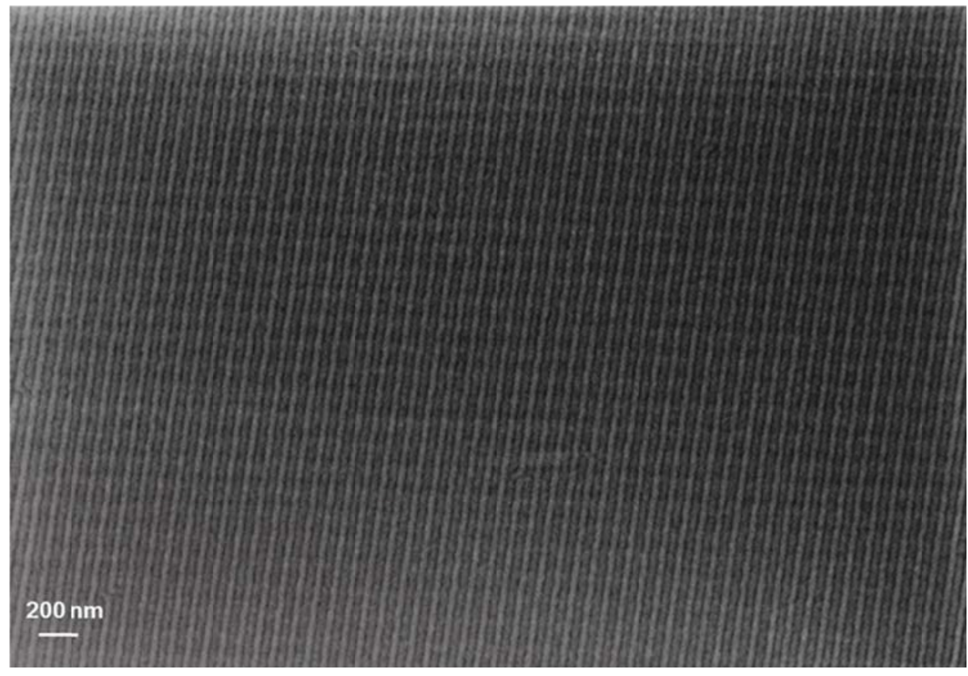

Figure 7.16 Top-down SEM image of self-assembly of SIM18 triblock copolymers, guided by chemical patterns. The periodicity of chemical pattern (L_s) is approximately 2 L_0, where L_0 denotes the lamellar periodicity of SIM18 ("2X density multiplication"). Courtesy of Paulina Rincon.

SIM28 exhibits completely different behavior, as shown in Figure 7.17. The SIM28 thin films consist of three distinct regions: R1 (complex), R2 (featureless), and R3 (perpendicular ordering) (Fig. 7.17a). The PMMA domains have been selectively removed in order to gain structural information about R1 and R2 regions. Figure 7.17b exhibits a top-down SEM image after the PMMA domain etching. Assuming that the etching process has not introduced artifacts to the structures, R1 appears to be a disordered structure. On the other hand, the interior of the R2 region is characterized by micellar structures without any indication of the length scale L_0. The proposed schematic illustration for the region R2 is shown in Figure 7.18; the free surface is wet by the PI

middle block, and the PMMA block constitutes the cores of the micellar structures surrounded by the PS matrix. The triblock copolymer chains are "looped" as illustrated in Figure 7.18.

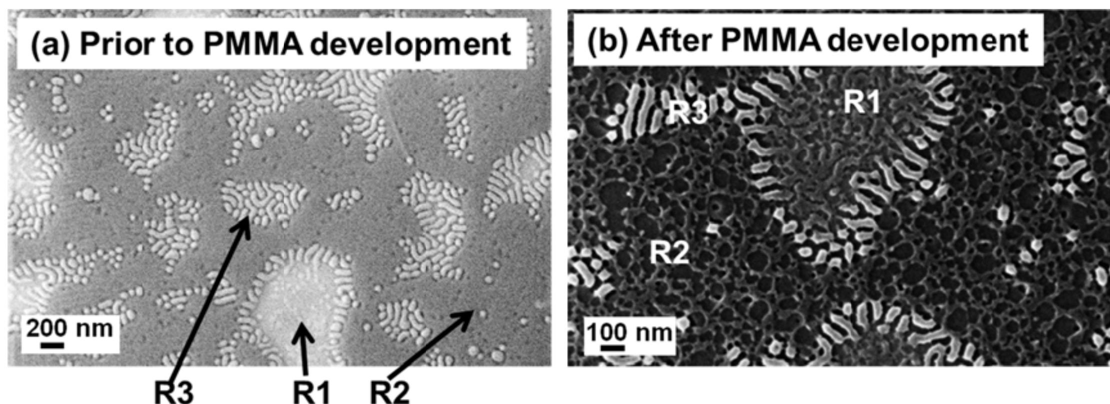

Figure 7.17 Top-down SEM images of thin-film SIM28 (<L>/L_0 = 0.8) above SMG60: (a) prior to and (b) after PMMA development. The thin films were thermally annealed for 160 °C for 24 hours. R1 – R3 refer to different characteristic regions in the micrographs.

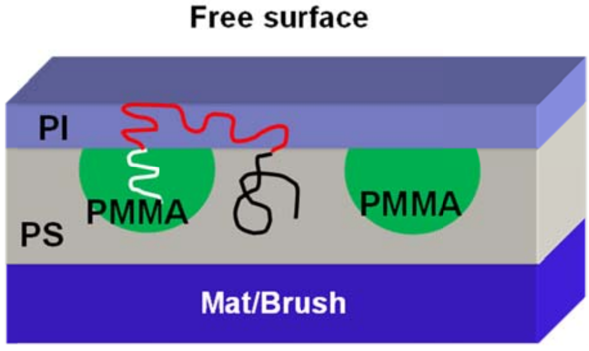

Figure 7.18 Schematic illustrating the structure of SIM28 thin films at the region R2.

A phenomenological model may be used in order to capture the dependence of the thin-film SIM behavior on the PI block size. The total Gibbs free energy (F) can be expressed as,

$$F = F_{elastic} + F_{interfacial} + F_{surface} \quad \text{(Eq. 7.1)}$$

where $F_{elastic}$, $F_{interfacial}$, and $F_{surface}$ denote the elastic, interfacial, and surface energy terms, respectively. For a lamellar domain size of L, $F_{elastic}$ per chain is equal to (3/8) ($k_B T\, L^2/a^2 N$), where a and N represent the statistical segment length and the degree of polymerization, respectively.[88] The difference in F between the looped conformation (‖) and the perpendicular ordering (†) may be approximated as,

$$F_{\|} - F_{\dagger} = F_{elastic}^{PI} + F_{interfacial}^{PS\text{-}PMMA} - (F_{surface}^{PS,\ PMMA} - F_{surface}^{PI}) - F_{surface}^{PI\text{-}mat} \quad \text{(Eq. 7.2)}$$

$F_{elastic}^{PI}$ accounts for the chain extension required for the PI domain segregation to the free surface in the looped conformation. $F_{interfacial}^{PS\text{-}PMMA}$ addresses the additional enthalpic penalty associated with creating the interface between the PS and PMMA domains in the looped configuration. Different components are expressed at the free surface depending on the thin-film morphology, leading to the difference in the total surface energy ($F_{surface}^{PS,\ PMMA} - F_{surface}^{PI}$). The term $F_{surface}^{PI\text{-}mat}$ accounts for the interaction between the PI block and the underlying mat for perpendicular ordering.

The SIM triblock copolymers exhibit thin-film morphology dependence on the volume fractions of the PI middle block. The interaction of the PI block with the underlying mat ($F_{surface}^{PI\text{-}mat}$), which renders perpendicular ordering unstable (*i.e.*, $\chi_{PS\text{-}PI} \approx \chi_{PI\text{-}PMMA} > \chi_{PS\text{-}PMMA}$), is expected to increase with the volume fraction of the PI block. The tendency for the SIM triblock copolymer thin films to segregate the PI block to the free surface is also favored by the low surface energy of the PI block with respect to other blocks ($F_{surface}^{PS,\ PMMA} - F_{surface}^{PI}$). However, this inevitably results in looped chain

conformations that entail not only entropic penalties ($F_{elastic}^{PI}$) but also new interface formation between the PS and the PMMA blocks ($F_{interfacial}^{PS\text{-}PMMA}$). The looped conformation would be less favorable with decreasing PI domain sizes. Therefore, the SIM triblock copolymers would respond differently to these competing factors depending on the relative size of the PI domains, as evidenced by the SIM18 and SIM28 results. While SIM18 and SIM28 share similarities in the bulk lamellar periodicity (42.5 nm and 48.7 nm) and the volume fraction of the PMMA block (41 % and 45 %), the only notable difference lies in the volume fractions of the PI block (18 % and 28 %) and the PS block (41% and 27%). The molecular weight of the PI block in SIM18 is apparently too small for looped conformation, and SIM18 forms the perpendicular lamellar structure in thin films. On the other hand, SIM28 that contains larger PI forms more complex structure, which likely involves the looped conformations.

Much remains to be further investigated. For example, it is still unknown at this moment the cause of forming multiple structures (R1 – R3) for SIM28. Though not shown here, the thin films annealed for an extended period of time still maintained such a medley of features. One possible origin for the persistence of a nonequilibrium structure is "pinning." On numerous occasions, a system is kinetically trapped at an intermediate stage and fails to proceed to the thermodynamic equilibrium, and some examples are mentioned in Chapter 5.

Partial epoxidation of the PI block has been implemented in order to verify the suggestion that the complex structure for SIM28 originates from the low surface energy of the PI block that drives the block to segregate to the free surface. The partial epoxidation is an effective method to increase the surface energy of the PI block, and it has been found that the surface energy of partially epoxidized PI becomes comparable to that of PS at 75 % partial modification.[247] As the surface energy of the PI block

approaches that of the PS block, or the PMMA block, the system would be driven less towards the PI block segregation to the free surface (looped chain conformation) and more towards the perpendicular lamellar morphology. Figure 7.19 illustrates the top-down SEM images of SIM28 with various degrees of partial epoxidation.

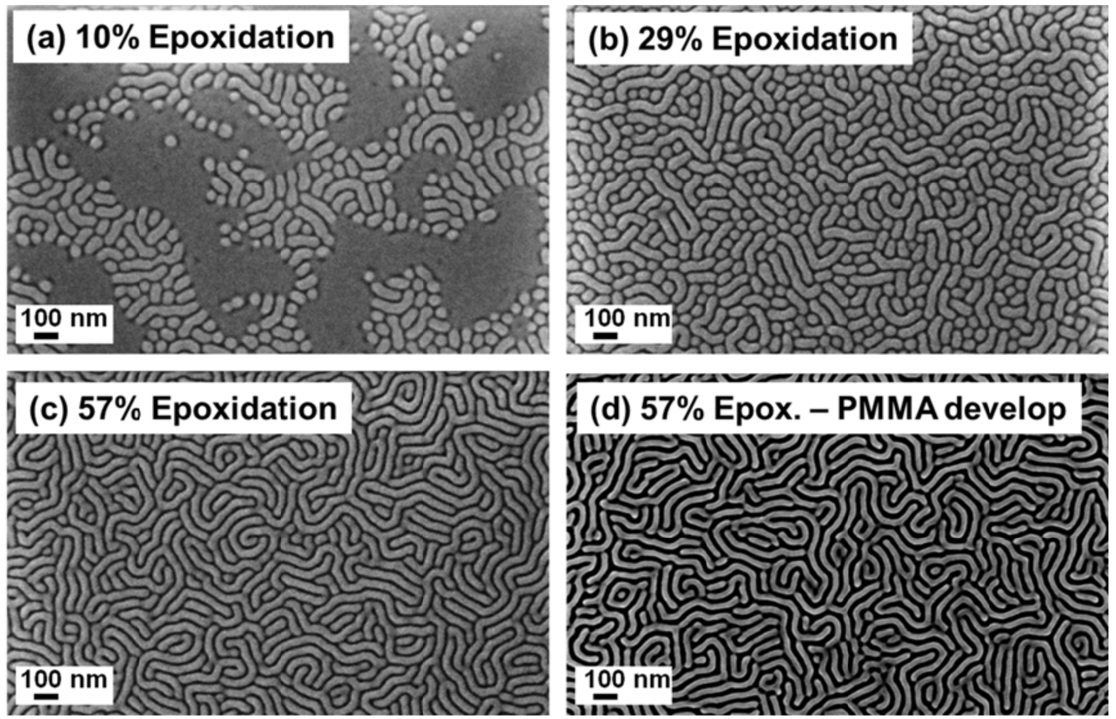

Figure 7.19 Top-down SEM images of thin-film SIM28 ($<L>/L_0 = 0.8$) with various degrees of partial epoxidation above SMG60: (a) 10%, (b) 29%, and (c-d) 57%. The thin films were thermally annealed for 178 °C for 24 hours.

At 10 % epoxidation, SIM28 exhibits only featureless regions and perpendicular ordering. The samples with 29 % epoxidation are characterized by a perpendicular lamellar morphology with a short correlation length. By 57% epoxidation, sizeable grains of perpendicular lamellar structures pervade through the thin-film samples. In

summary, as the surface energy of the middle block approaches those of the end blocks, the complex behavior of SIM28 disappears and the perpendicular ordering of the lamellar morphology is attained. The thin-film morphology dependence on the degrees of the partial modification indeed suggests that the thin film behavior of the SIM triblock copolymers is a consequence of the competition between enthalpic and entropic contributions. The bulk thermodynamics of the partially modified SIM samples remain to be investigated in the future.

Bibliography

1. Hiemenz, P. C.; Lodge, T. P., *Polymer Chemistry*. 2nd ed.; CRC Press,: Boca Raton, 2007.
2. Khandpur, A. K.; Forster, S.; Bates, F. S.; Hamley, I. W.; Ryan, A. J.; Bras, W.; Almdal, K.; Mortensen, K., *Macromolecules* 1995, *28* (26), 8796-8806.
3. Leibler, L., *Macromolecules* 1980, *13* (6), 1602-1617.
4. Fredrickson, G. H.; Helfand, E., *J. Chem. Phys.* 1987, *87* (1), 697-705.
5. Bates, F. S.; Fredrickson, G. H., *Phys. Today* 1999, *52* (2), 32-38.
6. Hashimoto, T.; Shibayama, M.; Kawai, H., *Macromolecules* 1980, *13* (5), 1237-1247.
7. Ohta, T.; Kawasaki, K., *Macromolecules* 1986, *19* (10), 2621-2632.
8. Keller, A.; Pedemonte, E.; Willmouth, F. M., *Colloid and Polymer Science* 1970, *238* (1-2), 385-389.
9. Hadziioannou, G.; Picot, C.; Skoulios, A.; Ionescu, M. L.; Mathis, A.; Duplessix, R.; Gallot, Y.; Lingelser, J. P., *Macromolecules* 1982, *15* (2), 263-267.
10. Chen, Z. R.; Kornfield, J. A.; Smith, S. D.; Grothaus, J. T.; Satkowski, M. M., *Science* 1997, *277* (5330), 1248-1253.
11. Amundson, K.; Helfand, E.; Davis, D. D.; Quan, X.; Patel, S. S.; Smith, S. D., *Macromolecules* 1991, *24* (24), 6546-6548.
12. Koppi, K. A.; Tirrell, M.; Frank, S. B.; Almdal, K.; Colby, R. H., *Journal De Physique II* 1992, *2*, 1941-1959.
13. Gupta, V. K.; Krishnamoorti, R.; Kornfield, J. A.; Smith, S. D., *Macromolecules* 1996, *29* (4), 1359-1362.
14. Zhang, Y. M.; Wiesner, U.; Spiess, H. W., *Macromolecules* 1995, *28* (3), 778-781.
15. Zheng, X.; Sauer, B. B.; Vanalsten, J. G.; Schwarz, S. A.; Rafailovich, M. H.; Sokolov, J.; Rubinstein, M., *Phys. Rev. Lett.* 1995, *74* (3), 407-410.
16. Zheng, X.; Rafailovich, M. H.; Sokolov, J.; Strzhemechny, Y.; Schwarz, S. A.; Sauer, B. B.; Rubinstein, M., *Phys. Rev. Lett.* 1997, *79* (2), 241-244.
17. Zhao, W.; Zhao, X.; Rafailovich, M. H.; Sokolov, J.; Composto, R. J.; Smith, S. D.; Satkowski, M.; Russell, T. P.; Dozier, W. D.; Mansfield, T., *Macromolecules* 1993, *26* (3), 561-562.
18. Reiter, G., *Europhysics Letters* 1993, *23* (8), 579-584.
19. Ellison, C. J.; Torkelson, J. M., *Nature Materials* 2003, *2* (10), 695-700.

20. Alcoutlabi, M.; McKenna, G. B., *Journal of Physics-Condensed Matter* 2005, *17* (15), R461-R524.

21. Jones, R. L.; Kumar, S. K.; Ho, D. L.; Briber, R. M.; Russell, T. P., *Nature* 1999, *400* (6740), 146-149.

22. Kraus, J.; Muller-Buschbaum, P.; Kuhlmann, T.; Schubert, D. W.; Stamm, M., *Europhysics Letters* 2000, *49* (2), 210-216.

23. Despotopoulou, M. M.; Frank, C. W.; Miller, R. D.; Rabolt, J. F., *Macromolecules* 1995, *28* (19), 6687-6688.

24. Frank, C. W.; Rao, V.; Despotopoulou, M. M.; Pease, R. F. W.; Hinsberg, W. D.; Miller, R. D.; Rabolt, J. F., *Science* 1996, *273* (5277), 912-915.

25. Jones, R. A. L.; Norton, L. J.; Kramer, E. J.; Bates, F. S.; Wiltzius, P., *Phys. Rev. Lett.* 1991, *66* (10), 1326-1329.

26. Krausch, G.; Dai, C. A.; Kramer, E. J.; Bates, F. S., *Phys. Rev. Lett.* 1993, *71* (22), 3669-3672.

27. Sung, L.; Karim, A.; Douglas, J. F.; Han, C. C., *Phys. Rev. Lett.* 1996, *76* (23), 4368-4371.

28. Krausch, G.; Dai, C. A.; Kramer, E. J.; Marko, J. F.; Bates, F. S., *Macromolecules* 1993, *26* (21), 5566-5571.

29. Reich, S.; Cohen, Y., *Journal of Polymer Science Part B: Polymer Physics* 1981, *19* (8), 1255-1267.

30. Nesterov, A.; Horichko, V.; Lipatov, Y., *Makromolekulare Chemie-Rapid Communications* 1991, *12* (10), 571-574.

31. Kang, S. J.; Bae, I.; Shin, Y. J.; Park, Y. J.; Huh, J.; Park, S. M.; Kim, H. C.; Park, C., *Nano Letters* 2011, *11* (1), 138-144.

32. Deshmukh, R. D.; Liu, Y.; Composto, R. J., *Nano Letters* 2007, *7* (12), 3662-3668.

33. Edrington, A. C.; Urbas, A. M.; DeRege, P.; Chen, C. X.; Swager, T. M.; Hadjichristidis, N.; Xenidou, M.; Fetters, L. J.; Joannopoulos, J. D.; Fink, Y.; Thomas, E. L., *Adv. Mater.* 2001, *13* (6), 421-425.

34. Kataoka, K.; Okano, T.; Sakurai, Y.; Nishimura, T.; Inoue, S.; Watanabe, T.; Maruyama, A.; Tsuruta, T., *Eur. Polym. J.* 1983, *19* (10-11), 979-984.

35. Park, M.; Harrison, C.; Chaikin, P. M.; Register, R. A.; Adamson, D. H., *Science* 1997, *276* (5317), 1401-1404.

36. Park, J. H.; Kirch, J.; Mawst, L. J.; Liu, C. C.; Nealey, P. F.; Kuech, T. F., *Appl. Phys. Lett.* 2009, *95* (11), 113111.

37. Thurn-Albrecht, T.; Schotter, J.; Kastle, C. A.; Emley, N.; Shibauchi, T.; Krusin-Elbaum, L.; Guarini, K.; Black, C. T.; Tuominen, M. T.; Russell, T. P., *Science* 2000, *290* (5499), 2126-2129.

38. Lopes, W. A.; Jaeger, H. M., *Nature* 2001, *414* (6865), 735-738.

39. Black, C. T.; Guarini, K. W.; Milkove, K. R.; Baker, S. M.; Russell, T. P.; Tuominen, M. T., *Appl. Phys. Lett.* 2001, *79* (3), 409-411.

40. Cheng, J. Y.; Ross, C. A.; Chan, V. Z. H.; Thomas, E. L.; Lammertink, R. G. H.; Vancso, G. J., *Adv. Mater.* 2001, *13* (15), 1174-1178.

41. Naito, K.; Hieda, H.; Sakurai, M.; Kamata, Y.; Asakawa, K., *IEEE Transactions on Magnetics* 2002, *38* (5), 1949-1951.

42. Yang, S. Y.; Ryu, I.; Kim, H. Y.; Kim, J. K.; Jang, S. K.; Russell, T. P., *Adv. Mater.* 2006, *18* (6), 709-712.

43. Croll, S. G., *J. Appl. Polym. Sci.* 1979, *23* (3), 847-858.

44. Zhang, X. J.; Harris, K. D.; Wu, N. L. Y.; Murphy, J. N.; Buriak, J. M., *ACS Nano* 2010, *4* (11), 7021-7029.

45. Park, S.; Lee, D. H.; Xu, J.; Kim, B.; Hong, S. W.; Jeong, U.; Xu, T.; Russell, T. P., *Science* 2009, *323* (5917), 1030-1033.

46. Berry, B. C.; Bosse, A. W.; Douglas, J. F.; Jones, R. L.; Karim, A., *Nano Letters* 2007, *7* (9), 2789-2794.

47. Angelescu, D. E.; Waller, J. H.; Adamson, D. H.; Register, R. A.; Chaikin, P. M., *Adv. Mater.* 2007, *19* (18), 2687-2690.

48. Angelescu, D. E.; Waller, J. H.; Adamson, D. H.; Deshpande, P.; Chou, S. Y.; Register, R. A.; Chaikin, P. M., *Adv. Mater.* 2004, *16* (19), 1736-1740.

49. De Rosa, C.; Park, C.; Thomas, E. L.; Lotz, B., *Nature* 2000, *405* (6785), 433-437.

50. Herr, D. J. C., *Journal of Materials Research* 2011, *26* (2), 122-139.

51. Plummer, J. D.; Deal, M. D.; Griffin, P. B., *Silicon VLSI Technology - Fundamentals, Practice and Modeling*. Prentice Hall: Upper Saddle River, NJ, 2000.

52. Levinson, H. J., *Principles of Lithography*. SPIE Press: Bellingham, WA, 2001.

53. Herr, D. J. C., *Future Fab International* 2007, *22* (22), 69.

54. Mack, C. A., *Future Fab International* 2007, *23* (23), 65.

55. Russell, T. P.; Coulon, G.; Deline, V. R.; Miller, D. C., *Macromolecules* 1989, *22* (12), 4600-4606.

56. Kellogg, G. J.; Walton, D. G.; Mayes, A. M.; Lambooy, P.; Russell, T. P.; Gallagher, P. D.; Satija, S. K., *Phys. Rev. Lett.* 1996, *76* (14), 2503-2506.

57. Mansky, P.; Liu, Y.; Huang, E.; Russell, T. P.; Hawker, C. J., *Science* 1997, *275* (5305), 1458-1460.

58. Mansky, P.; Russell, T. P.; Hawker, C. J.; Mays, J.; Cook, D. C.; Satija, S. K., *Phys. Rev. Lett.* 1997, *79* (2), 237-240.

59. Huang, E.; Rockford, L.; Russell, T. P.; Hawker, C. J., *Nature* 1998, *395* (6704), 757-758.

60. Huang, E.; Russell, T. P.; Harrison, C.; Chaikin, P. M.; Register, R. A.; Hawker, C. J.; Mays, J., *Macromolecules* 1998, *31* (22), 7641-7650.

61. Huang, E.; Pruzinsky, S.; Russell, T. P.; Mays, J.; Hawker, C. J., *Macromolecules* 1999, *32* (16), 5299-5303.

62. Ryu, D. Y.; Shin, K.; Drockenmuller, E.; Hawker, C. J.; Russell, T. P., *Science* 2005, *308* (5719), 236-239.

63. Bang, J.; Bae, J.; Lowenhielm, P.; Spiessberger, C.; Given-Beck, S. A.; Russell, T. P.; Hawker, C. J., *Adv. Mater.* 2007, *19* (24), 4552-4557.

64. Han, E.; In, I.; Park, S. M.; La, Y. H.; Wang, Y.; Nealey, P. F.; Gopalan, P., *Adv. Mater.* 2007, *19* (24), 4448-4452.

65. Kim, S. H.; Misner, M. J.; Xu, T.; Kimura, M.; Russell, T. P., *Adv. Mater.* 2004, *16* (3), 226-231.

66. Lin, Z. Q.; Kim, D. H.; Wu, X. D.; Boosahda, L.; Stone, D.; LaRose, L.; Russell, T. P., *Adv. Mater.* 2002, *14* (19), 1373-1376.

67. Kim, G.; Libera, M., *Macromolecules* 1998, *31* (8), 2569-2577.

68. Turturro, A.; Gattiglia, E.; Vacca, P.; Viola, G. T., *Polymer* 1995, *36* (21), 3987-3996.

69. Bosworth, J. K.; Paik, M. Y.; Ruiz, R.; Schwartz, E. L.; Huang, J. Q.; Ko, A. W.; Smilgies, D. M.; Black, C. T.; Ober, C. K., *ACS Nano* 2008, *2* (7), 1396-1402.

70. Peng, J.; Kim, D. H.; Knoll, W.; Xuan, Y.; Li, B. Y.; Han, Y. C., *J. Chem. Phys.* 2006, *125* (6), 064702.

71. Jeong, J. W.; Park, W. I.; Kim, M. J.; Ross, C. A.; Jung, Y. S., *Nano Letters* 2011, *11* (10), 4095-4101.

72. Amundson, K.; Helfand, E.; Quan, X.; Smith, S. D., *Macromolecules* 1993, *26* (11), 2698-2703.

73. Morkved, T. L.; Lu, M.; Urbas, A. M.; Ehrichs, E. E.; Jaeger, H. M.; Mansky, P.; Russell, T. P., *Science* 1996, *273* (5277), 931-933.

74. Thurn-Albrecht, T.; DeRouchey, J.; Russell, T. P.; Jaeger, H. M., *Macromolecules* 2000, *33* (9), 3250-3253.

75. Xu, T.; Zhu, Y. Q.; Gido, S. P.; Russell, T. P., *Macromolecules* 2004, *37* (7), 2625-2629.

76. Xu, T.; Hawker, C. J.; Russell, T. P., *Macromolecules* 2003, *36* (16), 6178-6182.

77. Wang, J. Y.; Xu, T.; Leiston-Belanger, J. M.; Gupta, S.; Russell, T. P., *Phys. Rev. Lett.* 2006, *96* (12), 128301.

78. Amundson, K.; Helfand, E.; Quan, X. N.; Hudson, S. D.; Smith, S. D., *Macromolecules* 1994, *27* (22), 6559-6570.

79. DeRouchey, J.; Thurn-Albrecht, T.; Russell, T. P.; Kolb, R., *Macromolecules* 2004, *37* (7), 2538-2543.

80. Boker, A.; Elbs, H.; Hansel, H.; Knoll, A.; Ludwigs, S.; Zettl, H.; Urban, V.; Abetz, V.; Muller, A. H. E.; Krausch, G., *Phys. Rev. Lett.* 2002, *89* (13), 135502.

81. Zvelindovsky, A. V.; Sevink, G. J. A., *Phys. Rev. Lett.* 2003, *90* (4), 049601.

82. Wang, J. Y.; Leiston-Belanger, J. M.; Sievert, J. D.; Russell, T. P., *Macromolecules* 2006, *39* (24), 8487-8491.

83. Rockford, L.; Liu, Y.; Mansky, P.; Russell, T. P.; Yoon, M.; Mochrie, S. G. J., *Phys. Rev. Lett.* 1999, *82* (12), 2602-2605.

84. Rockford, L.; Mochrie, S. G. J.; Russell, T. P., *Macromolecules* 2001, *34* (5), 1487-1492.

85. Kim, S. O.; Solak, H. H.; Stoykovich, M. P.; Ferrier, N. J.; de Pablo, J. J.; Nealey, P. F., *Nature* 2003, *424* (6947), 411-414.

86. Yang, X. M.; Peters, R. D.; Nealey, P. F.; Solak, H. H.; Cerrina, F., *Macromolecules* 2000, *33* (26), 9575-9582.

87. Solak, H. H.; David, C.; Gobrecht, J.; Golovkina, V.; Cerrina, F.; Kim, S. O.; Nealey, P. F., *Microelectronic Engineering* 2003, *67-68*, 56-62.

88. Edwards, E. W.; Montague, M. F.; Solak, H. H.; Hawker, C. J.; Nealey, P. F., *Adv. Mater.* 2004, *16* (15), 1315-1319.

89. Edwards, E. W.; Muller, M.; Stoykovich, M. P.; Solak, H. H.; de Pablo, J. J.; Nealey, P. F., *Macromolecules* 2007, *40* (1), 90-96.

90. Stoykovich, M. P.; Muller, M.; Kim, S. O.; Solak, H. H.; Edwards, E. W.; de Pablo, J. J.; Nealey, P. F., *Science* 2005, *308* (5727), 1442-1446.

91. Burgaz, E.; Gido, S. P., *Macromolecules* 2000, *33* (23), 8739-8745.

92. Stoykovich, M. P.; Kang, H.; Daoulas, K. C.; Liu, G.; Liu, C. C.; de Pablo, J. J.; Mueller, M.; Nealey, P. F., *ACS Nano* 2007, *1* (3), 168-175.

93. Wilmes, G. M.; Durkee, D. A.; Balsara, N. P.; Liddle, J. A., *Macromolecules* 2006, *39* (7), 2435-2437.

94. Ruiz, R.; Kang, H. M.; Detcheverry, F. A.; Dobisz, E.; Kercher, D. S.; Albrecht, T. R.; de Pablo, J. J.; Nealey, P. F., *Science* 2008, *321* (5891), 936-939.

95. Cheng, J. Y.; Rettner, C. T.; Sanders, D. P.; Kim, H. C.; Hinsberg, W. D., *Adv. Mater.* 2008, *20* (16), 3155-3158.

96. Liu, C. C.; Han, E.; Onses, M. S.; Thode, C. J.; Ji, S. X.; Gopalan, P.; Nealey, P. F., *Macromolecules* 2011, *44* (7), 1876-1885.

97. Liu, C. C.; Ramirez-Hernandez, A.; Han, E.; Craig, G. S. W.; Tada, Y.; Yoshida, H.; Kang, H. M.; Ji, S. X.; Gopalan, P.; de Pablo, J. J.; Nealey, P. F., *Macromolecules* 2013, *46* (4), 1415-1424.

98. Smith, H. I.; Flanders, D. C., *Appl. Phys. Lett.* 1978, *32* (6), 349-350.

99. Segalman, R. A.; Yokoyama, H.; Kramer, E. J., *Adv. Mater.* 2001, *13* (15), 1152-1155.

100. Segalman, R. A.; Hexemer, A.; Kramer, E. J., *Macromolecules* 2003, *36* (18), 6831-6839.

101. Segalman, R. A.; Hexemer, A.; Kramer, E. J., *Phys. Rev. Lett.* 2003, *91* (19), 196101.

102. Cheng, J. Y.; Ross, C. A.; Thomas, E. L.; Smith, H. I.; Vancso, G. J., *Appl. Phys. Lett.* 2002, *81* (19), 3657-3659.

103. Cheng, J. Y.; Zhang, F.; Smith, H. I.; Vancso, G. J.; Ross, C. A., *Adv. Mater.* 2006, *18* (5), 597-601.

104. Sundrani, D.; Darling, S. B.; Sibener, S. J., *Nano Letters* 2004, *4* (2), 273-276.

105. Cheng, J. Y.; Ross, C. A.; Thomas, E. L.; Smith, H. I.; Vancso, G. J., *Adv. Mater.* 2003, *15* (19), 1599-1602.

106. Sundrani, D.; Darling, S. B.; Sibener, S. J., *Langmuir* 2004, *20* (12), 5091-5099.

107. Park, S. M.; Stoykovich, M. P.; Ruiz, R.; Zhang, Y.; Black, C. T.; Nealey, P. E., *Adv. Mater.* 2007, *19* (4), 607-611.

108. Xiao, S.; Yang, X.; Edwards, E. W.; La, Y.-H.; Nealey, P. F., *Nanotechnology* 2005, *16* (7), S324-S329.

109. Chai, J.; Buriak, J. M., *ACS Nano* 2008, *2* (3), 489-501.

110. Odian, G., *Principles of Polymerization*. 4th ed.; Wiley Interscience: Hoboken, NJ, 2004.

111. Kambour, R. P.; Bendler, J. T.; Bopp, R. C., *Macromolecules* 1983, *16* (5), 753-757.

112. ten Brinke, G.; Karasz, F. E.; Macknight, W. J., *Macromolecules* 1983, *16* (12), 1827-1832.

113. Feldman, K. E.; Kade, M. J.; Meijer, E. W.; Hawker, C. J.; Kramer, E. J., *Macromolecules* 2009, *42* (22), 9072-9081.

114. Verploegen, E.; Zhang, T.; Murlo, N.; Hammond, P. T., *Soft Matter* 2008, *4* (6), 1279-1287.

115. Mansour, A. S.; Johnson, L. F.; Lodge, T. P.; Bates, F. S., *Journal of Polymer Science Part B: Polymer Physics* 2010, *48* (5), 566-574.

116. Wu, S., *Polymer Interface and Adhesion*. Marcel Dekker, Inc.: New York, 1982.

117. Toyama, M.; Watanabe, A.; Ito, T., *Journal of Colloid and Interface Science* 1974, *47* (3), 802-803.

118. Adao, M. H. V. C.; Saramago, B. J. V.; Fernandes, A. C., *Journal of Colloid and Interface Science* 1999, *217* (1), 94-106.

119. Donley, J. P.; Fredrickson, G. H., *Macromolecules* 1994, *27* (2), 458-467.

120. Han, E.; Stuen, K. O.; La, Y. H.; Nealey, P. F.; Gopalan, P., *Macromolecules* 2008, *41* (23), 9090-9097.

121. Choi, W. H.; Jo, W. H., *J. Power. Sourc.* 2009, *188* (1), 127-131.

122. Szczubialka, K.; Ishikawa, K.; Morishima, Y., *Langmuir* 1999, *15* (2), 454-462.

123. Ren, Y.; Lodge, T. P.; Hillmyer, M. A., *Macromolecules* 2000, *33* (3), 866-876.

124. Ren, Y.; Lodge, T. P.; Hillmyer, M. A., *Macromolecules* 2002, *35* (10), 3889-3894.

125. Bucholz, T. L.; Loo, Y. L., *Macromolecules* 2006, *39* (18), 6075-6080.

126. Kimishima, I.; Jinnai, H.; Hashimoto, T., *Macromolecules* 1999, *32* (8), 2585-2596.

127. Grubbs, R. B.; Broz, M. E.; Dean, J. M.; Bates, F. S., *Macromolecules* 2000, *33* (7), 2308-2310.

128. Brosse, J. C.; Campistron, I.; Derouet, D.; El Hamdaoui, A.; Houdayer, S.; Reyx, D.; Ritoit-Gillier, S., *J. Appl. Polym. Sci.* 2000, *78* (8), 1461-1477.

129. Mcgrath, M. P.; Sall, E. D.; Tremont, S. J., *Chemical Reviews* 1995, *95* (2), 381-398.

130. Siddiqui, S.; Cais, R. E., *Macromolecules* 1986, *19* (3), 595-603.

131. Bradbury, J. H.; Perera, M. C. S., *J. Appl. Polym. Sci.* 1985, *30* (8), 3347-3364.

132. Tutorskii, I. A.; Khodzhaeva, I. D.; Dogadkin, B. A., *Vysokomol. Soedin. Ser. A* 1974, *16*, 157.

133. Hayashi, O.; Takahashi, T.; Kurihara, H.; Ueno, H., *Polym. J.* 1981, *13* (3), 215-223.

134. Davidock, D. A.; Hillmyer, M. A.; Lodge, T. P., *Macromolecules* 2004, *37* (2), 397-407.

135. Ren, Y.; Lodge, T. P.; Hillmyer, M. A., *Journal of the American Chemical Society* 1998, *120* (27), 6830-6831.

136. Hildebrand, J. H.; Scott, R. L., *The Solubility of Nonelectrolyets*. 3rd ed.; Reinhold: New York, 1950.

137. Bates, F. S.; Schulz, M. F.; Rosedale, J. H.; Almdal, K., *Macromolecules* 1992, *25* (20), 5547-5550.

138. Suh, K. W.; Clarke, D. H., *Journal of Polymer Science Part A-1: Polymer Chemistry* 1967, *5*, 1671-1681.

139. Bristow, G. M.; Watson, W. F., *Transactions of the Faraday Society* 1958, *54*, 1731-1741.

140. Bristow, G. M.; Watson, W. F., *Transactions of the Faraday Society* 1958, *54*, 1742-1747.

141. Graessley, W. W.; Krishnamoorti, R.; Balsara, N. P.; Butera, R. J.; Fetters, L. J.; Lohse, D. J.; Schulz, D. N.; Sissano, J. A., *Macromolecules* 1994, *27* (14), 3896-3901.

142. Reichart, G. C.; Graessley, W. M.; Register, R. A.; Lohse, D. J., *Macromolecules* 1998, *31* (22), 7886-7894.

143. Graessley, W. W.; Krishnamoorti, R.; Balsara, N. P.; Fetters, L. J.; Lohse, D. J.; Schulz, D. N.; Sissano, J. A., *Macromolecules* 1994, *27* (9), 2574-2579.

144. Graessley, W. W.; Krishnamoorti, R.; Balsara, N. P.; Fetters, L. J.; Lohse, D. J.; Schulz, D. N.; Sissano, J. A., *Macromolecules* 1993, *26* (5), 1137-1143.

145. Krishnamoorti, R.; Graessley, W. W.; Balsara, N. P.; Lohse, D. J., *Macromolecules* 1994, *27* (11), 3073-3081.

146. Krishnamoorti, R.; Graessley, W. W.; Dee, G. T.; Walsh, D. J.; Fetters, L. J.; Lohse, D. J., *Macromolecules* 1996, *29* (1), 367-376.

147. Krause, S., Polymer-Polymer Compatibility. In *Polymer Blends*, Academic Press: New York, 1978.

148. Scott, R. L., *J. Polym. Sci.* 1952, *9* (5), 423-432.

149. Tillaev, R. S.; Khasankhanova, M.; Tashmukhamedov, S. A.; Usmanov, K. U., *Journal of Polymer Science Part C: Polymer Symposia* 1972, *39*, 107-111.

150. Gelling, I. R.; Tinker, A. J.; Rahman, H. A., *J. Nat. Rubb. Res.* 1991, *6* (1), 20-29.

151. Ng, S. C.; Chee, K. K., *Eur. Polym. J.* 1997, *33* (5), 749-752.

152. Stockmayer, W. H.; Moore, L. D., Jr; Fixman, M.; Epstein, B. N., *J. Polym. Sci.* 1955, *16* (82), 517-530.

153. Paul, D. R.; Barlow, J. W., *Polymer* 1984, *25* (4), 487-494.

154. Chiou, J. S.; Paul, D. R.; Barlow, J. W., *Polymer* 1982, *23* (10), 1543-1545.

155. Paul, D. R.; Bucknall, C. B., *Polymer Blends*. Wiley-Interscience: 2000.

156. Galvin, M. E., *Macromolecules* 1991, *24* (23), 6354-6356.

157. Poh, B. T.; Tan, B. K., *J. Appl. Polym. Sci.* 1991, *42* (5), 1407-1416.

158. Gelling, I. R.; Morrison, N. J., *Rubb. Chem. Technol.* 1985, *58* (2), 243-257.

159. Roland, C. M., *Macromolecules* 1992, *25* (25), 7031-7036.

160. Davies, C. K. L.; Wolfe, S. V.; Gelling, I. R.; Thomas, A. G., *Polymer* 1983, *24* (1), 107-113.

161. Barquins, M.; Roberts, A. D., *J. Chim. Phys.* 1987, *84* (2), 225-230.

162. Tanrattanakul, V.; Wattanathai, B.; Tiangjunya, A.; Muhamud, P., *J. Appl. Polym. Sci.* 2003, *90* (1), 261-269.

163. Ng, S. C.; Chee, K. K., *Rubb. Chem. Technol.* 1989, *62* (4), 585-591.

164. Cizravi, J. C.; Subramaniam, K., *Polym. Int.* 1999, *48* (9), 889-895.

165. Bussi, P.; Ishida, H., *Journal of Polymer Science Part B: Polymer Physics* 1994, *32* (4), 647-657.

166. Jayawardena, S.; Reyx, D.; Durand, D.; Pinazzi, C. P., *Makromol. Chem.* 1984, *185* (10), 2089-2097.

167. Brandrup, J.; Immergut, E. H., *Polymer Handbook*. John Wiley & Sons: 1999.

168. Zuchowska, D., *Polymer* 1980, *21* (5), 514-520.

169. Gemmer, R. V.; Golub, M. A., *Journal of Polymer Science Part A: Polymer Chemistry* 1978, *16* (11), 2985-2990.

170. Gnecco, S.; Pooley, A.; Krause, M., *Polym. Bull.* 1996, *37* (5), 609-615.

171. Wang, S. M.; Tsiang, R. C. C., *Journal of Polymer Science Part A: Polymer Chemistry* 1996, *34* (8), 1483-1491.

172. Udipi, K., *J. Appl. Polym. Sci.* 1979, *23* (11), 3301-3309.

173. Li, H. Q.; Zeng, X. R.; Wu, W. Q., *J. Elastom. Plast.* 2008, *40* (4), 317-330.

174. Huang, W. K.; Hsiue, G. H.; Hou, W. H., *Journal of Polymer Science Part A: Polymer Chemistry* 1988, *26* (7), 1867-1883.

175. Huang, W. K.; Hsiue, G. H., *Journal of Polymer Science Part A: Polymer Chemistry* 1989, *27* (1), 279-289.

176. Gelling, I. R., *Rubb. Chem. Technol.* 1985, *58* (1), 86-96.

177. Perera, M. C. S.; Elix, J. A.; Bradbury, J. H., *Journal of Polymer Science Part A: Polymer Chemistry* 1988, *26* (2), 637-651.

178. Patterson, D. J.; Koenig, J. L., *Makromol. Chem.* 1987, *188* (10), 2325-2337.

179. Gipstein, E.; Nichik, F.; Offenbac.Ja, *Analytica Chimica Acta* 1968, *43* (1), 129-131.

180. Dreyfuss, P.; Kennedy, J. P., *Analytical Chemistry* 1975, *47* (4), 771-774.

181. Derouet, D.; Brosse, J. C.; Challioui, A., *Eur. Polym. J.* 2001, *37* (7), 1327-1337.

182. Antonietti, M.; Forster, S.; Hartmann, J.; Oestreich, S., *Macromolecules* 1996, *29* (11), 3800-3806.

183. Bailey, T. S.; Rzayev, J.; Hillmyer, M. A., *Macromolecules* 2006, *39* (25), 8772-8781.

184. Montgomery, R. E., *Journal of American Chemical Society* 1974, *96* (25), 7820-7821.

185. Murray, R. W.; Jeyaraman, R., *J. Org. Chem.* 1985, *50* (16), 2847-2853.

186. Nikje, M. M. A.; Rafiee, A.; Haghshenas, A., *Designed Monomers Polymers* 2006, *9* (3), 293-303.

187. Rajabi, F. H.; Nikje, M. M. A.; Farahani, B. V.; Saboury, N., *Designed Monomers Polymers* 2006, *9* (4), 383-392.

188. Allen, R. D.; Long, T. E.; Mcgrath, J. E., *Polym. Bull.* 1986, *15* (2), 127-134.

189. Pangborn, A. B.; Giardello, M. A.; Grubbs, R. H.; Rosen, R. K.; Timmers, F. J., *Organometallics* 1996, *15* (5), 1518-1520.

190. Wiles, D. M.; Bywater, S., *Transactions of the Faraday Society* 1965, *61*, 150-158.

191. Zune, C.; Dubois, P.; Jerome, R.; Werkhoven, T.; Lugtenburg, J., *Macromolecular Chemistry and Physics* 1999, *200* (2), 460-467.

192. Davis, T. P.; Haddleton, D. M.; Richards, S. N., *Journal of Macromolecular Science-Reviews in Macromolecular Chemistry and Physics* 1994, *C34* (2), 243-324.

193. Fayt, R.; Forte, R.; Jacobs, C.; Jerome, R.; Ouhadi, T.; Teyssie, P.; Varshney, S. K., *Macromolecules* 1987, *20* (6), 1442-1444.

194. Varshney, S. K.; Hautekeer, J. P.; Fayt, R.; Jerome, R.; Teyssie, P., *Macromolecules* 1990, *23* (10), 2618-2622.

195. Ozaki, H.; Hirao, A.; Nakahama, S., *Macromolecular Chemistry and Physics* 1995, *196* (7), 2099-2111.

196. Curci, R.; Fiorentino, M.; Troisi, L.; Edwards, J. O.; Pater, R. H., *J. Org. Chem.* 1980, *45* (23), 4758-4760.

197. Grubbs, R. B.; Dean, J. M.; Broz, M. E.; Bates, F. S., *Macromolecules* 2000, *33* (26), 9522-9534.

198. Simekova, M.; Berek, D., *J. Chromatogr. A.* 2005, *1084* (1-2), 167-172.

199. Skoog, D. A.; Holler, F. J.; Crouch, S. R., *Principles of Instrumental Analysis*. 6th ed.; Brooks Cole,: 2006.

200. Roe, R.-J., *Methods of X-ray and Neutron Scattering in Polymer Science*. Oxford University Press: 2000.

201. Griffiths, D. J., *Introduction to Quantum Mechanics*. 2nd ed.; Prentice Hall,: 2005.

202. Ashcroft; Mermin, *Solid State Physics*. Saunders College Publishing: 1976.

203. Epps, T. H.; Cochran, E. W.; Bailey, T. S.; Waletzko, R. S.; Hardy, C. M.; Bates, F. S., *Macromolecules* 2004, *37* (22), 8325-8341.

204. Ferry, J. D., *Viscoelastic Properties of Polymers*. 3rd ed.; Wiley & Sons,: 1980.

205. Rosedale, J. H.; Bates, F. S., *Macromolecules* 1990, *23* (8), 2329-2338.

206. Ryu, C. Y.; Lee, M. S.; Hajduk, D. A.; Lodge, T. P., *Journal of Polymer Science Part B: Polymer Physics* 1997, *35* (17), 2811-2823.

207. Zhao, J.; Majumdar, B.; Schulz, M. F.; Bates, F. S.; Almdal, K.; Mortensen, K.; Hajduk, D. A.; Gruner, S. M., *Macromolecules* 1996, *29* (4), 1204-1215.

208. Goldstein, J. I.; Newbury, D. E.; Echlin, P.; Joy, D. C.; Romig, A. D. J.; Lyman, C. E.; Fiori, C.; Lifshin, E., *Scanning Electron Microscopy and X-ray Microanalysis*. 2nd ed.; Plenum Press: New York, 1992.

209. Taylor, G. N.; Wolf, T. M., *Polymer Engineering and Science* 1980, *20* (16), 1087-1092.

210. Egitto, F. D., *Pure and Applied Chemistry* 1990, *62* (9), 1699-1708.

211. Moss, S. J.; Jolly, A. M.; Tighe, B. J., *Plasma Chemistry and Plasma Processing* 1986, *6* (4), 401-416.

212. Clark, D. T.; Wilson, R., *Journal of Polymer Science Part A: Polymer Chemistry* 1983, *21* (3), 837-853.

213. Hall, J. R.; Westerdahl, C. A. L.; Devine, A. T.; Bodnar, M. J., *J. Appl. Polym. Sci.* 1969, *13* (10), 2085-2096.

214. Westerdahl, C. A. L.; Hall, J. R.; Schramm, E. C.; Levi, D. W., *Journal of Colloid and Interface Science* 1974, *47* (3), 610-620.

215. Occhiello, E.; Morra, M.; Cinquina, P.; Garbassi, F., *Polymer Preprints, ACS Division of Polymer Chemistry* 1990, *31* (1), 308-309.

216. Bates, F. S.; Fredrickson, G. H.; Hucul, D.; Hahn, S. F., *AIChE Journal* 2001, *47* (4), 762-765.

217. Bates, F. S.; Wignall, G. D., *Macromolecules* 1986, *19* (3), 932-934.

218. Jones, R. A. L.; Kramer, E. J.; Rafailovich, M. H.; Sokolov, J.; Schwarz, S. A., *Phys. Rev. Lett.* 1989, *62* (3), 280-283.

219. Perera, M. C. S.; Elix, J. A.; Bradbury, J. H., *J. Appl. Polym. Sci.* 1988, *36* (1), 105-116.

220. Lee, L. H., *J. Polym. Sci. Part A-2 Polym. Phys.* 1967, *5* (6), 1103-1118.

221. Wu, S., *Journal of Polymer Science Part C: Polymer Symposia* 1971, *34* (1), 19-30.

222. Morgan, J. L. R.; Neidle, M., *Journal of American Chemical Society* 1913, *35* (12), 1856-1865.

223. Suh, H. S.; Kang, H. M.; Nealey, P. F.; Char, K., *Macromolecules* 2010, *43* (10), 4744-4751.

224. Mansky, P.; Tsui, O. K. C.; Russell, T. P.; Gallot, Y., *Macromolecules* 1999, *32* (15), 4832-4837.

225. Anastasiadis, S. H.; Russell, T. P.; Satija, S. K.; Majkrzak, C. F., *Phys. Rev. Lett.* 1989, *62* (16), 1852-1855.

226. Foster, M. D.; Sikka, M.; Singh, N.; Bates, F. S.; Satija, S. K.; Majkrzak, C. F., *J. Chem. Phys.* 1992, *96* (11), 8605-8615.

227. Semenov, A. N., *Sov. Phys. JETP* 1985, *61* (4), 733-742.

228. van Krevelen, D. W., *Properties of Polymers*. Elsevier Publishing Company: Amsterdam, 1972.

229. Fetters, L. J.; Lohse, D. J.; Richter, D.; Witten, T. A.; Zirkel, A., *Macromolecules* 1994, *27* (17), 4639-4647.

230. Almdal, K.; Rosedale, J. H.; Bates, F. S.; Wignall, G. D.; Fredrickson, G. H., *Phys. Rev. Lett.* 1990, *65* (9), 1112-1115.

231. Bates, F. S.; Rosedale, J. H.; Fredrickson, G. H.; Glinka, C. J., *Phys. Rev. Lett.* 1988, *61* (19), 2229-2232.

232. Krause, S., *J. Polym. Sci.* 1959, *35* (129), 558-559.

233. Roe, R. J.; Zin, W. C., *Macromolecules* 1980, *13* (5), 1221-1228.

234. Chuayjujit, S.; Sakulkijpiboon, S.; Potiyaraj, P., *Polym. Polym. Comp.* 2010, *18* (3), 139-144.

235. Lodge, T. P.; Pan, C.; Jin, X.; Liu, Z.; Zhao, J.; Maurer, W. W.; Bates, F. S., *Journal of Polymer Science Part B: Polymer Physics* 1995, *33* (16), 2289-2293.

236. Fowler, M. E.; Barlow, J. W.; Paul, D. R., *Polymer* 1987, *28* (7), 1177-1184.

237. Nishimoto, M.; Keskkula, H.; Paul, D. R., *Polymer* 1991, *32* (7), 1274-1283.

238. Hinsberg, W.; Cheng, J.; Kim, H.; Sanders, D. P., *Proceedings of SPIE* 2010, *7637*, 76370G.

239. Bates, C. M.; Strahan, J. R.; Santos, L. J.; Mueller, B. K.; Bamgbade, B. O.; Lee, J. A.; Katzenstein, J. M.; Ellison, C. J.; Willson, C. G., *Langmuir* 2011, *27* (5), 2000-2006.

240. Bimberg, D.; Pohl, U. W., *Materials Today* 2011, *14* (9), 388-397.

241. Sambur, J. B.; Novet, T.; Parkinson, B. A., *Science* 2010, *330* (6000), 63-66.

242. Talapin, D. V.; Murray, C. B., *Science* 2005, *310* (5745), 86-89.

243. Yablonovitch, E., *Phys. Rev. Lett.* 1987, *58* (20), 2059-2062.

244. Tsui, O. K. C.; Russell, T., *Polymer Thin Films*. World Scientific: Singapore, 2008.

245. Park, C.; Yoon, J.; Thomas, E. L., *Polymer* 2003, *44* (22), 6725-6760.

246. Hillmyer, M. A., *Advances in Polymer Science* 2005, *190*, 137-181.

247. Kim, S.; Nealey, P. F.; Bates, F. S., *ACS Macro Letters* 2012, *1* (1), 11-14.

248. Coulon, G.; Russell, T. P.; Deline, V. R.; Green, P. F., *Macromolecules* 1989, *22* (6), 2581-2589.

249. Anastasiadis, S. H.; Russell, T. P.; Satija, S. K.; Majkrzak, C. F., *J. Chem. Phys.* 1990, *92* (9), 5677-5691.

250. Peters, R. D.; Yang, X. M.; Kim, T. K.; Sohn, B. H.; Nealey, P. F., *Langmuir* 2000, *16* (10), 4625-4631.

251. Maaloum, M.; Ausserre, D.; Chatenay, D.; Coulon, G.; Gallot, Y., *Phys. Rev. Lett.* 1992, *68* (10), 1575-1578.

252. Coulon, G.; Ausserre, D.; Russell, T. P., *Journal De Physique* 1990, *51* (8), 777-786.

253. Pickett, G. T.; Balazs, A. C., *Macromolecules* 1997, *30* (10), 3097-3103.

254. Han, E.; Kang, H. M.; Liu, C. C.; Nealey, P. F.; Gopalan, P., *Adv. Mater.* 2010, *22* (38), 4325-4329.

255. Mansky, P.; Russell, T. P.; Hawker, C. J.; Pitsikalis, M.; Mays, J., *Macromolecules* 1997, *30* (22), 6810-6813.

256. Huang, E.; Mansky, P.; Russell, T. P.; Harrison, C.; Chaikin, P. M.; Register, R. A.; Hawker, C. J.; Mays, J., *Macromolecules* 2000, *33* (1), 80-88.

257. Ji, S.; Liu, C. C.; Son, J. G.; Gotrik, K.; Craig, G. S. W.; Gopalan, P.; Himpsel, F. J.; Char, K.; Nealey, P. F., *Macromolecules* 2008, *41* (23), 9098-9103.

258. Cushen, J. D.; Bates, C. M.; Rausch, E. L.; Dean, L. M.; Zhou, S. X.; Willson, C. G.; Ellison, C. J., *Macromolecules* 2012, *45* (21), 8722-8728.

259. Clark, D. T.; Peeling, J.; Omalley, J. M., *Journal of Polymer Science Part A: Polymer Chemistry* 1976, *14* (3), 543-551.

260. Jung, Y. S.; Ross, C. A., *Nano Letters* 2007, *7* (7), 2046-2050.

261. Kennemur, J. G.; Hillmyer, M. A.; Bates, F. S., *Macromolecules* 2012, *45* (17), 7228-7236.

262. Rehse, N.; Knoll, A.; Magerle, R.; Krausch, G., *Macromolecules* 2003, *36* (9), 3261-3271.

263. Fasolka, M. J.; Mayes, A. M.; Magonov, S. N., *Ultramicroscopy* 2001, *90* (1), 21-31.

264. Smith, A. P.; Douglas, J. F.; Meredith, J. C.; Amis, E. J.; Karim, A., *Phys. Rev. Lett.* 2001, *87* (1), 015503.

265. Hasegawa, H.; Hashimoto, T., *Macromolecules* 1985, *18* (3), 589-590.

266. Lee, S. H.; Kang, H. M.; Kim, Y. S.; Char, K., *Macromolecules* 2003, *36* (13), 4907-4915.

267. Keen, I.; Yu, A. G.; Cheng, H. H.; Jack, K. S.; Nicholson, T. M.; Whittaker, A. K.; Blakey, I., *Langmuir* 2012, *28* (45), 15876-15888.

268. Joly, S.; Raquois, A.; Paris, F.; Hamdoun, B.; Auvray, L.; Ausserre, D.; Gallot, Y., *Phys. Rev. Lett.* 1996, *77* (21), 4394-4397.

269. Coulon, G.; Collin, B.; Ausserre, D.; Chatenay, D.; Russell, T. P., *Journal De Physique* 1990, *51* (24), 2801-2811.

270. Maaloum, M.; Ausserre, D.; Chatenay, D.; Gallot, Y., *Phys. Rev. Lett.* 1993, *70* (17), 2577-2580.

271. Cahn, J. W., *Transactions of the Metallurgical Society of AIME* 1968, *242* (1), 166-180.

272. Huang, J. S.; Goldburg, W. I.; Bjerkaas, A. W., *Phys. Rev. Lett.* 1974, *32* (17), 921-923.

273. Hashimoto, T.; Kumaki, J.; Kawai, H., *Macromolecules* 1983, *16* (4), 641-648.

274. Krausch, G.; Dai, C. A.; Kramer, E. J.; Bates, F. S., *Berichte Der Bunsen-Gesellschaft-Physical Chemistry Chemical Physics* 1994, *98* (3), 446-448.

275. Shull, K. R., *Macromolecules* 1992, *25* (8), 2122-2133.

276. Walton, D. G.; Kellogg, G. J.; Mayes, A. M.; Lambooy, P.; Russell, T. P., *Macromolecules* 1994, *27* (21), 6225-6228.

277. Lambooy, P.; Russell, T. P.; Kellogg, G. J.; Mayes, A. M.; Gallagher, P. D.; Satija, S. K., *Phys. Rev. Lett.* 1994, *72* (18), 2899-2902.

278. Koneripalli, N.; Singh, N.; Levicky, R.; Bates, F. S.; Gallagher, P. D.; Satija, S. K., *Macromolecules* 1995, *28* (8), 2897-2904.

279. Singh, N.; Kudrle, A.; Sikka, M.; Bates, F. S., *Journal De Physique II* 1995, *5* (3), 377-396.

280. Vignaud, G.; Gibaud, A.; Grubel, G.; Joly, S.; Ausserre, D.; Legrand, J. F.; Gallot, Y., *Physica B* 1998, *248* (1-4), 250-257.

281. Fredrickson, G. H., *Macromolecules* 1987, *20* (10), 2535-2542.

282. Grim, P. C. M.; Nyrkova, I. A.; Semenov, A. N.; ten Brinke, G.; Hadziioannou, G., *Macromolecules* 1995, *28* (22), 7501-7513.

283. Bassereau, P.; Brodbreck, D.; Russell, T. P.; Brown, H. R.; Shull, K. R., *Phys. Rev. Lett.* 1993, *71* (11), 1716-1719.

284. Ausserre, D.; Chatenay, D.; Coulon, G.; Collin, B., *Journal De Physique* 1990, *51* (22), 2571-2580.

285. Mayes, A. M.; Russell, T. P.; Bassereau, P.; Baker, S. M.; Smith, G. S., *Macromolecules* 1994, *27* (3), 749-755.

286. Collin, B.; Chatenay, D.; Coulon, G.; Ausserre, D.; Gallot, Y., *Macromolecules* 1992, *25* (5), 1621-1622.

287. Turner, M. S.; Maaloum, M.; Ausserre, D.; Joanny, J. F.; Kunz, M., *Journal De Physique II* 1994, *4* (4), 689-702.

288. Carvalho, B. L.; Thomas, E. L., *Phys. Rev. Lett.* 1994, *73* (24), 3321-3324.

289. Gido, S. P.; Gunther, J.; Thomas, E. L.; Hoffman, D., *Macromolecules* 1993, *26* (17), 4506-4520.

290. Bates, F. S.; Wiltzius, P., *J. Chem. Phys.* 1989, *91* (5), 3258-3274.

291. Hashimoto, T.; Takenaka, M.; Jinnai, H., *Journal of Applied Crystallography* 1991, *24* (5), 457-466.

292. Liu, Y.; Rafailovich, M. H.; Sokolov, J.; Schwarz, S. A.; Bahal, S., *Macromolecules* 1996, *29* (3), 899-906.

293. Henkee, C. S.; Thomas, E. L.; Fetters, L. J., *Journal of Materials Science* 1988, *23* (5), 1685-1694.

294. Hashimoto, T.; Takenaka, M.; Izumitani, T., *J. Chem. Phys.* 1992, *97* (1), 679-689.

295. Jain, S.; Bates, F. S., *Macromolecules* 2004, *37* (4), 1511-1523.

296. Lee, S.; Arunagirinathan, M. A.; Bates, F. S., *Langmuir* 2010, *26* (3), 1707-1715.

297. Shibayama, M.; Hashimoto, T.; Kawai, H., *Macromolecules* 1983, *16* (9), 1434-1443.

298. Smith, A. P.; Douglas, J. F.; Meredith, J. C.; Amis, E. J.; Karim, A., *Journal of Polymer Science Part B: Polymer Physics* 2001, *39* (18), 2141-2158.

299. Coulon, G.; Collin, B.; Chatenay, D.; Gallot, Y., *Journal De Physique II* 1993, *3* (5), 697-717.

300. Zhang, L. F.; Eisenberg, A., *Science* 1995, *268* (5218), 1728-1731.

301. Dalvi, M. C.; Lodge, T. P., *Macromolecules* 1993, *26* (4), 859-861.

302. Hamersky, M. W.; Tirrell, M.; Lodge, T. P., *Langmuir* 1998, *14* (24), 6974-6979.

303. Whitesides, G. M.; Grzybowski, B., *Science* 2002, *295* (5564), 2418-2421.

304. *International Technology Roadmap for Semiconductors 2007*. Semiconductor Industry Association.

305. Lin, Y.; Boker, A.; He, J. B.; Sill, K.; Xiang, H. Q.; Abetz, C.; Li, X. F.; Wang, J.; Emrick, T.; Long, S.; Wang, Q.; Balazs, A.; Russell, T. P., *Nature* 2005, *434* (7029), 55-59.

306. Nandan, B.; Vyas, M. K.; Bohme, M.; Stamm, M., *Macromolecules* 2010, *43* (5), 2463-2473.

307. Fukunaga, K.; Elbs, H.; Magerle, R.; Krausch, G., *Macromolecules* 2000, *33* (3), 947-953.

308. Bang, J.; Kim, B. J.; Stein, G. E.; Russell, T. P.; Li, X.; Wang, J.; Kramer, E. J.; Hawker, C. J., *Macromolecules* 2007, *40* (19), 7019-7025.

309. Grozea, C. M.; Li, I. T. S.; Grozea, D.; Walker, G. C., *Macromolecules* 2011, *44* (10), 3901-3909.

310. Wolff, T.; Burger, C.; Ruland, W., *Macromolecules* 1993, *26* (7), 1707-1711.

311. Rosedale, J.; Bates, F. S.; Almdal, K.; Mortensen, K.; Wignall, G. D., *Macromolecules* 1995, *28* (5), 1429-1443.

312. Bates, F. S.; Rosedale, J. H.; Fredrickson, G. H., *J. Chem. Phys.* 1990, *92* (10), 6255-6270.

313. Turner, M. S.; Rubinstein, M.; Marques, C. M., *Macromolecules* 1994, *27* (18), 4986-4992.

314. Ham, S.; Shin, C.; Kim, E.; Ryu, D. Y.; Jeong, U.; Russell, T. P.; Hawker, C. J., *Macromolecules* 2008, *41* (17), 6431-6437.

315. Pickett, G. T.; Witten, T. A.; Nagel, S. R., *Macromolecules* 1993, *26* (12), 3194-3199.

316. Torres, J. A.; Nealey, P. F.; de Pablo, J. J., *Phys. Rev. Lett.* 2000, *85* (15), 3221-3224.

317. Sakamoto, N.; Hashimoto, T., *Macromolecules* 1998, *31* (12), 3815-3823.

318. Alexander-Katz, A.; Fredrickson, G. H., *Macromolecules* 2007, *40* (11), 4075-4087.

319. Matsen, M. W.; Bates, F. S., *Macromolecules* 1996, *29* (4), 1091-1098.

320. Mori, K.; Hasegawa, H.; Hashimoto, T., *Polymer* 2001, *42* (7), 3009-3021.

321. Lescanec, R. L.; Muthukumar, M., *Macromolecules* 1993, *26* (15), 3908-3916.

322. Hajduk, D. A.; Harper, P. E.; Gruner, S. M.; Honeker, C. C.; Kim, G.; Thomas, E. L.; Fetters, L. J., *Macromolecules* 1994, *27* (15), 4063-4075.

323. Hamley, I. W.; Koppi, K. A.; Rosedale, J. H.; Bates, F. S.; Almdal, K.; Mortensen, K., *Macromolecules* 1993, *26* (22), 5959-5970.

324. Papadakis, C. M.; Almdal, K.; Mortensen, K.; Posselt, D., *Europhysics Letters* 1996, *36* (4), 289-294.

325. Matsen, M. W.; Bates, F. S., *J. Chem. Phys.* 1997, *106*, 2436-2448.

326. Knoll, A.; Horvat, A.; Lyakhova, K. S.; Krausch, G.; Sevink, G. J. A.; Zvelindovsky, A. V.; Magerle, R., *Phys. Rev. Lett.* 2002, *89* (3), 035501.

327. Yager, K. G.; Berry, B. C.; Page, K.; Patton, D.; Karim, A.; Amis, E. J., *Soft Matter* 2009, *5* (3), 622-628.

328. Fasolka, M. J.; Harris, D. J.; Mayes, A. M.; Yoon, M.; Mochrie, S. G. J., *Phys. Rev. Lett.* 1997, *79* (16), 3018-3021.

329. Park, S. M.; Berry, B. C.; Dobisz, E.; Kim, H. C., *Soft Matter* 2009, *5* (5), 957-961.

330. Brazovskii, S. A., *Sov. Phys. JETP* 1975, *41* (1), 85-89.

331. Sakamoto, N.; Hashimoto, T., *Macromolecules* 1995, *28* (20), 6825-6834.

332. Stuhn, B.; Mutter, R.; Albrecht, T., *Europhysics Letters* 1992, *18* (5), 427-432.

333. Ma, S.-k., *Modern Theory of Critical Phenomena*. Benjamin Inc.: Reading, MA, 1976.

334. Mader, S., *Thin Solid Films* 1976, *35* (2), 195-200.

335. Sirota, E. B.; Pershan, P. S.; Sorensen, L. B.; Collett, J., *Physical Review A* 1987, *36* (6), 2890-2901.

336. Stein, G. E.; Kramer, E. J.; Li, X. F.; Wang, J., *Macromolecules* 2007, *40* (7), 2453-2460.

337. Hu, H. W.; Granick, S., *Science* 1992, *258* (5086), 1339-1342.

338. Menelle, A.; Russell, T. P.; Anastasiadis, S. H.; Satija, S. K.; Majkrzak, C. F., *Phys. Rev. Lett.* 1992, *68* (1), 67-70.

339. Russell, T. P.; Hjelm, R. P.; Seeger, P. A., *Macromolecules* 1990, *23* (3), 890-893.

340. Rouault, Y.; Baschnagel, J.; Binder, K., *Journal of Statistical Physics* 1995, *80* (5-6), 1009-1031.

341. Li, H.; Paczuski, M.; Kardar, M.; Huang, K., *Physical Review B* 1991, *44* (15), 8274-8283.

342. Nakanishi, H.; Fisher, M. E., *J. Chem. Phys.* 1983, *78* (6), 3279-3293.

343. Miao, B.; Yan, D. D.; Han, C. C.; Shi, A. C., *J. Chem. Phys.* 2006, *124* (14), 144902.

344. Kim, E.; Choi, S.; Guo, R.; Ryu, D. Y.; Hawker, C. J.; Russell, T. R., *Polymer* 2010, *51* (26), 6313-6318.

345. Hammond, M. R.; Cochran, E.; Fredrickson, G. H.; Kramer, E. J., *Macromolecules* 2005, *38* (15), 6575-6585.

346. Khanna, V.; Cochran, E. W.; Hexemer, A.; Stein, G. E.; Fredrickson, G. H.; Kramer, E. J.; Li, X.; Wang, J.; Hahn, S. F., *Macromolecules* 2006, *39* (26), 9346-9356.

347. Green, P. F.; Christensen, T. M.; Russell, T. P.; Jerome, R., *Macromolecules* 1989, *22* (5), 2189-2194.

348. Tcherkasskaya, O.; Ni, S. R.; Winnik, M. A., *Macromolecules* 1996, *29* (2), 610-616.

349. Russell, T. P., *Macromolecules* 1993, *26* (21), 5819-5819.

Appendix A. ABA Triblock Copolymers

Poly(methyl methacrylate-*b*-styrene-*b*-methyl methacrylate) (MSM) triblock copolymers were prepared using a potassium naphthalenide difunctional initiator and characterized in the bulk state.

A.1 Experimental

After moisture and oxygen were removed from a graduated tower, known amounts of naphthalene and potassium metal (10 % molar excess) were added to the tower in an inert environment. Tetrahydrofuran (THF) was added using a cannula, and the dark green mixture was stirred using a glass stir bar for 2 – 4 days. The initiator concentration was estimated by titrating a water-quenched initiator solution with a standard hydrochloric acid solution while phenolphthalein was used as the indicator. The purification of styrene, methyl methacrylate, and 1,1-diphenylethylene was conducted as shown in Chapter 3.

First, the initiator was slowly added into a reactor with THF until the dark green color in THF stopped fading. Then, the controlled amount of the initiator was added. After the reactor temperature was lowered using a dry ice bath (-78 °C), styrene, 1,1-diphenylethylene, and methyl methacrylate were added subsequently after allowing 30 minutes of reaction per each. Finally, degassed methanol was added to terminate the reaction. The polymers were precipitated in methanol and dried prior to the use.

The number average molecular weight (M_n) and polydispersity index of MSM were measured using size exclusion chromatograph (SEC) (Hewlett-Packard 1100 HPLC, HP 1047A refractive index detector, chloroform mobile phase). The weight fractions of poly(styrene) and poly(methyl methacrylate) blocks in MSM were estimated

using nuclear magnetic resonance (^{1}H-NMR) (VAC-300 Autosampler, IBM Instruments). The glass transition temperature associated with each block in MSM was measured using differential scanning calorimetry (DSC) (Q1000 DSC, TA Instruments) taken at ±10 °C/min. After the specimens had been thermally annealed at 190 °C for 8 hours, small-angle x-ray scattering (SAXS) at Argonne National Laboratory was employed at room temperature in order to study the bulk morphology. The rheological properties of MSM were measured using a rheometer (ARES, Rheometric Scientific).

A.2 PRELIMINARY RESULTS

The summary of MSM characterization is shown in Table A.1. Figure A.1 demonstrates successful polymerization characterized by monodisperse profiles with low polydispersity index. The molecular weight and composition of MSM1 were calculated using the NMR results (Figure A.2).

Table A.1 Molecular characterization.

	M_n (kg/mol) [a]	f_{MMA1} [b]	f_S [b]	f_{MMA2} [b]	PDI	T_g (°C)
MSM1	14.1-28.9-14.1	0.23	0.54	0.23	1.13	110, 122

[a] The SEC measurement of the poly(styrene) block aliquots gave the result of 28.9 kg/mol. M_n of poly(methyl methacrylate) blocks was calculated by comparing the molecular weight of the poly(styrene) aliquot with the ratio between the poly(styrene) and the poly(methyl methacrylate) blocks estimated from the NMR measurement.

[b] Densities at 140 °C were used to calculate the volume fractions (f_S, f_{MMA}).

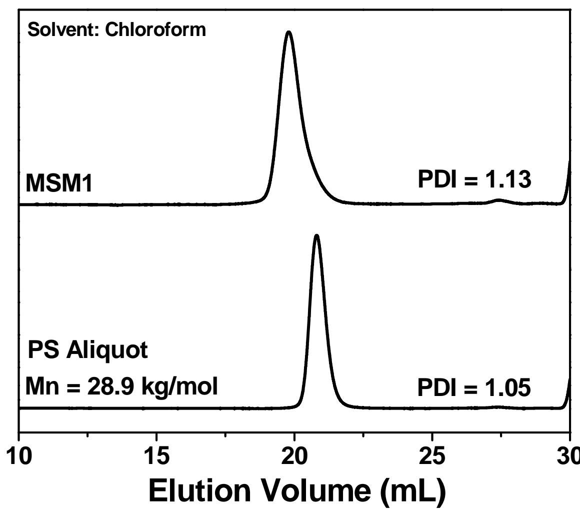

Figure A.1 SEC traces of MSM1 and its poly(styrene) aliquot.

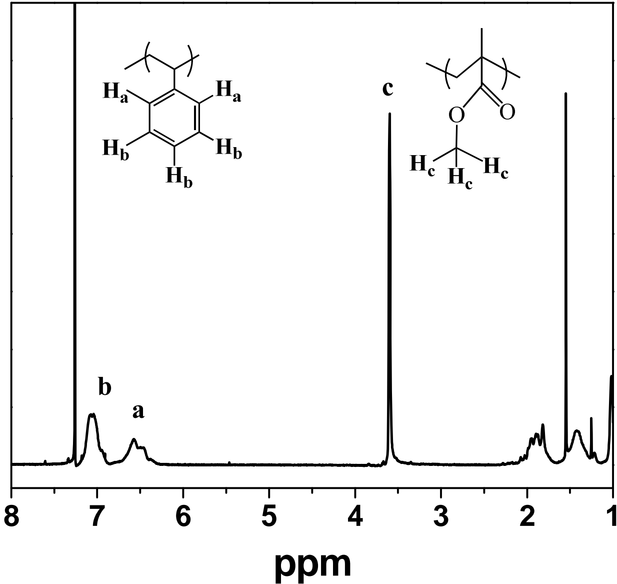

Figure A.2 ^{1}H-NMR spectrum for MSM1.

DSC traces in Figure A.3 show two glass transition at 110 °C and 122 °C, each associated with the poly(styrene) block and the syndiotactic poly(methyl methacrylate) block. As shown in Figure A.4, the peaks located at the integer multiples of the primary peak suggest that the bulk morphology of MSM1 is lamellar with the periodicity L_0 of 24.2 nm. MSM1 does not exhibit any abrupt change in G′, indicative of the absence of the order-disorder transition for the range of temperature probed (160 – 250 °C) (Figure A.5). Figure A.6a displays the master curve created from applying time temperature superposition to G′ and G″ taken at different temperatures (T_{ref} = 260 °C). The fit of the shift factors (a_T) to the Williams-Landel-Ferry (WLF) equation is shown in Figure A.6b. MSM1 exhibits non-terminal behavior (G′ ~ G″ ~ $\omega^{0.5}$), suggesting that MSM1 is ordered.

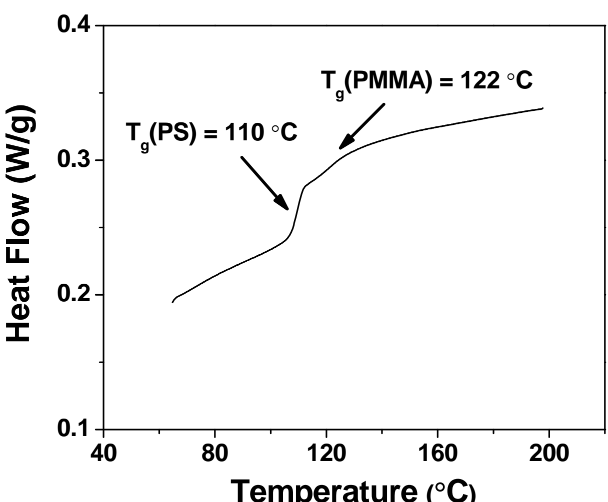

Figure A.3 DSC trace of MSM1.

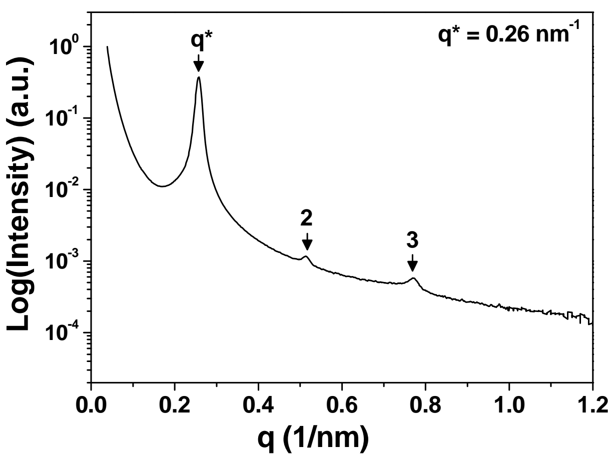

Figure A.4 SAXS of MSM1 taken at room temperature.

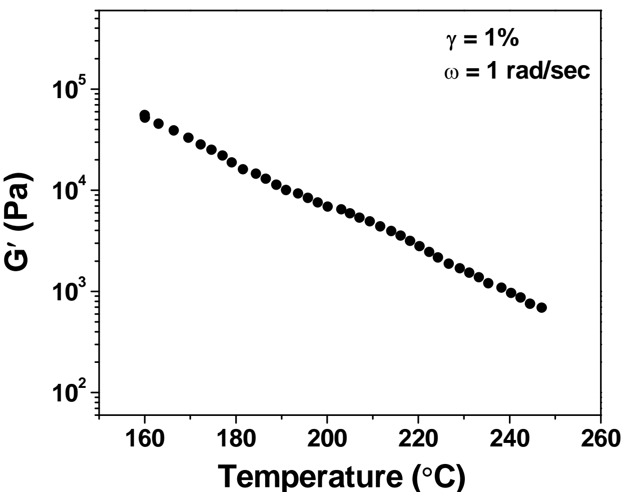

Figure A.5 Temperature dependence of the dynamic elastic modulus G′(ω = 1 rad/sec) for SI14E on heating (+10 °C/min) with 1% strain.

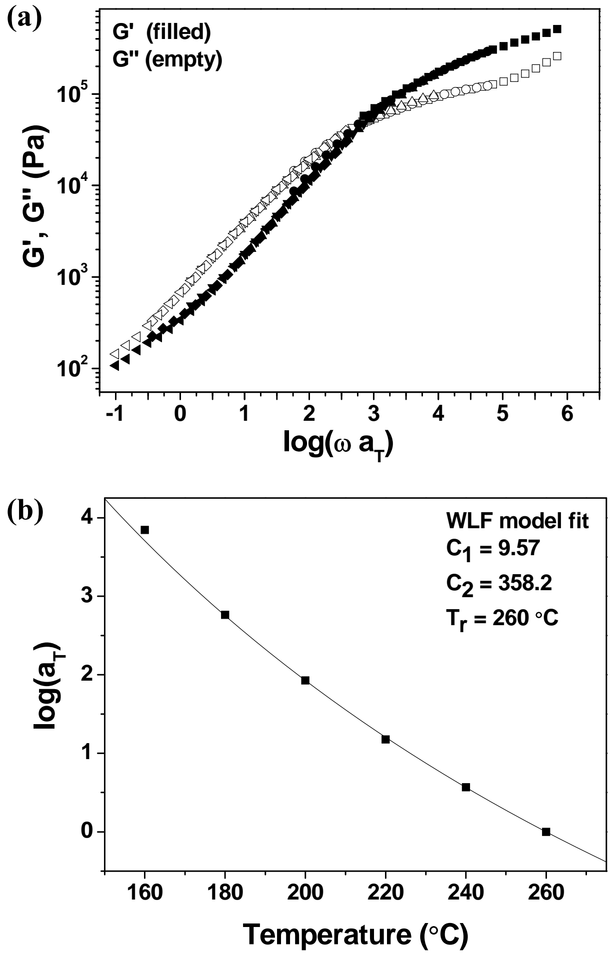

Figure A.6 (a) Reduced frequency (a_T ω) plot for dynamic storage modulus (G′) and loss modulus (G″) for MSM1. (b) The shift factors as a function of temperature. The fit to the Williams-Landel-Ferry (WLF) equation (solid line) leads to C_1 = 9.57 and C_2 = 358.2 (T_{ref} = 260 °C).